



metals

3D Printing of Metals

Edited by
Manoj Gupta

Printed Edition of the Special Issue Published in *Metals*

3D Printing of Metals

Special Issue Editor
Manoj Gupta

MDPI • Basel • Beijing • Wuhan • Barcelona • Belgrade



Special Issue Editor
Manoj Gupta
Materials Group
Singapore

Editorial Office
MDPI AG
St. Alban-Anlage 66
Basel, Switzerland

This edition is a reprint of the Special Issue published online in the open access journal *Metals* (ISSN 2075-4701) from 2016–2017 (available at: http://www.mdpi.com/journal/metals/special_issues/3D_printing).

For citation purposes, cite each article independently as indicated on the article page online and as indicated below:

Author 1; Author 2. Article title. *Journal Name Year, Article number, page range.*

First Edition 2017

ISBN 978-3-03842-591-5 (Pbk)
ISBN 978-3-03842-592-2 (PDF)

Articles in this volume are Open Access and distributed under the Creative Commons Attribution license (CC BY), which allows users to download, copy and build upon published articles even for commercial purposes, as long as the author and publisher are properly credited, which ensures maximum dissemination and a wider impact of our publications. The book taken as a whole is © 2017 MDPI, Basel, Switzerland, distributed under the terms and conditions of the Creative Commons license CC BY-NC-ND (<http://creativecommons.org/licenses/by-nc-nd/4.0/>).

Table of Contents

About the Special Issue Editor	v
Preface to “3D Printing of Metals”	vii
Manoj Gupta	
3D Printing of Metals	
Reprinted from: <i>Metals</i> 2017, 7(10), 403; doi: 10.3390/met7100403	1
Vyasaraj Manakari, Gururaj Parande and Manoj Gupta	
Selective Laser Melting of Magnesium and Magnesium Alloy Powders: A Review	
Reprinted from: <i>Metals</i> 2017, 7(1), 2; doi: 10.3390/met7010002	3
Wei Quan Toh, Pan Wang, Xipeng Tan, Mui Ling Sharon Nai, Erjia Liu and Shu Beng Tor	
Microstructure and Wear Properties of Electron Beam Melted Ti-6Al-4V Parts: A Comparison	
Study against As-Cast Form	
Reprinted from: <i>Metals</i> 2016, 6(11), 284; doi: 10.3390/met6110284	39
Volker Weißmann, Philipp Drescher, Rainer Bader, Hermann Seitz, Harald Hansmann and Nico Laufer	
Comparison of Single Ti6Al4V Struts Made Using Selective Laser Melting and Electron	
Beam Melting Subject to Part Orientation	
Reprinted from: <i>Metals</i> 2017, 7(3), 91; doi: 10.3390/met7030091	52
Riccardo Casati, Jannis N. Lemke, Ausonio Tuissi and Maurizio Vedani	
Aging Behaviour and Mechanical Performance of 18-Ni 300 Steel Processed by	
Selective Laser Melting	
Reprinted from: <i>Metals</i> 2016, 6(9), 218; doi: 10.3390/met6090218	74
Li Tang, Chunbing Wu, Zhixiong Zhang, Jianzhong Shang and Chao Yan	
A Lightweight Structure Redesign Method Based on Selective Laser Melting	
Reprinted from: <i>Metals</i> 2016, 6(11), 280; doi: 10.3390/met6110280	87
Lianfeng Wang, Jiubin Jue, Mujian Xia, Lijie Guo, Biao Yan and Dongdong Gu	
Effect of the Thermodynamic Behavior of Selective Laser Melting on the Formation of	
In situ Oxide Dispersion-Strengthened Aluminum-Based Composites	
Reprinted from: <i>Metals</i> 2016, 6(11), 286; doi: 10.3390/met6110286	108
Shahir Mohd Yusuf, Yifei Chen, Richard Boardman, Shoufeng Yang and Nong Gao	
Investigation on Porosity and Microhardness of 316L Stainless Steel Fabricated by Selective	
Laser Melting	
Reprinted from: <i>Metals</i> 2017, 7(2), 64; doi: 10.3390/met7020064	119
Markus Bambach, Alexander Sviridov, Andreas Weisheit and	
Johannes Henrich Schleifenbaum	
Case Studies on Local Reinforcement of Sheet Metal Components by Laser	
Additive Manufacturing	
Reprinted from: <i>Metals</i> 2017, 7(4), 113; doi: 10.3390/met7040113	131

**Xin Wang, Jun Du, Zhengying Wei, Xuewei Fang, Guangxi Zhao, Hao Bai, Wei Liu,
Chuanqi Ren and Yunfei Yao**

Morphology Analysis of a Multilayer Single Pass via Novel Metal Thin-Wall Coating Forming

Reprinted from: *Metals* **2016**, *6*(12), 313; doi: 10.3390/met6120313 145

About the Special Issue Editor

Manoj Gupta was a former Head of Materials Division of the Mechanical Engineering Department and Director designate of Materials Science and Engineering Initiative at NUS, Singapore. He did his Ph.D. from University of California, Irvine, USA (1992), and postdoctoral research at University of Alberta, Canada (1992). He is among among Top 2.5% Scientists in the World as recorded by ResearchGate. To his credit are: (i) Disintegrated Melt Deposition technique and (ii) Hybrid Microwave Sintering technique, an energy efficient solid-state processing method to synthesize alloys/micro/nano-composites. He has published over 455 peer reviewed journal papers and owns two US patents. His current h-index is 55, RG index is 46 and citations are greater than 12000. He has also co-authored five books, published by John Wiley and Springer in 2015. A multiple award winner, he actively collaborate/visit Japan, France, Saudi Arabia, Qatar, China, USA and India.

Preface to “3D Printing of Metals”

3D printing is a futuristic technology capable of transforming the ways in which we make components and devices. It is almost certain that this technique will find its niche in manufacturing sector in very near future. In view of the growing importance of 3D printing, this book addresses key issues related to emerging science and technology in this area. Detailed and informative articles are presented in this book related to a wide variety of materials including those based on critical engineering metals such as aluminum, magnesium, titanium and composites. Advancement in various techniques such as electron beam melting and selective laser melting are discussed. Of key importance in the area of materials science is the end properties of the materials following processing. Accordingly, the articles presented critically discusses the effects of microstructural features such as porosity, forming defects and the heat treatment induced effects on the mechanical properties. Applications targeted in these articles are targeted at aerospace, automobile, defense and aerospace sectors. Overall, the information presented in this book is of significant importance for academic and industry based researchers who wishes to update themselves with this upcoming marvellous and promising manufacturing technique.

Manoj Gupta

Special Issue Editor

Editorial

3D Printing of Metals

Manoj Gupta

Department of Mechanical Engineering, National University of Singapore, 9 Engineering Drive 1, Singapore 117576, Singapore; mpegm@nus.edu.sg; Tel.: +65-6516-6358

Academic Editor: Hugo F. Lopez

Received: 26 September 2017; Accepted: 28 September 2017; Published: 29 September 2017

3D printing is an emerging technique of immense engineering importance, capable of transforming the way we make components. It has been explored worldwide for metals, ceramics and polymers. 3D printing offers several advantages such as the following [1,2]:

- (a) Shorter lead time
- (b) Low cost
- (c) Small volume of parts without the need of tooling or fixture
- (d) Capability to fabricate near net shapes
- (e) Design freedom that allows the fabrication of simple and complex shapes
- (f) Potential to handle conventional and specialized materials.

The potential benefits that could be derived if the science and technology of 3D printing were to be established have been the crux behind monumental efforts by governments, in most countries, that invest billions of dollars to develop this manufacturing technology. Multiple engineering sectors are targeting the integration of 3D printing in their manufacturing section, especially where the batch size is not big and the parts are specialized. These requirements are particularly applicable to automotive [2], aerospace [3,4] and biomedical sectors [5,6].

The current Special Issue was targeted at metal-based materials as 3D printing of metals is particularly challenging due to a host of microstructural changes that are encountered, especially when the metals and alloys are exposed to high temperatures. Control of the dimensional accuracy and end properties is still being explored by researchers for different types of metals and alloys as the results of one compositional system cannot be translated to another compositional system. Overall, nine papers (one review and eight research papers) have been published in this issue. The materials investigated were the following:

- a. Aluminum-based materials
- b. Magnesium-based materials
- c. Steels
- d. Titanium-based materials
- e. Oxide dispersion-strengthened aluminum-based composites

This suggests that there is no preferred metal system that is targeted by researchers but all important metallic materials are equally targeted.

3D printing techniques that were utilized in the papers published in this issue included the following:

- a. Micro-coating metal additive manufacturing (MCMAM)—new technique
- b. Electron beam melting
- c. Selective laser melting
- d. Laser metal deposition

Most of the papers, including the review paper, targeted selective laser melting, suggesting its popularity among researchers. The research issues addressed in these papers included the following:

- a. Sheet metal forming
- b. Effect of heat treatment
- c. Failure under compression
- d. Porosity distribution, microstructure and hardness
- e. Forming defects as a function of processing parameters
- f. Wear properties
- g. Interrelation between structure size, mechanical characteristics and process defect
- h. Interrelation between aging behavior and mechanical performance.

The above indicated research issues broadly indicate that researchers are in the process of tailoring their processing parameters to control the microstructure, including process defects, so that their targeted properties are not compromised and remain suitable for their targeted applications.

Targeted industrial sectors mentioned in these papers included the following:

- a. Aerospace sector
- b. Biomedical sector
- c. Defense
- d. Automobile

This suggests the main drivers of 3D printing in the research community. The present Special Issue, in general, is very informative as the nine articles cover a variety of topics and challenges and for different metallic materials (ferrous and non-ferrous) covering four different types of 3D printing techniques and issues related to microstructure, process defects, mechanical properties and heat treatments for a wide spectrum of applications.

Finally, I would like to thank all the authors for their excellent contribution to this issue, to the reviewers for making useful comments and to the *Metals* editorial staff for their timely publication of these articles.

Conflicts of Interest: The author declares no conflict of interest.

References

1. ASTM. *Standard Terminology for Additive Manufacturing Technologies*; F2792-12a; ASTM International: West Conshohocken, PA, USA, 2015.
2. Guo, N.; Leu, M. Additive manufacturing: Technology, applications and research needs. *Front. Mech. Eng.* **2013**, *8*, 215–243. [CrossRef]
3. Nickels, L. AM and aerospace: An ideal combination. *Met. Powder Rep.* **2015**, *70*, 300–303. [CrossRef]
4. Schiller, G.J. Additive manufacturing for Aerospace. In Proceedings of the IEEE Aerospace Conference, Big Sky, MT, USA, 7–14 March 2015.
5. Bose, S.; Vahabzadeh, S.; Bandyopadhyay, A. Bone tissue engineering using 3D printing. *Mater. Today* **2013**, *16*, 496–504. [CrossRef]
6. Ho, C.M.B.; Ng, S.H.; Yoon, Y.-J. A review on 3D printed bioimplants. *Int. J. Precis. Eng. Manuf.* **2015**, *16*, 1035–1046. [CrossRef]



© 2017 by the author. Licensee MDPI, Basel, Switzerland. This article is an open access article distributed under the terms and conditions of the Creative Commons Attribution (CC BY) license (<http://creativecommons.org/licenses/by/4.0/>).

Review

Selective Laser Melting of Magnesium and Magnesium Alloy Powders: A Review

Vyasaraj Manakari, Gururaj Parande and Manoj Gupta *

Department of Mechanical Engineering, National University of Singapore, 9 Engineering Drive 1, Singapore 117576, Singapore; mbvyasaraj@u.nus.edu (V.M.); gururaj.parande@u.nus.edu (G.P.)

* Correspondence: mpegm@nus.edu.sg; Tel.: +65-6516-6358

Academic Editor: Hugo F. Lopez

Received: 9 September 2016; Accepted: 15 December 2016; Published: 26 December 2016

Abstract: Magnesium-based materials are used primarily in developing lightweight structures owing to their lower density. Further, being biocompatible they offer potential for use as bioresorbable materials for degradable bone replacement implants. The design and manufacture of complex shaped components made of magnesium with good quality are in high demand in the automotive, aerospace, and biomedical areas. Selective laser melting (SLM) is becoming a powerful additive manufacturing technology, enabling the manufacture of customized, complex metallic designs. This article reviews the recent progress in the SLM of magnesium based materials. Effects of SLM process parameters and powder properties on the processing and densification of the magnesium alloys are discussed in detail. The microstructure and metallurgical defects encountered in the SLM processed parts are described. Applications of SLM for potential biomedical applications in magnesium alloys are also addressed. Finally, the paper summarizes the findings from this review together with some proposed future challenges for advancing the knowledge in the SLM processing of magnesium alloy powders.

Keywords: selective laser melting (SLM); magnesium; additive manufacturing; microstructure; mechanical properties; corrosion behavior

1. Introduction

Magnesium (Mg) is the sixth most abundant element in the earth's crust comprising about 2.7% of its composition [1]. Magnesium based materials are preferred when targeting weight-sensitive applications, as they are the lightest structural material available with a density of only 1.74 g/cc which is ~33%, ~61% and ~77% lower than that of aluminium, titanium, and iron, respectively [2]. Increasing demand for light weighting drives the interest for magnesium to be used in various engineering applications to achieve higher fuel economy, emission reduction etc. Other than its low density, magnesium based materials also exhibit high specific mechanical properties, excellent castability and machinability, high damping characteristics, high thermal stability, high thermal and electrical conductivity, and resistance to electromagnetic radiation [3–7]. However, the application areas of magnesium have been limited by its low corrosion resistance and relatively poor mechanical properties, such as low elastic modulus, low strength, limited room temperature ductility and toughness, rapid loss of strength with temperature, and poor creep resistance [8,9].

Even though magnesium based materials are not suitable where a high modulus is required, a range of applications has been evaluated in the biomaterials area in the recent past. The combination of superior biocompatibility, biodegradability, elastic modulus closer to human bone, and favourable mechanical properties makes magnesium one of the most sought after materials for orthopaedic applications like implants and fixation devices [10]. In the recent past, many magnesium alloys have been developed targeting biomedical applications ranging from maxillofacial reconstruction, to paediatric orthopaedics, vascular stents, surgical clips, screws, plates, and bone-interfacing

implants [11–13]. Magnesium based materials have lower Young's modulus (41–45 GPa) than commonly used metallic biomaterials such as titanium (55–110 GPa), 316L stainless steel (210 GPa), and cobalt chromium alloys (240 GPa) and show no indications of local or systemic toxicity [14–16]. In addition, they are also osteo-conductive, facilitate bone cell in-growth, and have a role in cell attachment [17]. Due to these advantages, new types of magnesium implant materials have been developed which effectively aid in the mitigation of stress-shielding effects and have potential for use as a bioresorbable material for degradable bone replacement, eliminating the need of secondary surgical procedures [10]. Although magnesium has many advantages, suitable for hard tissue implant and tissue engineering scaffold material, usage of magnesium is still limited in clinical applications due to its poor formability, rapid degradation in a high chloride physiological environment and hydrogen evolution [18]. Therefore, continuous efforts are being made by researchers to develop new types of magnesium alloys and composites to meet specific property requirements and explore new processing technologies to fabricate patient-specific implant components that can be provided with additional functions to further broaden the horizon of magnesium utilization in bio-medical applications.

Magnesium based materials are usually fabricated by conventional manufacturing methods such as deformation processing, casting, and powder metallurgy (P/M) techniques. Usually lightweight engineering parts with high performance can be obtained from deformation processing of magnesium based materials. However, due to the hexagonal closed packing (HCP) structure of magnesium, magnesium alloys exhibit poor cold workability at room temperature. Deformation processing of magnesium therefore needs to be performed at elevated forming temperatures to activate more slip systems and to allow better formability, which leads to poor surface quality and oxidation of parts and limits efficiency [19]. As a result, consumption of wrought magnesium products only represent a small fraction, merely about 1.5% of total magnesium consumption [20]. Presently, casting is the most conventional and dominant synthesis route used for the manufacture of magnesium alloys and composites. Although, casting techniques ensure great efficiency with higher precision, it is difficult to fabricate near-net shape structures of complex shapes and intricate internal architectures. Moreover, it is often the case that product quality is degraded by the thermodynamically stable phases that are formed during solidification from the melt and strong oxidising tendency of magnesium [21]. It is not possible to control the morphology and/or distribution of these phases during cooling. Therefore, several P/M routes are being explored to target unique microstructures, novel alloy compositions, and high performance in magnesium alloys [22]. Promising results were obtained by reinforcing magnesium with nanocrystalline and amorphous alloy powders. For example, Mg-Zn-Y alloys having very high tensile yield strengths in the range of 480–610 MPa with an elongation between 5% and 16% were developed using a rapidly solidified P/M approach [23]. Also, advanced powder based manufacturing processes such as additive manufacturing (AM), cold spray, metal injection moulding, and friction stir processing are being developed to fabricate magnesium alloys having non-equilibrium compositions and limited defects [22]. These techniques can be successfully employed to design intricate and near net shaped structures. In a recent study, Tandon et al. [24] showed that magnesium alloy powders can be potentially used to manufacture and repair lightweight components for aerospace applications by using cold spray and laser assisted deposition processes.

As magnesium is expanding into a more promising lightweight regime and medical technology applications, there is a great need for intelligent selection of manufacturing processes to provide unique functional properties, crash performance, and corrosion resistance. Customised components and implants with improved mechanical and physical properties can be manufactured by additive manufacturing (AM) techniques. AM includes a whole host of "bottom up" approaches, wherein the processes involve creating three-dimensional objects fabricated directly from computer aided design (CAD) models by gradually building them up, layer-by-layer within a powder bed. Among the AM methods, laser-based AM has an immense potential for producing fully dense metallic structures using a variety of available metal powders and has attracted more and more attention [25]. Selective laser melting (SLM) is one such process that uses high intensity laser as an energy source to directly fuse

the high-temperature metallic powder layers successively deposited one over the other as ultrathin two-dimensional cross-sections [26]. Generally, the geometrically complex components have been fabricated by SLM with a high dimensional precision and good surface integrity without other subsequent process requirements, which the conventional techniques (e.g., casting and machining) cannot keep pace with easily [27]. SLM is an efficient approach that can significantly shorten the lead time and the costs involved in the manufacturing of high-value components and offers advantages of design freedom with a wide choice of materials, reduced material wastage, and elimination of expensive tooling. Over the years, the process of SLM has become very well established for titanium alloys [28], steel and iron alloys [29], nickel base super alloys [30,31], cobalt base alloys [32], and aluminium alloys [33] and is providing an ideal platform to fabricate complex products, novel shapes, hollow and functionally graded structures to exact dimensions for the aerospace, medical, and military industries.

Despite the continuing advancement, there are very few examples that have fully utilized the potential of SLM to produce fully dense near-net shape components of magnesium and to gain an understanding of laser processability. Accordingly, this review aims to identify the advancements to date in SLM processing of magnesium and magnesium alloy powders and outlines the trend for future research to expand the application range of magnesium based materials further.

2. Selective Laser Melting (SLM) Technology

SLM is a powder bed fusion process, wherein selective regions of the pre-spread powder particles are melted and fused by a high intensity laser energy source in a layer by layer manner according to computer aided design (CAD) data. The term “laser” implies that a laser is used for processing, “melting” refers to the particular situation in which powders are completely melted and the term “selective” specifies that only partial powder is processed [28]. The SLM system generally is comprised of a processing laser, an automatic powder delivery system, a building platform, a controlling computer system, and main accessory parts (e.g., inert gas system protection, roller/scrapper for powder deposition, and an overflow container) [34]. The focus and the movement of the laser beam on the build table is controlled by using a beam deflection system consisting of galvano-mirrors and a flat field-focusing lens. The entire process including the powder feeding, deposition system, scanning, temperature, atmosphere, and build are controlled by a manufacturing software. The overall processing stages of SLM include (i) designing a 3D object model of the component to be fabricated using CAD software and then slicing the designed part into many layers with every layer defined by a layer thickness (typically 20–100 μm); (ii) a substrate is fixed and levelled for part fabrication on the build platform; (iii) a protective atmosphere (e.g., argon or nitrogen) is fed into the build chamber to minimize possible surface oxidation and hydrogen pickup; (iv) spreading of a thin layer of metal powder by powder re-coater on a substrate plate with a thickness as the aforementioned sliced layer thickness; (v) scanning/processing the powder bed in a predefined pattern in order to produce layer wise shape based on the geometry defined by the CAD model; and (vi) lowering of the building platform by a predetermined distance and repeating the last two stages for successive layers of powder until the required components are completely built. In SLM, each layer is fabricated by first generating an outline of the key component features which is referred to as contouring and subsequently the powder within the contour is melted using an appropriate scanning strategy. Once the laser scanning process is completed, specimens from the substrate plate are separated either manually or by electrical discharge machining (EDM).

SLM is a deposition welding process wherein the laser beam melts the powder particles in welding beads and shows phenomena usually observed for welding processes [26]. The physical behaviour of the SLM process includes absorption, reflection, radiation, and heat transfer, melting and coalescence of powder particles, phase transformations, a moving interface between solid phase and liquid phase, fluid flow caused by the surface tension gradient and mass transportation within the molten pool followed by solidification, and chemical reactions [26,35]. Because of the use of

high-intensity laser, the powder particles are heated at a faster rate as the energy is absorbed via both bulk-coupling and powder-coupling mechanisms [36]. The energy is converted into heat and eventually the powder particles melt, coalesce, and form an agitated melt pool for some milliseconds (typically 0.5 to 25 ms). The molten pool formed, acquires the shape of a circular or segmental cylinder under the effect of surface tension [37]. Extremely short interaction time between the laser beam and the powder bed results in the formation of a transient temperature field with a high temperature up to 10^5 °C and a significant rapid quenching effect with very high cooling rates up to 10^{6-8} °C/s [38]. Rapid solidification may cause development of non-equilibrium metallurgical phenomena such as microstructural refinement, solid solution hardening and the formation of metastable phases, which can have a substantial effect in improving the resultant mechanical properties and corrosion resistance of the laser processed materials [39,40].

Literature has shown that components produced by SLM are completely dense and homogeneous without microscopic pores or voids and do not require any post-processing (such as infiltration with other materials or heat treatment) usually needed to improve the SLS (Selective Laser Sintered) components, other than the removal of parts and supports from the substrate plate. Another major advantage of SLM lies in its high feasibility in processing non-ferrous pure metals like Ti, Al, Cu, Mg, etc., which to date cannot be well processed using SLS [39]. Some common materials that have been investigated for SLM include: ferrous alloys, titanium, cobalt-chrome, nickel, aluminium, magnesium, copper, zinc, tungsten, and gold [41]. SLM also has the potential to produce components of very complex geometries with a gradient porosity which in turn allows the choice of property distribution to achieve required functions [42]. SLM is unique in that it can be used for the additive manufacturing (AM) of functionally graded and pure-metal parts, as well as for laser cladding/repair. Additive repair of damaged turbine engine hot-section components [43,44] made from nickel base super alloys is one example of such repairs. SLM is also capable of multi-material processing, i.e., utilizing different feedstock materials simultaneously to produce various alloys and functionally graded materials (FGMs) [45,46].

The main goal in SLM is to produce metallic parts with 100% density. Obtaining this objective is not easy because there is no mechanical pressure during SLM, and fluid dynamics in SLM is mainly driven by gravity and capillary forces along with thermal effects. Also, the absence of mechanical pressure during the processing may lead to reduced solubility of some elements in the melt during solidification causing discontinuous melting of the tracks and formation of pores resulting in an uneven surface [47,48] as shown in Figure 1a, where distribution of porosity and unmelted area within ZK60 sample produced by SLM is revealed. The materials also experience varying degrees of thermal fluctuation during the SLM process which may induce residual stresses in the laser melted layer undergoing rapid solidification [41]. This can lead to formation of hot cracks and delamination of parts as shown in Figure 1b. High heating/cooling rates during SLM can also lead to the formation of narrow heat affected zone (HAZ) around the melt pool. Presence of HAZ can alter the composition and/or microstructure of material influencing the quality and properties of the SLM-processed sample [28]. The transient thermal behaviour during the SLM process can be controlled considerably by processing parameters, such as laser power, scan speed, hatch spacing, layer thickness, and scanning pattern. Figure 2 provides an illustration of these process parameters commonly studied in SLM. These process parameters are adjusted such that a single melt vector can fuse completely with the neighbouring melt vectors and the preceding layer. Application of inappropriate processing conditions can lead to various undesirable effects such as irregularities in the surface morphology, thermal cracks, and balling effects. Therefore, it is important to establish the relationships between the principal SLM parameters and surface morphology and to optimize the SLM processing parameters to produce metallic parts with 100% density without cracks and fusion defects.

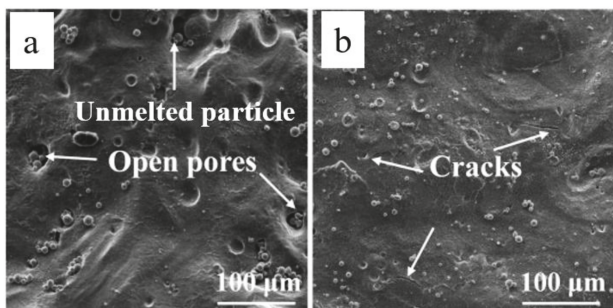


Figure 1. Scanning electron microscopy (SEM) microstructure of selective laser melting (SLM) produced ZK60 sample, showing (a) distribution of porosity and unmelted area and (b) formation of hot cracks within the ZK60 matrix [49].

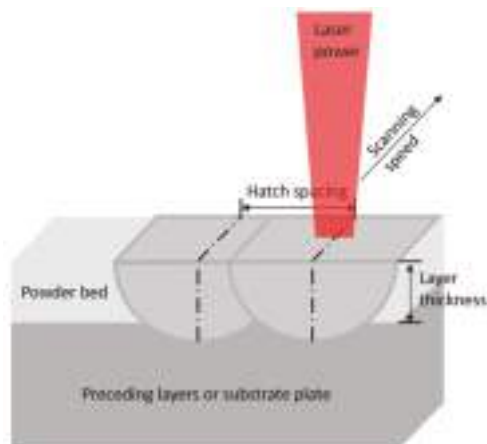


Figure 2. Schematic of SLM processing parameters [41].

3. Effects of Processing Parameters and Powder Properties on SLM Processing and Densification of Powders

SLM of metals requires careful selection of processing parameters to address the difficulties associated with the process such as oxidation, balling, thermal fluctuation, loss of alloying elements, and dross formation in the melt pool which lead to poor interlayer bonding, low density, instability of the tracks, crack formation, and delamination of the SLM processed part [50–52]. In order to gain a holistic understanding of the factors that influence the process of tracks formation, densification mechanism, part characteristics, and quality consistency of the fabricated parts by SLM, several processing and material parameters have been identified and are listed in Table 1. In an attempt to overcome these inherent difficulties along with ensuring good consolidation of the deposited material layers in SLM of metals, various approaches have been employed by researchers such as combination of preheating, selection of the right scanning strategy and process parameters to ensure minimal balling, utilisation of overpressure process chamber to control the vaporisation of powders, and melting in a shielded gas atmosphere of argon or helium to moderate the oxidation process [29,53]. Accordingly, this section focuses on the possible effects of the various parameters related to laser, scan, and powder during the building process on the formability, microstructure, and resulting properties of components produced from magnesium and magnesium alloy powders.

Table 1. Variables influencing the processing and densification mechanism of selective laser melting (SLM) processed parts [54].

SLM Processing Parameters		Material Properties
Laser type		Viscosity
Laser power		Surface tension
Mechanical layering of powder		Thermal conductivity
Atmospheric control		Specific heat
Gas flow		Absorptivity/reflectivity
Heaters (bed temperature)		Emissivity
Scan radius		Particle size distribution
Scan vector length		Particle shape
Scan spacing		Melting Temperature
Scan rates		Boiling Temperature
Scanning time interval		Chemical composition
Thickness of layers		Oxidation tendency

3.1. SLM Processing Windows of Magnesium and Magnesium Alloy Powders

From their preliminary experiments, Ng et al. [55] were able to successfully achieve full melting of single magnesium tracks using a miniature SLM system in an inert argon gas atmosphere and demonstrated the potential to employ magnesium powders in the fabrication of objects using SLM. Further, the interactions between laser sources and magnesium powder tracks under different processing conditions, including laser powers, scanning speeds, and irradiation modes (i.e., continuous wave and pulsed mode) were investigated and the processing window for the single track formation was established [56,57]. Also, several other investigations [58–65] have focused on developing processing windows based on the formability of magnesium and magnesium alloy powders such as Mg-9%Al, AZ91D, ZK60 and WE43 for fabricating single layer and multi-layer three dimensional parts. The details of the parameters used in these studies can be seen in Table 2. Figure 3 presents an example of a process map developed for SLM Mg-9%Al powders in which several distinct zones are observed.

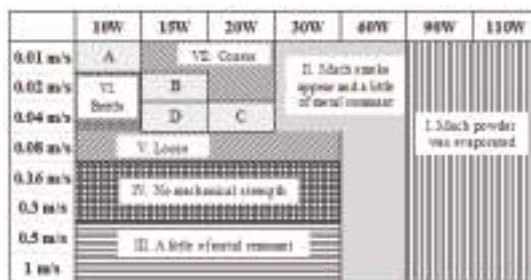


Figure 3. Process map for Mg-9%Al, results as function of the range of laser powers and scan speeds (modified from reference [60]).

During the process of SLM, the melting of the powder layer strongly depends on the input of laser energy supplied to the material. In this article, in order to have a single parameter to compare the processing conditions for single layer and multiple layer parts, specific laser energy density, E , is defined as:

$$E = \frac{\text{Laser power } (P)}{\text{Scanning velocity } (v) \times \text{Hatch spacing } (s)} \quad (1)$$

$$E = \frac{\text{Laser power } (P)}{\text{Scanning velocity } (v) \times \text{Hatch spacing } (s) \times \text{Layer thickness } (t)} \quad (2)$$

Table 2. Manufacturing parameters that have been used in the studies.

Materials System	Powder Characteristics	Laser Type	Spot Size (μm)	Power (W)	Layer Thickness (μm)	Hatch Spacing (μm)	Scanning Speed (mm/s)	Scanning Pattern
Mg [56;57]*	Spherical shape, mean particle size 25 μm, layer density 0.918 g /cc	Continuous and pulsed wave Nd:YAG Laser	600	13–26	500	—	10–200	Overlap (each layer was built by scanning numerous short vectors of 0.65 nm in the transverse direction with 98% overlapping)
Mg [58]*	Spherical shape, mean particle size 25 μm, layer density 0.918 g /cc, powders were preheated for 30 min to reach a temperature of 180 °C	Pulsed mode Nd: YAG Laser	270	8.9–17.7	150–300	—	10–200	—
Mg [59]	Gas atomised, spherical shape, particle size 250 μm (D_{50} = 25.85 μm) with apparent density of 0.78 g /cc and -400 mesh (D_{50} = 43.32 μm) with apparent density of 0.92 g /cc	Continuous Wave Nd: YAG Laser	100	15–150	30	100	50–100	Zigzag (scanning each layer in a direction rotated counter clockwise by 63.5° to its precursor)
Mg-9%Al [60]	Al-irregular shape, particle size (D_{50})=42 μm; Al-spherical shape, particle size (D_{50})=7 μm; blended for 45 min according to Mg: Al weight ratio of 9:1.9	Continuous wave Nd: YAG laser	34–75	10–110	50	80	10–1000	Linear
AZ91D [61]	Gas atomised, spherical shape, mean particle size 59 μm, apparent density 0.95 g /cc	Continuous wave IPG YLR-200 fibre laser	100	200	40	70–130	166.6–1000	Zigzag (scanning each layer in a direction rotated by 90° to its precursor)
ZK60 [62]	Spherical shape, mean particle size 30 μm	Continuous wave IPG YLR-200 fibre laser	150	200	20	80	100–900	Zigzag (scanning each layer in a direction rotated by 90° to its precursor)
ZK60 [49]	Spherical shape, mean particle size 50 μm	Fibre laser	150	50	100	100	6.7–11.7	—
Mg-Mn [66]	Mg-spherical shape; Mn-irregular shape mechanical mixing under a gas atmosphere of CO ₂ and SF ₆	Fibre laser	100	70	100	50	11.7	Linear
Mg-hydroxyapatite (HAP) [63]	Mg-irregular shape, particle size 200 μm; HAP particle size 20 nm; blended together according to Mg:HAP volume ratio of 98:2	Continuous wave fibre Laser	200	20–120	100	1000	1–160	Linear

* Only single tracks were used.

The above equations ((1) and (2)) present the energy density that is available to heat up and melt the powders for fabricating single (J/mm^2) and multiple layers (J/mm^3), respectively. The occurrence of various regions in the processing window as well as the resulting microstructure is dependent on the laser energy density, rather than laser power or scanning rate in isolation. Based on the formation quality of the specimens during the SLM process, four regions of behaviour could be defined over the considered range of the laser power and the scanning speed for different magnesium and magnesium alloy powders:

- I High energy input zone: In this zone the input energy density is too high under a high laser power for all speeds used. As a result, high temperatures witnessed in the molten pools causes evaporation and ionisation of the powders due to the low boiling point of magnesium ($1093\text{ }^\circ\text{C}$). The evaporated powders expand rapidly inducing a strong recoil effect on the molten pool and blowing the liquid and powder away resulting in no track formation. Vaporization of magnesium powders often results in condensation of volatilized materials on the laser window, disrupting the delivery of the laser power [50]. Moreover, effective temperature in the melt pool increased by the high-energy input affects the dynamic viscosity of the overheated liquid magnesium resulting in the instability of the melt pool. Molten magnesium possesses a much lower dynamic viscosity ($1.5\text{ Pa}\cdot\text{s}$) than iron ($6.93\text{ Pa}\cdot\text{s}$) and titanium ($2.2\text{ Pa}\cdot\text{s}$) alloys which are well established in the SLM process. The high energy input during laser processing induces high thermal stresses resulting in reduced viscosity of the melt pool which may lead to deformation of parts [64].
- II Low energy input zone: The presence of this zone is influenced by the lowest energy density for all the scanning speeds used combined with relatively low laser power. Using a low laser power and a relatively high scanning speed may not allow the melting temperature of magnesium ($650\text{ }^\circ\text{C}$) to be reached which results in partial melting of the powders. The laser energy density is insufficient to generate adequate liquid phase and consequently leads to a poor bond neck between the particulates. Even though there was some fusion between the particles, fragile samples without mechanical strength are obtained and numerous unmolten metal fragments existed on the surface. Samples fabricated using the laser parameters in this zone have many defects such as delamination, brittle fracture and high porosity [67]. Furthermore, a prominent heat-affected zone (HAZ) can be developed during the melting of the tracks. HAZ is developed as a result of partial melting of particles due to radial heat conduction from the centre of the molten pool to the neighbouring powders [8]. If the scanning speed was too fast, more powders, due to the low density and chemical activity of magnesium, were blown up and then oxidized to form a black fog MgO contaminating the protect-gas chamber [59]. It can be observed from Table 3 that there exists a minimum critical laser energy density above which the SLM of magnesium powders occurred.
- III Formation zone: In this zone, acceptable melting of magnesium powders can be achieved in a relatively stable melt pool which yields tracks with good metallurgical bonding. As the formation of a fully molten powder bed is essential in SLM processing to successfully build near full-density parts, sufficient laser energy density is applied to powder materials. Fairly dense structures (i.e., 75%–99.5%) without obvious macro-defects can be built in a proper range of energy densities which are derivable from the ranges of laser power and scan rates as shown in Table 3 for different magnesium alloy powders. It is believed that the range of energy densities in the formation zone increase the powder bed temperature, while reducing the viscosity of the melt pool such that the melt can be spread properly on the formerly processed powder layer, thereby facilitating more efficient densification with solid powdered particles as elucidated by Attar et al. in SLM processing of commercially pure Ti [68] and Ti-TiB₂ composites [69].
- IV Balling region: Occurrence of “balling” region is characterised by the agglomeration of a series of ball like particles to form large size melt pools due to insufficient input laser energy density caused by a combination of low laser power, high scanning speed, and large layer thickness [41]. Balling effect is caused due to lack of wetting of the molten pool with the preceding layer which

affects the coherency of the formed tracks thereby hindering the construction of subsequent layers [70,71]. The balling phenomenon is a complex metallurgical process caused by the instability of the melt pool and the Marangoni effect [51]. Balling is also found to occur at very low scanning speeds owing to the reduction in the surface energy of the liquid at short length scale and long lifetime of the liquid. Occurrence of balling causes a more deteriorated surface resulting from the combination of thermal stresses and weak interlayer bonding between grains and layers. Effects of balling will be discussed further in subsequent sections.

The occurrence of various regions in the processing windows of magnesium and magnesium alloy powders are similar to the regions reported for SLM processing maps studies on aluminium [72], stainless steel [73], gold [74], and iron powders [67].

Table 3. Reported laser energy densities and relative density of SLMed magnesium-based alloys.

Materials System	Specific Laser Energy Densities in the Formation Zone	Relative Density (%)
Mg [56,57] *	1.27×10^3 – 7.84×10^3 J/mm ² (continuous wave irradiation) 1.13×10^6 – 9.8×10^6 J/mm ² (pulsed wave irradiation)	-
Mg [59]	200–300 J/mm ³	95.3–96.1
Mg-9Al [60]	93.75–250 J/mm ³	74.5–82
AZ91D [61]	83–167 J/mm ³	73–99.5
ZK60 [62]	138–416 J/mm ³	82.25–94.05
ZK60 [49]	420–750 J/mm ³	72.8–97.4

* Only single tracks were used.

3.2. Effects of Laser Processing Parameters on the Processing and Densification of Metal Powders

Laser processing parameters such as laser power, scanning speed, hatch spacing, and layer thickness have significant impacts on the resulting relative density of SLM-produced samples [75]. Therefore, it is important to understand the effects of laser processing parameters during the building process and obtain suitable combination of these parameters to successfully build near fully density parts. Also, the range of suitable processing parameters obtained is found to be dependent on the chemical composition of the primary alloys [52].

Generally, it has been reported that a minimum laser energy density (or speed below a critical value) is required to produce parts with maximum density [76,77]. Zhang et al. [60] studied the influence of laser energy densities on the densification of Mg-9%Al alloy parts by setting the laser power and laser scan speed using a continuous wave Nd:YAG laser. It was observed that the increase in laser energy density from 7.5 J/mm² to 15 J/mm² resulted in improved relative density of the melted samples from 74.5% to 82%. At lower laser energy densities (higher speeds), there is a significant porosity caused by incomplete melting leading to formation of discontinuous scanning tracks with large sized balls. With increase in laser energy density, better melting of the powders was achieved enabling more liquid phase to flow and infiltrate the voids between the particles and consequently, the pores dispersed and diminished to form a relatively smooth surface with increased density. Maximum densification was achieved under a lower laser power input of 15 W and a scanning speed of 0.02 m/s. However, further increment in the laser energy density to 20 J/mm² led to a reduction in relative density to 76.1%. Though a sufficient amount of liquid phase was generated at higher laser powers, reduced scan speed causes reduction in the surface energy of the liquid at short length scale causing spheroidisation and breakdown in the melt pool [67]. Further. They concluded that a critical scanning speed of 0.02 m/s was required to ensure complete melting of the powders without evaporation and a sound part was not obtained above a speed of 0.04 m/s for all the laser powers used. A similar phenomenon has been reported in SLM-processed commercially pure Ti [68] and Ti-24Nb-4Zr-8Sn alloy [78] wherein it was concluded that, once the powder is fully molten, there was no benefit in increasing the laser energy density further due to occurrence of some detrimental phenomena such as balling and dross formation in the melt pool, resulting in a poor surface finish and lower density. The

densification level obtained was restricted at 82% and a narrow processing window was obtained due to limitations in the SLM system as operating at a laser power beyond 20 W, caused severe evaporation and subsequent oxidation of magnesium owing to its low boiling point and a low evaporation heat (5.272 kJ/kg) at ambient pressure [64]. The lower densification levels achieved in this study may also be attributed to the irregular shape of magnesium particles used as it affects the flowability of the powder layers. As was postulated by Attar et al. [79] in SLM processing of Ti-TiB composite powders, usage of non-spherical shaped powder particles negatively influences the uniform deposition of powders, as powders with irregular shape may not flow easily and tend to interlock mechanically and entangle with each other, causing an obstruction in powder flow, consequently leading to the formation of porosities. It is also worth noting that, though SLM is normally processed based on the complete melting mechanism, application of lower laser energy densities can lead to partial melting of the metal powder surface [80]. These surface-melted powders join together due to the presence of liquid metal at the particle interfaces, leaving some interparticle residual porosity. Thus, the partial melting mechanism, wherein complete melting of the powder is avoided, can be effectively used to produce complex shaped porous structures [80]. Partial melting of the powder surface could also lead to formation of partially molten zones within each particle as a result of different melting temperatures of the phases present in magnesium alloys, affecting the microstructure and mechanical properties of SLM processed samples. Comparisons can be drawn to selective laser surface melting (SLSM) process, wherein application of lower laser energy input leads to melting of just the secondary phases without altering the properties of the Mg α -matrix, causing changes in the phase morphology and distribution [81].

Wei et al. [61] investigated the role of SLM laser processing parameters on the formability and densification behaviour of AZ91D alloy to optimize the processing window to obtain parts with higher density and lower porosity. The results are extracted from the published graphs to the best possible accuracy and are reported in Table 4, which shows the effect of variation in scanning speed and hatch spacing on the relative densities of the AZ91D parts formed. It was observed that the relative densities of the parts decreased with increase in both the scanning speed and hatch spacings. At a constant laser power ($p = 200$ W), decreasing the scanning speed caused a longer dwelling time of the laser beam on the surface of the molten pool, thereby boosting the laser energy density delivered to the powder bed resulting in better densification [82]. Hatch spacing which is also called “scan spacing” is another important parameter that determines the degree of overlap of the laser spot when a new laser line scans over the previously scanned line. The hatch spacing is usually chosen in such a way that it varies between the half width and the full width of melt pool to ensure good bonding of the adjacent tracks [28]. Decreasing the hatch spacing increased the part’s density as flowing and spreading of the liquid was increased when the scan lines were brought closer to one another. Also, when the hatch spacing more than the spot size of the laser beam (100 μm) was chosen, overlapping was found to reduce as adjacent melt lines did not fuse together completely resulting in increased porosity. Maximum densification of 99.52% was achieved under a lower scanning speed of 0.33 m/s and a hatch spacing of 90 μm . Energy density of 166.7 J/mm³ was sufficient to break up any surface oxide layers formed to produce almost fully dense (>99.5%) AZ91D parts. Near full densification levels achieved in this study can also be attributed to the strict control of concentrations of both H₂O and O₂ below 50 ppm in the build chamber, as no peaks corresponding to MgO and Al₂O₃ were found in the XRD patterns of the SLMed sample built at different energy inputs (Figure 4). Similar results were observed for ZK60 alloys [62], when the effect of scanning speed on part density was investigated with laser power, layer thickness, hatch spacing and laser spot size held at constant values of 200 W, 20 μm , 80 μm , and 150 μm , respectively. When the scanning speed was increased from 100 mm/s to 900 mm/s, it was observed that relative density of the part peaked with a value of 94.05% at 300 mm/s. At 100 mm/s, severe vaporization and burning out of the metal powders was observed, leaving an ablated pit on the substrate surface, resulting in termination of the process. At scanning speeds higher

than 500 mm/s, powder particles were not melted completely and caused voids between the unmelted powders, resulting in a sharp drop in the relative density of the sample to 82.25%.

Table 4. Relative densities of AZ91 parts formed with varying scanning speed and hatch spacings at laser power = 200 W.

Scanning Speed (mm/s)	Relative Density (%) at Different Hatch Spacings			
	70 μm	90 μm	110 μm	130 μm
333	99.4	99.5	99.2	98.8
500	99.2	99.3	99	98.4
667	99.1	98.8	93.5	89.1
833	97.4	95.9	84.4	77.2
1000	91.8	89	76.5	73.4

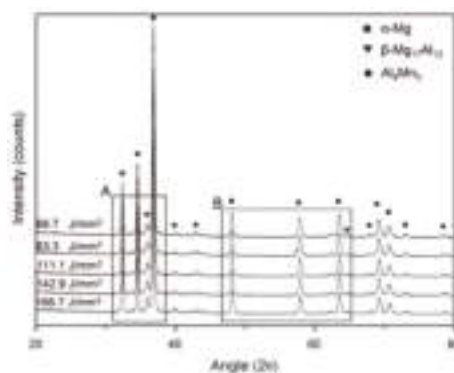


Figure 4. X-ray diffraction (XRD) patterns of the SLMed AZ91D samples fabricated at different laser energy densities indicating absence of any surface oxide films [61].

Layer thickness is another important parameter that has a significant impact on the porosity and layer bonding in the fabricated parts affecting the tensile strength, hardness and dimensional accuracies in the direction of the build [83]. For instance, a higher powder layer thickness will result in less fusion between the particles because the same amount of energy has to be radiated to a greater amount of material as compared to a lower layer thickness. Consequently, less dense parts with more pores and voids will be formed as the laser energy density penetrating the powder bed will be insufficient to completely melt the powder particles. Therefore, an optimum layer thickness must be established to achieve finer resolution and allow for good connectivity between the powder layers with lesser degree of spheroidisation leading to formation of denser parts. Minimum layer thickness can help in improving the quality of the metallurgical bond between successive layers as it helps increasing the penetration depth of the molten pools resulting in multiple remelting of the previously deposited layer and improving the wetting characteristics [61]. Layer thickness also has a close inverse relationship with the total processing time and determines the amount of energy required to melt a layer of powder. The effect of layer thickness on the dimensional and mechanical features of the fabricated tracks from magnesium powder, such as melting depth, melting width, oxidation, elastic modulus, and nanohardness was studied by Savalani et al. [58]. In their study, pulsed mode Nd: YAG laser with a wavelength of 1.06 μm , spot size of 270 μm , pulse duration of 20 ns and a maximum power of 30 W was used to process the magnesium powder. Scanning speeds were adjusted between 10 and 200 mm/s while the layer thickness varied from 150 to 300 μm . The results demonstrated that there exists a critical value of layer thickness beyond which successful remelting of the previously processed layers was not possible leading to formation of irregular and disrupted surfaces, which was 250 μm in that

study. Flatter surfaces without any surface defects were obtained at a lower layer thickness values of 150–250 μm as seen in Figure 5. Also, no heat affected zone was observed at lower layer thickness values. Since the amount of material to be melted is significantly less, heat conducted in the molten pool has sufficient energy to completely melt the neighbouring particles as opposed to being partially melted. However, lowering the layer thickness below minimal permissible level for a powder system can create problems in spreading homogenous layers of fresh powder [84]. In general, densification is improved with the increase in laser power and decrease in the scan speed, layer thickness and hatch spacing. Similar trends in the densification behaviour is also found to be true for other materials such as Al-12Si [84], Ni-alloy-Cu and Fe-Cu [85].

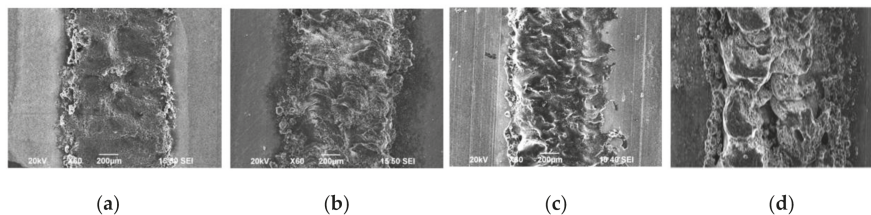


Figure 5. Effect of variation in layer thickness on the microstructure of laser melted magnesium powder at laser power of 17.7 W, scan rates of 1 mm/s; (a) 150 μm ; (b) 200 μm ; (c) 250 μm and (d) 300 μm [58].

3.3. Effects of Powder Properties on the SLM Densification Mechanism

The characteristics and quality of the powder have a strong influence on the process stability and in determining the resulting materials properties. The quality of the powder is determined by size, shape, surface morphology, composition, and amount of internal porosity. The quality of powder also determines physical variables, such as flowability (how well a powder flows) and apparent density (how well a powder packs) [86]. Powder morphology is one important factor in SLM affecting the processing conditions such as flowability, packing of the powders, and nature of heat transfer as well as being a crucial factor in defining the layer thickness and surface roughness during the SLM process [79]. High build rates and part accuracy can be achieved in SLM by employing spherical particles rather than irregular particles as they contribute towards improved flowability of the powders [87]. The powder particles used should be free of defects such as satellites and inter-agglomerate pores, because the presence of such defects can cause lack of fusion between the particles affecting the densification behaviour. The distribution of the powder particle sizes also affects the flowability of the powders as fine powders with a narrow particle size distribution tend to agglomerate and coarse particles with a broader particle size distribution tend to segregate leading to process instabilities [88]. The fraction of smaller particles should be as small as possible to avoid inhomogeneous distribution of the powder over the build platform as friction among the particles increases with decrease in the particle size [29,59]. A wider particle size distribution (more fine particles) in SLM of stainless steel 316L was observed to result in high density (>99%) across a wider range of process parameters (beam diameter, beam speed) than powder with a smaller particle size distribution [89]. It should be also noted that, powders of different size behave differently during laser processing. Higher size powders melt slower than smaller size. Therefore, in case of wider size distribution, more attention is required for optimizing the process parameters to avoid partial melting of the metal powder surface leading to inter particle residual porosities [90]. Although, higher density parts with better surface finish can be built with lower laser energy density for the finer particles than the coarser particles, they can be easily blown away by the gas flow in the shielding chamber and adhere on the scanning surface impeding the deposition of a thin layer of powder critical to the SLM process [59]. Also, owing to the low density of magnesium particles, very strong interparticle cohesion may take place due to Van der Waals forces affecting the flowability of the powders. It has been shown in some studies that powders with a narrow range of particle size

and spherical shape can contribute towards improvement of the thermal conductivity of the powder bed resulting in increased density of the SLM processed part [89,91]. A study by Hu et al. [59] suggests that smaller magnesium powders with a mesh size of 400 ($D_{50} = 25.85 \mu\text{m}$) require a lower laser energy input than powders with a mesh size of 250 ($D_{50} = 43.32 \mu\text{m}$) to be melted. Similar observations were made during SLM processing of 316L stainless steel powders, wherein powders with D_{50} of 15 μm and 28 μm required a lower laser energy input to achieve 99% density than powders with D_{50} of 38 μm [92]. However, severe oxidation and balling phenomena were observed for the parts made with finer particles as the melt pool temperature was observed to be higher than that of coarser particles for the same energy input. Further, Hu et al. observed the appearance of small grooves parallel to the spreading direction at the starting edge of specimen fabricated with 400 mesh size powder during the spreading process as shown in Figure 6. At the starting edge of the specimen, as the scan speed increased from zero to 100 mm/s, longer interaction time between powder and the laser beam caused the molten pool to exist for a long time resulting in absorption of powder from the heat affected zone. As a result, grooves near the protuberance edge are formed due to insufficient powder availability. Furthermore, no grooves were formed in the case of coarser particles as they cannot be absorbed by the melting pool as easily as the finer particles. However, the effects of powder size or size distribution on the processing maps of different magnesium alloys are still unclear as they have yet to be investigated independently.



Figure 6. Macro-morphologies of specimens fabricated using magnesium powders with granularity of 400 mesh (a) and 250 mesh (b) [59].

The effectiveness of SLM processing has been found to be a function of physical properties of the material (Table 5) such as low absorptivity to the laser beam, low boiling point elements, high thermal conductivity, high co-efficient of thermal expansion, tendency to form low melting point eutectic phases, and low viscosity [52]. One of the integral aspects of SLM is the direct interaction of the powders with a laser beam and the absorption of energy by the powder. The absorptance, defined as the ratio of the absorbed radiation to the incident radiation, affects the energy efficiency of the SLM process. Determining the way energy is absorbed is essential to the thermal development since it allows for the determination of a suitable processing window, free of superheating and evaporation due to excessive laser energy input or a non-response of powder due to an insufficient laser energy input [93]. Initially, incident photons are absorbed at the outer surface of the particles in a narrow layer determined by the bulk properties of the material, leading to an increase in the temperature of the particle surfaces during interaction. Until a local steady state of temperature within the powder is reached, the heat flow will be from the surface to the centre of the particles after which the thermal development takes place through heat transfer determined by the surrounding powder properties [36]. This local non-uniformity in the absorptance characteristics of powders can lead to selective area vaporisation during the interaction between laser and powder particles [36]. Magnesium is highly reflective of the laser energies in the infrared region, having an absorptivity of 8%–20% for a Nd:YAG laser beam with a wavelength of 1.06 μm and an absorptivity of ~3% for a CO₂ laser beam with a wavelength of 10.6 μm at room temperature [94]. In comparison to the absorptance

of bulk materials with smooth surfaces, powder materials have significantly higher absorptance regardless of the wavelength of irradiation. For example, at $\lambda = 1.06 \mu\text{m}$, the absorptance of Ti powder was observed to be 77%, which is nearly 2.5 times greater than for Ti bulk material, which was just 30% [36,95]. Although powder materials will have significantly higher absorptance in comparison to bulk materials owing to multiple absorption and reflections in the powder bed, higher than expected laser energies are required to overcome issues such as strong evaporation and reflection of the laser radiation [95]. Also, temperature gradients likely to be formed during the use of overlapping scan tracks caused by difference in the absorptivity of already melted magnesium and the neighbouring powder, may lead to balling. SLM processing of metal powders was reported to be significantly better with the Nd: YAG laser compared to CO₂ laser due to its shorter wavelength, which in turn reduced the threshold irradiance required for melting of powders at equivalent penetration depth and scanning speed. Also, a Nd:YAG laser beam produces a slightly larger and more stable scan track than a CO₂ laser beam during SLM processing [96]. However, it is noteworthy that the absorptivity of magnesium oxide (MgO) for Nd:YAG laser beam is ~20% whereas it has an energy absorptivity of 93%–98% for a CO₂ laser beam implying that MgO surface layers on melted parts can effectively increase the absorptivity of laser beams [97]. Therefore, it would be an interesting and worthwhile task to investigate if application of a CO₂ laser beam can melt or even evaporate the oxides present in the molten pool owing to enhanced energy absorption, thereby reducing the oxide inclusions in fabricated parts.

Table 5. Properties of pure and alloyed magnesium at its melting point [94].

Properties (Unit)	Pure Mg
Ionisation energy (Ev)	7.6
Specific heat (J/(kg·K))	1360
Specific heat of fusion (J/kg)	3.7×10^5
Melting point (K)	650
Boiling point (K)	1090
Viscosity (Pa·s)	0.00125
Surface tension (N/m)	0.559
Thermal conductivity (W/(m·K))	78
Thermal diffusivity (m ² /s)	3.73×10^{-5}
Expansion co-efficient (1/K)	25×10^{-6}
Density (kg/m ³)	1590
Elastic modulus (N/m ³)	4.47×10^{10}
Vapour pressure (Pa)	360

Magnesium alloys also possess very high thermal conductivity in addition to high reflectivity. However, deposited powders have relatively poor thermal conductivity and can be considered thermally insulating compared to the solid part of the substrate [86]. As heat is applied, it flows more slowly through the powder, which can lead to overheating of the melt surface located, impacting the size of the melt pool formed and causing density differences between the solid and the powder [98]. Meanwhile, due to high reflectivity and high thermal conductivity of magnesium powder, the SLM process is difficult to control compared with producing other metal powders such as stainless steels or titanium alloys. Also, more laser energy is required to melt the magnesium powders than for materials with lower conductivity.

During SLM processing of Mg-9%Al powders, Zhang et al. [60], witnessed formation of cauliflower like grains with interconnected pores on the surface of the metal as shown in Figure 7 caused by a metal evaporation–solidification process. Though the majority of the laser energy was reflected because of low absorptivity of both magnesium and aluminium, adequate amount of Mg-Al powder could be melted and a molten pool was formed even at lower energy densities. Due to differences in the thermal properties, the molten pool would absorb much more laser energy than the surrounding powder layer, leading to increase in the molten pool temperature beyond the boiling point of magnesium (1093 °C). Subsequently, an increase in vapour pressure of magnesium from 0.36 KPa at

its melting point to 51 KPa at its boiling point led to faster evaporation of the powders and the surface of the molten pool was covered by the melt vapour. Further, the magnesium vapours solidified and deposited on the surface of the metal causing formation of cauliflower like grains.

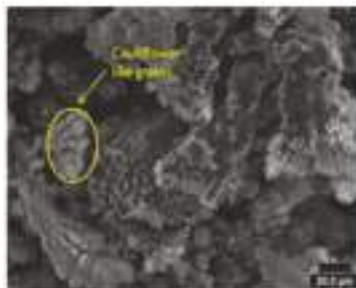


Figure 7. Cauliflower like grains observed during SLM processing of Mg-9%Al powders [60].

As higher energy input is required to obtain parts with higher density, development of a suitable processing window at higher laser energy densities becomes challenging due to minimal difference between melting and vaporization temperatures of magnesium. However, this problem was overcome by working in an overpressure process chamber having an absolute pressure of 0.3 MPa, which increased the boiling point of magnesium by 127 °C to 1220 °C allowing for a wider range of laser power and scanning speed to be applied [64]. In contrast to the effect of laser processing parameters, little work has been performed to study the influence of powder properties of magnesium on formation and densification of SLM processed parts. Much more work, therefore is needed to systematically investigate the characteristics of different magnesium alloy powders on the development of a processing window to build fully dense parts.

4. Microstructure

Transient cooling patterns employed in SLM dictate the microstructures formed in a deposited layer, due to the rapid and directional solidification resulting in finer microstructures. SLM possesses the capability to control grain sizes and shapes, phase percentages, and phase compositions by manipulation of process parameters as per the design requirements to fabricate parts with tailored mechanical properties. The microstructural characteristics of the consolidated materials fabricated by SLM are strongly sensitive to their thermal history during the build, which may include high heating/cooling rates, significant temperature gradients, bulk temperature rises, and more. The resulting microstructures, which are very fine and far from equilibrium are a consequence of very high solidification rates observed in the SLM process, ranging between 10^6 and 10^{11} °C/s [96]. Since many process variables/parameters impact the thermal history, predicting the microstructural features of SLM parts, and the degree of their dependence on the process parameters, is still a major challenge. However, overcoming this challenge is vital for establishing the effective control mechanisms for fabricating SLM parts with superior mechanical properties. Various authors have investigated the effects of certain parameters on the microstructural characteristics and material properties of SLMed magnesium parts [58–65]. However, it is still unclear how to apply these findings to fabricate complex parts with various shapes since their microstructures will have a unique dependence on thermal history. The solidified microstructure obtained when the SLM processing parameters are varied is dependent on: local solidification rates within the melt pool, the ratio of cooling rate to thermal gradient, R , and the temperature gradient at the solid-liquid interface, G . Two critical solidification parameters are the ratio, G/R , which affects the solid-liquid interface shape controlling the type of microstructure, and the cooling rate, $G \times R$, which affects the undercooling controlling the scale of microstructure [99,100]. Different G and R values may result in three major structure morphologies

within SLM parts: columnar (elongated grain morphology), columnar-plus-equiaxed, and equiaxed (isotropic grain morphology). It has been found that a higher solidification rate promotes the transition from columnar to equiaxed grain morphologies [101] and that increasing the cooling rate, $G \times R$, leads to a finer microstructure. The tendency to form a columnar structure increases by increasing the ratio G/R , while decreasing G/R is favourable for equiaxed structures [99].

Microstructural features along with resulting properties observed for different SLMed magnesium alloy powders are compiled and tabulated for ease of comparison in Table 6. Conventionally cast magnesium alloys are generally characterized by a coarse microstructure consisting of primary α -Mg and lamellar eutectic (α -Mg + intermetallic) phases with an average grain size in the range of 50–150 μm . However, rapid cooling rates associated along with epitaxial solidification in the SLM process, results in a highly refined microstructure in magnesium alloys with grain sizes of α -Mg matrix in the range of 1–20 μm and often favour the formation of partially or fully divorced eutectic (separation of eutectic phases) homogenously distributed along the grain boundaries of dendritic/columnar primary α -Mg (Figure 8) [49,61]. SLM, being a non-equilibrium process, can extend the solubility of alloying elements in Mg and obtain single-phase Mg alloys with wider composition range [61]. SLM also results in compositional and microstructural changes caused by the combined effects of selective evaporation of elements like Mg and Zn having very high vapour pressures, and consequent enrichment in the relative content of elements like Al and Zr at the surface by “solute capture” phenomenon. In the process of laser rapid melting, very high temperature gradients generated in the melt pool contribute to the formation of a strong Marangoni convection and result in improved homogenous dispersion of alloying elements in the melt pool [62]. Then a subsequent high rate growth of the solid/liquid interface contributes towards “solute capture” phenomenon in α -Mg matrix, resulting in larger amounts of solute atoms to be captured, extending the solid solution limit of alloying elements in α -Mg and retarding the nucleation β -phases [49,61]. Such compositional changes can influence the microstructure, mechanical properties, and corrosion behaviour of laser-melted magnesium alloys.

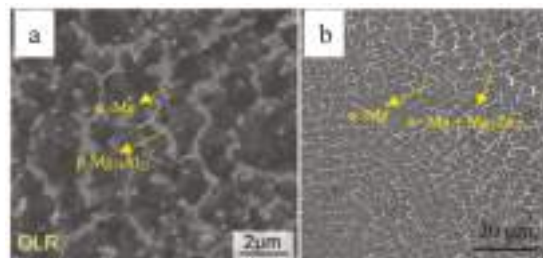


Figure 8. Homogenous distribution of the precipitates formed around the grains during SLM processing of (a) AZ91D alloy at 166.7 J/mm^3 [61] and (b) ZK60 alloy at 600 J/mm^3 [49].

Table 6. Summary of microstructural features and properties achieved for various SLMed magnesium alloy powders.

Materials System	General Microstructure/Intermetallic Phase	Hardness (HV)	Young's Modulus (GPa)	Surface Roughness (μm)
Mg [56,57] *	Equiaxed α -Mg grains, precipitates of MgO along grain boundaries	60–97 (from GPa)	20.8–38.2	-
Mg [58] *	-	66–74 (from GPa)	29.9–33.1	19–33
Mg [59]	-	44.7–52.4	-	38.6–51.8
Mg-9Al [60]	Equiaxed α -Mg grains/ $\text{Mg}_{17}\text{Al}_{12}$, MgO , Al_2O_3	66–85	-	-
AZ91D [61]	Equiaxed α -Mg grains/ β - $\text{Mg}_{17}\text{Al}_{12}$, Al_8Mn_5	85–100	-	-
ZK60 [62]	Oriented dendrites/ MgZn , Mg_7Zn_3	78	-	-
ZK60 [49]	Dendritic/columnar α -Mg; Mg_7Zn_3	70.1–89.2	-	-

* Only single tracks were used (Details regarding process parameters used in these studies can be found in Table 2).

Microstructures obtained in magnesium alloys with SLM processing are comparable to that achieved by other laser processing techniques such as laser surface melting (LSM) and selective laser surface melting (SLSM). Figure 9 shows the different types of microstructure that can be achieved by laser processing of AZ91D alloy. The commercial die cast AZ91 alloy (Figure 9a) is composed of α -Mg solid solution and β - $\text{Mg}_{17}\text{Al}_{12}$ lamellar eutectic phase distributed along the grain boundaries and its microstructure presents large grains due to the slow cooling rate of the casting process used. Figure 9b,c present the typical appearance of the surface of AZ91 alloy, after modification by LSM and SLSM, respectively. Surface modification by LSM (with a laser power of 600 W and scanning speed of 45 mm/s) revealed that the microstructure was characterized by very small isolated β - $\text{Mg}_{17}\text{Al}_{12}$ phase particles immersed in a continuous supersaturated solution of Al in α -Mg matrix, producing a homogeneous and continuous modified layer. SLSM, which is a modification of the LSM process, can be achieved by the application of lower laser energy input (375 W and 90 mm/s) causing modification of the β - $\text{Mg}_{17}\text{Al}_{12}$ phase only, without any change in the α -Mg matrix. SLSM also resulting in a eutectic microstructure based on fine plates of β - $\text{Mg}_{17}\text{Al}_{12}$ and α -Mg phase. Modification β -phase and its surrounding led to a reduction in its hardness and its dispersion, resulting in a more homogenous and continuous material. Figure 9d presents the microstructure of SLMed AZ91 (at a laser energy input of 166.7 J/mm³), which also presents a feature of equiaxed α -Mg with fully divorced eutectic β - $\text{Mg}_{17}\text{Al}_{12}$ distributed reticularly along the grain boundaries. As the morphology of the eutectic in the hypo eutectic Mg-Al alloys depends on the cooling rate [102], change in the form of β phase between LSM, SLSM, SLM, and die-cast AZ91D is induced by the high cooling rates inherent to laser melting processes.

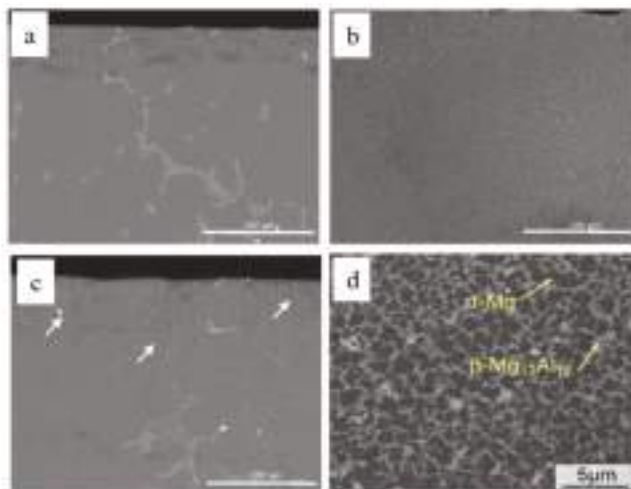


Figure 9. SEM micrographs of the microstructure of AZ91D alloys: (a) as-received alloy [81]; (b) laser surface melting (LSM) [81]; (c) Selective Laser Surface Melting (SLSM) of the β -phase (arrow marked) [81] and (d) Selective laser melting (SLM) [61].

Under an optical microscope with lower magnifications, the SLM formation features are shown clearly. For example, the curve-like regular laser melted tracks on the cross-section correspond to laser scanning strategy, and the laminar material structure and columnar architecture throughout the vertical section are determined by the specimen building strategy, such as the scanning pattern, hatch spacing, and thickness of layers. The cut ends of melted tracks in the form of a series of arcs on the vertical section which are aligned layer by layer, are induced by the Gauss energy distribution of laser as shown in Figure 10a [61]. The penetration depth of the molten pools was observed to be up to $312\text{ }\mu\text{m}$, which was approximately eight times the layer thickness ($40\text{ }\mu\text{m}$) used in the study for AZ91D alloys (fabricated at a laser energy density of 166.7 J/mm^3) indicating that each layer of the as deposited sample undergoes a remelting process more than once. The multiple remelting process plays a significant role in determining the microstructure of SLMed samples as different thermal histories experienced by different layers of the part, led to variation of microstructures along the height direction, as the conduction, convection, and radiation conditions change [61]. The as processed microstructure contains at least two distinct regions: one significantly finer than the other, as shown in Figure 10c,d for AZ91D and ZK60 alloys, respectively. At the edges of the melt pool, the material experiences more cycles of the remelting process caused by both overlapping of the scan lines and creation of subsequent layers to induce relatively lower cooling rates, resulting in localized coarsening of the microstructure. This difference in thermal history between the edges and centre of the melt pool can induce non-uniform distribution of microstructure in the scale of several microns. As can be seen from Figure 10c in the case of AZ91D alloy, the grains on the centre of the scanning tracks (CST) were finer ($\sim 1\text{ }\mu\text{m}$) than those near the overlapping edges (OLR) because of the decreasing cooling rate and multiple remelting cycles experienced at the edges of the melt pool. Also, decreasing the temperature gradient inside the melt pool, can lead to occurrence of columnar-to-equiaxed transition towards the centre of the melt pool. As can be seen from Figure 10d, columnar α -Mg grains dominate the margin zone of the molten pool whereas α -Mg grains in the centre zone of the molten pool presented an equiaxed morphology in the case of ZK60 alloys.

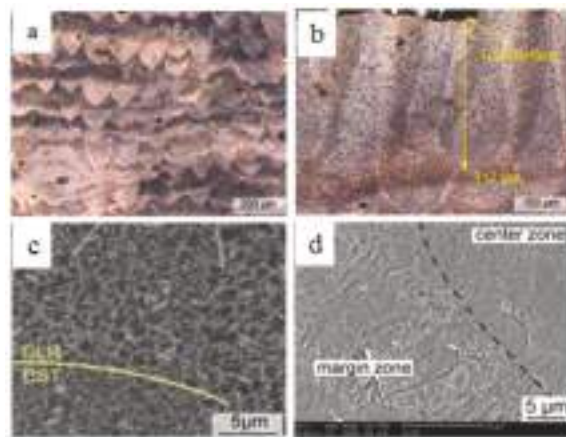


Figure 10. Microstructure of (a–c) AZ91 [61] and (d) ZK60 [62] alloys after selective laser melting: in (a), half-moon shaped melt pools are clearly visible, (b) vertical section indicating multiple remelting of each layer, while (d) shows columnar α -Mg grains dominating the margin zone of the molten pool and equiaxed α -Mg grains in the centre zone of the molten pool.

Microstructural features of SLM processed magnesium alloys can be significantly influenced by the processing parameters used. The combination of higher scanning speeds and lower laser power results in a lower incident energy at the top of the part, typically resulting in finer microstructures due to higher cooling rates. In contrast, lower cooling rates and coarser microstructures can be obtained by decreasing scanning speed and increasing laser power. At relatively lower scanning speeds, prolonged interaction of the laser beam with powders results in the restraining of heat dissipation in the melt pool. As a result, relatively equivalent cooling rates during solidification can be achieved due to larger heat accumulation and thus providing enhanced kinetic qualifications for epitaxial growth of the grains [49]. With the increase of laser energy density, the crystalline structure of magnesium alloys experience successive changes in the order of clustered finer dendrites, uniform equi-axed grains to coarsened equi-axed grains. As can be seen from the microstructure of SLM processed ZK60 alloys, extremely fine dendrites ($\sim 2 \mu\text{m}$) which clustered severely together, were observed at a relatively lower laser energy input of 420 J/mm^3 (Figure 11a). The dendrites coarsened to some extent ($\sim 4 \mu\text{m}$) and changed to a column shaped structure with an increase in laser energy input to 500 J/mm^3 (Figure 11b), but still exhibited a disordered distribution. Further increase in the laser energy input to 600 J/mm^3 and 750 J/mm^3 resulted in orderly dispersed, equi-axed grains of $\sim 6 \mu\text{m}$ (Figure 11c) and $\sim 8 \mu\text{m}$ (Figure 11d), respectively. The dendritic crystalline structure was formed through the heterogenous nucleation of α -Mg and subsequent dendrite growth, whereas, the equi-axed crystalline structure was formed through the homogenous nucleation of α -Mg and subsequent equi-axed growth of grains [49]. Similar results were observed in the investigation of SLM of Mg-9%Al alloy powders by Zhang et al. [60] wherein significant grain refinement in the laser-melted region was observed with grain sizes in the range of $10\text{--}20 \mu\text{m}$. The microstructure the Mg-Al alloy consisted of equi-axed grains, transformed from dendritic grains under a high temperature gradient. An XRD analysis of the laser-melted samples indicated the presence of phases like α -Mg, $\text{Mg}_{17}\text{Al}_{12}$, MgO , Al_2O_3 . The Al_2O_3 phase was formed as a result of incomplete reaction between Mg and Al, only under a low energy density input of 93.75 J/mm^3 . Further, it was also observed that the content of Mg decreased in the laser-melted region because of selective evaporation with the increase in laser energy density.

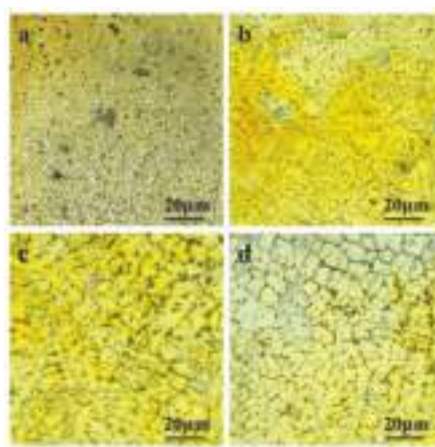


Figure 11. Optical images showing characteristic crystalline structures of laser melted ZK60 prepared at different laser energy densities: (a) 420 J/mm^3 ; (b) 500 J/mm^3 ; (c) 600 J/mm^3 ; (d) 750 J/mm^3 [49].

Reports also indicate that the type and mode of the laser beam used can affect the microstructures formed in SLM processed magnesium as the resultant consolidation mechanism of metallic powders is a function of energy density delivered [39]. Ng et al. [57] compared microstructures of the tracks formed in SLM processing of magnesium powders, processed under both continuous and pulsed mode of irradiation. Under continuous wave irradiation, laser melting led to the formation of fully recrystallized grains in the melted zones with grain sizes in the range of $2.3\text{--}4.87 \mu\text{m}$ (laser energy densities varied from $1.27 \times 10^9 \text{ J/m}^2$ to $7.84 \times 10^9 \text{ J/m}^2$). The $\alpha\text{-Mg}$ single phase solidified in the form of equi-axed crystals as seen in Figure 12a. However, in the case of tracks melted under pulsed mode of irradiation, incomplete growth of the $\alpha\text{-Mg}$ phase was observed (Figure 12b). Full growth of $\alpha\text{-Mg}$ was inhibited as the solidification rates achieved under pulsed mode was higher than continuous irradiation. Besides, due to the shorter interaction time in case of pulsed mode, there is insufficient time for the crystals to arrange themselves such that thermodynamic equilibrium prevails at the solid/liquid interface. The average size of grains obtained under pulsed mode were smaller than those obtained in the continuous mode laser melted tracks. Also, smaller laser spot size ($50\text{--}180 \mu\text{m}$) and layer thickness (typically $20\text{--}50 \mu\text{m}$) used in the SLM process when compared to other laser processing technologies such as direct laser deposition (DLD), laser rapid forming (LRF) and laser net shape manufacturing (LNSM) led to the formation of a smaller melting pool, thereby resulting in the formation of a refined microstructure [29]. Normally, layer thickness, alone, has little influence on the microstructure, but its influence is dependent on other parameters, such as laser power, scanning speed, specific energy density, and powder mass flow rate. For example, as the specific laser energy density is lowered, thinner layer thickness will be required, as the energy per unit area to melt the powder is reduced. However, it was observed by Savalani et al. [58] that different layer thicknesses directly affect the oxygen content in the matrix material thereby resulting in phase and microstructural changes. Oxidation occurring during SLM processing of magnesium at different layer thicknesses ranged from approximately 9.1 to 11.7 at %. The level of oxidation was found to be inversely proportional to the layer thickness, as it decreased from 11.7% to 9.1% with the increase in layer thickness from $150 \mu\text{m}$ to $300 \mu\text{m}$.

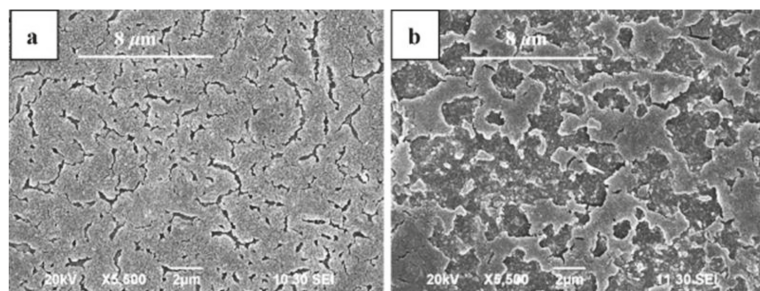


Figure 12. Typical microstructural images of laser-melted magnesium under, (a) continuous wave irradiation at $1.27 \times 10^9 \text{ J/m}^2$ and (b) pulsed wave irradiation at $1.13 \times 10^{12} \text{ J/m}^2$ [57].

5. Metallurgical Defects

5.1. Oxide Inclusions

The presence of surface oxide film on the preceding layer impedes interlayer bonding which in turn inhibits the densification mechanism and leads to balling as liquid metals generally do not wet oxide films in the absence of a chemical reaction. In combination with thermal stresses, poor interlayer bonding can also cause delamination of SLM processed parts. Similar to the casting process as pointed out by Campbell [103], oxide may get into the melt pool either via alloying addition into the metal powder during primary processing or air/gas entrapment via surface turbulent flow during SLM processing. Also, as the vaporization of alloying elements in the scan tracks is not uniform while the scan track positions vary with time, rapidly fluctuating scan tracks tend to entrap the shielding gas or even air which may contain traces of oxide particles. Consequently, the surface of the liquid metal in the melt pool then become oxidized to form oxide film as a result of the entrapment of air or shielding gas into the melt pool.

The oxidation of a metal M may be represented by



The free energy of formation δG of the oxide is given by

$$\delta G = -RT \ln K \quad (4)$$

where R is the gas constant, T is the temperature in Kelvin and K is the equilibrium constant given by

$$K = (\text{PO}_2)^{-1} \quad (5)$$

where PO_2 is the partial pressure of oxygen when reaction (3) is at equilibrium. For magnesium at 700°C , a PO_2 of 10^{-54} atm or higher will give oxidation of magnesium [104]. Thus, thermodynamically, it should not be possible to prevent oxidation of the magnesium. Since the formation of oxide films cannot be avoided completely, the SLM process must break up these oxides if fully dense parts are to be formed, and this is why SLM fabrication of high density parts requires high laser power. According to Louvis et al. [105], the oxide film on the upper surface of the pool evaporates under a laser beam. Marangoni forces that stir the pool are the most likely mechanism by which these oxide films are disrupted, allowing fusion to the underlying layer. However, the oxides at the sides of the pool remain intact and, thus, create regions of weakness and porosity, as the pool fails to wet the surrounding material. Therefore, further research on the SLM of magnesium should be primarily

orientated towards new methods of controlling the oxidation process and disrupting oxide films formed within the components.

It has been shown that significant amounts of oxide are present within the selective laser melted magnesium and tended to form between scan tracks rather than between layers, as shown in Figure 13. It is also expected that the oxide would form on top of the melt pool, which may retard its spreading and alter the wetting characteristics and result in a porous structure with weak mechanical properties. However, provided that sufficient energy is imparted, this surface oxide will break up and become encapsulated within the melt pool. However, it may then act as a micro crack in the system and, therefore, be detrimental to the final mechanical properties of the product. Just as oxide films are damaging to magnesium alloy castings, so they are to SLM processed parts made in magnesium alloys. However, the potential role of oxide films affecting the densification, mechanical properties, and corrosion behaviour of SLM processed magnesium alloy parts has not been elucidated due to abundance of some defects such as porosity and loss of alloying elements. It is expected that the potential role of oxide films will possibly be highlighted by SLM processing of magnesium alloys in the future, once these defects are eliminated.

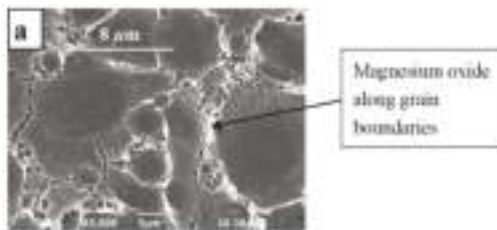


Figure 13. SLMed magnesium track fabricated at a laser energy density of $7.89 \times 10^3 \text{ J/mm}^2$ [57].

5.2. Loss of Alloying Elements

Higher vapour pressure and low boiling points of elements like magnesium and zinc can lead to preferential element vaporization during the interaction between laser and magnesium alloys [94]. It is also well known that the temperatures reached within melt pools during the SLM process are far greater than the boiling temperatures of magnesium, aluminium, or zinc. Thus, the preferential evaporative losses during SLM will consist primarily of zinc and magnesium. Intrinsic vaporization of elements at the melt pool surface during laser processing takes place initially by the transportation of vaporization elements from the bulk to the surface of the molten pool, followed by vaporization of elements at the liquid/vapour interface; then the vaporized species are transported into the surrounding gas phases [106]. Sometimes, because of low diffusivity, the vaporized species are re-condensed and deposited back immediately around the laser irradiated zones and are remelted during subsequent scanning to compensate for the initial losses [62]. However, condensation of volatile alloy constituents on the surface of the molten pool to a greater extent can lead to formation of a black coating [107]. During SLM of AZ91D alloys, Wei et al. [61] observed that selective vaporization of magnesium caused an increase in the concentration of aluminium in the molten pool. Increasing the laser energy density from 83.3 J/mm^2 to 166.7 J/mm^2 caused an increase in the content of Al in α -Mg solid solution from 8.31 wt % to 10.98 wt % signifying a higher burning loss rate of Mg atoms. Further, due to the interaction of “solute capture” and element evaporation, the content of the hard-brittle β -phase and the solubility of solute elements in the α -Mg matrix increased simultaneously with increasing laser energy inputs. Similar results were observed in case of ZK60 alloys [62], wherein a larger reduction in the content of both Mg and Zn was reported at slower scanning speed with subsequent enrichment of Zr after processing. Also, a higher Mg:Zn ratio in the final parts was observed when compared to raw material. Though evaporation during SLM is known to be a problem for aluminium alloys, it did not appear to be so detrimental in the processing of Mg-9%Al alloys [60]. However, evaporative

losses can be more problematic in case of low zinc zirconium alloys wherein evaporation and decline in the content of alloying elements can be detrimental to the mechanical performance and can lead to degradation of functional properties of SLMed sample.

Evaporation of alloying elements taking place at higher laser energy densities during laser melting will affect the stability of the molten pool along with causing a variation in composition and microstructure of the deposited layers [106]. Metal vaporization leads to formation of recoil pressure in the molten pool, which tends to push the liquid away from the melt zone, resulting in formation of a keyhole defect [108]. Formation of key hole defects results in inferior surface quality of the specimen showing varying depths as observed during SLM of ZK60 alloys [62]. The depletion of alloying elements leads to a higher degree of porosity in the laser processed parts limiting the level of maximum densification that can be achieved. Composition inhomogeneities resulting from selective evaporation of elements is a function of the vaporization rate and the volume of the molten pool [94]. Thus, careful control and manipulation of SLM process parameters is required to ensure reduction in the occurrence of elemental redistribution and porosity. Loss of high vapour pressure alloying elements can be effectively minimized by regulating the molten pool temperature, which in turn can be achieved by controlling the beam power density distribution in case of continuous wave irradiation and adjusting the pulsing parameters in case of pulsed wave irradiation [52]. Although, high laser energy densities lead to greater evaporative losses, compositional inhomogeneities are most pronounced at low energy density levels due to small size, and the high surface-to-volume ratio, of the molten pool [94]. In order to avoid vaporization of elements during SLM processing of magnesium alloys, it is recommended to employ laser processing parameters combining medium or high power with high scanning speeds and also it is necessary to further understand the mechanism, to investigate the main influencing factors and to build up the quantitative relationship between the vaporization losses and SLM process parameters.

5.3. Balling

Balling phenomena are regarded as the typical microstructure occurring on surfaces of SLM-processed parts from a bed of loose powder [39]. Balling is defined as an agglomeration of the particles, occurring where the liquid phase breaks up into a row of spheres to reduce surface energy. As discussed previously, occurrence of “balling” region is characterised by the agglomeration of a series of ball like particles to form large size melt pools due to insufficient input laser energy density caused by a combination of low laser power, high scanning speed, and large layer thickness [41]. The main factor leading to balling is the Gibbs-Marangoni effect, which is the mass transfer along an interface between two fluids due to the surface tension gradient [109]. In terms of temperature association, this phenomenon is also called thermo-capillary convection. During SLM, laser scanning is performed line by line and the laser energy causes melting along a row of powder particles, forming a continuous liquid scan track in a cylindrical shape. The diminishing in the surface energy of the liquid track continues until the final equilibrium state through the breaking up of the cylinder into several metallic agglomerates in spherical shape [39]. Three kinds of balling mechanisms have been identified by Gu et al. [73,110] during SLS processing of Cu-30CuSn-10CuP and stainless steel powder. “First line scan balling” is observed when initial tracks on a cold powder bed are scanned, caused by high thermal gradients imposed on the melt. “Shrinkage induced balling” is caused by the capillary instability of the melt pool when higher scanning speeds are used. “Splash-induced balling” with the formation of a large amount of micrometre-scale balls occurs at a high laser power combined with a low scan speed, because of the considerably low viscosity and long lifetime of the liquid.

Figure 14 shows the occurrence of balling phenomenon observed during SLM processing of Mg-9%Al powders [60], wherein a large amount of micrometer-scaled (diameter of 10–20 μm) spherical splashes, formed around the sintered surface, can be seen. When relatively higher scanning speeds were applied, laser energy density of the laser input decreased causing a significant shrinkage in inter particle areas, leading to capillary instability of the molten pool. Therefore, due to the reduction

in surface energy of the liquid at short length scales, small sized liquid droplets splashed from the liquid surface. Further, balling obstructed the formation of continuous melt lines, forming rough and bead-shaped surfaces. In more severe cases, balling may aggravate in subsequent layers and jam the powder coating mechanism with large metallic beads that extend above the powder bed. The balling effect can be avoided if the stability of the melt pool is improved by reducing the length/width ratio of melt pool and/or increasing contact width, which can be achieved by increasing the laser power or decreasing the scanning speed [111]. According to Li et al. [112], lowering the oxygen level during the process and introducing repeat exposure of laser to break up the oxide films are ways to minimize the occurrence of balling, as balling behaviour during the SLM process is related to the oxidation of metals [112]. In their study regarding SLM processing of Ni and stainless steel powders, it was observed that balling could be reduced significantly by keeping the oxygen level at 0.1%, and by applying a combination high laser power and low scanning speed or applying re-scanning of laser [112]. However, even though the oxygen content in the chamber was kept below 0.2%, Hu et al. [59] observed the occurrence of balling during SLM processing of magnesium, as magnesium being very active is susceptible to oxidation.

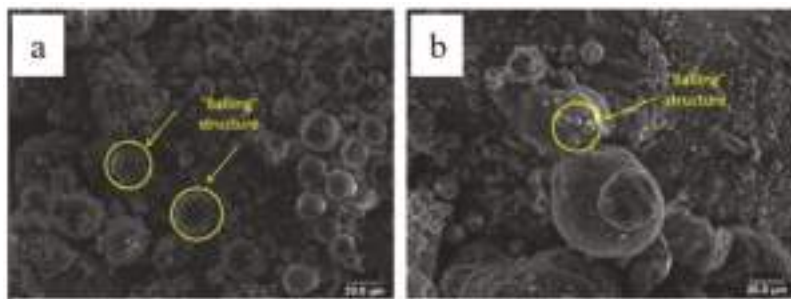


Figure 14. SEM image showing cluster of balls (balling effect) in SLM processed Mg-9%Al due to non-optimized laser processing parameters [60].

6. Mechanical Properties

Properties observed for different SLMed magnesium alloy powders are compiled and shown in Table 6. Figure 15 presents the comparison of hardness and Young's modulus values reported for laser melted parts with conventionally cast and wrought magnesium alloys in literature. SLM of magnesium alloys results in high surface hardness than that of as-cast alloys, as a result of solid solution strengthening effects (because of solute supersaturation with rapid cooling or solute enrichment with selective evaporation of elements). The microhardness is found to gradually fluctuate from the centre of the molten pool to the margin zone due to the variations in the microstructure between the two regions. However, the microhardness for deposited samples showed directional independence [61]. According to Mercelis and Kruth [113], residual stresses are not always disadvantageous in SLM fabricated parts because their retention at a reasonable level enhances the part's hardness provided sufficiently high densification without formation of cracks or pores could be achieved. Moreover, the rapid solidification effect imparted on the as-processed parts by the SLM which results in grain refinement of the microstructure is another reason that could be attributed to increased hardness of the SLM fabricated parts. Figure 16 shows the variation of hardness of SLM processed magnesium tracks with different laser energy inputs as measured by Ng et al. [57]. It is evident that the resulting hardness values can effectively be controlled by adjusting the laser energy densities in the formation zone. The hardness values were found to increase with decrease in the laser energy input. The higher cooling rate induced by low laser energy density resulted in smaller grain sizes, so that the hardness values were mainly related to the grain size in the melted zone. Also, the reported Young's modulus values

for various magnesium alloys are in the range of 20–35 GPa, which are close to the corresponding ones of human bones (3–20 GPa), indicating that they can be considered as a potential candidate for biomedical implants [114].

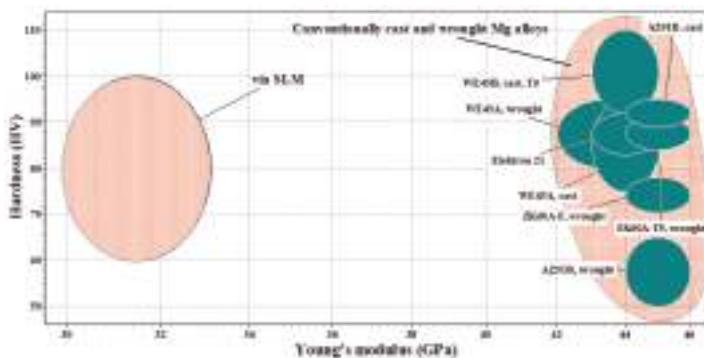


Figure 15. Comparison of hardness and Young's modulus values of SLM processed parts with conventionally cast and wrought magnesium alloys.

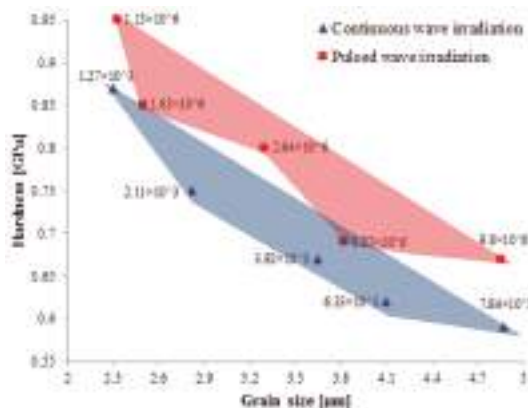


Figure 16. Grain size against the microhardness values of single track magnesium samples [56].

Figure 17 presents the comparison of tensile properties reported for laser melted parts with conventionally cast and wrought magnesium alloys in the literature. As can be seen from Figure 17, the yield strengths of SLM parts are comparable or superior to those fabricated from cast and wrought materials in most cases. This is generally attributed to the nature of the SLM process, where a very small amount of material is melted at a time and rapid solidification takes place. This results in a more uniform microstructure throughout the part. For alloys, the segregation of the alloying elements takes place on a much smaller scale. The chemical composition is more uniform throughout the part, resulting in higher strength than for cast parts [115]. However, the elongation to failure is typically lower for SLM parts and this could be attributed to micro-porosity and oxide inclusions within the parts—a result of the non-optimized SLM process. Wei et al. [61] investigated the tensile properties of SLM processed AZ91D alloy at different laser energy inputs. It was established that laser energy input had a significant influence on tensile properties as the average ultimate tensile strength and yield strength of the SLMed samples were found to decrease gradually from 296 MPa and 254 MPa at 166.7 J/mm^3 to 274 and 237 MPa at 83.3 J/mm^3 . This is as a result of poor relative densities of

SLMed samples obtained at lower energy inputs coupled with lower solid solubility of the α -Mg matrix and a smaller quantity of intermetallic β phase induced by lower energy inputs. Analysis of the fracture behaviour of SLM parts showed features of ductile-brittle hybrid fracture. Owing to the layer by layer manufacturing approach, it was observed that the part's building orientation during SLM was found to affect the resultant tensile properties of the part. Specimens deposited in the direction along (e.g., parallel to) the length of the tensile samples (e.g., X-direction) typically exhibit higher tensile strength than those with layers deposited perpendicular to their length (e.g., Y or Z-direction) [116]. Although the reasons for this have not been well investigated, it does show that the effects of the building orientation for magnesium alloys is more involved and requires further investigation. Also, performing a hot isostatic pressing (HIP) procedure after SLM can significantly reduce the anisotropic mechanical behaviour of the SLMed parts by reducing manufacturing induced porosity [116].

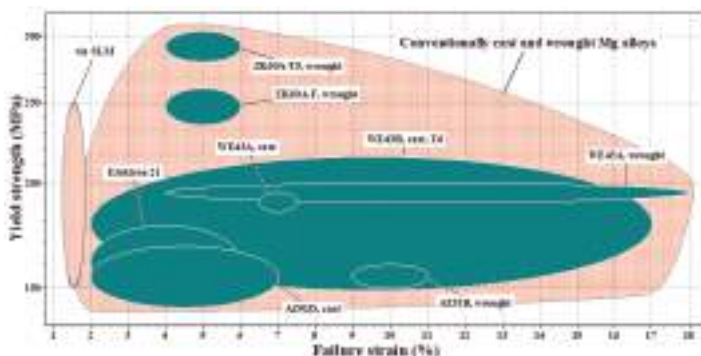


Figure 17. Comparison of tensile properties of SLM processed parts with conventionally cast and wrought magnesium alloys.

7. Corrosion Behaviour

Magnesium alloys, generally, reveal a poor corrosion resistance, which is mainly associated with their high chemical activity and the lack of a protective passive oxide film [117,118]. This disadvantage has been a major obstacle restricting their further application in automotive, aerospace, and electronics industries. Also, magnesium has a high negative standard electrode potential, which leads to the rapid corrosion of magnesium based alloys in chloride physiological conditions [119]. This has delayed the introduction of magnesium based materials for therapeutic applications to date, as the hydrogen gas produced at a high rate from corrosion cannot be dealt with by the host tissue [18]. Additionally, shift in alkaline pH in the region surrounding the corroding surface is also a concern for biomedical applications [119]. Therefore, development of magnesium alloys with improved corrosion behaviour may help to resolve the current limitations of magnesium alloys for use in the aforementioned industries. Rapid solidification has been identified as an effective method to improve the strength and corrosion resistance of magnesium alloys for structural and corrosive media utilization [40]. Laser melting is one such rapid solidification process involving cooling rates up to 10^{6-8} °C/s and is capable of modifying surface properties as it can homogenize and refine the microstructure, and dissolve secondary phases [120,121]. However, so far, little effort has been made to examine the corrosion behaviour of the SLM-produced magnesium parts as most studies on the SLM of magnesium alloy powders have been focussed on the densification and mechanical properties of the SLM-produced samples.

Because of the paucity of literature dealing with corrosion behaviour and its associated mechanism during SLM of magnesium alloys, it would be useful to examine the effect of laser surface melting

(LSM) treatment on the corrosion behaviour of magnesium alloys, as corrosion is essentially a surface degradation process. LSM treatment has been effective in improving the corrosion resistance of AZ and AM type of magnesium alloys, such as AZ31, AZ61, AZ91, and AM60 [122–128]. Improved corrosion resistance of these alloys was mainly attributed to the pronounced refinement of α -Mg grains and uniform redistribution of inter metallic compounds after laser treatment. In the case of magnesium alloys, it has been observed that, grain refinement and homogenization of compositional distribution can decrease the volume fraction of the effective cathodes, thereby limiting the cell action caused by the accumulation of cathodic phases [129]. In addition, the corrosion resistance also increased with the enrichment of aluminium content in the laser-melted zone because of the selective evaporation of magnesium, providing passive characteristics to the melted surface [124]. Enrichment of alloying elements can shift the corrosion potential of α -Mg to the positive direction, lowering the corrosion susceptibility of α -Mg matrix [130]. Furthermore, rapid laser-melting could increase the solid solubility of alloying elements, such as Mn, Al, and Cr, promoting the formation of more protective and self-healing films and thus limiting the occurrence of local galvanic corrosion [129]. It is expected that insights gained from how LSM treatment can enhance the corrosion resistance of magnesium alloys, could be helpful in understanding the mechanisms associated with corrosion behaviour of SLM processed magnesium alloys.

In a recent study, Shuai et al. [49] investigated the corrosion behaviour of SLM-processed ZK60 alloy by performing immersion tests in Hanks's solution ($\text{pH } 7.4 \pm 0.1$) at $37 \pm 0.5^\circ\text{C}$ for 48 h. Hydrogen volume evolution rates observed were in the range of $0.006\text{--}0.019 \text{ mL}\cdot\text{cm}^{-2}\cdot\text{h}^{-1}$ as the laser energy input varied from 420 J/mm^3 to 750 J/mm^3 . The lowest hydrogen evolution volume rate of $0.006 \text{ mL}\cdot\text{cm}^{-2}\cdot\text{h}^{-1}$ was observed at a laser energy input of 600 J/mm^3 , for which a maximum densification of 97.4% was achieved. Such low volume release rate of hydrogen achieved, is within the limit of $0.01 \text{ mL}\cdot\text{cm}^{-2}\cdot\text{h}^{-1}$ that can be tolerated by the body without posing any serious threat [131]. SLM processed ZK60 alloy showed significant enhancement in corrosion resistance compared to casted ZK60, which had a hydrogen volume evolution rate of $0.154 \text{ mL}\cdot\text{cm}^{-2}\cdot\text{h}^{-1}$ (~80 times higher) during immersion in Hank's solution [132]. However, the outcome from Shuai et al. [49] contradicts the findings from studies carried out by Dai et al. [133,134] who reported that SLM-produced Ti-6Al-4V has an unfavourable corrosion resistance compared to its traditional counterparts. The reported contradiction about the effects of laser melting on the corrosion behaviour of SLM processed metal powders might have been possibly engineered by different mechanisms of microstructure evolution and corrosion reactions, occurring during laser processing of different materials. The exact nature of the corrosion reactions and the associated mechanisms affecting the corrosion behaviour for various metallic powders need to be explored further in future studies.

When ZK60 alloy was soaked in Hank's solution, the following reactions occurred [49]:



The corrosion of ZK60 in Hank's solution accompanied a release of H_2 . The reactions were driven by the relative potential difference between the relative anode and cathode. As for the ZK60 alloy, homogeneously distributed Mg_7Zn_3 secondary phase served as a cathode and formed a galvanic couple with the Mg matrix resulting in macroscopic homogenous corrosion characteristics. The corrosion was triggered by the dissolution of the α -Mg matrix adjacent to intermetallic compounds. The enhanced corrosion resistance observed in SLM processed ZK60 alloy can partly be ascribed to the increase in the corrosion potential caused by enrichment of the solid solution of Zn (caused by increased "solute capture" effect), which possessed a higher corrosion potential (-0.76 V) than that of Mg (-2.34 V). Thus, increase in the corrosion potential of Mg matrix, namely, decrease in the relative potential difference, had a beneficial effect on reducing the relative anodic and cathodic reaction

supported by the Mg alloy. In addition, once the corrosion was initiated, the refined Mg_7Zn_3 phases distributed evenly and mainly served as a barrier to impede corrosion process. Similarly, Yang et al., during SLM processing of Mg-Mn alloys [66], observed that corrosion resistance of pure magnesium was enhanced by the addition Mn of up to 2 wt % during immersion testing carried out in simulated body fluid (SBF) (pH 7.4) at 37 °C for 48 h. The hydrogen volume evolution observed for Mg-2Mn alloy ($0.017\text{ mL}\cdot\text{cm}^{-2}\cdot\text{h}^{-1}$) was significantly lower than that of pure Mg ($0.068\text{ mL}\cdot\text{cm}^{-2}\cdot\text{h}^{-1}$). The enhancement of Mg corrosion resistance was attributed to the increase in corrosion potential and grain refinement caused by the solid solution of Mn. Further, they suggested SLM processed Mg-2Mn alloy as a potential candidate for future bone implants. However, corrosion in body fluids is influenced by various factors such as pH, concentration and types of ions, protein adsorption on orthopedic implant, and influence of the biochemical activities of surrounding tissues [135,136]. Therefore, further investigations are still necessary to develop the reliability of SLM processed magnesium parts for biomedical applications.

8. Potential of SLM to Fabricate Porous Magnesium Structures

Human bone has a hierarchical structure with three major anatomic cavities of different sizes which are haversian canals ($50\text{ }\mu\text{m}$) [137], osteocytic lacunae (few micrometres) [15,138,139], and canaliculi ($<1\text{ }\mu\text{m}$) [140,141]. Each of the three cavities has a major role in remodelling the processes and mechanical integrity of the bone [14]. A porous structure allows adequate spaces for transportation of nutrients and for growth of living tissues [142]. Especially for metallic orthopaedic applications, by adjusting the porosity levels, the modulus of the materials can be greatly controlled which provides an opportunity to design materials with a modulus closer to that of natural bone thereby mitigating problems related to stress shielding [143]. Metal cellular structures can be classified into structures with stochastic and non-stochastic geometries. Metal stochastic porous structures typically have a random distribution of open or closed voids, whereas metal periodic cellular lattice structures have uniform structures that are generated by repeating a unit cell [144]. Apart from medical fields, metallic cellular/porous structures have also been broadly utilized in the automotive, aerospace, and chemical industries as they possess lower weight, good energy absorption characteristics, and good thermal and acoustic properties [145,146]. However, it is difficult to fabricate structures of such complex external shapes and intricate internal architectures by conventional casting and powder metallurgy methods. Although the shape and size of the pores can be adjusted by changing the parameters of these manufacturing processes, only a randomly organized porous structure can be achieved [144]. However, additive manufacturing (AM) technologies can fabricate porous metals with a predefined external shape and internal architecture to match the modulus or stiffness of bone, thereby minimizing or eliminating stress shielding [147,148]. Selective laser melting (SLM) offers a significant advantage of producing such very fine and porous structures while at the same time accommodating a variety of shapes that are not only limited to prismatic ones [26]. This makes it the preferred technology for producing metallic scaffolds and implants. Also, Studies on SLM have shown that the internal and surface finish of the implants can be tailored to have selectively porous and/or lattice-like structures to promote osseo-integration (bonding between the bones and the implant) in the implants [42]. SLM technology has been used to produce complex porous/cellular structures directly from different engineering materials such as stainless steel [144] and titanium alloys [108,149–151] and therefore has the potential to produce porous structures in magnesium alloys. In a recent study, Jauer et al. [65] were successful in fabricating scaffold-like structures with designed interconnected porosity out of WE43 by means of SLM (Figure 18). However, the processing parameters for fabricating such structures are currently under development and details of research in this area are not available in the open literature.

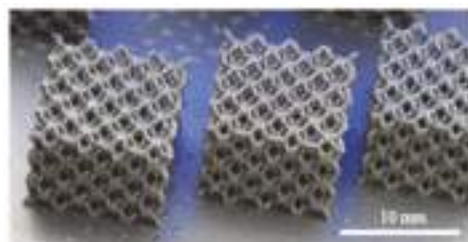


Figure 18. Scaffold-like structures with designed inter-connected porosity out of WE43 made by SLM [65].

9. Concluding Remarks

The available studies on the selective laser melting (SLM) of magnesium and magnesium alloy powders are reviewed in this work. Processing parameters involved during SLM and their effects on formability, densification, microstructure and mechanical properties of different magnesium materials are described. It was also demonstrated that the appropriate control of processing parameters is of prime importance for achieving the highest possible dense magnesium parts, and the subsequently required mechanical properties. Analysis of the literature revealed that microstructural evolution in SLM fabricated magnesium alloys has been greatly controlled by the specific laser energy input and because of the high cooling rates achieved, the microstructures produced have been extremely fine. SLM is able to produce bulk magnesium parts with comparable mechanical properties and superior corrosion behaviour to those of as-cast and wrought alloys. Metallurgical defects observed during SLM processing of magnesium alloys such as porosity, thermal cracking, oxide inclusions, and loss of alloying elements were also reviewed.

Research on additive manufacturing (AM) of magnesium based materials has increased in recent years due to the combination of the geometrical freedom offered by AM along with its capability to manufacture components and implants with unique functional properties. The potential of SLM to fabricate topology optimized lightweight magnesium components that are tailored to actual loading cases as well as to produce implants with defined, interconnected pore structures that can substantially improve bone ingrowth has attracted significant interest from the automotive, aerospace, and biomedical sectors. However, compared to iron, titanium, nickel, and aluminium alloys, research on SLM of magnesium based materials is still in its infancy and a considerable amount of research is necessary before these materials see a widespread use in industrial applications. One area that is crucial to establish the SLM process for magnesium powder materials is the ability to produce fully dense parts devoid of balling and oxidation. Only when this capability is routinely and easily achieved can work begin on understanding the influence of processing parameters as well as powder properties on thermal gradients, solidification, residual stresses, and eventually the microstructure/mechanical properties of the SLM fabricated magnesium alloy components. From this, studies can begin to branch out to determine the response of these materials to different loading conditions, as well as to determine the influence of temperature and environmental conditions on their performance towards more understanding of the corrosion behaviour and biological response in order to further ascertain the reliability of the products and suitability of SLM technology in producing magnesium alloys.

A critical review shows that the understanding of the microstructural aspects of magnesium alloys produced by SLM is well now developed but the mechanical properties are not widely available. Most available studies have reported only density and hardness values and the mechanical properties such as tensile, compression, and fatigue have not been reported. In the absence of such detailed data, the development of theoretical models is not keeping pace with the experimental work. In addition to the experimental work, modelling and simulation are needed to optimize the properties of the fabricated parts. Particular areas that should be focussed on are the effect of various

processing and powder properties. This remains an open research area due to the large number of process/design parameters (e.g., laser power, traverse speed, powder feed rate, layer thickness, hatching pitch, scanning pattern, etc.) involved during SLM. Most of the existing studies have sought only optimal process parameters via extensive experimental work. A major limitation of this approach is that the resulting optimal process parameters may not be useful when experimental conditions (e.g., process or material) change, with the result that new experiments need to-be-conducted from scratch. Further research is needed to lever the information from similar earlier studies and to systematically characterize the relation between process parameters and part features so that the SLM process can be optimized in a more efficient manner. Models that correlate processing conditions to the microstructure and quality of the final product are also needed to minimize the cost and timeline associated with process development. Process specifications for laser melting should be developed to avoid the occurrence of defects to enable reliable production of magnesium alloys. With additional knowledge and application of specific tailoring of the properties, it is likely that SLM of magnesium alloys will see increased usage in forthcoming days.

Author Contributions: Vyasaraj Manakari and Gururaj Parande outlined the review, performed the literature search and wrote the manuscript. Manoj Gupta helped in compiling the wide information related to the topic and data presentation and performed technical editing for all corrections. Manoj Gupta also helped in writing the manuscript and developed the idea of the topic and was responsible for the correspondence.

Conflicts of Interest: The authors declare no conflict of interest.

References

1. Gupta, M.; Sharon, N.M.L. *Magnesium, Magnesium Alloys, and Magnesium Composites*; John Wiley & Sons: Hoboken, NJ, USA, 2011.
2. Mordike, B.; Ebert, T. Magnesium: Properties—Applications—Potential. *Mater. Sci. Eng. A* **2001**, *302*, 37–45. [CrossRef]
3. Froes, F.; Eliezer, D.; Aghion, E. The science, technology, and applications of magnesium. *JOM* **1998**, *50*, 30–34. [CrossRef]
4. Winzer, N.; Atrens, A.; Song, G.; Ghali, E.; Dietzel, W.; Kainer, K.U.; Hort, N.; Blawert, C. A critical review of the stress corrosion cracking (SCC) of magnesium alloys. *Adv. Eng. Mater.* **2005**, *7*, 659–693. [CrossRef]
5. Song, G.L.; Atrens, A. Corrosion mechanisms of magnesium alloys. *Adv. Eng. Mater.* **1999**, *1*, 11–33. [CrossRef]
6. Jun, J.; Kim, J.; Park, B.; Kim, K.; Jung, W. Effects of rare earth elements on microstructure and high temperature mechanical properties of ZC63 alloy. *J. Mater. Sci.* **2005**, *40*, 2659–2661. [CrossRef]
7. Itoi, T.; Takahashi, K.; Moriyama, H.; Hirohashi, M. A high-strength Mg-Ni-Y alloy sheet with a long-period ordered phase prepared by hot-rolling. *Scr. Mater.* **2008**, *59*, 1155–1158. [CrossRef]
8. Toda-Caraballo, I.; Galindo-Navia, E.I.; Rivera-Díaz-del-Castillo, P.E. Understanding the factors influencing yield strength on Mg alloys. *Acta Mater.* **2014**, *75*, 287–296. [CrossRef]
9. Johnston, S.; Shi, Z.; Atrens, A. The influence of pH on the corrosion rate of high-purity Mg, AZ91 and ZE41 in bicarbonate buffered Hanks' solution. *Corros. Sci.* **2015**, *101*, 182–192. [CrossRef]
10. Gupta, M.; Meenashisundaram, G.K. *Insight into Designing Biocompatible Magnesium Alloys and Composites: Processing, Mechanical and Corrosion Characteristics*; Springer: New York, NY, USA, 2015.
11. Walker, J.; Shadabzai, S.; Woodfield, T.B.; Staiger, M.P.; Dias, G.J. Magnesium biomaterials for orthopedic application: A review from a biological perspective. *J. Biomed. Mater. Res. B Appl. Biomater.* **2014**, *102*, 1316–1331. [CrossRef] [PubMed]
12. Witte, F. The history of biodegradable magnesium implants: A review. *Acta Biomater.* **2010**, *6*, 1680–1692. [CrossRef] [PubMed]
13. Windhagen, H.; Radtke, K.; Weizbauer, A.; Diekmann, J.; Noll, Y.; Kreimeyer, U.; Schavan, R.; Stukenborg-Colsman, C.; Waizy, H. Biodegradable magnesium-based screw clinically equivalent to titanium screw in hallux valgus surgery: Short term results of the first prospective, randomized, controlled clinical pilot study. *Biomed. Eng. Online* **2013**, *12*, 62. [CrossRef] [PubMed]
14. Sietsema, W. Animal models of cortical porosity. *Bone* **1995**, *17*, S297–S305. [CrossRef]

15. Ramirez, J.M.; Hurt, W.C. Bone remodeling in periodontal lesions. *J. Periodontol.* **1977**, *48*, 74–77. [CrossRef] [PubMed]
16. Staiger, M.P.; Pietak, A.M.; Huadmai, J.; Dias, G. Magnesium and its alloys as orthopedic biomaterials: A review. *Biomaterials* **2006**, *27*, 1728–1734. [CrossRef] [PubMed]
17. Alvarez, K.; Nakajima, H. Metallic scaffolds for bone regeneration. *Materials* **2009**, *2*, 790–832. [CrossRef]
18. Agarwal, S.; Curtin, J.; Duffy, B.; Jaiswal, S. Biodegradable magnesium alloys for orthopaedic applications: A review on corrosion, biocompatibility and surface modifications. *Mater. Sci. Eng. C* **2016**, *68*, 948–963. [CrossRef] [PubMed]
19. Gehrmann, R.; Frommert, M.M.; Gottstein, G. Texture effects on plastic deformation of magnesium. *Mater. Sci. Eng. A* **2005**, *395*, 338–349. [CrossRef]
20. Kulekci, M.K. Magnesium and its alloys applications in automotive industry. *Int. J. Adv. Manuf. Technol.* **2008**, *39*, 851–865. [CrossRef]
21. Bettles, C.J. Magnesium powder metallurgy: Process and materials opportunities. *J. Mater. Eng. Perform.* **2008**, *17*, 297–301. [CrossRef]
22. Tandon, R.; Madan, D. Emerging applications for magnesium alloy powders. *Powder Metall.* **2014**, *57*, 236–241. [CrossRef]
23. Kawamura, Y.; Hayashi, K.; Inoue, A.; Masumoto, T. Rapidly solidified powder metallurgy Mg97Zn1Y2Alloys with excellent tensile yield strength above 600 MPa. *Mater. Trans.* **2001**, *42*, 1171–1174. [CrossRef]
24. Tandon, R. Potential for Advanced Magnesium Alloy Powders in Aerospace Applications. In Proceedings of the 24th Advanced Aerospace Materials and Processes (AeroMat) Conference and Exposition, Bellevue, WC, USA, 2–5 April 2013.
25. Osakada, K.; Shiomi, M. Flexible manufacturing of metallic products by selective laser melting of powder. *Int. J. Mach. Tools Manuf.* **2006**, *46*, 1188–1193. [CrossRef]
26. Riza, S.; Masood, S.; Wen, C. Laser-assisted additive manufacturing for metallic biomedical scaffolds. In *Comprehensive Materials Processing*; Elsevier: London, UK, 2014.
27. Jia, Q.; Gu, D. Selective laser melting additive manufacturing of Inconel 718 superalloy parts: Densification, microstructure and properties. *J. Alloy. Compd.* **2014**, *585*, 713–721. [CrossRef]
28. Zhang, L.C.; Attar, H. Selective laser melting of titanium alloys and titanium matrix composites for biomedical applications: A review. *Adv. Eng. Mater.* **2016**, *18*, 463–475. [CrossRef]
29. Wang, X.; Gong, X.; Chou, K. Review on powder-bed laser additive manufacturing of Inconel 718 parts. In Proceedings of the ASME 2015 International Manufacturing Science and Engineering Conference, Charlotte, NC, USA, 8–12 June 2015.
30. Lu, Z.; Cao, J.; Jing, H.; Liu, T.; Lu, F.; Wang, D.; Li, D. Review of main manufacturing processes of complex hollow turbine blades: This paper critically reviews conventional and advanced technologies used for manufacturing hollow turbine blades. *Virtual Phys. Prototyp.* **2013**, *8*, 87–95. [CrossRef]
31. Amato, K.; Gaytan, S.; Murr, L.; Martinez, E.; Shindo, P.; Hernandez, J.; Collins, S.; Medina, F. Microstructures and mechanical behavior of Inconel 718 fabricated by selective laser melting. *Acta Mater.* **2012**, *60*, 2229–2239. [CrossRef]
32. Oyagüe, R.C.; Sánchez-Turrión, A.; López-Lozano, J.F.; Montero, J.; Albaladejo, A.; Suárez-García, M.J. Evaluation of fit of cement-retained implant-supported 3-unit structures fabricated with direct metal laser sintering and vacuum casting techniques. *Odontology* **2012**, *100*, 249–253. [CrossRef] [PubMed]
33. Sercombe, T.; Li, X. Selective laser melting of aluminium and aluminium metal matrix composites: Review. *Mater. Technol.* **2016**, *31*, 77–85. [CrossRef]
34. Kruth, J.-P.; Mercelis, P.; van Vaerenbergh, J.; Froyen, L.; Rombouts, M. Binding mechanisms in selective laser sintering and selective laser melting. *Rapid Prototyp. J.* **2005**, *11*, 26–36. [CrossRef]
35. Yadroitsev, I.; Smurov, I. Surface morphology in selective laser melting of metal powders. *Phys. Procedia* **2011**, *12*, 264–270. [CrossRef]
36. Fischer, P.; Romano, V.; Weber, H.-P.; Karapatis, N.; Boillat, E.; Glardon, R. Sintering of commercially pure titanium powder with a Nd:YAG laser source. *Acta Mater.* **2003**, *51*, 1651–1662. [CrossRef]
37. Yadroitsev, I.; Yadroitseva, I.; Smurov, I. Strategy of fabrication of complex shape parts based on the stability of single laser melted track. *SPIE Proc.* **2011**, *7921*. [CrossRef]
38. Li, Y.; Gu, D. Parametric analysis of thermal behavior during selective laser melting additive manufacturing of aluminum alloy powder. *Mater. Des.* **2014**, *63*, 856–867. [CrossRef]

39. Gu, D. *Laser Additive Manufacturing of High-Performance Materials*; Springer: New York, NY, USA, 2015.
40. Zhang, H.; Zhang, D.; Ma, C.; Guo, S. Improving mechanical properties and corrosion resistance of Mg-6Zn-Mn magnesium alloy by rapid solidification. *Mater. Lett.* **2013**, *92*, 45–48. [CrossRef]
41. Yap, C.; Chua, C.; Dong, Z.; Liu, Z.; Zhang, D.; Loh, L.; Sing, S.L. Review of selective laser melting: Materials and applications. *Appl. Phys. Rev.* **2015**, *2*, 041101. [CrossRef]
42. Sing, S.L.; An, J.; Yeong, W.Y.; Wiria, F.E. Laser and electron-beam powder-bed additive manufacturing of metallic implants: A review on processes, materials and designs. *J. Orthop. Res.* **2016**, *34*, 369–385. [CrossRef] [PubMed]
43. Acharya, R.; Bansal, R.; Gambone, J.J.; Das, S. A coupled thermal, fluid flow, and solidification model for the processing of single-crystal alloy CMSX-4 through scanning laser epitaxy for turbine engine hot-section component repair (part I). *Metall. Mater. Trans. B* **2014**, *45*, 2247–2261. [CrossRef]
44. Acharya, R.; Bansal, R.; Gambone, J.J.; Kaplan, M.A.; Fuchs, G.E.; Rudawski, N.; Das, S. Additive manufacturing and characterization of rené 80 superalloy processed through scanning laser epitaxy for turbine engine hot-section component repair. *Adv. Eng. Mater.* **2015**, *17*, 942–950. [CrossRef]
45. Liu, Z.; Zhang, D.; Sing, S.; Chua, C.; Loh, L. Interfacial characterization of SLM parts in multi-material processing: Metallurgical diffusion between 316L stainless steel and C18400 copper alloy. *Mater. Charact.* **2014**, *94*, 116–125. [CrossRef]
46. Sing, S.; Lam, L.; Zhang, D.; Liu, Z.; Chua, C. Interfacial characterization of SLM parts in multi-material processing: Intermetallic phase formation between AlSi10Mg and C18400 copper alloy. *Mater. Charact.* **2015**, *107*, 220–227. [CrossRef]
47. Kruth, J.-P.; Badrossamay, M.; Yasa, E.; Deckers, J.; Thijss, L.; van Humbeeck, J. Part and material properties in selective laser melting of metals. In Proceedings of the 16th International Symposium on Electromachining, Shanghai, China, 19–23 April 2010.
48. Kruth, J.-P.; Levy, G.; Klocke, F.; Childs, T. Consolidation phenomena in laser and powder-bed based layered manufacturing. *CIRP Ann. Manuf. Technol.* **2007**, *56*, 730–759. [CrossRef]
49. Shuai, C.; Yang, Y.; Wu, P.; Lin, X.; Liu, Y.; Zhou, Y.; Feng, P.; Liu, X.; Peng, S. Laser rapid solidification improves corrosion behavior of Mg-Zn-Zr alloy. *J. Alloy. Compd.* **2017**, *691*, 961–969. [CrossRef]
50. Das, S. Physical aspects of process control in selective laser sintering of metals. *Adv. Eng. Mater.* **2003**, *5*, 701–711. [CrossRef]
51. Gu, D.; Meiners, W.; Wissenbach, K.; Poprawe, R. Laser additive manufacturing of metallic components: Materials, processes and mechanisms. *Int. Mater. Rev.* **2012**, *57*, 133–164. [CrossRef]
52. Olakanmi, E.; Cochrane, R.; Dalgarno, K. A review on selective laser sintering/melting (SLS/SLM) of aluminium alloy powders: Processing, microstructure, and properties. *Prog. Mater. Sci.* **2015**, *74*, 401–477. [CrossRef]
53. Niu, H.; Chang, I. Selective laser sintering of gas atomized M2 high speed steel powder. *J. Mater. Sci.* **2000**, *35*, 31–38. [CrossRef]
54. Agarwala, M.; Bourell, D.; Beaman, J.; Marcus, H.; Barlow, J. Direct selective laser sintering of metals. *Rapid Prototyp. J.* **1995**, *1*, 26–36. [CrossRef]
55. Ng, C.; Savalani, M.; Man, H.; Gibson, I. Layer manufacturing of magnesium and its alloy structures for future applications. *Virtual Phys. Prototyp.* **2010**, *5*, 13–19. [CrossRef]
56. Ng, C.C.; Savalani, M.M.; Man, H.C. Fabrication of magnesium using selective laser melting technique. *Rapid Prototyp. J.* **2011**, *17*, 479–490.
57. Ng, C.C.; Savalani, M.M.; Lau, M.L.; Man, H.C. Microstructure and mechanical properties of selective laser melted magnesium. *Appl. Surf. Sci.* **2011**, *257*, 7447–7454. [CrossRef]
58. Savalani, M.M.; Pizarro, J.M.; Campbell, R.I.; Gibson, I. Effect of preheat and layer thickness on selective laser melting (SLM) of magnesium. *Rapid Prototyp. J.* **2016**, *22*, 115–122. [CrossRef]
59. Hu, D.; Wang, Y.; Zhang, D.; Hao, L.; Jiang, J.; Li, Z.; Chen, Y. Experimental investigation on selective laser melting of bulk net-shape pure magnesium. *Mater. Manuf. Process.* **2015**, *30*, 1298–1304. [CrossRef]
60. Zhang, B.; Liao, H.; Coddet, C. Effects of processing parameters on properties of selective laser melting Mg-9%Al powder mixture. *Mater. Des.* **2012**, *34*, 753–758. [CrossRef]
61. Wei, K.; Gao, M.; Wang, Z.; Zeng, X. Effect of energy input on formability, microstructure and mechanical properties of selective laser melted AZ91D magnesium alloy. *Mater. Sci. Eng. A* **2014**, *611*, 212–222. [CrossRef]

62. Wei, K.; Wang, Z.; Zeng, X. Influence of element vaporization on formability, composition, microstructure, and mechanical performance of the selective laser melted Mg-Zn-Zr components. *Mater. Lett.* **2015**, *156*, 187–190. [CrossRef]
63. Zhang, C. *Parametric Study on Selective Laser Melting of Magnesium Micropowder with Hydroxyapatite (HA) Nanoparticles*; University of California: Los Angeles, CA, USA, 2015.
64. Gieseke, M.; Noelke, C.; Kaierle, S.; Wesling, V.; Haferkamp, H.; Hort, N. Selective laser melting of magnesium and magnesium alloys. *Magnes. Technol.* **2013**, *2013*, 65–68.
65. Jauer, L.; Jülich, B.; Voshage, M.; Meiners, W. Selective laser melting of magnesium alloys. In Proceedings of the 7th Symposium on Biodegradable Metals, Carovigno, Italy, 23–28 August 2015; p. 1.
66. Yang, Y.; Wu, P.; Wang, Q.; Wu, H.; Liu, Y.; Deng, Y.; Zhou, Y.; Shuai, C. The enhancement of Mg corrosion resistance by alloying Mn and laser-melting. *Materials* **2016**, *9*, 216. [CrossRef]
67. Song, B.; Dong, S.; Deng, S.; Liao, H.; Coddet, C. Microstructure and tensile properties of iron parts fabricated by selective laser melting. *Opt. Laser Technol.* **2014**, *56*, 451–460. [CrossRef]
68. Attar, H.; Calin, M.; Zhang, L.; Scudino, S.; Eckert, J. Manufacture by selective laser melting and mechanical behavior of commercially pure titanium. *Mater. Sci. Eng. A* **2014**, *593*, 170–177. [CrossRef]
69. Attar, H.; Bönisch, M.; Calin, M.; Zhang, L.-C.; Scudino, S.; Eckert, J. Selective laser melting of in situ titanium-titanium boride composites: Processing, microstructure and mechanical properties. *Acta Mater.* **2014**, *76*, 13–22. [CrossRef]
70. Yadroitsev, I.; Krakhmalev, P.; Yadroitseva, I. Hierarchical design principles of selective laser melting for high quality metallic objects. *Addit. Manuf.* **2015**, *7*, 45–56. [CrossRef]
71. Niu, H.; Chang, I. Instability of scan tracks of selective laser sintering of high speed steel powder. *Scr. Mater.* **1999**, *41*, 1229–1234. [CrossRef]
72. Olakanmi, E. Selective laser sintering/melting (SLS/SLM) of pure Al, Al-Mg, and Al-Si powders: Effect of processing conditions and powder properties. *J. Mater. Process. Technol.* **2013**, *213*, 1387–1405. [CrossRef]
73. Gu, D.; Shen, Y. Balling phenomena in direct laser sintering of stainless steel powder: Metallurgical mechanisms and control methods. *Mater. Des.* **2009**, *30*, 2903–2910. [CrossRef]
74. Khan, M.; Dickens, P. Selective laser melting (SLM) of gold (Au). *Rapid Prototyp. J.* **2012**, *18*, 81–94. [CrossRef]
75. Gu, D.; Hagedorn, Y.-C.; Meiners, W.; Meng, G.; Batista, R.J.S.; Wissenbach, K.; Poprawe, R. Densification behavior, microstructure evolution, and wear performance of selective laser melting processed commercially pure titanium. *Acta Mater.* **2012**, *60*, 3849–3860. [CrossRef]
76. Thijss, L.; Verhaeghe, F.; Craeghs, T.; van Humbeeck, J.; Kruth, J.-P. A study of the microstructural evolution during selective laser melting of Ti-6Al-4V. *Acta Mater.* **2010**, *58*, 3303–3312. [CrossRef]
77. Aboulkhair, N.T.; Everitt, N.M.; Ashcroft, I.; Tuck, C. Reducing porosity in AlSi10Mg parts processed by selective laser melting. *Addit. Manuf.* **2014**, *1*, 77–86. [CrossRef]
78. Zhang, L.; Klemm, D.; Eckert, J.; Hao, Y.; Sercombe, T. Manufacture by selective laser melting and mechanical behavior of a biomedical Ti-24Nb-4Zr-8Sn alloy. *Scr. Mater.* **2011**, *65*, 21–24. [CrossRef]
79. Attar, H.; Prashanth, K.G.; Zhang, L.-C.; Calin, M.; Okulov, I.V.; Scudino, S.; Yang, C.; Eckert, J. Effect of powder particle shape on the properties of in situ Ti-TiB composite materials produced by selective laser melting. *J. Mater. Sci. Technol.* **2015**, *31*, 1001–1005. [CrossRef]
80. Krishna, B.V.; Bose, S.; Bandyopadhyay, A. Low stiffness porous Ti structures for load-bearing implants. *Acta Biomater.* **2007**, *3*, 997–1006. [CrossRef] [PubMed]
81. Taltavull, C.; Torres, B.; López, A.; Rodrigo, P.; Otero, E.; Rams, J. Selective laser surface melting of a magnesium-aluminium alloy. *Mater. Lett.* **2012**, *85*, 98–101. [CrossRef]
82. Amorim, F.L.; Lohrengel, A.; Neubert, V.; Higa, C.F.; Czelusniak, T. Selective laser sintering of Mo-CuNi composite to be used as EDM electrode. *Rapid Prototyp. J.* **2014**, *20*, 59–68. [CrossRef]
83. Hon, K.K.B. *Digital Additive Manufacturing: From Rapid Prototyping to Rapid Manufacturing*; Springer: London, UK, 2007; pp. 337–340.
84. Olakanmi, E.; Cochrane, R.; Dalgarno, K. Densification mechanism and microstructural evolution in selective laser sintering of Al-12Si powders. *J. Mater. Process. Technol.* **2011**, *211*, 113–121. [CrossRef]
85. Tolochko, N.; Mozzharov, S.; Laoui, T.; Froyen, L. Selective laser sintering of single-and two-component metal powders. *Rapid Prototyp. J.* **2003**, *9*, 68–78. [CrossRef]
86. Sames, W.; List, F.; Pannala, S.; Dehoff, R.; Babu, S. The metallurgy and processing science of metal additive manufacturing. *Int. Mater. Rev.* **2016**, *61*, 315–360. [CrossRef]

87. Niu, H.; Chang, I. Selective laser sintering of gas and water atomized high speed steel powders. *Scr. Mater.* **1999**, *41*, 25–30. [CrossRef]
88. Simchi, A. The role of particle size on the laser sintering of iron powder. *Metall. Mater. Trans. B* **2004**, *35*, 937–948. [CrossRef]
89. Liu, B.; Wildman, R.; Tuck, C.; Ashcroft, I.; Hague, R. Investigation the effect of particle size distribution on processing parameters optimisation in selective laser melting process. In *International Solid Freeform Fabrication Symposium: An Additive Manufacturing Conference*; University of Texas: Austin, TX, USA, 2011; pp. 227–238.
90. Kumar, S. 10.05—Selective Laser Sintering/Melting A2—Hashmi, Saleem. In *Comprehensive Materials Processing*; Batalha, G.F., Tyne, C.J.V., Yilbas, B., Eds.; Elsevier: Oxford, UK, 2014; pp. 93–134.
91. Olatunde Olakanmi, E.; Dalgarno, K.W.; Cochrane, R.F. Laser sintering of blended Al-Si powders. *Rapid Prototyp. J.* **2012**, *18*, 109–119. [CrossRef]
92. Bourell, D.; Stucker, B.; Spierings, A.; Herres, N.; Levy, G. Influence of the particle size distribution on surface quality and mechanical properties in AM steel parts. *Rapid Prototyp. J.* **2011**, *17*, 195–202.
93. Glardon, R.; Karapatis, N.; Romano, V.; Levy, G. Influence of Nd:YAG parameters on the selective laser sintering of metallic powders. *CIRP Ann. Manuf. Technol.* **2001**, *50*, 133–136. [CrossRef]
94. Cao, X.; Jahazi, M.; Immarigeon, J.; Wallace, W. A review of laser welding techniques for magnesium alloys. *J. Mater. Process. Technol.* **2006**, *171*, 188–204. [CrossRef]
95. Tolochko, N.K.; Khlopkov, Y.V.; Mozzharov, S.E.; Ignatiev, M.B.; Laoui, T.; Titov, V.I. Absorptance of powder materials suitable for laser sintering. *Rapid Prototyp. J.* **2000**, *6*, 155–161. [CrossRef]
96. Steen, W. Laser material processing—An overview. *J. Opt. A Pure Appl. Opt.* **2003**, *5*, S3. [CrossRef]
97. John, F. *Ready: LIA Handbook of Laser Materials Processing*; Laser Institute of America Magnolia Publishing Inc.: Orlando, FL, USA, 2001; pp. 181–183.
98. Shen, N.; Chou, K. Thermal modeling of electron beam additive manufacturing process: Powder sintering effects. In Proceedings of the ASME 2012 International Manufacturing Science and Engineering Conference collocated with the 40th North American Manufacturing Research Conference and in participation with the International Conference on Tribology Materials and Processing, Notre Dame, IN, USA, 4–8 June 2012; pp. 287–295.
99. Selcuk, C. Laser metal deposition for powder metallurgy parts. *Powder Metall.* **2011**, *54*, 94–99.
100. Basu, B.; Date, A. Rapid solidification following laser melting of pure metals—I. Study of flow field and role of convection. *Int. J. Heat Mass Transf.* **1992**, *35*, 1049–1058. [CrossRef]
101. Bontha, S.; Klingbeil, N.W.; Kobryn, P.A.; Fraser, H.L. Thermal process maps for predicting solidification microstructure in laser fabrication of thin-wall structures. *J. Mater. Process. Technol.* **2006**, *178*, 135–142. [CrossRef]
102. Dahle, A.K.; Lee, Y.C.; Nave, M.D.; Schaffer, P.L.; StJohn, D.H. Development of the as-cast microstructure in magnesium-aluminium alloys. *J. Light Met.* **2001**, *1*, 61–72. [CrossRef]
103. Campbell, J. *Castings*; Butterworth-Heinemann: Oxford, UK, 2003.
104. Aarstad, K. Protective Films on Molten Magnesium. Ph.D. Thesis, Norwegian University of Science and Technology, Trondheim, Norway, May 2004.
105. Louvis, E.; Fox, P.; Sutcliffe, C.J. Selective laser melting of aluminium components. *J. Mater. Process. Technol.* **2011**, *211*, 275–284. [CrossRef]
106. Collur, M.; Paul, A.; DebRoy, T. Mechanism of alloying element vaporization during laser welding. *Metall. Trans. B* **1987**, *18*, 733–740. [CrossRef]
107. Sanders, P.; Keske, J.; Leong, K.; Kornecki, G. High power Nd: YAG and CO₂ laser welding of magnesium. *J. Laser Appl.* **1999**, *11*, 96–103. [CrossRef]
108. Liu, Y.; Li, S.; Wang, H.; Hou, W.; Hao, Y.; Yang, R.; Sercombe, T.B.; Zhang, L.C. Microstructure, defects and mechanical behavior of beta-type titanium porous structures manufactured by electron beam melting and selective laser melting. *Acta Mater.* **2016**, *113*, 56–67. [CrossRef]
109. Asgharzadeh, H.; Simchi, A. Effect of sintering atmosphere and carbon content on the densification and microstructure of laser-sintered M2 high-speed steel powder. *Mater. Sci. Eng. A* **2005**, *403*, 290–298. [CrossRef]
110. Gu, D.; Shen, Y. Balling phenomena during direct laser sintering of multi-component Cu-based metal powder. *J. Alloy. Compd.* **2007**, *432*, 163–166. [CrossRef]

111. Zhang, L.-C.; Attar, H.; Calin, M.; Eckert, J. Review on manufacture by selective laser melting and properties of titanium based materials for biomedical applications. *Mater. Technol.* **2016**, *31*, 66–76. [CrossRef]
112. Li, R.; Liu, J.; Shi, Y.; Wang, L.; Jiang, W. Balling behavior of stainless steel and nickel powder during selective laser melting process. *Int. J. Adv. Manuf. Technol.* **2012**, *59*, 1025–1035. [CrossRef]
113. Mercelis, P.; Kruth, J.-P. Residual stresses in selective laser sintering and selective laser melting. *Rapid Prototyp. J.* **2006**, *12*, 254–265. [CrossRef]
114. Parande, G.; Manakari, V.; Meenashisundaram, G.K.; Gupta, M. Enhancing the hardness/compression/damping response of magnesium by reinforcing with biocompatible silica nanoparticulates. *Int. J. Mater. Res. 2016*, *107*, 1091–1099. [CrossRef]
115. Casavola, C.; Campanelli, S.; Pappalettere, C. Preliminary investigation on distribution of residual stress generated by the selective laser melting process. *J. Strain Anal. Eng. Des.* **2009**, *44*, 93–104. [CrossRef]
116. Shamsaei, N.; Yadollahi, A.; Bian, L.; Thompson, S.M. An overview of Direct Laser Deposition for additive manufacturing: Part II: Mechanical behavior, process parameter optimization and control. *Addit. Manuf.* **2015**, *8*, 12–35. [CrossRef]
117. Atrens, A.; Song, G.-L.; Cao, F.; Shi, Z.; Bowen, P.K. Advances in Mg corrosion and research suggestions. *J. Magnes. Alloy.* **2013**, *1*, 177–200. [CrossRef]
118. Song, G.; Atrens, A. Understanding magnesium corrosion—A framework for improved alloy performance. *Adv. Eng. Mater.* **2003**, *5*, 837–858. [CrossRef]
119. Ghali, E. *Corrosion Resistance of Aluminum and Magnesium Alloys: Understanding, Performance, and Testing*; John Wiley & Sons: Hoboken, NJ, USA, 2010.
120. Singh, A.; Harimkar, S.P. Laser surface engineering of magnesium alloys: A review. *JOM* **2012**, *64*, 716–733. [CrossRef]
121. Guan, Y.; Zhou, W.; Zheng, H.; Li, Z. Solidification microstructure of AZ91D Mg alloy after laser surface melting. *Appl. Phys. A* **2010**, *101*, 339–344. [CrossRef]
122. Liu, C.; Liang, J.; Zhou, J.; Wang, L.; Li, Q. Effect of laser surface melting on microstructure and corrosion characteristics of AM60B magnesium alloy. *Appl. Surf. Sci.* **2015**, *343*, 133–140. [CrossRef]
123. Cui, Z.-Q.; Shi, H.-X.; Wang, W.-X.; Xu, B.-S. Laser surface melting AZ31B magnesium alloy with liquid nitrogen-assisted cooling. *Trans. Nonferr. Met. Soc. China* **2015**, *25*, 1446–1453. [CrossRef]
124. Taltavull, C.; Torres, B.; Lopez, A.; Rodrigo, P.; Otero, E.; Atrens, A.; Rams, J. Corrosion behaviour of laser surface melted magnesium alloy AZ91D. *Mater. Des.* **2014**, *57*, 40–50. [CrossRef]
125. Paital, S.R.; Bhattacharya, A.; Moncayo, M.; Ho, Y.H.; Mahdak, K.; Nag, S.; Banerjee, R.; Dahotre, N.B. Improved corrosion and wear resistance of Mg alloys via laser surface modification of Al on AZ31B. *Surf. Coat. Technol.* **2012**, *206*, 2308–2315. [CrossRef]
126. Coy, A.; Viejo, F.; Garcia-Garcia, F.; Liu, Z.; Skeldon, P.; Thompson, G. Effect of excimer laser surface melting on the microstructure and corrosion performance of the die cast AZ91D magnesium alloy. *Corros. Sci.* **2010**, *52*, 387–397. [CrossRef]
127. Raman, R.S.; Murray, S.; Brandt, M. Laser assisted modification of surface microstructure for localised corrosion resistance of magnesium alloys. *Surf. Eng.* **2013**, *23*, 107–111. [CrossRef]
128. Abbas, G.; Liu, Z.; Skeldon, P. Corrosion behaviour of laser-melted magnesium alloys. *Appl. Surf. Sci.* **2005**, *247*, 347–353. [CrossRef]
129. Makar, G.; Kruger, J. Corrosion of magnesium. *Int. Mater. Rev.* **2013**, *38*, 138–153. [CrossRef]
130. Liu, C.; Li, Q.; Liang, J.; Zhou, J.; Wang, L. Microstructure and corrosion behaviour of laser surface melting treated WE43 magnesium alloy. *RSC Adv.* **2016**, *6*, 30642–30651. [CrossRef]
131. Song, G. Control of biodegradation of biocompatible magnesium alloys. *Corros. Sci.* **2007**, *49*, 1696–1701. [CrossRef]
132. Gu, X.; Li, N.; Zheng, Y.; Ruan, L. In vitro degradation performance and biological response of a Mg-Zn-Zr alloy. *Mater. Sci. Eng. B* **2011**, *176*, 1778–1784. [CrossRef]
133. Dai, N.; Zhang, L.-C.; Zhang, J.; Chen, Q.; Wu, M. Corrosion behavior of selective laser melted Ti-6Al-4V alloy in NaCl solution. *Corros. Sci.* **2016**, *102*, 484–489. [CrossRef]
134. Dai, N.; Zhang, L.-C.; Zhang, J.; Zhang, X.; Ni, Q.; Chen, Y.; Wu, M.; Yang, C. Distinction in corrosion resistance of selective laser melted Ti-6Al-4V alloy on different planes. *Corros. Sci.* **2016**, *111*, 703–710. [CrossRef]

135. Xin, Y.; Hu, T.; Chu, P. In vitro studies of biomedical magnesium alloys in a simulated physiological environment: A review. *Acta Biomater.* **2011**, *7*, 1452–1459. [CrossRef] [PubMed]
136. Rettig, R.; Virtanen, S. Time-dependent electrochemical characterization of the corrosion of a magnesium rare-earth alloy in simulated body fluids. *J. Biomed. Mater. Res. A* **2008**, *85*, 167–175. [CrossRef] [PubMed]
137. Martin, R. Porosity and specific surface of bone. *Crit. Rev. Biomed. Eng.* **1983**, *10*, 179–222.
138. Bentolila, V.; Boyce, T.; Fyhrie, D.; Drumb, R.; Skerry, T.; Schaffler, M. Intracortical remodeling in adult rat long bones after fatigue loading. *Bone* **1998**, *23*, 275–281. [CrossRef]
139. Prendergast, P.; Huiskes, R. Microdamage and osteocyte-lacuna strain in bone: A microstructural finite element analysis. *J. Biomech. Eng.* **1996**, *118*, 240–246. [CrossRef] [PubMed]
140. Wang, X.; Ni, Q. Determination of cortical bone porosity and pore size distribution using a low field pulsed NMR approach. *J. Orthop. Res.* **2003**, *21*, 312–319. [CrossRef]
141. Kufahl, R.H.; Saha, S. A theoretical model for stress-generated fluid flow in the canaliculi-lacunae network in bone tissue. *J. Biomech.* **1990**, *23*, 171–180. [CrossRef]
142. Zardiackas, L.D.; Parsell, D.E.; Dillon, L.D.; Mitchell, D.W.; Nunnery, L.A.; Poggie, R. Structure, metallurgy, and mechanical properties of a porous tantalum foam. *J. Biomed. Mater. Res.* **2001**, *58*, 180–187. [CrossRef]
143. Lefebvre, L.-P.; Banhart, J.; Dunand, D. Porous metals and metallic foams: Current status and recent developments. *Adv. Eng. Mater.* **2008**, *10*, 775–787. [CrossRef]
144. Yan, C.; Hao, L.; Hussein, A.; Young, P.; Raymont, D. Advanced lightweight 316L stainless steel cellular lattice structures fabricated via selective laser melting. *Mater. Des.* **2014**, *55*, 533–541. [CrossRef]
145. Nakajima, H. Fabrication, properties and application of porous metals with directional pores. *Prog. Mater. Sci.* **2007**, *52*, 1091–1173. [CrossRef]
146. Evans, A.G.; Hutchinson, J.W.; Fleck, N.A.; Ashby, M.; Wadley, H. The topological design of multifunctional cellular metals. *Prog. Mater. Sci.* **2001**, *46*, 309–327. [CrossRef]
147. Bose, S.; Vahabzadeh, S.; Bandyopadhyay, A. Bone tissue engineering using 3D printing. *Mater. Today* **2013**, *16*, 496–504. [CrossRef]
148. Hollister, S.J. Porous scaffold design for tissue engineering. *Nat. Mater.* **2005**, *4*, 518–524. [CrossRef] [PubMed]
149. Challis, V.J.; Xu, X.; Zhang, L.C.; Roberts, A.P.; Grotowski, J.F.; Sercombe, T.B. High specific strength and stiffness structures produced using selective laser melting. *Mater. Des.* **2014**, *63*, 783–788. [CrossRef]
150. Liu, Y.; Li, X.; Zhang, L.; Sercombe, T. Processing and properties of topologically optimised biomedical Ti-24Nb-4Zr-8Sn scaffolds manufactured by selective laser melting. *Mater. Sci. Eng. A* **2015**, *642*, 268–278. [CrossRef]
151. Attar, H.; Löber, L.; Funk, A.; Calin, M.; Zhang, L.; Prashanth, K.; Scudino, S.; Zhang, Y.S.; Eckert, J. Mechanical behavior of porous commercially pure Ti and Ti-TiB composite materials manufactured by selective laser melting. *Mater. Sci. Eng. A* **2015**, *625*, 350–356. [CrossRef]



© 2016 by the authors. Licensee MDPI, Basel, Switzerland. This article is an open access article distributed under the terms and conditions of the Creative Commons Attribution (CC BY) license (<http://creativecommons.org/licenses/by/4.0/>).

Article

Microstructure and Wear Properties of Electron Beam Melted Ti-6Al-4V Parts: A Comparison Study against As-Cast Form

Wei Quan Toh ¹, Pan Wang ², Xipeng Tan ^{1,*}, Mui Ling Sharon Nai ², Erjia Liu ^{1,*} and Shu Beng Tor ¹

¹ Singapore Centre for 3D Printing, School of Mechanical and Aerospace Engineering, Nanyang Technological University, 50 Nanyang Avenue, Singapore 639798, Singapore; tohw0023@e.ntu.edu.sg (W.Q.T.); msbtor@ntu.edu.sg (S.B.T.)

² Singapore Institute of Manufacturing Technology, 73 Nanyang Drive, Singapore 637662, Singapore; wangp@simtech.a-star.edu.sg (P.W.); mlhai@simtech.a-star.edu.sg (M.L.S.N.)

* Correspondence: xptan1985@gmail.com (X.T.); mejliu@ntu.edu.sg (E.L.); Tel.: +65-6790-5504 (X.T. & E.L.)

Academic Editor: Manoj Gupta

Received: 29 October 2016; Accepted: 15 November 2016; Published: 18 November 2016

Abstract: Ti-6Al-4V (Ti64) parts of varying thicknesses were additively manufactured (AM) by the powder-bed-based electron beam melting (EBM) technique. Microstructure and wear properties of these EBM-built Ti-6Al-4V parts have been investigated in comparison with conventionally cast Ti64 samples. Sliding wear tests were conducted using a ball-on-disc micro-tribometer under ambient conditions. Experimental results reveal that EBM-built Ti64 samples exhibited higher microhardness and an overall larger coefficient of friction as compared to the as-cast counterpart. Of interest is that the corresponding specific wear volumes were lower for EBM-built Ti64 samples, while the as-cast Ti64 showed the poorest wear resistance despite its lower coefficient of friction. Wear mechanisms were provided in terms of quantitative microstructural characterization and detailed analysis on coefficient of friction (COF) curves.

Keywords: additive manufacturing; 3D printing; electron beam melting; titanium alloys; microstructure; wear properties

1. Introduction

Metal additive manufacturing (AM), popularly known as metal three-dimensional (3D) printing, is changing the way how metals or alloys are manufactured. Powder-bed fusion is the latest developed metal AM technology, which opens up new opportunities to create complex metallic components with relatively high resolution and good dimensional accuracy control [1–3]. Ti-6Al-4V (Ti64) is the most commonly investigated metallic material in AM because of its high specific strength, excellent corrosion resistance, and good biocompatibility, which are highly demanded in aerospace and biomedical industries [4,5]. Electron beam melting (EBM[®]) is a representative powder-bed fusion metal AM technique that is being increasingly employed to process Ti64. It utilizes an electron beam to selectively melt a metallic powder bed given an input of a computer-aided design (CAD) model [6]. The distinct advantages associated with EBM are its ability to fabricate metallic parts more rapidly and with greater energy-efficiency as compared to its comparative technique of selective laser melting (SLM). Moreover, EBM-built parts were shown to have less residual stress than their counterparts fabricated by laser-based systems [6–9]. Hence, post-heat treatment may not be required for EBM-built metal parts, giving an added advantage that leads to greater saving of resources.

Many studies have reported on the processing, microstructure, and mechanical properties of powder-bed fusion AM Ti64 parts [5–7,9–13]. It has been found that some of the mechanical properties,

particularly for tensile properties of metal AM Ti64, are comparable to those of wrought material and much better than its as-cast form [12,13]. However, there are still very limited studies involved in their wear properties that are critical for some specific applications under wear and friction conditions [14]. As known, Ti64 possesses poor wear resistance under dry sliding due to low protection exerted by tribo-oxides formed at the surface [15,16]. Therefore, it is imperative to study on wear behavior of AM Ti64 parts and know their wear properties in comparison with the counterparts manufactured via conventional methods. In our previous works published elsewhere [5,6,17–21], the microstructure and mechanical properties of the EBM-built Ti64 parts have been systematically studied. The present work aims at investigating the wear properties of EBM-built Ti64 parts with various thicknesses and making a comparative study against commercially as-cast Ti64 sample. It is supposed to be an important supplementary study to achieve better understanding for practical applications of EBM-manufactured Ti64 parts.

2. Experimental Section

2.1. Materials, Fabrication, and Sample Preparation

All the EBM-built samples were fabricated via an Arcam A2XX (Arcam AB, Mölndal, Sweden) EBM machine, which has a build chamber of $\Phi 420$ mm \times 380 mm. A schematic diagram of a typical EBM machine is illustrated in Figure 1. The powder used in this process was Ti-6Al-4V ELI (Grade 23) (Batch No. 877) supplied by Arcam AB, and was mainly spherical in shape, as shown in Figure 2a. The spherical nature of the powder assures good followability and thus consistency in the spreading of powder during raking. The powder had a size distribution ranging from 45 to 105 μm , while the mean particle size was $61.8 \mu\text{m} \pm 23.8 \mu\text{m}$. A summary on the powder size distribution of Ti64 used during fabrication is as depicted in Figure 2b. The nominal composition of the Ti64 powder is as follows: 6.0Al-4.0V-0.03C-0.1Fe-0.1O-0.01N-<0.003H and the balance being Ti (wt. %). The EBM-built samples of varying thicknesses of 0.5 mm, 1 mm, 5 mm, 10 mm, and 20 mm by 100 mm in length and 30 mm in height are shown in Figure 3a. They were termed 0.5 mm, 1 mm, 5 mm, 10 mm, and 20 mm samples, respectively. The build chamber was under a controlled vacuum environment having a temperature range of 600 to 650 °C. The samples were built on a 210 mm \times 210 mm stainless steel (SS) start plate. The samples were subsequently removed from the SS start plate via knocking on the backside of the SS plate and cleaned with the use of the powder recovering system (PRS). PRS primarily functioned as a grit blaster where blasting media (Ti64) were accelerated towards the sample surface with the aid of high velocity compressed air with the aim to remove any residual partially-sintered and unmelted powder particles surrounding the samples' surface. The as-cast samples were supplied in the form of a rod by Titan Engineering Pte. Ltd. (Singapore, Singapore), cast to the specification ASEM B348 GR5 and had a dimension of $\Phi 25.4$ mm \times 1500 mm. The EBM-built samples were sliced from the middle section (X-Z plane) into squares of 20 mm \times 20 mm, while the as-cast sample was sliced into a disc of $\Phi 25.4$ mm \times 5 mm. All the samples were then hot mounted with phenolic polymer and subsequently polished to a mirror-like finish.

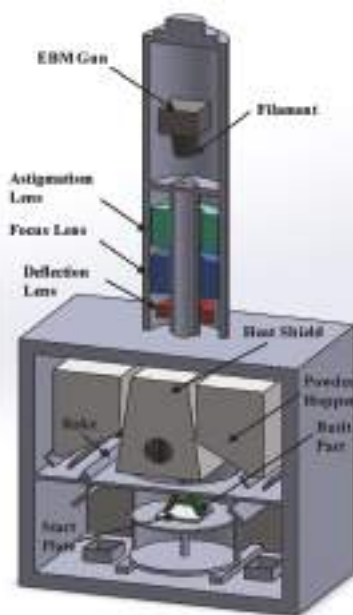


Figure 1. Schematic of an Arcam A2XX EBM machine.

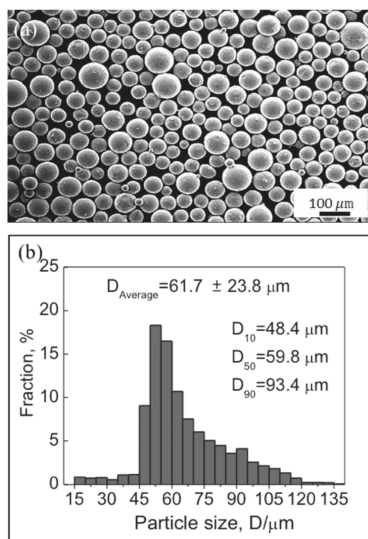


Figure 2. (a) SEM image and (b) powder size distribution of Ti64 powder supplied by Arcam AB.

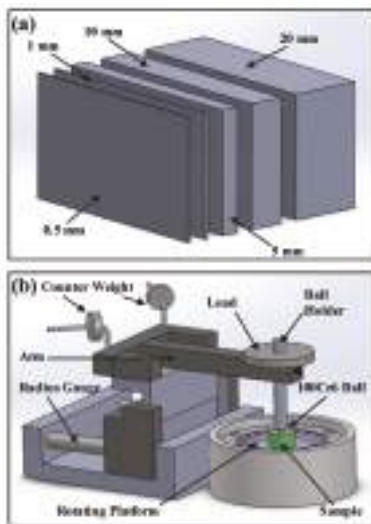


Figure 3. (a) Schematic of EBM-built Ti64 samples with thicknesses of 0.5, 1, 5, 10, and 20 mm; (b) Schematic configuration of the ball-on-disc micro-tribometer.

2.2. Powder Analysis

Morphological characteristics of the Ti64 powder were determined using a Malvern Morphologi G3 S (Malvern Instruments Ltd., Worcestershire, UK). Powder samples of 5 mm^3 in volume were dispersed on the glass plate. A $5\times$ objective was used for the measurement of this study. Four parameters of particle size viz. D_{10} , D_{50} , D_{90} , and D_{average} (size below which 10%, 50%, 90%, and average particle size are present, respectively) were calculated from the particle size distribution curve.

2.3. Surface Analysis

Surface roughness of as-built and as-polished Ti64 samples, and worn surfaces were examined using a surface profilometer (Talyscan 150) (Taylor Hobson Inc., Rolling Meadows, IL, USA) with a diamond stylus of $4\text{ }\mu\text{m}$ in diameter. Chemical compositions of as-built and as-polished surfaces were analyzed with the aid of X-ray photoelectron spectroscopy (XPS; Kratos AXIS Ultra, Kratos Analytical Ltd., Manchester, UK). Both the as-built and the as-polished samples were sliced from the other side of the squares and cut into pieces of $10\text{ mm} \times 10\text{ mm} \times 2\text{ mm}$. All of the Ti64 samples were ultrasonically cleaned in acetone and ethanol for 30 min respectively and stored in dry box overnight before analysis was carried out.

2.4. Microstructural Characterisation Techniques

Microstructure, wear morphology and wear debris were examined using a scanning electron microscope (SEM; JEOL-JSM-5600LV; 20 kV, JEOL Ltd., Akishima, Japan). Chemical composition of the wear debris was examined by energy-dispersive X-ray spectroscopy (EDX) (Oxford Instruments Plc., Abingdon, UK) equipped within the SEM. In addition, X-ray diffraction (XRD; PANalytical Empyrean; Cu K α ; 40 mA; 40 mV; step size of 0.01°) (PANalytical, Almelo, The Netherlands) was employed for phase identification.

2.5. Mechanical Properties Evaluation

Vickers microhardness tests were carried out on the slightly-etched samples using a Vickers micro-indentor (Future-tech FM-300e) (FUTURE-TECH Corp., Fujisaki, Japan) with an applied load

of 1 kg and a dwell time of 15 s. Sliding wear tests were carried out on polished surfaces, using a ball-on-disc micro-tribometer (CSM model, Anton Paar GmbH, Graz, Austria) as shown in Figure 3b at room temperature of 23 °C and in the ambient environment. A 100Cr6 steel ball of Ø6 mm was used as counter-face with an applied load of 1 N on the rotating Ti64 samples in a circular path of 3 mm in diameter at a linear sliding velocity of 2 cm/s for 50,000 laps. For all of the EBM-built samples, the X-Z plane was wear tested. Based on the measured wear width and wear depth, wear volume was calculated via a simple geometrical equation. Specific wear rates [22] were then evaluated by normalizing the wear volume with the load applied (N) and sliding distance (m).

3. Results and Discussion

3.1. Microstructure

Figure 4 shows the microstructure of the EBM-built and as-cast Ti64 samples. It can be clearly seen that both the 0.5 mm and 1 mm samples have similar alternate α/β microstructures mixed with acicular α' martensite, which is different from the rest of the EBM-built samples and the as-cast sample, which have α/β microstructures. Of particular difference is that coarse β was observed in the as-cast sample. Additionally, the results obtained from the XRD patterns shown in Figure 5 revealed peak shifting phenomenon in the EBM-built 1 mm sample as compared to the 20 mm and the as-cast Ti64 sample. This peak shifting phenomenon is in line with the studies by Zeng et al. [23] that suggest the presence of α' martensite. The appearance of α' phase in 0.5 mm and 1 mm was also confirmed by TEM observation [5,18]. In the case of the EBM-built samples two types of typical transformed α/β structure was observed, namely, the colony and the basket-weave (also known as Widmanstätten) morphologies. As a result of the difference in microstructure, they have different microhardness values which will be given in the following sections. From the results, it is known that the acicular α' phase causes a higher hardness value as compared to the α/β microstructure seen in the rest of the EBM-built samples. In addition, the microhardness of EBM-built Ti64 samples decreases with the increase in sample thickness. This is due to the fast cooling rate coupled with the EBM build temperature, favoring the formation of α' martensite in the thin samples [10,18]. The as-cast sample has the lowest hardness value due to its coarse α/β microstructure, which is largely caused by the moderate cooling rate during the casting process [14,24].

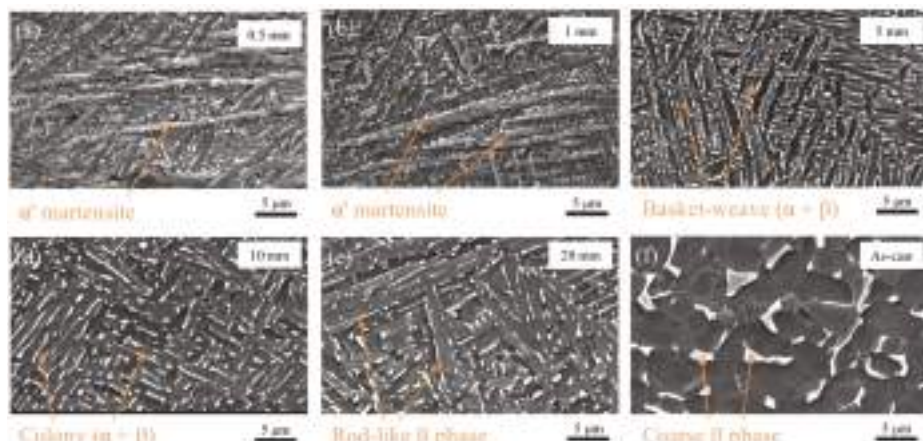


Figure 4. (a–f) SEM micrographs of EBM-built Ti64 samples with thicknesses of 0.5, 1, 5, 10, and 20 mm and the as-cast Ti64 samples, respectively. Microstructural features are indicated by arrows.

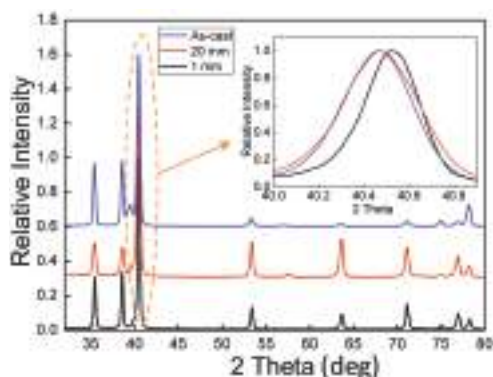


Figure 5. XRD patterns for 1 mm and 20 mm EBM-built and as-cast Ti64 samples.

3.2. Surface Conditions

Figure 6 shows 3D surface mappings of the EBM as-built 20 mm sample and the as-polished 20 mm sample for dry sliding wear tests. To our authors' best knowledge, the rough build surface of AM-fabricated parts may be the main obstacle to their direct practical applications. From Figure 6, it can be obtained that EBM as-built Ti64 samples have an average surface roughness of 34.4 μm . In order to avoid the influence of rough surfaces on wear properties, all of the samples were polished to a mirror-like finish with roughness of $\sim 0.3 \mu\text{m}$. XPS survey spectra for both the EBM-built 20 mm Ti64 sample and Ti64 powder used for EBM fabrication are shown in Figure 7. In both XPS spectra, it was dominated by strong signals of titanium (Ti), carbon (C), and oxygen (O). Of particular interest is that the signal for aluminum (Al) was detected on the Ti64 powder surface. But not on the sample surface. This may suggest that the surface oxide form on the EBM samples were predominately Ti and O. The presence of carbon on both instances were not unusual based on previous literatures [25] and the detection of carbon is mainly a result of adsorption of organic molecules from the environment. A detailed scan of the elements present on the surface of the Ti64 samples were carried out and illustrated in Figure 8a,b, where the Ti 2p and O 1s peak of the EBM-built 20 mm sample were revealed, respectively. The Ti 2p peak has symmetrical peak shapes, which is in line with the formation of titanium dioxide (TiO_2). Correspondingly, the asymmetrical shape of the O 1s peak put forward that oxide was formed with more than one metal element. Following the decomposition of the O 1s peak in Figure 8b revealed that both TiO_2 and Al_2O_3 were formed. However, since Al is not detectable via XPS on the EBM-built surface, it is strongly suggested that the surfaces of all the EBM-built samples are mainly comprised of TiO_2 . The instantaneous formation of a surficial TiO_2 layer is supposed to be the influential factor inducing poor wear resistance of Ti64.

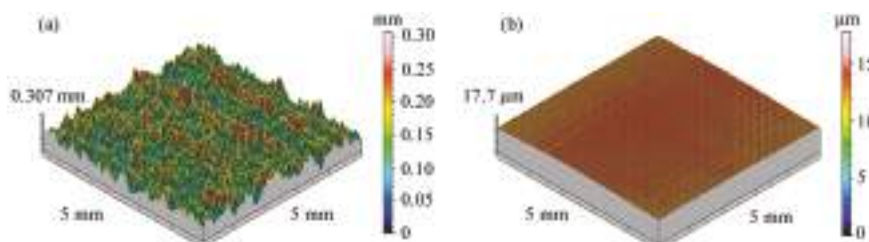


Figure 6. Representative surface profiles of the EBM Ti64 20 mm samples of (a) as-built and (b) as-polished.

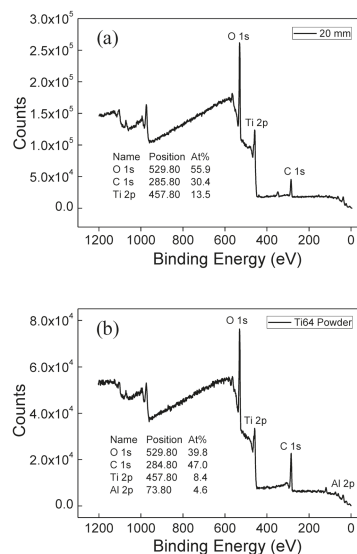


Figure 7. XPS survey spectra for (a) the 20 mm EBM-built Ti64 sample and (b) the Ti64 powder.

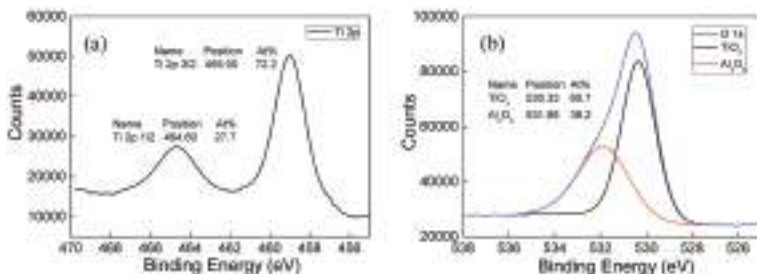


Figure 8. XPS spectra of the (a) Ti 2p peak and (b) O 1s peak on the surface of the 20 mm EBM-built Ti64 sample.

3.3. Dry Sliding Wear Behaviour

The representative coefficient of friction (COF) curves are displayed in Figure 9a. Similar wear characteristics were observed, regardless of the different microstructures existed inside the EBM-built and the as-cast samples. In the insert shown in Figure 9a, it is noted that the wear characteristics of the Ti64 sample can be classified into four major stages:

- I Wearing-in period, where the friction coefficient increases rapidly when the ball is in direct contact with the oxide layer of sample surface.
- II Cushioning of the oxide layer, which is characterized by a slight decrease in COF, probably due to surface oxide that prevents direct metal-metal contact between the ball and the Ti64 sample.
- III Breakage of the oxide layer into fragments, which was indicated by a significant increase in COF. In this stage, the oxide debris generated were fragmented as a result of repeated cycles of stress and load during sliding. This, coupled with the complete removal of the oxide layer, allows the direct metal-metal contact and, as such, causes the increase in COF.
- IV Stabilization of COF, which occurs after ~10,000 laps.

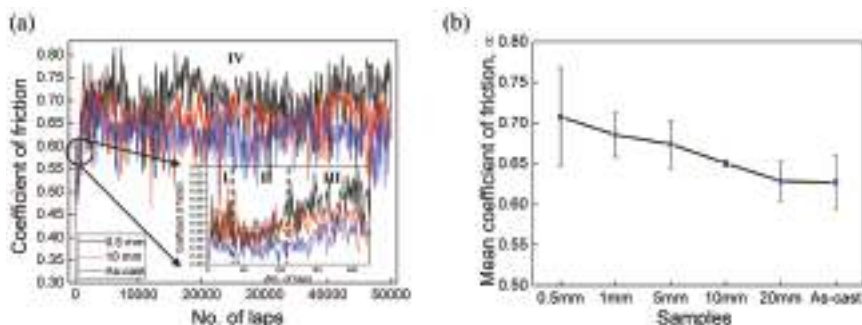


Figure 9. (a) COF curves of Ti64 samples as a function of number of sliding laps. (b) Mean COFs of EBM-built and as-cast Ti64 samples.

Figure 9b shows the mean COF values calculated from three groups of experimental data. It is revealed that the thin 1 mm sample has a higher COF than the 10 mm sample, and the lowest being the as-cast sample. The larger deviation of COF values in 0.5 mm sample is mainly attributed to the obvious martensite protrusions within its microstructure. Moreover, we observed that the mean COF of the 20 mm sample was nearly the same as the as-cast sample, while COFs of the rest of the EBM-built samples increased with the decrease in sample thickness. Interestingly, the thinnest EBM-built sample with the highest mean COF has the lowest specific wear rate (as seen in Figure 10a). Moreover, the specific wear rate increased with increase in sample thickness. Figure 10b reveals the 2-D depth profiles of the samples' wear tracks correspondingly. The decrease in specific wear rate with decrease in sample thickness is mainly due to the increased hardness as a result of the finer microstructure and the presence of α' in the thinner EBM-built samples. In general, an increase in hardness will correspondingly lead to an increase in shear strength of the material, and it possibly results in a higher friction coefficient [22]. A higher shear strength defines a higher ability to resist plastic shearing during sliding and as such a higher wear resistance [22]. Therefore, it may suggest that the thinner EBM-built sample, which has a higher hardness because of the fast cooling rate as compared to the as-cast sample, exhibits high wear resistance and, as such, reduces the roughening of the surface during rubbing and, thus, produces lesser wear debris. This, consequently, results in a lower specific wear rate but a high mean COF.

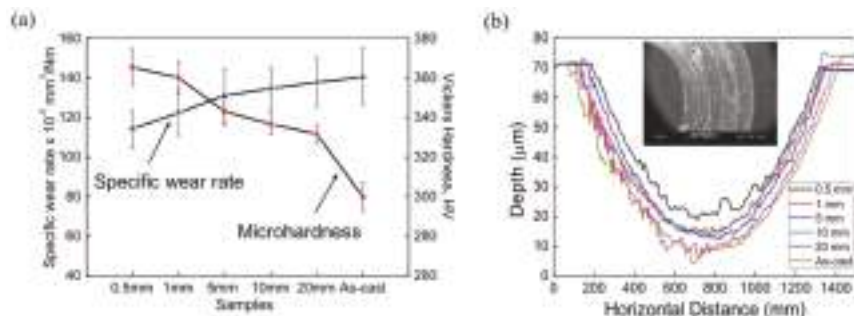


Figure 10. (a) Specific wear rates and microhardness values of EBM-built and as-cast Ti64 samples; (b) Surface profiles measured across the wear tracks of the worn Ti64 samples.

The global wear rate (W_{global}) of a Ti64 sample can be depicted by the combination of oxidative wear ($W_{\text{oxidative}}$) and delamination wear ($W_{\text{delamination}}$) and is given by [16,26,27]:

$$W_{\text{global}} = W_{\text{oxidative}} + W_{\text{delamination}} = \frac{A_r C^2 A}{v z_c \exp\left(-\frac{Q}{R T_f}\right)} + k \frac{F_N}{H} \quad (1)$$

where A_r is the real area of contact, C is the material constant, A is the Arrhenius constant for oxidation, v is the sliding speed, z_c is the critical thickness of oxide film, Q is the activation energy for oxidation, R is the molar gas constant, T_f is the flash temperature, k is the wear coefficient, F_N is the normal load, and H is the hardness. Figure 11a,b reveal the SEM images of the wear debris and the wear track of the 0.5 mm sample respectively. The indication of the transfer layers and oxide particles in Figure 11a and the surface cracks that are perpendicular to the sliding direction in Figure 11b give a valuable insight into the wear mechanism of Ti64, which is consistent with the global wear rate proposed by Al Molinari et al. [16]. Nevertheless, a simple calculation of the theoretical delamination wear rate using the sample's respective average hardness value obtained from the earlier Vickers hardness measurement as shown in Table 1, even without consideration of oxidative wear, revealed a higher wear rate as compared to the experimental obtained global wear rate value by two factors. This may be owing to the formation of a tribo-layer that avoids the direct metal-metal contact between the asperities of the steel ball and the asperities of the Ti64 sample, thereby preventing further wear through sliding.

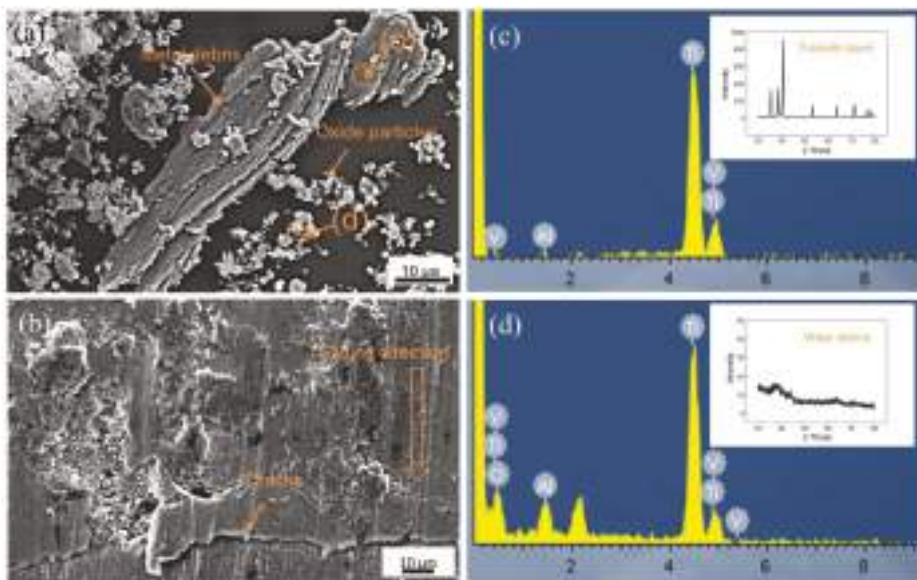


Figure 11. (a) SEM micrograph of the transfer layers generated by sliding on the 0.5 mm EBM-built sample; (b) SEM micrograph of the wear track on the 0.5 mm EBM-built sample after wear test; (c) EDX spectrum and inserted XRD patterns of the transfer layers and (d) EDX spectrum and inserted XRD patterns of the oxide particles that were generated during sliding on the 0.5 mm EBM-built sample. The detection locations of (c) and (d) were indicated in (a).

Table 1. Comparison between the calculated theoretical delamination wear rate (W_d) and the actual global wear rate ($W_{G(\text{exp})}$).

Samples	$W_d (\times 10^{-12} \text{ m}^3/\text{m})$	$W_{G(\text{exp})} (\times 10^{-12} \text{ m}^3/\text{m})$
0.5 mm	198.3	1.1
1 mm	195.6	1.2
5 mm	200.9	1.3
10 mm	195.3	1.3
20 mm	194.4	1.3
As-cast	208.7	1.4

The tribo-layer is commonly formed on a metal surface when rubbed by a counterface during a sliding wear test [28]. In order to further explore the wear characteristics and mechanisms of the EBM-built and as-cast Ti64, it is first necessary to delineate the terms of the non-oxide tribo-layer and tribo-oxide layer. In the case of non-oxide tribo-layer, it merely refers to the oxides that could not be identified by XRD and are not completely absent of an oxide on the Ti64 sample surface. On the other hand, the tribo-oxide layer refers to the formation of a strong and compact oxide layer during sliding process that serves as a protection to the worn surface [28–30]. Inherently, in an EBM process where the built condition is under high vacuum environment, the thickness of surface oxide layer only ranges from 5 to 7 nm [31]. Moreover, all the wear tests were conducted at room temperature. As a result, the formed oxide layer was weak and incompact, thus allowing the ease of delamination of the oxide layer. In our experiment, white fragmented particles were observed from both the SEM images of the 0.5 mm sample in Figure 11a, where the white particles indicate the breakdown of the oxide layer into oxide particles. This observation can be reinforced from the EDX spectra in Figure 11c,d. Moreover, due to the harsh nature during sliding, the wear debris formed was black and powdery in nature. Subsequent XRD analysis of the wear debris suggests that the oxide particles were mainly amorphous in nature. On the contrary, EDX was unable to detect the presence of oxygen on the transfer layer (see Figure 11c) that was removed from the bulk sample lying beneath the oxide surface.

Making reference to all the results obtained in the analysis, a wear mechanism was proposed and exemplified in Figure 12. Because of the reactive nature of titanium, TiO_2 was subsequently formed as an oxide layer on the sample surface, which has been proven by the XPS results in Figure 8. During dry sliding, the TiO_2 layer which serves as a protection layer of the substrate surface was first removed, thus generating flakes of oxide debris. Consequently, under loading and repeated rubbing, coupled with the brittle nature of the oxide debris, some of these debris were further broken up into fragmented oxide particles. Further sliding results in the compete removal of the oxide layer, thereby allowing the direct metal-metal contact between the asperities of the counter ball and the sample surface. Accordingly, bulk metal material was removed, which formed the metal debris. As the removal of the bulk metal from the substrate surface is continuous and instantaneous, oxide may not be able to form readily on the metal debris surface and as such allowing these metal debris layers to adhere (transfer layer) together. However, as the sliding process in the experiment was relatively slow to the ones reported in the literature, the centrifugal force induced during sliding was not able to remove the oxide debris, particles, and transfer layer from the sample surface. Therefore, these remaining materials allow for the formation of a compact tribo-layer that subsequently prevents further removal of the metal material from the substrate surface.

In our present experiment of low speed sliding (2 cm/s), the non-oxide tribo-layer was formed as a result of both oxide particles and metal debris. Additionally, our current experiment results also reveal that the global wear rate is two orders lower compared to that from the theoretical calculation. This could be owing to the fact that the theoretical equation may not take into account the actual physical condition during sliding. With reference to the proposed wear mechanism illustrated in Figure 12, at a very low speed of 2 cm/s, it was observed that the oxide particles and metal debris still remain on the wear track surface. Hence, this tribo-layer was not pushed away through centrifugation

movement during the sliding process and thus acted as a protection layer between the counter ball and Ti64 sample, thereby preventing direct metal-metal contact, leading to a lower wear rate.

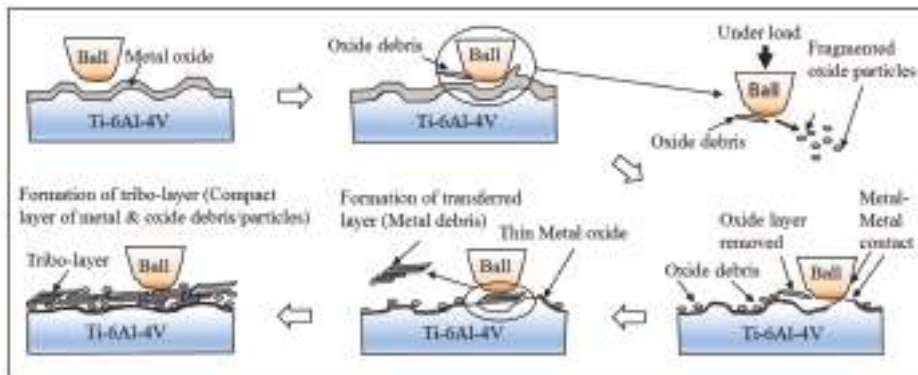


Figure 12. Schematic road-map on the formation of tribo-layer during sliding wear of Ti64 samples.

4. Summary

Due to the fast cooling rate that was inherently involved in a typical EBM process, it was observed that the thinner EBM-built Ti64 samples (0.5 mm and 1 mm thick) had much finer microstructure and higher microhardness as compared to the as-cast form. However, they showed similar wear characteristics, regardless of the different microstructures within the EBM-built and the as-cast samples. The higher hardness of the EBM-built samples resulted in their higher wear resistance and intrinsically lower wear rate. It is worth noting that all of the wear rates obtained in our experiment were lower as compared to the theoretical estimation. It could be due to the mild wear conditions (e.g., a very low sliding speed of 2 cm/s) and the formation of the tribo-layer that remained on the wear track, acting as a protection barrier between the counter ball and the Ti64 substrate. We can conclude that the EBM process is capable of manufacturing Ti64 parts with superior wear properties compared to the as-cast counterparts.

Acknowledgments: The authors are grateful for financial support provided by A*Star Industrial Additive Manufacturing Program: Work Package 3. We acknowledge the use of resources in Singapore Centre for 3D Printing (SC3DP) funded by the National Research Foundation (NRF), Singapore.

Author Contributions: W.Q.T. examined the specimens and wrote the main paper. X.T. designed the experiments and fabricated the Ti64 samples using EBM. W.Q.T., X.T., P.W. and M.L.S.N. performed specimen preparation and characterization. E.L. and S.B.T. supervised the project. All authors discussed the results and finalized the paper.

Conflicts of Interest: The authors declare no conflict of interest.

References

1. Frazier, W.E. Metal Additive Manufacturing: A Review. *J. Mater. Eng. Perform.* **2014**, *23*, 1917–1928. [CrossRef]
2. Gibson, I.; Rosen, D.W.; Stucker, B. *Additive Manufacturing Technologies*; Springer: Berlin, Germany, 2010.
3. Chua, C.K.; Leong, K.F. *3D Printing and Additive Manufacturing: Principles and Applications*; World Scientific: Singapore, 2015.
4. Boyer, R.; Welsch, G.; Collings, E.W. *Materials Properties Handbook: Titanium Alloys*; ASM International: Materials Park, OH, USA, 1994.
5. Tan, X.P.; Kok, Y.; Toh, W.Q.; Tan, Y.J.; Descoins, M.; Mangelinck, D.; Tor, S.B.; Leong, K.F.; Chua, C.K. Revealing martensitic transformation and α/β interface evolution in electron beam melting three-dimensional-printed Ti-6Al-4V. *Sci. Rep.* **2016**, *6*, 26039. [CrossRef] [PubMed]

6. Kok, Y.; Tan, X.P.; Tor, S.B.; Chua, C.K. Fabrication and microstructural characterisation of additive manufactured Ti-6Al-4V parts by electron beam melting. *Virtual Phys. Prototyp.* **2015**, *10*, 13–21. [CrossRef]
7. Yadroitsev, I.; Yadroitsava, I. Evaluation of residual stress in stainless steel 316L and Ti6Al4V samples produced by selective laser melting. *Virtual Phys. Prototyp.* **2015**, *10*, 67–76. [CrossRef]
8. Sun, Z.J.; Tan, X.P.; Tor, S.B.; Yeong, W.Y. Selective laser melting of stainless steel 316L with low porosity and high build rates. *Mater. Des.* **2016**, *104*, 197–204. [CrossRef]
9. Do, D.K.; Li, P. The effect of laser energy input on the microstructure, physical and mechanical properties of Ti-6Al-4V alloys by selective laser melting. *Virtual Phys. Prototyp.* **2016**, *11*, 41–47. [CrossRef]
10. Al-Bermani, S.S.; Blackmore, M.L.; Zhang, W.; Todd, I. The Origin of Microstructural Diversity, Texture, and Mechanical Properties in Electron Beam Melted Ti-6Al-4V. *Metall. Mater. Trans. A* **2010**, *41*, 3422–3434. [CrossRef]
11. Rafi, H.K.; Karthik, N.V.; Gong, H.; Starr, T.L.; Stucker, B.E. Microstructure and mechanical properties of Ti6Al4V parts fabricated by selective laser melting and electron beam melting. *J. Mater. Eng. Perform.* **2013**, *22*, 3872–3883. [CrossRef]
12. Lewandowski, J.; Seifi, M. Metal additive manufacturing: A review of mechanical properties. *Annu. Rev. Mater. Res.* **2016**, *46*, 151–186. [CrossRef]
13. Qian, M.; Xu, W.; Brandt, M.; Tang, H.P. Additive manufacturing and postprocessing of Ti-6Al-4V for superior mechanical properties. *MRS Bull.* **2016**, *41*, 775–783. [CrossRef]
14. Attar, H.; Prashanth, K.G.; Chaubey, A.K.; Calin, M.; Zhang, L.C.; Scudino, S.; Eckert, J. Comparison of wear properties of commercially pure titanium prepared by selective laser melting and casting processes. *Mater. Lett.* **2015**, *142*, 38–41. [CrossRef]
15. Budinski, K.G. Tribological properties of titanium alloys. *Wear* **1991**, *151*, 203–217. [CrossRef]
16. Molinari, A.; Straffolini, G.; Tesi, B.; Bacci, T. Dry sliding wear mechanisms of the Ti6Al4V alloy. *Wear* **1997**, *208*, 105–112. [CrossRef]
17. Wang, P.; Nai, M.L.S.; Sin, W.J.; Wei, J. Effect of Building Height on Microstructure and Mechanical Properties of Big-Sized Ti-6Al-4V Plate Fabricated by Electron Beam Melting. *MATEC Web Conf.* **2015**, *30*, 02001. [CrossRef]
18. Tan, X.P.; Kok, Y.; Tan, Y.J.; Vastola, G.; Pei, Q.X.; Zhang, G.; Zhang, Y.W.; Tor, S.B.; Leong, K.F.; Chua, C.K. An experimental and simulation study on build thickness dependent microstructure for electron beam melted Ti-6Al-4V. *J. Alloy. Compd.* **2015**, *646*, 303–309. [CrossRef]
19. Tan, X.P.; Kok, Y.; Tan, Y.J.; Descoins, M.; Mangelinck, D.; Tor, S.B.; Leong, K.F.; Chua, C.K. Graded microstructure and mechanical properties of additive manufactured Ti-6Al-4V via electron beam melting. *Acta Mater.* **2015**, *97*, 1–16. [CrossRef]
20. Wang, P.; Tan, X.P.; Nai, M.L.S.; Tor, S.B.; Wei, J. Spatial and geometrical-based characterization of microstructure and microhardness for an electron beam melted Ti-6Al-4V component. *Mater. Des.* **2016**, *95*, 287–295. [CrossRef]
21. Kok, Y.; Tan, X.P.; Loh, N.H.; Tor, S.B.; Chua, C.K. Geometry dependence of microstructure and microhardness for selective electron beam melted Ti-6Al-4V parts. *Virtual Phys. Prototyp.* **2016**, *11*, 183–191. [CrossRef]
22. Hutchings, I.M. *Tribology: Friction and Wear of Engineering Materials*; Edward Arnold: London, UK, 1992.
23. Zeng, L.; Bieler, T.R. Effects of working, heat treatment, and aging on microstructural evolution and crystallographic texture of α , α' , α'' and β phases in Ti-6Al-4V wire. *Mater. Sci. Eng. A* **2005**, *392*, 403–414. [CrossRef]
24. Jovanović, M.T.; Tadić, S.; Zec, S.; Mišković, Z.; Bobić, I. The effect of annealing temperatures and cooling rates on microstructure and mechanical properties of investment cast Ti-6Al-4V alloy. *Mater. Des.* **2006**, *27*, 192–199. [CrossRef]
25. Karlsson, J.; Snis, A.; Engqvist, H.; Lausmaa, J. Characterization and comparison of materials produced by electron beam melting of two different Ti-6Al-4V powder fractions. *J. Mater. Process. Technol.* **2013**, *213*, 2109–2118. [CrossRef]
26. Lim, S.; Ashby, M. Overview No. 55 wear-mechanism maps. *Acta Metall.* **1987**, *35*, 1–24. [CrossRef]
27. Ashby, M.; Lim, S. Wear-mechanism maps. *Scr. Metall. Mater.* **1990**, *24*, 805–810. [CrossRef]
28. Zhang, Q.Y.; Zhou, Y.; Wang, L.; Cui, X.H.; Wang, S.Q. Investigation on tribo-layers and their function of a titanium alloy during dry sliding. *Tribol. Int.* **2016**, *94*, 541–549. [CrossRef]

29. Alam, M.O.; Haseeb, A. Response of Ti-6Al-4V and Ti-24Al-11Nb alloys to dry sliding wear against hardened steel. *Tribol. Int.* **2002**, *35*, 357–362. [CrossRef]
30. Dong, H.; Bloyce, A.; Morton, P.; Bell, T. Surface engineering to improve tribological performance of Ti-6Al-4V. *Surf. Eng.* **1997**, *13*, 402–406. [CrossRef]
31. Karlsson, J.; Norell, M.; Ackelid, U.; Engqvist, H.; Lausmaa, J. Surface oxidation behavior of Ti-6Al-4V manufactured by Electron Beam Melting (EBM[®]). *J. Manuf. Process.* **2015**, *17*, 120–126. [CrossRef]



© 2016 by the authors. Licensee MDPI, Basel, Switzerland. This article is an open access article distributed under the terms and conditions of the Creative Commons Attribution (CC BY) license (<http://creativecommons.org/licenses/by/4.0/>).

Article

Comparison of Single Ti₆Al₄V Struts Made Using Selective Laser Melting and Electron Beam Melting Subject to Part Orientation

Volker Weißmann ^{1,2,*}, Philipp Drescher ³, Rainer Bader ², Hermann Seitz ³, Harald Hansmann ¹ and Nico Laufer ⁴

¹ Faculty of Engineering, University of Applied Science, Technology, Business and Design, Philipp-Müller-Str. 14, 23966 Wismar, Germany; h.hansmann@ipt-wismar.de

² Biomechanics and Implant Technology Research Laboratory, Department of Orthopedics, University Medicine Rostock, Doberaner Strasse 142, 18057 Rostock, Germany; rainer.bader@med.uni-rostock.de

³ Fluidic Technology and Microfluidics, Faculty of Mechanical Engineering and Marine Technology, University of Rostock, 18059 Rostock, Germany; philipp.drescher@uni-rostock.de (P.D.); hermann.seitz@uni-rostock.de (H.S.)

⁴ Institute for Polymer Technologies e.V., Alter Holzhafen 19, 23966 Wismar, Germany; laufer@ipt-wismar.de

* Correspondence: weissmann@ipt-wismar.de; Tel.: +49-03841-758-2388; Fax: +49-03841-758-2399

Academic Editor: Manoj Gupta

Received: 1 December 2016; Accepted: 9 March 2017; Published: 11 March 2017

Abstract: The use of additive manufacturing technologies to produce lightweight or functional structures is widespread. Especially Ti₆Al₄V plays an important role in this development field and parts are manufactured and analyzed with the aim to characterize the mechanical properties of open-porous structures and to generate scaffolds with properties specific to their intended application. An SLM and an EBM process were used respectively to fabricate the Ti₆Al₄V single struts. For mechanical characterization, uniaxial compression tests and hardness measurements were conducted. Furthermore, the struts were manufactured in different orientations for the determination of the mechanical properties. Roughness measurements and a microscopic characterization of the struts were also carried out. Some parts were characterized following heat treatment (hot isostatic pressing). A functional correlation was found between the compressive strength and the slenderness ratio (λ) as well as the equivalent diameter (d) and the height (L) of EBM and SLM parts. Hardness investigations revealed considerable differences related to the microstructure. An influence of heat treatment as well as of orientation could be determined. In this work, we demonstrate the influence of the fabrication quality of single struts, the roughness and the microstructure on mechanical properties as a function of orientation.

Keywords: Ti₆Al₄V; selective laser melting; electron beam melting; single strut; mechanical properties

1. Introduction

The development of structures using modern AM (additive manufacturing) technologies is a steadily growing research field in recent years. Here, complex and weight-saving structures arouse special interest. One important goal is frequently the targeted dimensioning of mechanical properties.

The progress in additive manufacturing technology makes this more tangible. An essential prerequisite is to develop a better understanding of the technological contexts of additive manufacturing technologies.

Of strong interest is the relationship between the materials used, the process parameters, especially in the application field of open-porous load-bearing lattice structures, and their effects

on mechanical properties. Other methods, in particular, electron beam melting (EBM), are widely used in addition to selective laser melting (SLM). Their suitability for the manufacture of components for applications with a bio-medical background has in many cases been confirmed [1–3].

Besides pure titanium and titanium alloys [4,5], pure tantalum [6,7] is also used as a material for the production of sufficiently resilient mechanical load-bearing elements.

Additive manufacturing and the three-dimensional design of components or structures using Ti₆Al₄V powder offer a wide range of unprecedented applications in medical technology thanks to their multifarious properties (biomedical compatibility, corrosion resistance, mechanical properties). The mechanical properties essentially define the suitability and successful application of mechanically optimized structures, such as bone substitutes, in biomedical fields [8–10].

The geometrical shape as well as the properties of the structures produced can be influenced directly through the manufacturing parameters [11–13] and through heat treatment [14,15].

In the development of open porous load-bearing structures, the orientation of the load-bearing rods and the load angle [16–19] as well as the relationship between elastic modulus and porosity play an important role [20,21].

Open porous load-bearing lattice structures consist of a regularly or irregularly composed form of geometrically describable individual elements. Here, simple lattice structures [22] play just as great a role as geometrically complicated forms (gyroid) [23]. Efforts to characterize the widespread lattice structures [24] range from studies of the mechanical properties to macroscopic and microscopic investigations.

The large number of research projects shows the high relevance of grid structures in engineering applications. The intention here is to create specific qualities by producing structures with a high degree of freedom, as for example in medical applications. The mechanical qualities again are the central consideration. The characterization of the relevant properties is carried out primarily on complete lattice structures [25], standard specimens [26,27] or on application models with a biomedical background [28–30].

The efforts of many research groups focus on the estimation of the mechanical properties using numeric methods. Labes et al. [31] developed a method for studying the structural response and failure process of open stainless steel 316 L lattice structures manufactured using SLM. They predicted the elastic modulus of several lattice structures with various strut ratios. To predict the quasi-static response and failure of different core lattice structures he used linear static and non-linear elasto-plastic analysis. Ahmadi et al. [32] present a new analytical solution and closed-form relationship for predicting mechanical properties, such as the elastic modulus and critical buckling load. To estimate the mechanical properties of the diamond lattice, they used an analytical solution based on the Euler–Bernoulli theory and an analytical solution based on the Timoshenko beam theory.

In addition to the estimation of the mechanical properties, work is focused on obtaining results and comparing them to predictions. Ushijima et al. [33] compared analytical and FE predictions of lattice structures with experimental results. To predict the initial stiffness and plastic collapse strength of lattice structures, he used beam elements as well as a BCC (body-centered cubic) unit cell topology. Suard et al. [34] presented a standardized method for predicting the mechanical response of lattice structures manufactured using EBM. Two equivalent diameters were defined to simulate the properties of the lattice structure while taking the manufacturing constraints into account. Deshpande et al. [35] discussed the mechanism of bending and stretching dominated architectures from cellular solids using experimental and theoretical techniques. Mazur et al. [36] theoretically predicted the deformation behavior of lattice structures in different cell topologies, cell sizes and cell numbers, and experimentally validated the results.

Lastly, the mechanical properties are experimentally determined, evaluated and compared between the test partners and relationships. McKown et al. [37] tested a range of metallic lattice structures to investigate their collapse behavior, failure mechanisms and strain-rate sensitivity.

In the present work are described the properties of the individual elements used for the formation of the lattice structures. The identification of properties was therefore carried out on elements that correspond to real geometric conditions as for the lattice structures. It is of major interest to determine the properties of individual bars integrated into specialized applications. This is particularly interesting for applications where the rods within a component show different orientations to the load (see Figure 1) and the structural parameters cannot be compared with typical scaffolds (as shown in the literature). Therefore, the strut elements are considered in this work. The strut elements form the basis for load-bearing porous structures. Variations in the geometry of the test specimen as well as in the manufacturing process can be excluded here. In addition to characterizing production quality and surface quality of the individual struts, selected mechanical properties were determined. The samples were manufactured using additive technologies with variations in dimension (variations in the height/diameter ratio) and also installation space orientation. Selective laser melting and electron beam melting were the two manufacturing processes used to provide the possibility to compare both methods. Furthermore, the directional dependencies can be represented with reference to the properties.

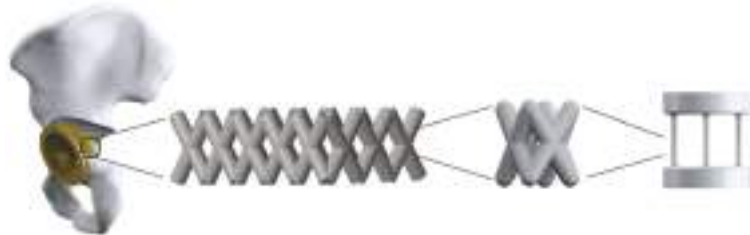


Figure 1. Exemplary representation of part of a pelvis with an acetabular cup. The surface is provided with a load bearing porous structure. The load bearing structure consists of a layer of repeating structural elements. The smallest element in any case is the rod.

Previous works comparing the two manufacturing methods mentioned above refer to test specimens with geometric dimensions that greatly differ from those of the individual elements of the grid structures [38]. In addition, the focus is always placed on determining such properties that would presuppose tensile loading. Simonelli et al. [39] studied the tensile properties of SLM Ti₆Al₄V specimens in three directions consisting of 2000, 200 and 60 layers. Qiu et al. [40] examined the tensile properties of Ti₆Al₄V specimens in dimensions that are not relevant in small lattice structures. A load situation that often is of interest in biomedical applications is the pressure load (for example, in orthopedic cases). The present work therefore studies the mechanical properties of the manufactured test specimens under an applied pressure load.

The aim was to characterize the individual struts macroscopically, microscopically and mechanically. The results obtained shall be used to gain a better understanding of the behavior of the individual elements. The results can be transferred into medical applications. These primarily include the structural areas for implants constructed from grid elements.

2. Materials and Methods

2.1. Parts Design and Configuration

The specimens for mechanical testing within this study were designed using CAD software (PTC Creo, Version 2.0, Parametric Technology Corporation, Needham, MA, USA). The samples are shown in Figure 2. The single strut specimen consists of a base area and a top area. These areas are important as supports during part manufacturing and for reworking (face cutting to obtain two parallel surfaces) after additive manufacturing. In both areas, there are punched-out clearances to reduce

the material fraction and the energy applied during manufacturing. The single struts are positioned between these two areas. All parts are designed with four symmetrically arranged single struts. For the determination of the mechanical characteristics in the compression test, the dimensions of the strut specimen were modified in two ways. The geometric parameters for the investigated strut specimen are listed in Table 1.



Figure 2. Structural design of the single strut specimen. The test specimen consists of two parallel areas (base and top) and four single struts. The single struts are arranged at an angle of 90 degrees to the base and top area. The crossovers between the base and top area to the single strut are produced with a radius of 1 mm.

Table 1. Overview of the geometric parameters for the strut specimen. A first variation with constant diameter (d) and variable height and a second variation with constant height (L) and variable diameter were designed. All other parameters in both series were constant. All values were derived from CAD data and are given in mm.

Variation 1				Variation 2			
Height L (mm)				Height L (mm)			
12 10 8 6				12			
Diameter d (mm)				Diameter d (mm)			
1.1				1.1 1.3 1.5 1.7			

2.2. Fabrication of the Scaffolds via the SLM Process and the EBM Process

In this work, all parts were built via the SLM process and the EBM process. Figure 3 shows the experimental design. The aim of the experimental plan was to obtain the greatest possible information from the smallest possible number of tests. Figure 4 shows representative parts of the two manufacturing processes in association with building orientation.

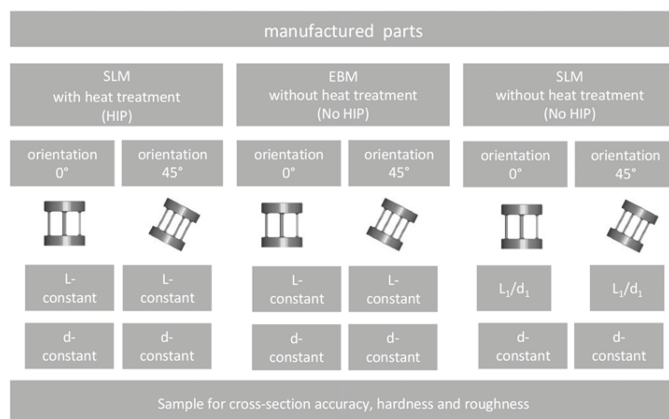


Figure 3. Overview of all manufactured parts as well as heat treatment conditions and orientation. Parts were built for compression testing (SLM (HIP) and EBM (No HIP) d - and L -constant; SLM (No HIP) d -constant and L_1/d_1), fabrication accuracy, determining cross section areas, hardness and roughness.

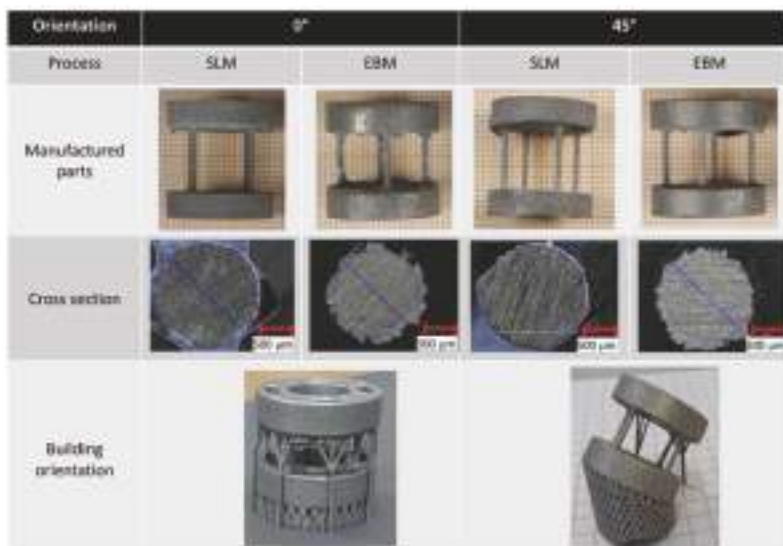


Figure 4. Samples respectively of the parts manufactured in the EBM and SLM process in both orientations—0° and 45°—after removal from the substrate plate and face cutting the top and base area of the test specimen as well as of characteristic cross-sectional areas.

Based on the datasets of the CAD samples, all scaffolds were fabricated via selective laser melting using titanium powder (Ti_6Al_4V) under an ultra-pure argon atmosphere. The powder complies with the requirements of ASTM F 67 and has a determined mean particle size of 43.5 μm . The parts were fabricated with the SLM 280 by SLM solutions GmbH, Lübeck, Germany, using a continuous-wave Ytterbium fiber laser. All parts were built using an identical energy density (J/mm^3). The energy density E is defined by the following equation [41]:

$$E = \frac{P}{v \times d \times t} \quad (1)$$

where P is laser power, v is scan speed, d is hatch spacing and t is layer thickness.

All parts were built on a substrate plate with a support structure and in the same orientation. The samples were heat-treated under hot isostatic pressing conditions after fabrication and were subsequently removed from the substrate plate. The heat treatment was performed at 920 °C under a pressure of 1000 bar for a duration of 120 min under an argon atmosphere by Bodycote Hot Isostating Pressing, Bruxelles, Belgium. The support structures were removed mechanically by hand. One manufacturing series without heat treatment was removed from the substrate plate for a comparison with the EBM-manufactured parts.

The electron beam melting system A1 by Arcam AB, Mölndal, Sweden, was used to build the parts for compression testing and for comparing the values with the parts made by SLM. The process was carried out using Ti_6Al_4V powder from Arcam AB with a mean particle size of 70 μm . The chamber, where the powder is applied and melted, was evacuated until a pressure of 5×10^{-4} mbar was reached and a layer thickness of 50 μm was chosen. The process consisted of a preheat theme and a melt theme. The preheat theme sinters the powder prior to melting it for stability reasons [42]. A comparison with SLM of the process parameters (Tables 2 and 3) is not easy since scan speed and beam current (i.e., beam power) change during the process due to various algorithms such as the thickness equation, turning point or speed function. However, an average energy density can be calculated for comparative reasons.

Table 2. Overview of energy-relevant process parameters used to build all samples, SLM process.

Parameter	Description	Unit	Process Parameter
P	Laser Power	W	275
v	Scan speed	mm/s	805
d	Hatch spacing	μm	120
t	Layer thickness	μm	50

Table 3. Overview of the energy-relevant process parameters used to build all samples; EBM process.

Parameter	Description	Unit	Process Parameter
P	Beam current	mA	~21
	Acceleration voltage	kV	60
v	Scan speed	mm/s	~4530
d	Hatch spacing	μm	100
t	Layer thickness	μm	50

2.3. Measurements

A digital microscope—Keyence VHX 2000 (KEYENCE Deutschland GmbH; Neu-Isenburg, Germany)—was used for the determination of the manufacturing quality, in particular, of the real cross section of the parts and of part dimension. For each orientation and diameter variation, the cross sections were measured. For this measurement, the struts from one part were removed and imbedded in resin. The surfaces were polished, and after a measurement, some μm from the sample were removed for a new measurement. This part was produced together with the parts intended for the pressure test. Every result for the cross sections consisted of 10 measurements. For a qualitative judgment, the external diameters as well as the inner diameter of a circle were determined in the cross section (Figure 5).

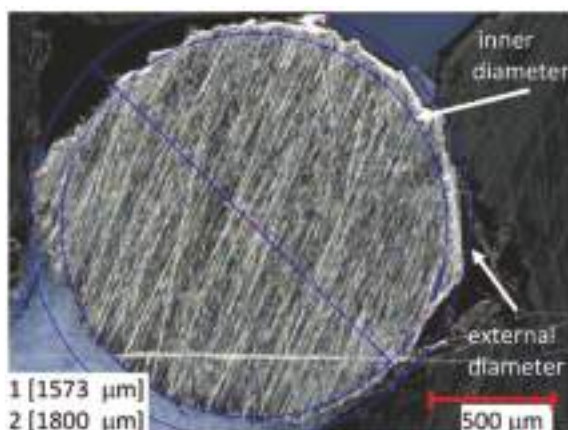


Figure 5. Sample of cross section area and the measured diameter inside the cross section area as inner diameter as well as the external diameter. In this picture is seen a 45° oriented SLM part.

Surface quality measurements (Figure 6) were performed with a 3D digital laser-scanning microscope VK-X260 (KEYENCE Deutschland GmbH; Neu-Isenburg, Germany) according to ISO 25178. R_a , as the arithmetic average of the absolute values, and R_Z , as the maximum height were determined, respectively, for the SLM and EBM parts in both orientations (0 and 45°). Measurements were carried out on all four struts of a part after manufacturing before the mechanical testing on the outside of the

struts. At a measurement length of 4 mm, the λ_C used was 0.25 and the number of measurement lines was 9. The distance between the lines was 40 μm .

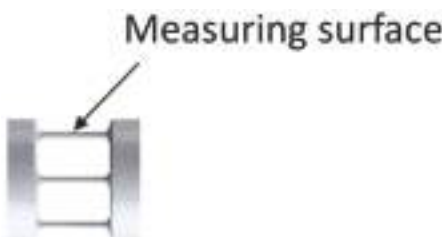


Figure 6. Position for surface roughness measurements on all four struts.

Representative samples were prepared to obtain information on the microstructure. Polished samples were etched by immersion in a mixture of 100 mL H_2O , 3 mL HNO_3 and 3 mL HF. The microstructures were examined under the digital microscope—Keyence VHX 2000.

In order to study the mechanical properties of the produced samples, two mechanical tests were performed:

(1) All scaffolds were mechanically tested via uniaxial compression according to DIN standard (DIN EN 50106). A universal testing machine (INSTRON E 10,000; Instron GmbH, Darmstadt, Germany) was used to conduct the mechanical testing. Compression testing of the samples was performed with a constant traverse velocity of 2 mm/min. The strain rate for the present results is approximately $1.6 \times 10^{-2} \text{ s}^{-1}$. All tests were performed under standard atmospheric conditions (24°C , 50% rel. humidity). The parts were tested with the rods oriented perpendicular to the load direction. The top and bottom areas of the specimen were aligned parallel to the load bearing capacity. Values for load and displacement were continuously recorded during testing. All fabricated scaffolds were tested with five specimens until mechanical failure occurred.

Evaluation was always based on the cross section area A determined with the digital microscope and the maximum load F before the first fracture or decrease in load occurred.

Based on these data, the compression strength was determined as

$$\sigma = \frac{F}{A} \quad (2)$$

All determined strengths were considered with respect to the slenderness ratio λ . The slenderness ratio λ was determined as the quotient of the product of column effective length factor β times Length of the strut L and gyration radius i . The column effective length factor for all calculations was 0.5, equivalent to the Euler loading case 4.

$$\lambda = \frac{\beta \times L}{i} \quad (3)$$

The gyration radius i was calculated as root of the quotient of the geometrical moment of inertia I and the cross section area A .

$$i = \sqrt{\frac{I}{A}} \quad (4)$$

Based on the strut cross section areas determined, the equivalent diameter (Figure 7) was used to calculate the gyration radius. The equivalent diameter matched the diameter of a comparable circular strut and was calculated from the results for the cross section areas determined with the digital microscope—Keyence VHX 2000.

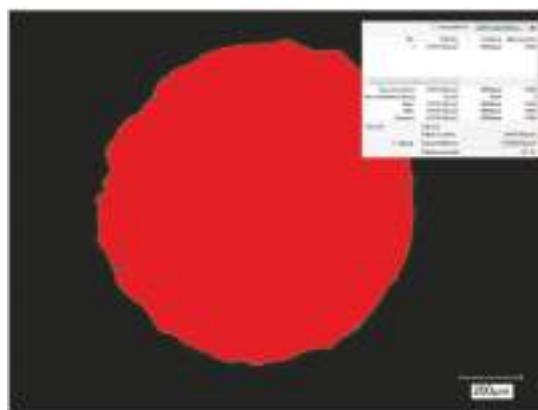


Figure 7. Sample of cross section area and the measured area for the determination of the equivalent diameter. In this picture, a 0° oriented SLM part is seen.

(2) Vickers hardness HV 10 (according to DIN standard—DIN EN ISO 6507-1) was measured on both sites of the back and top areas of the specimen (Figure 8) using the hardness tester, Zwick 3212.002 (Zwick GmbH Co KG, Ulm, Germany). The parts were tested with a test load of 98.07 N within a test time of about 10 seconds. On average, 10 indents per surface were taken for each condition. Prior to the measurement of the back and top areas, the part was face cut (between 10 and 50 μm) to achieve a practical reference surface.



Figure 8. Test specimen for hardness determination. Hardness was measured on both sides ($n = 10$ for each case and side).

2.4. Statistical Analysis

All data are expressed as means \pm standard deviation (SD). The association between the geometrical influences (length and diameter of the strut as well as the slenderness ratio λ) and the compression strength was assessed by linear regression. All statistical analyses were performed using SPSS, software version 22 for Windows (SPSS® Inc. Chicago, IL, USA). A two-sample t -test was performed to statistically examine significant differences between the means. This test was used for measuring the hardness of manufactured parts dependent on manufacturing type and heat-treatment variation. Moreover, the test was performed for determining the surface quality of SLM and EBM parts. Differences of $p < 0.05$ were considered as statistically significant.

3. Results and Discussion

In this study, parts were built using two additive manufacturing processes. To characterize the influence of the processes, of the orientation and of a heat treatment of the part on mechanical properties, the geometrical dimensions as well as the orientation in the building process was varied. The obtained results are presented and discussed in the following chapter.

3.1. Cross-Section Accuracy of Fabricated Struts

Table 4 lists the results of the manufactured and measured SLM- and EBM-processed parts. Figure 9 shows the estimated equivalent diameters and Figure 10 shows the inner and external diameters of the SLM and EBM parts in dependence on diameter and orientation.

Table 4. Results from determinations of the equivalent diameter ($n = 10$ for each part).

$d_{\text{CAD}}\text{-Orientation}$	EBM (μm)	SLM (μm)
1.1 mm 0°	995 ± 7	1057 ± 7
1.1 mm 45°	949 ± 14	1063 ± 14
1.3 mm 0°	1148 ± 48	1235 ± 17
1.3 mm 45°	1155 ± 30	1299 ± 16
1.5 mm 0°	1314 ± 32	1436 ± 22
1.5 mm 45°	1358 ± 47	1486 ± 8
1.7 mm 0°	1505 ± 21	1640 ± 9
1.7 mm 45°	1538 ± 38	1646 ± 10

All SLM parts have smaller equivalent diameters than the CAD target specifications. In all variants, the components from the SLM process are closer to the target specification than the EBM-manufactured parts. Although using a scaling factor to obtain the proper geometries in accordance to the CAD specifications, the EBM parts differ between 10% and 12% from the CAD data specifications in the zero degree orientation. In the 45-degree orientation, the deviation is 9% to 14%. SLM component deviations in the zero-degree orientation are between 4% and 5% while the deviations in the 45-degree orientation are between 0% and 3%. SLM components show minor deviations.

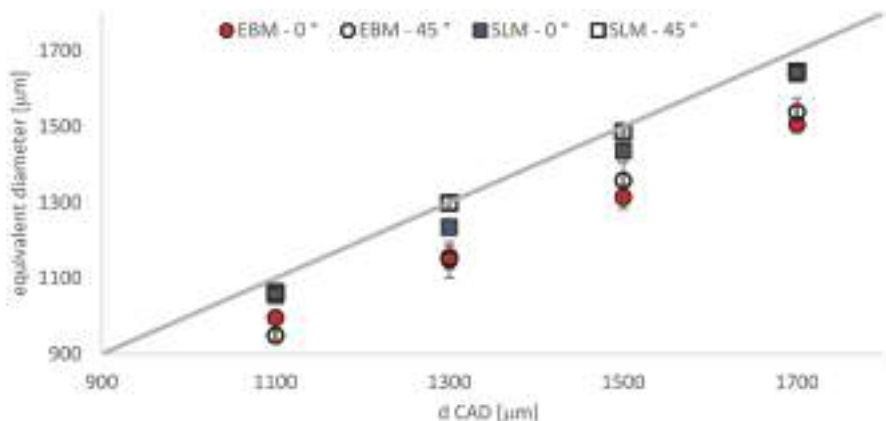


Figure 9. Estimated equivalent diameters of SLM and EBM parts in dependence on diameter and orientation. Results are shown as mean values with the corresponding standard deviations ($n = 10$ for each design).

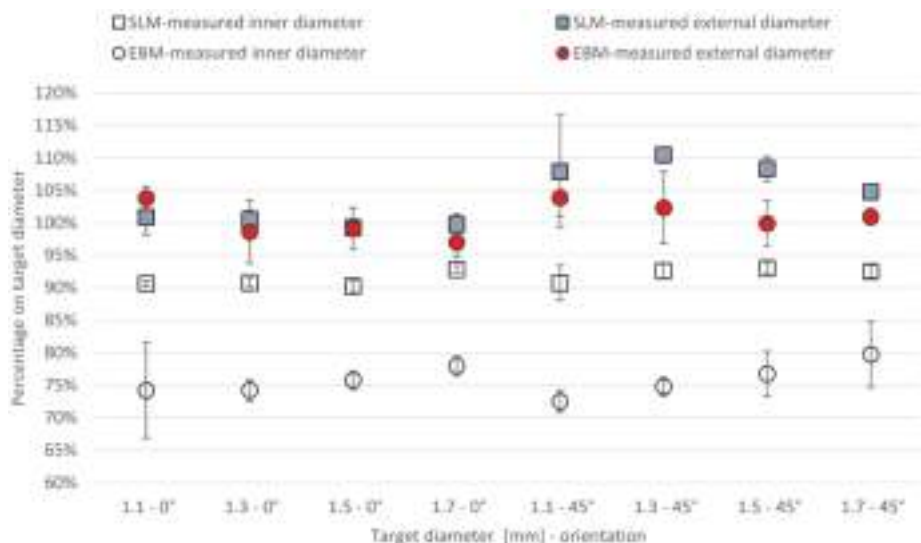


Figure 10. Measured external diameters and measured inner diameters for single struts. Results are shown as mean values with the corresponding standard deviations ($n = 10$ for each design).

As shown in Figure 4, the additively manufactured struts deviate from the ideal circular shape. The measurements of the inner circle in the maximum permissible orientation as well as of the possible external circle diameter offer an interesting insight on manufacturing quality. The struts produced using SLM show smaller deviations than the EBM-manufactured struts. The 45-degree oriented samples are always larger than the 0-degree oriented samples. While the large outer cross-sections of the 0-degree oriented samples very slightly differ from the CAD data specifications, the differences from the desired values shown for the 45-degree oriented samples are significantly larger. The deviations of the outer diameters tend to be smaller with increasing nominal values. The supporting cross-sections also increasingly approach desired specification values with larger diameters. Large measurable diameters increasingly tend towards zero deviation. The deviations are process dependent and lead, in particular at 45 degrees, to an enhancement of the effect.

The deviation of the 45-degree oriented specimens from a circular shape as seen in Figure 4 leads to an increase in the outer diameter. The more pronounced splitting of the surface in the EBM process clearly reduces the coherently formed material area in the interior of the strut. Thus, while the values measured outside are closer to CAD data specifications than in the case of the SLM samples, the internal structures nevertheless deviate more measurably from the desired dimension.

Comparison of SLM Manufactured Parts with and without Heat Treatment

The fabrication accuracies determined in Section 3.1 were identified for the samples originating from the series named in Section 2.1. These were the heat-treated SLM samples and the EBM samples without heat treatment. The influence of heat treatment in combination with an effective pressure (HIP) on component accuracy was then determined (Figure 11). Compared were SLM specimens with diameters according to the design specification of 1.1 mm in the orientations 0° and 45°. Special emphasis was again placed on comparing post-treatments using heat and pressure (difference between HIP and No HIP).

A two-sample t -test was performed to statistically examine significant differences between the means. No statistically significant difference was determined when the results were compared. It can be concluded that the treatment of the SLM-produced samples with HIP treatment has no effect on

the manufacturing precision of the manufactured items. The results listed in Section 3.1 (SLM with HIP) are transferable to the SLM-manufactured samples without HIP treatment. It also allows the conclusion that a HIP process has no influence on the stability of the diameter of the EBM samples.

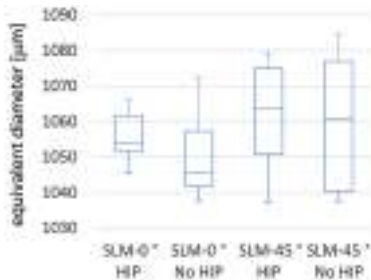


Figure 11. Box plots of the measured equivalent diameters of SLM and EBM manufactured parts. Box plots give the median value, the interquartile range (IQR: interval between the 25th and 75th percentile, blue rectangle) and the extremum values ($n = 10$ measurements).

3.2. Surface Quality

For the qualification of the outer as-built surface quality of the struts, a roughness measurement was carried out. The roughness values R_a and R_z were obtained, as shown in Figure 12.

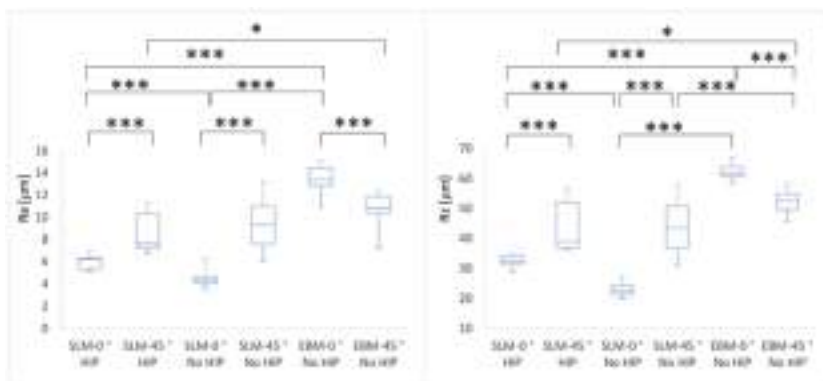


Figure 12. Box plots of the measured R_a and R_z values for the SLM- and EBM-manufactured parts. Box plots give the median value, the interquartile range (IQR: interval between the 25th and 75th percentile, blue rectangle) and the extremum values ($n = 4$ struts); statistical significance levels (* $p < 0.05$; *** $p < 0.001$).

The roughness R_a of SLM-manufactured (HIP and No HIP) parts was significantly ($p < 0.001$) lower in the 0° orientation than in the 45° orientation. The EBM parts showed the opposite behavior. Here, the R_a values in the 45° orientation are lower than in 0° orientation. As Suard et al. [34] have described, surface roughness and the resulting strut shape depend on the orientation during the building process. Whereas vertically oriented struts display uniform roughness values, a horizontal or oblique orientation leads to increased roughness. The reason is the energy flow into the powder bed. Due to this energy flow, powder particles repeatedly tend to adhere to the struts on the underside. This phenomenon causes deviations from the present geometry as well as porosity deviations. The effect of powder adhesion is also described in [43]. This phenomenon causes differences in the roughness as a function of the orientation. The SLM parts have a higher roughness R_a of the

45° oriented parts because particles adhere on the strut side facing the powder bed. On EBM parts, the same phenomenon leads to a lower roughness of the 45° oriented parts. The particles that adhere on the surface decrease the roughness because some unevenness gets filled.

Fox et al. [44] found in their work a shift between surfaces dominated by partially melted powder particles and surfaces dominated by material from the re-solidified melt track. With a decrease of the surface angle, the R_a value increased. A decreased surface angle is equivalent to the 45° in this work. The 0° orientation in this work means a higher surface angle. These results are consistent with the previous results of Triantaphyllou et al. [45] who found differences between upskin and downskin surfaces as well as the orientation angles. The differences in average roughness R_a found between the EBM and the SLM method are also confirmed here.

There is a significant difference between the SLM parts (HIP and No HIP) in the 0° orientation ($p < 0.001$). In production this difference, however, is likely to be within the accuracy fluctuations range. The roughness R_a of SLM-manufactured (HIP and No HIP) parts were significantly ($p < 0.001$) lower for the 0° orientation than for the EBM parts. In the 45° orientation, the roughness was only different between SLM HIP and EBM (SLM HIP < EBM; $p < 0.05$). These relationships are also seen for the roughness R_z .

The values obtained for SLM- and EBM-manufactured Ti_6Al_4V parts correspond to those from the literature. Accordingly, the SLM-parts show a far lower deviation from a theoretical smooth surface that can be considered an indicator for a stable and accurate manufacturing process. Besides powder size distribution, the layer thickness in the powder feed and the powder bed system, the laser beam diameter itself has an influence on surface roughness [13]. Higher roughness values of EBM parts are typically due to the process parameters. A smoother surface and therefore lower roughness is therefore possible through the optimization of process parameters.

3.3. Vickers Hardness

The hardness of parts manufactured in the 45° orientation were significantly (SLM-No HIP $p < 0.05$; EBM-No HIP $p < 0.001$) lower than in those manufactured in the 0° orientation. This correlation is not seen in the heat-treated SLM-manufactured parts. Heat treatment of the SLM-manufactured parts led to a significantly lower hardness (in both orientations $p < 0.001$). When SLM- and EBM-manufactured parts with no heat treatment were compared, the SLM parts had in both orientations a significantly ($p < 0.001$) lower hardness than the EBM parts. The results for hardness are shown in Figure 13.

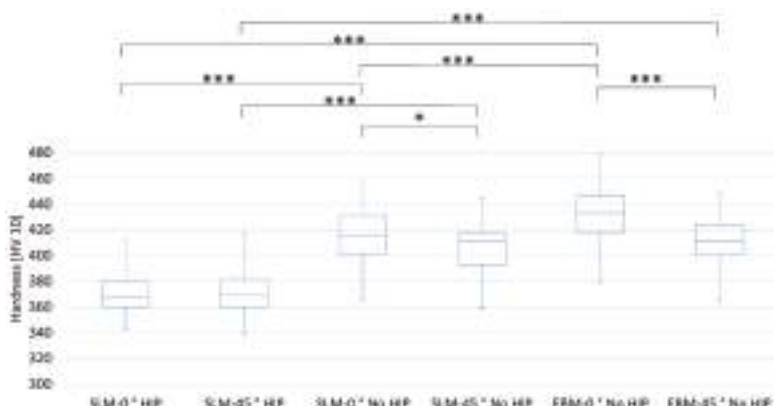


Figure 13. Box plots of the measured hardness HV 10. Box plots give the median value, the interquartile range (IQR: interval between the 25th and 75th percentile, blue rectangle) and the extremum values ($n = 40$); statistical significance levels (* $p < 0.05$; *** $p < 0.001$). No significant differences from similar other possible manufacturing systems were revealed.

The values determined for hardness correlate to values found in the literature [38,46,47]. By Song et al. [13] was shown that mechanical properties depend on the processing parameters. The determined value for hardness for a perfect SLM-manufactured part without heat treatment was 450 HV. Murr et al. [48] have shown the differences between the selective laser melting and the electron beam melting process and the influence on the mechanical properties, especially hardness. Hardness values for EBM-manufactured parts were found in the range of 410 to 427 HV. Wu et al. [49] investigated the positive effect of hot isostatic pressing on the improvement of the anisotropies of bending and impact properties. They found that hot isostatic pressing and building direction affect mechanical properties. While the as-built parts have a hardness of 41 and 42 HRC, the HIPed parts have a hardness of 34 HRC. In the work of Wu et al. the influence of the HIP process is greater than the orientation in the building process. The phase transformation of the α' -martensite to $\alpha + \beta$ structures is an essential reason for the differences in mechanical properties.

These results, show in comparison with each other, that a hardness typical for Ti₆Al₄V material and additively manufactured parts was achieved. In addition, this elucidates that, as a complementary measure, hardness measurement is excellently suited as a qualitative manufacturing control. Significant differences are caused mainly by the differences in the structure. The heat-treated parts consist predominantly of a microstructure with an α phase and a lamellar β phase (brighter than the α phase). The primary α phase was distributed along the prior β grain boundary. The structure is uniformly built and aligned parallel to the building direction (Figure 14) in the 0° orientation.

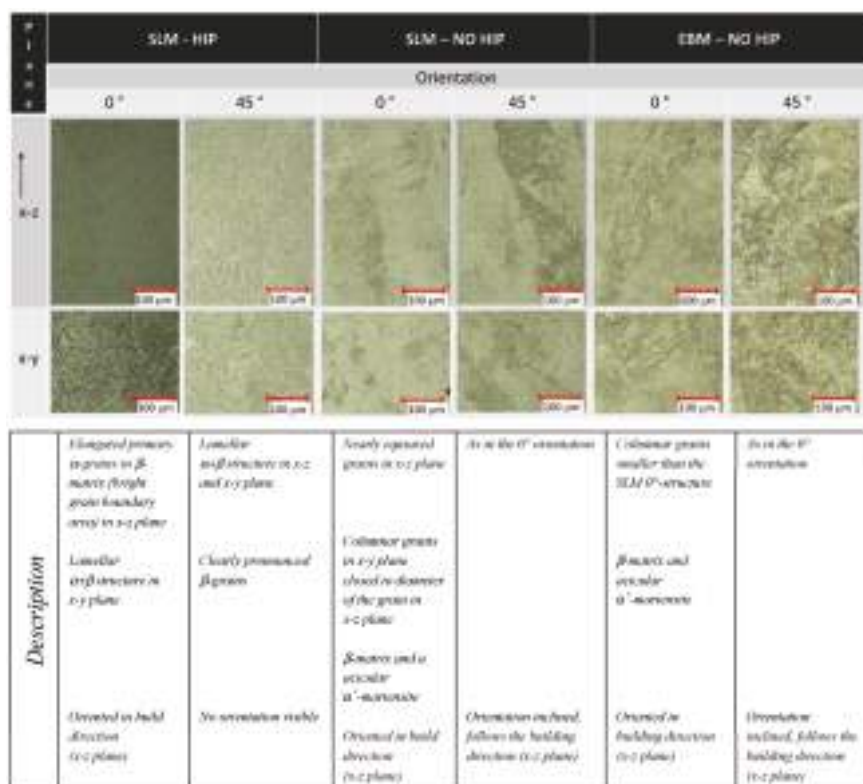


Figure 14. Overview about the microstructure of all manufactured parts in relation to the building orientation (0° and 45°) as well as to post-treatment conditions (heat treatment—HIP—hot isostatic pressing or No HIP). The arrow shows the building direction.

In the 45° orientation ($x-z$ plane) as well in the 0° and 45° orientation ($x-y$ plane), this alignment is not seen. It seems that all microstructural anisotropy was eliminated. The parts that did not receive any heat treatment after manufacture, showed a primarily acicular martensitic alpha (α') and fine lamellar beta (β) microstructure. The β grains appear to be brighter and the α' grains darker. This microstructure and its inhomogeneity was the result of fast heating and cooling during the process. The prevailing α' grains grew almost parallel to the building direction. This is visible in both the 0° and 45° building directions. Parts with α' grains in comparison to parts without α' grains have a higher hardness. The higher hardness of the α' phase as against the $\alpha + \beta$ structures is typical for this structure. The representative cross-section microstructures in Figure 14 confirm these relationships. The HIPed SLM parts show a uniform $\alpha + \beta$ structure with a clearly visible building orientation only in 0° orientation. The as-built parts, however, show a clearly oriented structure (in $x-z$ plane and in $x-y$ plane) with acicular martensite. The higher hardness of the 0° oriented parts is the result of the better and uniform orientation of the α' grains (martensite). In the 45° oriented parts, the structure is more irregular. This leads to a smaller resistance to an applied compressive force, because the 0° oriented struts are vertical to the acting force. The force required to overcome the resistance is then greater.

3.4. Compressive Strength as a Function of Geometrical Parameter

All fabricated parts were tested until the maximum possible load was exceeded. The samples showed two types of failure behavior independent from the output quantity.

Figure 15 shows representative examples for failure behavior. In Table 5 are listed all tested samples that were considered for the evaluation of results.

The compression tests performed in this work on these specimens lead to the deformations as shown in Figure 15. As specified by the Maxwell criterion ($M < 0$), the occurring deformations are typical for flexure-dominated structures [36]. According to the literature, the stability failure of the rod-like elements that are present in the specimens under investigation can be explained by differing buckling behaviors (load cases). Load cases showing this are known. The deformations that have occurred here are clearly assignable to such known load cases. While Case 1 showing the typical deformation for symmetrical buckling, Case 2 is an example for antimetrical buckling. As described by Sattler [50], the path of the deformation is the curve of a parabola. The same buckling length coefficient that is of interest for determining the slenderness ratio applies in both cases. For the deformation pattern, similar results were found by Ushijima et al. [33] in their theoretical considerations of compressive properties. The stability failure in both the natural modes shown is characterized by an abrupt event.

Case 1: (long curve)

Here, the strain gradually and steadily increases, reaches a short plateau until it abruptly decreases. This can be caused by imperfections (due to quality deficiencies during manufacturing) that lead to a reduction in the stiffness.

Case 2: (steep abrupt decrease)

The strain increases and, after exceeding the stability limit, abruptly drops.

In Case 2 stability failure occurs at a higher stiffness level than in Case 1 (strain increase is steeper than in Case 1). The imperfections in Case 2 have a lower influence on stiffness (i.e., the stiffness based on the material-dependent elastic modulus and the manufacturing dependent property) until the stability limit is abruptly exceeded.

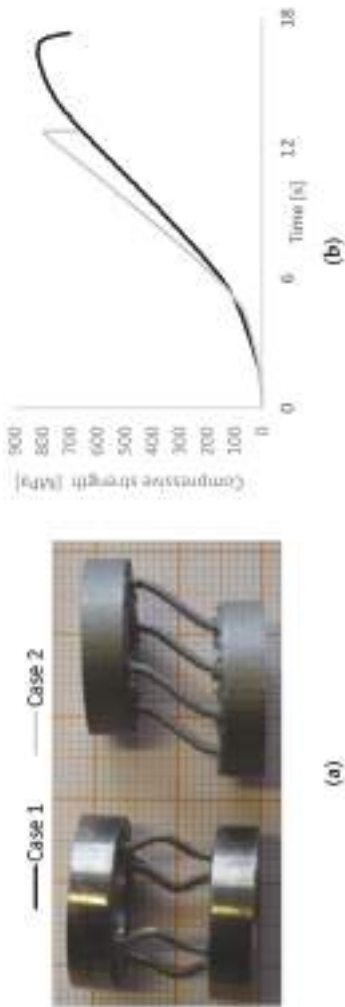


Figure 15. (a) Representative failure behavior of tested samples. Both samples show the same compression strength. (b) Strength-time curve representing the two kinds of failure behavior. Both samples exhibit the same compression strength.

Table 5. Overview of the results from compression testing (compressive strength σ ; $n = 5$ for each design) for all geometrical variations taking account of the orientation and slenderness ratio λ . The diameter d and height L are defined by CAD.

Dimension	d_{CAD} (mm)	L_{CAD} (mm)	SLM HIP 0°		EBM No HIP 0°		SLM HIP 45°		SLM No HIP 45°		EBM No HIP 45°	
			σ (MPa)	λ								
1.7	1.7	925 ± 8	14.6 ± 0.1	811 ± 37	15.6 ± 0.1	947 ± 18	14.6 ± 0.1	838 ± 25	15.4 ± 0.1	838 ± 25	15.4 ± 0.1	838 ± 25
	1.5	860 ± 11	16.7 ± 0.1	722 ± 37	17.8 ± 0.1	821 ± 22	16.2 ± 0.2	741 ± 40	17.4 ± 0.1	741 ± 40	17.4 ± 0.1	741 ± 40
1.3	1.2	838 ± 32	19.4 ± 0.1	629 ± 23	20.3 ± 0.2	793 ± 59	18.5 ± 0.1	634 ± 29	20.3 ± 0.1	634 ± 29	20.3 ± 0.1	634 ± 29
	1.2	787 ± 22	22.8 ± 0.1	773 ± 10	22.3 ± 0.1	748 ± 97	21.6 ± 0.1	711 ± 47	22.4 ± 0.1	588 ± 33	25.5 ± 0.1	588 ± 33
1.1	1.0	795 ± 56	19.0 ± 0.1	832 ± 46	18.5 ± 0.1	658 ± 85	20.1 ± 0.2	791 ± 73	18.0 ± 0.1	645 ± 30	21.2 ± 0.1	645 ± 30
	1.1	900 ± 36	15.2 ± 0.1	1033 ± 56	14.3 ± 0.1	726 ± 41	16.1 ± 0.2	879 ± 28	14.4 ± 0.1	1053 ± 61	14.9 ± 0.1	739 ± 18
6	8	961 ± 43	11.4 ± 0.1	1220 ± 18	10.8 ± 0.1	841 ± 39	12.1 ± 0.2	960 ± 28	10.8 ± 0.1	1169 ± 15	11.1 ± 0.1	891 ± 33
	6	961 ± 43	11.4 ± 0.1	1220 ± 18	10.8 ± 0.1	841 ± 39	12.1 ± 0.2	960 ± 28	10.8 ± 0.1	1169 ± 15	11.1 ± 0.1	891 ± 33

The failure types described occur independently of geometric variation and orientation in manufacturing. The required maximum loading to exceed stability and thus compressive strength remains similar. The established results provide evidence that regardless of geometrical considerations (different heights, diameters) and the method (EBM, SLM) the determined deformation behavior is characteristic of the specimens under investigation. It remains unclear how great the influences are that are caused by probable deviations of rod positions from the acting load (plane parallelism) or by production-related faults (e.g., the crossover between the base and top area of the rod). Just as interesting would be any functional associations between the orientation of the specimens tested and the level of influencing imperfections.

Figure 16 shows the relation between equivalent diameter and compression strength.

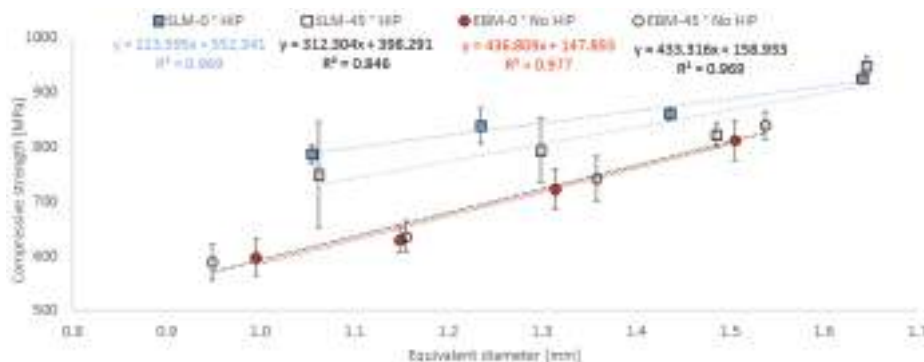


Figure 16. Relation between equivalent diameter and compressive strength for SLM parts (HIP) and EBM parts (No HIP) in the orientations 0° and 45°.

Both manufacturing systems in principle behave identically. Compression strength increases as expected with increasing equivalent diameters. SLM parts showed higher compression strength values than the EBM parts. While the difference between the orientations of the EBM-manufactured parts is not relevant, the difference in the SLM-manufactured parts is clearly visible.

A linear relationship was found between equivalent diameter and compression strength. EBM parts in both orientations showed a high correlation (0°— $R^2 = 0.977$; 45°— $R^2 = 0.969$). In contrast, the SLM parts in the 45° orientation showed a lower correlation ($R^2 = 0.846$). The correlation in the 0° orientation is provided in the range of the EBM parts ($R^2 = 0.969$).

As shown in Figure 10, it appears that the specific manufacturing accuracy of the struts (diameter) has an influence on the course of the results. EBM parts showed the same course in results, especially in the measured inner diameter. This area is the most important area for the acceptance of loading force. The values for 0° and 45° oriented parts are comparable. The SLM parts however show differences in the 0° and 45° orientation. The differences in the 45° orientation are greater than in 0° orientation. This provides clear information that the compression strength value is definitely affected by the area of the strut that can hold the acting force in a clear defined structure of a circle. This was compared to Suard et al. [34] who have described the influence of the diameter on mechanical properties. It confirms that strut orientation in the manufacturing process influences the formation of the surfaces and thus also the roughness. This increase in the roughness R_a of the SLM specimens leads to a reduction in the cross-section and thus to a low compressive strength.

Figure 17 showed the relation between height and compression strength.

SLM- and EBM-manufactured parts in principle showed an identical behavior. Compression strength decreased as expected with increasing height. SLM parts showed higher values for compression strength than the EBM parts. The differences between the orientations of the EBM-manufactured and SLM-manufactured parts are small.

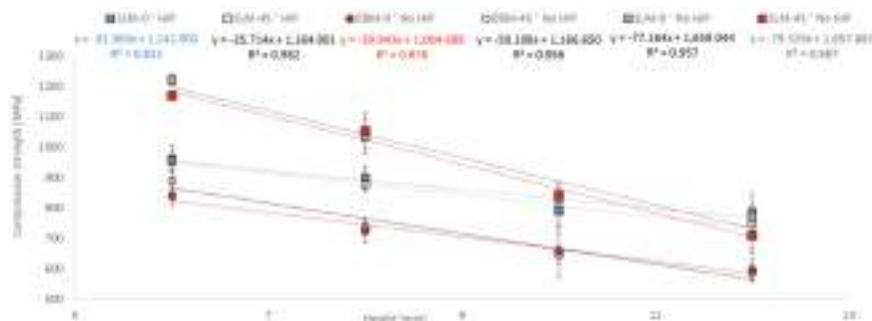


Figure 17. Relation between height and compressive strength for SLM parts (HIP) and EBM parts (No HIP) in 0° and 45° orientation in comparison to SLM parts (No HIP) in 0° and 45° orientation

A linear relationship was found between equivalent diameter and compression strength. EBM parts showed a high correlation in both orientations (0° — $R^2 = 0.976$; 45° — $R^2 = 0.956$). SLM parts also showed a high correlation in the tested orientation (0° — $R^2 = 0.922$; 45° — $R^2 = 0.982$). The correlation of the SLM parts without heat treatment was within the range of all other parts (0° — $R^2 = 0.957$; 45° — $R^2 = 0.987$).

The differences between HIPed and No HIPed parts that affect the mechanical properties are well-known [40,46,51]. Especially HIPing leads to decreased strength. The reason is the transformation of martensite into α and β phases. The marginally lower strength is characteristic for the $\alpha + \beta$ phase. This correlation applies to the SLM parts. The difference between HIPed and No HIPed parts dwindles away with increasing height until it is gone.

Although the EBM samples achieved higher values in the hardening measurement, the compressive strength values are below the values for SLM samples. Here lies the reason for the significantly higher roughness R_Z and R_a of the EBM parts. Kasperovich et al. [46] described that the rough “as-built” surface needs to be considered as crack initiator and that its lower strength has to be taken into account. This leads to lower compression strength of EBM parts compared to SLM parts without heat treatment.

The influence of the geometric conditions can be described very well by indicating the degree of slenderness λ (see Equation (3)). The correlation between the compressive strength and the slenderness ratio also revealed linear dependencies with high coefficients of determination of over 90% as shown in Figures 18 and 19. The coefficients were lower only in two cases (45° oriented parts with variable d).

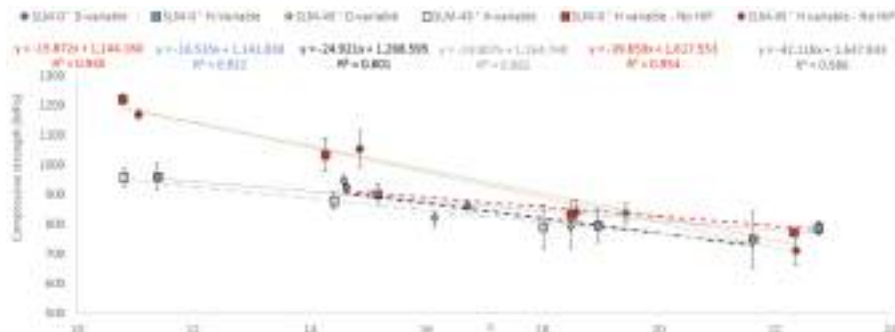


Figure 18. Correlation between compressive strength and slenderness ratio of SLM-manufactured parts. Results are shown as mean values with the corresponding standard deviations. For the linear regressions, the coefficient of determination is shown.

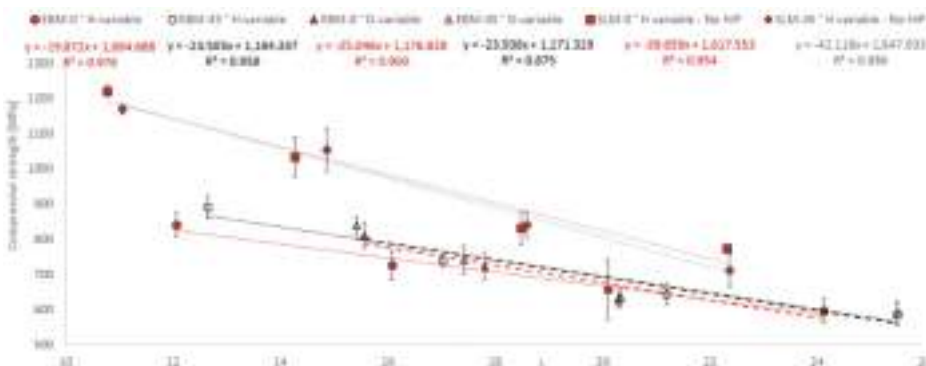


Figure 19. Correlation between compressive strength and slenderness ratio of EBM-manufactured parts. Results are shown as mean values with the corresponding standard deviations. For the linear regressions, the coefficient of determination is shown.

Compressive strength increased with a decreasing slenderness ratio for all tested variations. The slopes show, that the possible change in compressive strength by variations in the geometrical parameters (diameter or height) leads at least to the same result in the case of the HIPed parts. The results from the No HIPed parts differ clearly from the HIPed parts. Here is seen a more different behavior. Nevertheless, the relation between the obtained mechanical properties and the geometrical properties is well described with the linear relationships found.

These results show that the orientation of the part during the building process plays an important role in view of mechanical properties. The 45° oriented parts show by variation of the diameter a direct influence on the mechanical properties. The influence of a modification in the diameter is greater than a change in the height while retaining the same slenderness ratio. A good indicator for this are the different slopes in the correlations found. The influence of orientation on the microstructure and on the mechanical properties is known [19,25]. This influence also becomes clear here. With increases in the diameter, the proportion of the structure-oriented structural areas also grows. These obliquely oriented structural regions can absorb increasingly less load. For the 0° oriented samples, it is less important whether the diameter is increased or the height is varied.

The difference between the SLM parts (HIP and No HIP) is clearly caused by the microstructural difference. The HIPed parts have a uniform $\alpha + \beta$ structure with a lower hardness than the No HIPed structure with a martensitic fraction. This relationship is also seen for compression strength.

In the EBM parts, the compressive strength also increased with a decreasing slenderness ratio for all tested variations. Here is noteworthy that the 45° oriented samples behave similar. Regardless of whether the diameter or the height varies, the result is the same. However, differences are seen in the 0° oriented samples. Here, a change in the diameter has a greater effect on changes in the mechanical properties than a change in height. The EBM samples deviate more and more from the default (d_{Cad}) in their measured outer diameter (Figure 10). Since all EBM samples were produced without heat treatment, a direct comparison with the SLM samples (0° and 45°) is possible here. The EBM samples, though achieving higher values in the hardness measurements, have in comparison to the SLM parts (both without heat treatment) the lower compressive strength. The reason lies, as already explained, on the significantly higher roughness values R_Z and R_a of the EBM parts. The crack initiation of the rough “as-built” surface leads to a lower compression strength of EBM parts.

4. Conclusions

The properties of single Ti₆Al₄V struts fabricated via SLM and EBM were examined experimentally for selected different geometrical dimensions. Two building orientations with variations in the height and diameter of the individual struts were integrated in the tests.

The following specific conclusions have been reached:

- Cross-section accuracy of fabricated struts
 - All manufactured struts deviate from the given diameter from CAD data.
 - The SLM parts show a higher accuracy than the EBM parts.
 - No geometric differences could be determined between the HIPed and NO HIPed SLM parts.
- The values of roughness obtained for SLM- and EBM-manufactured Ti6Al4V parts correspond to those from the literature. The SLM parts have significantly lower Ra and R_Z values in both orientations.
- Different hardness values between EBM and SLM were determined and supported by their different respective microstructures. The No HIPed EBM parts showed the highest values for hardness. The HIPed SLM parts showed the lowest values according to microstructure. The hardness of the 45° oriented parts without heat treatment was significantly lower than of the 0° oriented parts. Heat-treated parts showed no differences in dependence on the orientation.
- Based on tests under uniaxial loading conditions, the influence of strut orientation on compression strength was demonstrated.
 - A functional correlation between compressive strength and slenderness ratio (λ) as well as between equivalent diameter (d) and height (L) of EBM and SLM parts could be established.
 - Modifications in diameter lead to a larger influence on compressive strength than modifications in height.
 - A strut orientation of 45 degrees leads to a moderate decrease in the compression strength of EBM and SLM parts.
 - Both the microstructure and the cross-section accuracy of fabricated struts as well as roughness are responsible for differences in compressive strength.
 - The specimens produced show 2 types of stability failure—symmetric and antimetric buckling—at the same compressive strength levels.

In our work, we could demonstrate the importance of the exact fabrication and what influence the quality of a single strut has on mechanical properties. The results are strongly affected by the microstructure and the roughness of struts. Hardness and compressive strength exactly confirm the dependence of material behavior as a function of orientation. Orientation is a crucial determining fundamental analysis factor of mechanical characteristics and thus forms, taking into consideration geometrical influences, an essential basis for the constructive design of medical-engineering applications in which rod structures are used. The results obtained the influence of the slenderness ratio and especially the influence of the diameter on the mechanical properties provides an excellent basis for a transfer into medical applications. The knowledge gained from the comparisons of the EBM- and SLM-manufactured single struts can be practically applied to problems in the field of additive manufactured parts.

Of special interest are the influences that resulted in the different failure types of the specimens. Both the influences from specimen orientation during mechanical testing as well as from production-caused inhomogeneities need to be regarded separately in future.

Besides compressive stresses, results from bend loading also need to be taken into consideration both in static as well as vibration tests. The results brought forward here represent only a part of the necessary information required for the translation into medical applications.

Acknowledgments: We are grateful for the financial support provided by the Federal Ministry of Education and Research (03FH005IX5).

Author Contributions: We point out that all authors were fully involved in the study and in preparing the manuscript. V.W., P.D. and H.S. designed the study. V.W. generated the CAD samples with support of H.H. and was involved in the manufacturing process of the scaffolds. V.W. and P.D. performed the experiments, analyzed the data with support of N.L. and wrote the initial manuscript. H.H. and R.B. organized the research funding. All authors ensured the accuracy of the data and the analyses and reviewed the manuscript in its current state.

Conflicts of Interest: The authors declare no conflict of interest.

References

- Heinl, P.; Müller, L.; Körner, C.; Singer, R.F.; Müller, F.A. Cellular Ti-6Al-4V structures with interconnected macro porosity. *Acta Biomater.* **2008**, *4*, 1536–1544. [CrossRef] [PubMed]
- Geetha, M.; Singh, A.K.; Asokamani, R.; Gogia, A.K. Ti based biomaterials, the ultimate choice for orthopaedic implants—A review. *Prog. Mater. Sci.* **2009**, *54*, 397–425. [CrossRef]
- Hazlehurst, K.; Wang, C.J.; Stanford, M. Evaluation of the stiffness characteristics of square pore CoCrMo cellular structures manufactured using laser melting technology for potential orthopaedic applications. *Mater. Des.* **2013**, *51*, 949–955. [CrossRef]
- Attar, H.; Calin, M.; Zhang, L.C.; Scudino, S.; Eckert, J. Manufacture by selective laser melting and mechanical behavior of commercially pure titanium. *Mater. Sci. Eng. A* **2014**, *593*, 170–177. [CrossRef]
- Attar, H.; Löber, L.; Funk, A.; Calin, M.; Zhang, L.C.; Prashanth, K.G. Mechanical behavior of porous commercially pure Ti and Ti-TiB composite materials manufactured by selective laser melting. *Mater. Sci. Eng. A* **2015**, *625*, 350–356. [CrossRef]
- Wauthle, R.; van der Stok, J.; Yavari, S.A.; van Humbeeck, J.; Kruth, J.P.; Zadpoor, A.A.; Weinans, H.; Mulier, M.; Schrooten, J. Additively manufactured porous tantalum implants. *Acta Biomater.* **2015**, *14*, 217–225. [CrossRef] [PubMed]
- Thijs, L.; Sistiaga, M.L.M.; Wauthle, R.; Qingge, X.; Kruth, J.-P.; Humbeeck, J.V. Strong morphological and crystallographic texture and resulting yield strength anisotropy in selective laser melted tantalum. *Acta Mater.* **2013**, *61*, 4657–4668. [CrossRef]
- Öhmann, C.; Baleani, M.; Pani, C.; Taddei, F.; Alberghini, M.; Viceconti, M.; Manfrini, M. Compressive behaviour of child and adult cortical bone. *Bone* **2011**, *49*, 2011. [CrossRef] [PubMed]
- Grimal, Q. Assessment of cortical bone elasticity and strength: Mechanical testing and ultrasound provide complementary data. *Med. Eng. Phys.* **2009**, *31*, 1140–1147. [CrossRef] [PubMed]
- Lewis, G. Properties of open-cell porous metals and alloys for orthopaedic applications. *J. Mater. Sci. Mater. Med.* **2013**, *24*, 2293–2325. [CrossRef] [PubMed]
- Abele, E.; Stoffregen, H.A.; Kniepkamp, M.; Lang, S. Selective laser melting for manufacturing of thin-walled porous elements. *J. Mater. Process. Technol.* **2015**, *215*, 114–122. [CrossRef]
- Guo, C.; Ge, W.; Lin, F. Effects of scanning parameters on material deposition during Electron Beam Selective Melting of Ti-6Al-4V powder. *J. Mater. Process. Technol.* **2015**, *217*, 148–157. [CrossRef]
- Song, B.; Dong, S.; Zhang, B.; Liao, H.; Coddet, C. Effects of processing parameters on microstructure and mechanical property. *Mater. Des.* **2012**, *35*, 120–125. [CrossRef]
- Yadroitsev, I.; Krakhmalev, P.; Yadroitsava, I. Selective laser melting of Ti₆Al₄V alloy for biomedical applications temperature monitoring and microstructural evolution. *J. Alloy. Compd.* **2014**, *583*, 404–409. [CrossRef]
- Vrancken, B.; Thijs, L.; Kruth, J.P.; van Humbeeck, J. Heat treatment of Ti₆Al₄V produced by Selective Laser Melting: Microstructure and mechanical properties. *J. Alloy. Compd.* **2012**, *541*, 177–185. [CrossRef]
- Luxner, M.H.; Stampfl, J.; Pettermann, H.E. Finite element modeling concepts and linear analyses of 3D regular open cell structures. *J. Mater. Sci.* **2005**, *40*, 5859–5866. [CrossRef]
- Gibson, L.J.; Ashby, M.F.; Schajer, G.S.; Robertson, C.I. Mechanics of two-dimensional cellular materials. *Proc. R. Soc. Lond. Ser. A Math. Phys. Sci.* **1982**, *382*, 25–42. [CrossRef]
- Campoli, G.; Borleffs, M.S.; Yavari, S.A.; Wauthle, R.; Weinans, H.; Zadpoor, A.A. Mechanical properties of open-cell metallic biomaterials manufactured using additive manufacturing. *Mater. Des.* **2013**, *49*, 957–965. [CrossRef]

19. Weißmann, V.; Bader, R.; Hansmann, H.; Laufer, N. Influence of the structural orientation on the mechanical properties of selective laser melted Ti₆Al₄V open-porous scaffolds. *Mater. Des.* **2016**, *95*, 188–197. [CrossRef]
20. Challis, V.J.; Roberts, A.P.; Grotowski, J.F.; Zhang, L.C.; Sercombe, T.B. Prototypes for Bone Implant Scaffold Designed via Topology Optimization and Manufactured by Solid Freeform Fabrication. *Adv. Eng. Mater.* **2010**, *12*, 1106–1110. [CrossRef]
21. Weißmann, V.; Wieding, J.; Hansmann, H.; Laufer, N.; Wolf, A.; Bader, R. Specific Yielding of Selective Laser-Melted Ti₆Al₄V Open-Porous Scaffolds as a Function of Unit Cell Design and Dimensions. *Metals* **2016**, *6*, 166. [CrossRef]
22. Mahshid, R.; Hansen, H.N.; Højbjørre, K.L. Strength analysis and modeling of cellular lattice structures manufactured using selective laser melting for tooling applications. *Mater. Des.* **2016**, *104*, 276–283. [CrossRef]
23. Xu, S.; Shen, J.; Zhou, S.; Huang, X.; Xie, Y.M. Design of lattice structures with controlled anisotropy. *Mater. Des.* **2016**, *93*, 443–447. [CrossRef]
24. Rashed, M.G.; Ashraf, M.; Mines, R.A.; Hazell, P.J. Metallic microlattice materials a current state of the art on manufacturing, mechanical properties and applications. *Mater. Des.* **2016**, *95*, 518–533. [CrossRef]
25. Wauthle, R.; Vrancken, B.; Beynaerts, B.; Jorissen, K.; Schrooten, J.; Kruth, J.P.; van Humbeeck, J. Effects of build orientation and heat treatment on the microstructure and mechanical properties of selective laser melted Ti₆Al₄V lattice structures. *Addit. Manuf.* **2015**, *5*, 77–84. [CrossRef]
26. Cain, V.; Thijss, L.; van Humbeeck, J.; van Hooreweder, B.; Knutzen, R. Crack propagation and fracture toughness of Ti₆Al₄V alloy produced by selective laser melting. *Addit. Manuf.* **2015**, *5*, 68–76. [CrossRef]
27. Wu, M.-W.; Lai, P.-H.; Chen, J.-K. Anisotropy in the impact toughness of selective laser ledded Ti₆Al₄V alloy. *Mater. Sci. Eng. A* **2015**, *650*, 295–299. [CrossRef]
28. De Wild, M.; Schumacher, R.; Mayer, K.; Schkommodau, E.; Thoma, D.; Bredell, M.; Gujer, A.K.; Grätz, K.W.; Weber, F.E. Bone regeneration by the osteoconductivity of porous titanium implants manufactured by selective laser melting: A histological and micro computed tomography study in the rabbit. *Tissue Eng. Part A* **2013**, *19*, 2645–2654. [CrossRef] [PubMed]
29. Kumar, A.; Nune, K.C.; Murr, L.E.; Misra, R.K. Biocompatibility and Mechanical Behaviour of 3D Scaffolds for biomedical devices: Process-structure-property paradigm. *Int. Mater. Rev.* **2016**, *61*, 20–45. [CrossRef]
30. Taniguchi, N.; Fukibayashi, S.; Takemoto, M.; Sasaki, K.; Otsuki, B.; Nakamura, T.; Matsuhita, T.; Kokubo, T.; Matsuda, S. Effect of pore size on bone ingrowth into porous titanium implants fabricated by dditive manufacturing an invivo experiment. *Mater. Sci. Eng. C* **2015**, *59*, 690–701. [CrossRef] [PubMed]
31. Labeas, G.N.; Sunaric, M.M. Investigation on the Static Response and Failure Process of Metallic Open Lattice Cellular Structures. *Strain* **2010**, *46*, 195–204. [CrossRef]
32. Ahmadi, S.M.; Campoli, G.; Yavari, S.A.; Sajadi, B.; Wauthle, R.; Schrooten, J.; Weinans, H.; Zadpoor, A.A. Mechanical behavior of regular open-cellporous biomaterials made of diamond lattice unit cells. *J. Mech. Behav. Biomed. Mater.* **2014**, *34*, 106–115. [CrossRef] [PubMed]
33. Ushijima, K.; Cantwell, W.J.; Mines, R.A.; Tsopanos, S.; Smith, M. An investigation into the compressive properties of stainless steel micro-lattice structures. *J. Sandw. Struct. Mater.* **2010**, *13*, 303–329. [CrossRef]
34. Suard, M.; Martin, G.; Lhuissier, P.; Dendievel, R.; Vignat, F.; Blandin, J.-J. Mechanical equivalent diameter of single struts for the stiffness prediction of lattice structures produced by electron beam melting. *Addit. Manuf.* **2015**, *8*, 124–131. [CrossRef]
35. Desphande, V.S.; Ashby, M.F.; Fleck, N.A. Foam topology bending versus stretching dominated architectures. *Acta Mater.* **2001**, *49*, 1035–1040.
36. Mazur, M.; Leahy, M.; Sun, S.; Vcelka, M.; Shidid, D.; Brandt, M. Deformation and failure behaviour of Ti-6Al-4V lattice structures manufactured by selective laser melting (SLM). *Int. J. Adv. Manuf. Technol.* **2016**, *84*, 1391–1411. [CrossRef]
37. McKnown, S.; Shen, Y.; Brooks, W.K.; Sutcliffe, C.J.; Cantwell, W.J.; Langdon, G.S.; Nurrick, G.N.; Theobald, M.D. The quasi-static and blast loading response of lattice structures. *Int. J. Impact Eng.* **2008**, *35*, 795–810. [CrossRef]
38. Gong, H.; Rafi, K.; Gu, H.; Ram, G.J.; Starr, T.; Strucker, B. Influence of defects on mechanical properties of Ti-6Al-4V components produced by selective laser melting and electron beam melting. *Mater. Des.* **2015**, *86*, 545–554. [CrossRef]

39. Simonelli, M.; Tse, Y.; Tuck, C. Effect of the build orientation on the Mechanical Properties and Fracture Modes of SLM Ti-6Al-4V. *Mater. Sci. Eng. A* **2014**, *616*, 1–11. [CrossRef]
40. Qiu, C.; Adkins, N.; Attalah, M. Microstructure and tensile properties of selectively laser-melted and of HIPed laser-melted Ti-6Al-4V. *Mater. Sci. Eng. A* **2013**, *578*, 230–239. [CrossRef]
41. Bartolomeu, F.; Faria, S.; Carvalho, O.; Pinto, E.; Alves, N.; Silva, F.S.; Miranda, G. Predictive models for physical and mechanical properties of Ti6Al4V produced by selective laser melting. *Mater. Sci. Eng. A* **2016**, *663*, 181–192. [CrossRef]
42. Sigl, M.; Lutzmann, S.; Zaeh, M.F. Transient Physical Effects in Electron Beam Sintering. In Proceedings of the Solid Freeform Fabrication Symposium, Austin, Texas, 7–9 August 2006.
43. Drescher, P.; Reimann, T.; Seitz, H. Investigation of powder removal of net-structured titanium parts made from electron beam melting. *Int. J. Rapid Manuf.* **2014**, *4*, 81–89. [CrossRef]
44. Fox, J.C.; Moylan, S.P.; Lane, B.M. Effect of process parameters on the surface roughness of overhanging structures in laser powder bed fusion additive manufacturing. *Procedia CIRP* **2016**, *45*, 131–134. [CrossRef]
45. Triantaphyllou, A.; Giusca, C.L.; Macaulay, G.D.; Roerig, F.; Hoebel, M.; Leach, R.K.; Tomita, B.; Milne, K.A. Surface texture measurement for additive manufacturing. *Surf. Topogr. Metrol. Prop.* **2015**, *3*, 024002. [CrossRef]
46. Kasperovich, G.; Hausmann, J. Improvement of fatigue resistance and ductility of TiAl₆V₄ processed by selective laser melting. *J. Mater. Process. Technol.* **2015**, *220*, 202–214. [CrossRef]
47. Campanelli, S.L.; Contuzzi, N.; Ludovico, A.D.; Caiazzo, F.; Cardaropoli, F.; Sergi, V. Manufacturing and characterization of Ti₆Al₄V lattice components manufactured by selective laser melting. *Materials* **2014**, *7*, 4803–4822. [CrossRef]
48. Murr, L.E.; Quinones, S.A.; Gaytan, S.M.; Lopez, M.I.; Rodela, A.; Martinez, E.Y.; Hernandez, D.H.; Martinez, E.; Medina, F.; Wicker, R.B. Microstructure and mechanical behavior of Ti-6Al-4V produced by rapid layer manufacturing, for biomedical applications. *J. Mech. Behav. Biomed. Mater.* **2009**, *2*, 20–32. [CrossRef] [PubMed]
49. Wu, M.-W.; Lai, P.-H. The positive effect of hot isostatic pressing on improving the anisotropies of bending and impact properties in selective laser melted Ti6Al4V alloy. *Mater. Sci. Eng. A* **2016**, *658*, 429–438. [CrossRef]
50. Sattler, K. *Lehrbuch der Statik: Theorie und ihre Anwendungen. Erster Band: Grundlagen und Fundamentale Berechnungsverfahren*; Springer Verlag GmbH: Heidelberg/Berlin, Germany, 1969; p. 132.
51. Leuders, S.; Thöne, M.; Riemer, A.; Niendorf, T.; Tröster, T.; Richard, H.A.; Maier, H.J. On the mechanical behaviour of titanium alloy TiAl₆V₄ manufactured by selective laser melting Fatigue resistance and crack growth performance. *Int. J. Fatigue* **2013**, *48*, 300–307. [CrossRef]



© 2017 by the authors. Licensee MDPI, Basel, Switzerland. This article is an open access article distributed under the terms and conditions of the Creative Commons Attribution (CC BY) license (<http://creativecommons.org/licenses/by/4.0/>).

Article

Aging Behaviour and Mechanical Performance of 18-Ni 300 Steel Processed by Selective Laser Melting

Riccardo Casati ¹, Jannis N. Lemke ¹, Ausonio Tuissi ² and Maurizio Vedani ^{1,*}

¹ Dipartimento di Meccanica, Politecnico di Milano, Milano I-20156, Italy; riccardo.casati@polimi.it (R.C.); jannisnicolas.lemke@polimi.it (J.N.L.)

² Institute for Condensed Matter Chemistry and Technologies for Energy, CNR, Lecco I-23900, Italy; ausonio.tuissi@cnr.it

* Correspondence: maurizio.vedani@polimi.it; Tel.: +39-02-2399-8230

Academic Editor: Manoj Gupta

Received: 2 August 2016; Accepted: 5 September 2016; Published: 8 September 2016

Abstract: An 18-Ni 300 grade maraging steel was processed by selective laser melting and an investigation was carried out on microstructural and mechanical behaviour as a function of aging condition. Owing to the rapid cooling rate, the as-built alloy featured a full potential for precipitate strengthening, without the need of a solution treatment prior to aging. The amount of reversed austenite found in the microstructure increased after aging and revealed to depend on aging temperature and time. Similarly to the corresponding wrought counterpart, also in the selective laser-melted 18-Ni 300 alloy, aging promoted a dramatic increase in strength with respect to the as-built condition and a drop in tensile ductility. No systematic changes were found in tensile properties as a function of measured amount of austenite. It is proposed that the submicrometric structure and the phase distribution inherited by the rapid solidification condition brought by selective laser melting are such that changes in tensile strength and ductility are mainly governed by the effects brought by the strengthening precipitates, whereas the concurrent reversion of the γ -Fe phase in different amounts seems to play a minor role.

Keywords: selective laser melting; maraging steel; aging behaviour; reversed austenite

1. Introduction

Maraging steels are ultra-high strength Fe-Ni alloys developed mainly for aircraft, aerospace, and tooling applications. Their outstanding combination of strength and toughness results from the aging of a relatively soft martensite formed by cooling at moderate rates from the Ni-containing γ -Fe solid solution. Aging leads to the formation of strengthening precipitates. It is reported that in the 18-Ni 300 alloy and in similar grades, the Ni_3Ti phase (or more generally, Ni_3X where $\text{X} = \text{Ti}, \text{Mo}, \text{V}, \text{and W}$) readily form on short-term aging at low temperatures ($400\text{--}450\text{ }^\circ\text{C}$), followed by Fe_2Mo or Fe_7Mo_6 precipitation [1–6]. Aging at temperatures exceeding $500\text{ }^\circ\text{C}$ concurrently promotes the formation of austenite by a diffusion-controlled reaction, which is also favoured by the release of Ni into the matrix due to decomposition of Ni_3Ti phase [1,3,5–9].

Due to their good ductility and weldability, maraging steels recently attracted the attention as candidate alloys for additive manufacturing processes, such as selective laser melting (SLM). During SLM, layers of powder are selectively molten by a scanning laser beam and consolidated on top of each other. Fully dense parts can thus be generated featuring mechanical properties comparable to those of components processed by standard routes [10–12].

The mechanical behaviour of SLM parts is strongly affected by the refined microstructure inherited from fast cooling and by generation of small solidification faults [13–16]. Indeed, the localized melting process experienced during SLM is not yet fully understood. It is governed by laser beam

parameters, but also by surface morphology given by the pre-deposited layers and the stochastic particle distribution on the powder bed, as well as by the physical surface and bulk properties of the powder itself [17]. The solidification process and the resulting microstructure assume, therefore, an important role that still needs a deeper understanding and control. Concurrently, alloy optimization should consider these issues by deliberately promoting enhanced damage tolerance properties, especially when considering opportunities offered by tuning of alloy chemistry and the selection of post-SLM thermal treatments.

In wrought maraging parts requiring increased toughness, over-aged temper conditions are preferably selected in order to allow the formation of a controlled amount of austenite that remains stable even at room temperature. Such over-aging promotes softening and increases crack blunting effects [1]. However, this beneficial influence may be counterbalanced by matrix embrittlement when too coarse particles start acting as crack nucleation sites [8].

The present study is, therefore, aimed at investigating the mechanical behaviour of 18-Ni 300 maraging alloy samples produced by SLM as a function of specific microstructural conditions obtained by different thermal treatments. Analyses will be particularly focused on the possibility of improving the combination of strength and ductility by tailored aging treatments.

2. Materials and Methods

An 18-Ni 300 maraging alloy (1.2709) supplied by Sandvik Osprey LTD (Neath, UK) as gas-atomized powder was investigated. The alloy chemical composition is given in Table 1, while Figure 1 shows the general morphology of the batch of powder considered. From the particle size distribution obtained by laser diffraction analysis, an average particle size of 35 μm was obtained and it could be stated that 90% of the particles did not exceed the size of 54 μm .

Table 1. Chemical composition (weight fraction, %) of the investigated 18-Ni 300 steel powder.

Ni	Mo	Co	Ti	Al	Si
17.6	5.3	9.6	0.7	0.09	0.2

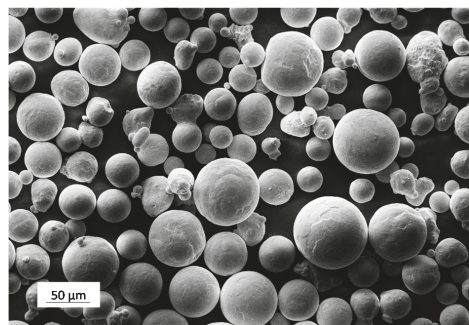


Figure 1. View of the 18-Ni 300 alloy powder investigated.

A Renishaw AM250 SLM system (Wotton-under-Edge, UK) was used to produce a set of samples consisting of horizontal and vertical bars (10 mm \times 10 mm \times 75 mm), as depicted in Figure 2. Melting of powder was performed under Ar atmosphere by a single mode fiber laser with a power of 200 W and an estimated beam diameter at a focal point of 75 μm . Laser melting was performed by discrete and partially overlapped spots exposed to the radiation for a fixed time (t) and their distance is called point distance (d_p). At the end of each scan line, the laser shifts to a partially overlapped adjacent line to scan the selected surface of the layer. The distance between adjacent scan lines is

defined as the hatch distance (d_H). Based on parameter optimization and manufacturer data, d_H , d_P , and t were set to 80 μm , 65 μm , and 80 μs , respectively. The thickness of each powder layer was set to 40 μm . Finally, samples were produced using a meander scanning strategy and by rotating the scanning direction by 67° after each layer.

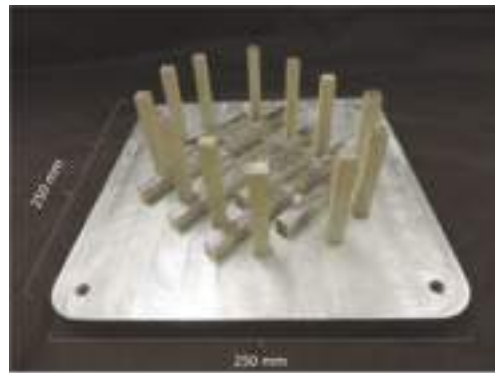


Figure 2. Geometry of SLM processed bars.

After removal from the steel base plate, the samples were sectioned and machined for further analyses. Microstructural observations were carried out by optical microscope (Leica Microsystems, Richmond Hill, ON, Canada), and by scanning electron microscope (SEM, Oberkochen, Germany) equipped with energy dispersive X-ray analysis (EDX, Oxford Instruments, Abingdon-on-Thames, UK) and electron back-scattered diffraction (EBSD, Oxford Instruments, Abingdon-on-Thames, UK) detectors. Samples were prepared by standard grinding and polishing followed by etching with Picral or modified Fry's reagent.

Aging response of the SLM samples was evaluated starting from samples both in the as-built condition and after a standard solution treatment, carried out at 815 °C for 30 min, followed by water quenching.

Differential scanning calorimetry (DSC, Labsys Setaram, Caluire, France) analyses were carried out on the as-built and on the solution treated samples (weight of about 50 mg) by temperature scans, at a rate of 20 °C/min in Ar atmosphere to assess precipitation sequence of strengthening phases. Isothermal aging curves (hardness vs. aging time at constant temperature) were then collected at 460, 490, 540, and 600 °C for times ranging from 10 min, up to 14 days. The evolution of hardness was followed by performing Vickers indentations with a load of 2 kg.

X-ray diffraction (XRD) patterns were collected using a X-Pert PRO (PANalitical, Almelo, The Netherlands) instrument equipped with a RTMS X'Celerator sensor. Cu K α ($k = 0.15418 \text{ nm}$) radiation was employed. Peaks identification and quantitative analysis of phases was performed by Rietveld method using Maud software. Samples for XRD were sectioned by diamond blade and polished down to 1 μm grit size, applying conventional metallographic methods. In order to avoid substantial structural modification, samples were carefully prepared by a very gentle and prolonged polishing stage.

Dog-bone tensile specimens having a gauge length of 20 mm and diameter of 4 mm were machined from bars treated according to different conditions investigated. In the present study only specimens built with their longitudinal axis oriented along the horizontal direction are considered. Tensile tests were performed at room temperature with a crosshead speed of 0.5 mm/min (corresponding to an initial strain rate of $4.2 \times 10^{-4} \cdot \text{s}^{-1}$) using a MTS Alliance RT/100 universal testing machine (MTS, Eden Prairie, MN, USA). At least three specimens for each condition were tested. Finally, fractographic analyses were carried out by SEM to identify the main fracture mechanisms.

3. Results

Figure 3 shows low-magnification views of the as built structure. The width and depth of the distinct laser tracks could be clearly identified after etching on lateral sections (Figure 3a). Views obtained from cross-sections taken perpendicularly to the build direction, hereafter referred to as top views, highlight the discontinuous nature of the melting process induced by the pulsed laser beam: distinct pools pertaining to different layers are visible on the same track (Figure 3b). High magnification micrographs taken by SEM reveal the expected cellular solidification structure and evidence of the epitaxial growth across different track boundaries, as shown in Figure 4.

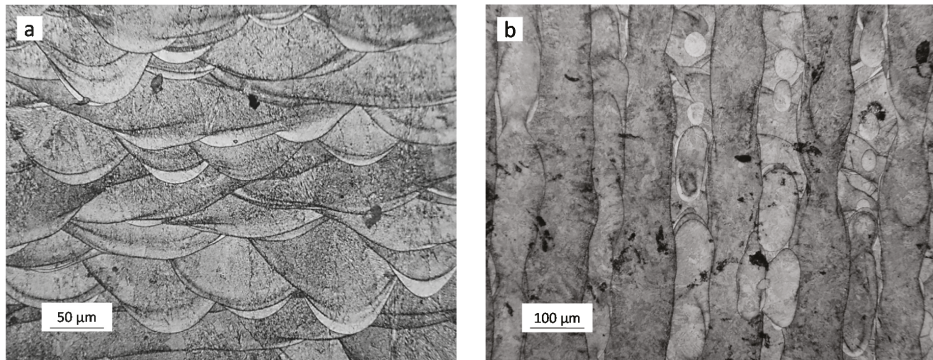


Figure 3. Optical images of the as built microstructure of the steel investigated. (a) Lateral view; and (b) top view.

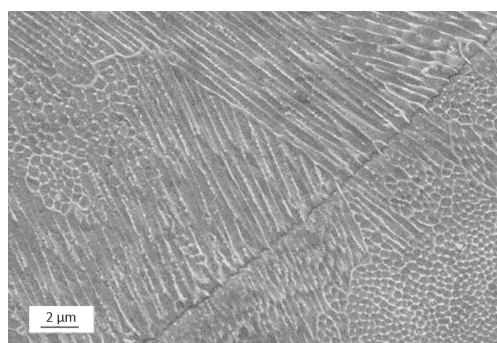


Figure 4. SEM image of the cellular solidification microstructure and epitaxial growth across a track boundary.

After solution treatment, the traces of solidification completely disappeared and the cellular structure was replaced by a martensitic structure, as depicted in Figure 5a. EBSD analyses showed that the martensitic structure was fairly coarse. According to literature, the detected microstructural features can be interpreted as massive martensite blocks or packets (depicted in Figure 5b by the EBSD orientation image), consisting of fine bundles of parallel, heavily dislocated laths [8,18]. Traces of reversed austenite (γ -Fe phase) were also revealed by phase maps based on crystallographic information. It can be stated that the γ -Fe phase is mainly located at boundaries of the martensite blocks (Figure 5c).

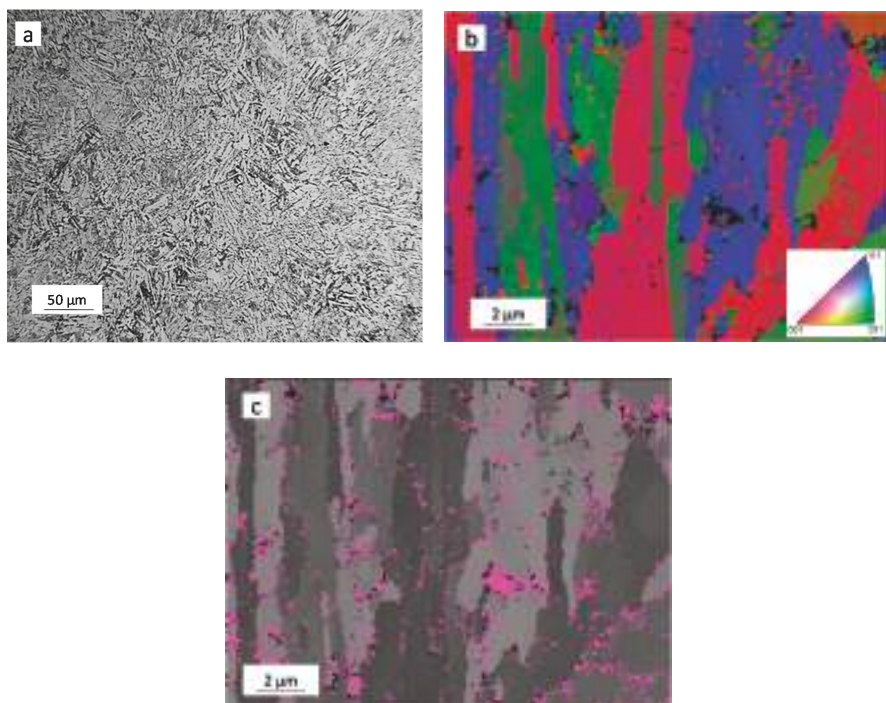


Figure 5. Representative micrographs of the solution treated sample, (a) revealed by optical microscopy; (b) EBSB orientation image; and (c) phase map highlighting γ -Fe phase (coloured in pink).

The aging behaviour of the SLM-treated 18-Ni 300 steel was first investigated by DSC analyses. A comparative study between samples cut from the as built and from solution treated materials, shown in Figure 6a, allowed to state that the aging sequence for these two tempers was substantially equivalent. Both DSC curves exhibited four peaks. The first exothermic peak (peak #1) is believed to be produced by the formation of carbide or coherent precipitation zones, whereas the second exothermic peak (peak #2) is usually associated in the literature to the formation of the main strengthening precipitates, namely the Ni_3Ti phase followed by Fe_2Mo or Fe_7Mo_6 [1–4,19]. The endothermic peaks (peaks #3 and #4) are likely due to the austenite reversion and to the dissolution of precipitates [4,19].

Isothermal aging treatments were carried out at selected temperatures on both the as-built and the solution-treated samples to evaluate possible differences in the achievable strength. In Figure 6b the hardness evolution during aging at 490 °C is reported. The solution annealing leads to a hardness drop from 371 HV to 279 HV which is believed to be due to stress relieving effects and to slight coarsening of the microstructure. However, this gap in hardness is readily bridged after only 30 min of aging. Thereafter, the hardness of the two samples remains comparable for all of the aging times considered here, in full agreement with observations derived from the DSC results.

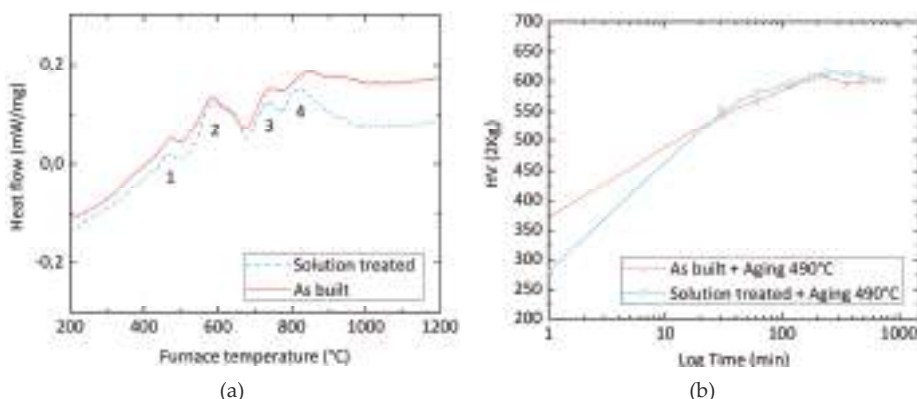


Figure 6. DSC scans at a heating rate of 20 °C/min comparing the aging behaviour of as-built and solution-treated samples (a). Hardness evolution of the two corresponding samples during isothermal holding at 490 °C (b).

Isothermal aging curves collected starting from as built samples are depicted in Figure 7. The expected strengthening trend as a function of aging time is revealed for all of the investigated temperatures. Peak aging times can be identified as: 10 min, 1 h, 4 h, and 8 h for the temperatures of 600, 540, 490, and 460 °C, respectively. Marked over-aging effects (i.e., sharp hardness drop once the peak hardness time is exceeded) were observed for the highest temperature levels (540 and 600 °C), while over-aging at 460 and 490 °C only led to moderate loss in hardness.

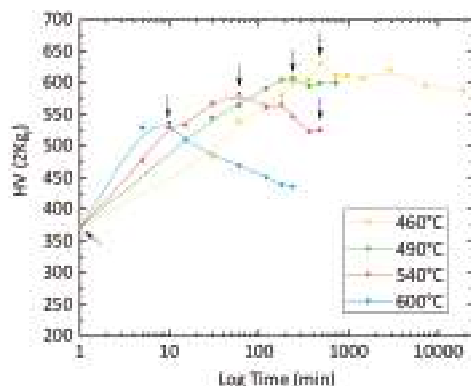


Figure 7. Vickers hardness vs. aging time of as-built samples collected at different aging temperatures. Samples selected for further analyses are marked with arrows.

Based on the above results, further analyses on mechanical behaviour were focussed on samples aged to their peak hardness conditions at the different aging temperatures. An additional condition was selected by over-aging for 8 h at 540 °C. This temper allows comparisons to be made with a 600 °C peak-aged sample (comparable hardness but different aging times) and a 460 °C peak-aged sample (same aging time but different resulting hardness).

Since holding at temperatures exceeding 500 °C is expected to promote extensive reversion of martensite into austenite in wrought maraging steels [1,3,5–9], XRD and microstructural analyses were carried out to assess phase balance in the investigated samples. Figure 8 summarizes the XRD spectra

acquired from samples treated according to different aging conditions, while quantitative evaluation of the γ -Fe phase fraction is reported in Table 2. A marked increase in austenite content is induced by aging. Further slight decomposition of martensite could be achieved by also increasing the aging temperature and by extensively over-aging the samples (e.g., aging 8 h at 540 °C).

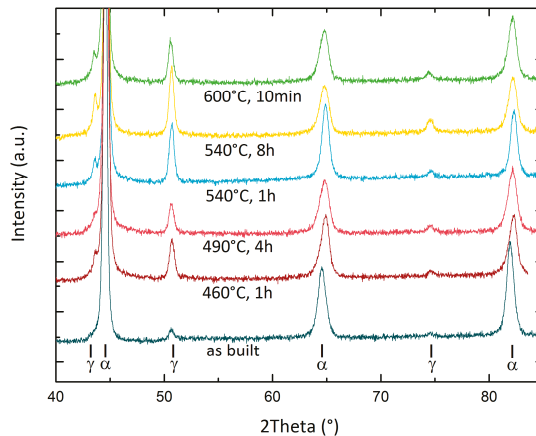


Figure 8. XRD spectra of the 18-Ni 300 steel as a function of aging condition.

Table 2. Austenite (γ -Fe) fraction and corresponding tensile properties as a function of aging temper. Standard deviation of data is also given in brackets.

Condition	γ -Fe Fraction (%)	YS (MPa)	UTS (MPa)	Elongation (%)
as built	11.38 (1.02)	914.9 (12.5)	1187.6 (10.4)	6.14 (1.33)
460 °C 8 h	15.55 (0.73)	1956.8 (43.3)	2017.1 (57.7)	1.51 (0.20)
490 °C 4 h	16.12 (0.57)	1793.3 (96.5)	1814.6 (95.1)	1.20 (0.13)
540 °C 1 h	17.17 (0.68)	1870.3 (53.8)	1956.9 (54.2)	2.07 (0.32)
540 °C 8 h	21.30 (0.77)	1545.9 (103.1)	1655.5 (87.5)	1.77 (0.05)
600 °C 10 min	17.15 (0.68)	1557.2 (140.4)	1659.1 (119.4)	1.60 (0.09)

The measured modifications also reflected into changes of the observed microstructure. In Figure 9, a collection of representative SEM micrographs is given. On aging, an increased amount of austenite (bright constituent in Figure 9) decorating cell boundaries became visible while over-aging additionally promoted precipitation of austenite at intragranular sites (Figure 9d,f).

Table 2 also summarizes the main average data collected by room temperature tensile tests. Low-temperature aging promotes a dramatic increase in strength over the as built condition. The yield strength improved from 915 MPa of the as built steel to 1957 and 1793 MPa for samples peak-aged at 460 and 490 °C, respectively. Conversely, fracture elongation underwent a drop from 6.1% to 1.5% and 1.2% for the same materials. The ultimate tensile strength (UTS) and 0.2% yield strength (YS) given in Table 2 for standard peak aging at 490 °C are substantially consistent with specifications for wrought products (e.g., ASTM A 538, AMS 6514, and MIL-S-46850 standards) and in good agreement with literature data on SLMed type 300 maraging steel [10]. Tensile ductility values between 1.2% and 2.1% were recorded from tests, irrespective of aging temperature and resulting austenite fraction. The poor fracture elongation of SLMed specimens after peak aging is also consistent with literature [10]. Figure 10 reports the tensile curves of samples peak aged at 460 °C and of as built samples to highlight the dramatic differences in tensile behaviour between these two conditions.

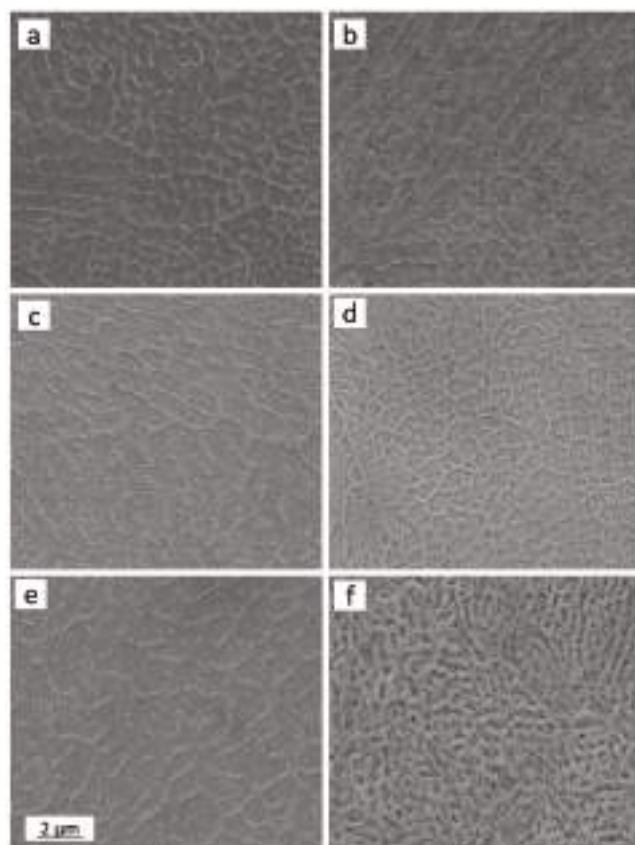


Figure 9. Microstructure (top view) of SLM processed 18-Ni 300 alloy samples aged at different temperatures and times. (a) 460 °C 8 h; (b) 490 °C 4 h; (c) 540 °C 1 h; (d) 540 °C 8 h; (e) 600 °C 10 min; and (f) 600 °C 4 h.

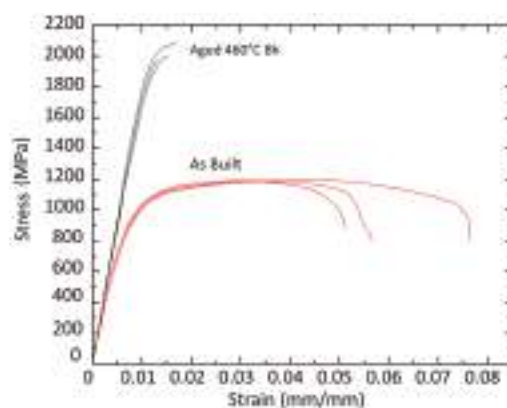


Figure 10. Tensile curves of as built and peak aged 18-Ni 300 steel.

Analysis of the fracture surfaces of broken tensile specimens clearly showed that fracture of the as-built samples was based on a ductile-type failure mechanism consisting in void nucleation, growth and their coalescence. Larger voids mainly originated from pre-existing defects, such as unmelted powder particles (see spherical particles in Figure 11a), splats (larger remelted particles that are blown away from the molten pool and are then engulfed into the following layers), cavities originated by incomplete melting between adjacent tracks. Peak aged samples (Figure 11b) featured similar fracture nucleation sites but the development of cracks was mainly ruled by a quasi-cleavage decohesion mechanism, presumably across the martensite blocks (compare Figures 5 and 11b).

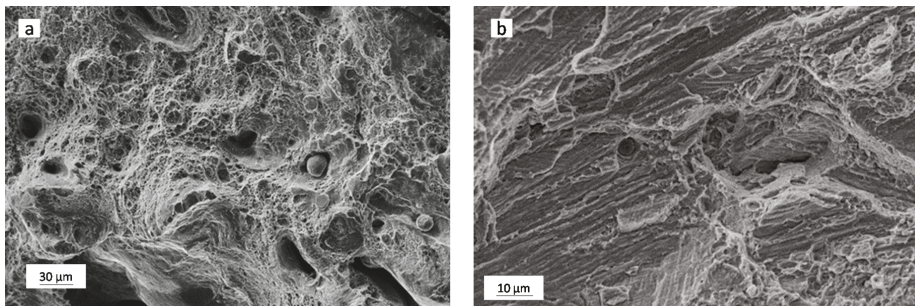


Figure 11. Fracture surfaces of broken tensile specimens: (a) as-built sample; and (b) 460 °C peak-aged sample.

Additional information about development of cracks under tension can be drawn by observing longitudinally-sectioned specimens close to the fracture line, as shown in Figure 12. The low magnification image (Figure 12a) allows one to highlight the growth of relatively large cracks starting from boundaries of adjacent laser tracks, whereas, from higher magnification views (Figure 12b), it can be suggested that the presence of reversed austenite located at boundaries of cells does not play a crucial role on fracture process.

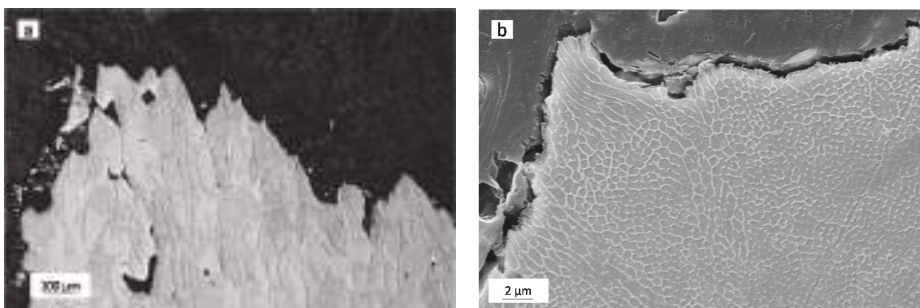


Figure 12. Low-magnification views of longitudinally-sectioned broken tensile specimens close to the fracture line. (a) As-built sample, optical image; and (b) 460 °C peak-aged sample, SEM image.

4. Discussion

Wrought maraging steels are usually aged after a solution treatment carried out at high temperature to homogenize the microstructure inherited from previous operations and to fully transform it into martensite on cooling. Even though it is stated that martensite can form even after moderate cooling rates, in published research works either water cooling [2,4] or air cooling [5,8]

were adopted. From the present results (DSC scans and evolution of hardness during isothermal aging) it can be inferred that the solidification and cooling rates induced by SLM processing are fast enough to preserve the full aging potential of the 18-Ni 300 maraging alloy without any need to perform an additional post-SLM solution treatment. This result is in full agreement with the research work published by Jägle and coauthors [6]. By atom probe tomography, these researchers were able to show that, in a Co-containing maraging steel similar to the present alloy, no precipitates or clusters of atoms were present in the SLM as-built state, even considering that each layer had been subjected to significant reheating during the layer-by-layer manufacturing process.

Further literature referred to welding of a wrought 18-Ni 250 grade maraging steel [18] also reports that, in the absence of high-temperature homogenizing treatments, the as-welded microstructure might contain segregation of Mo and Ti at cell boundaries. Especially, Mo can enhance the reversion rate of martensite into austenite on aging due to early formation of Fe_2Mo , resulting in local enrichment in Ni of the matrix. Molinari et al. [19] also claimed that aging and austenite reversion is accelerated by enhanced density of structural defects in maraging steel processed by spark plasma sintering. A similar effect is expected to be active also in the rapidly solidified samples here investigated. Microstructure observations (Figure 9) confirmed that austenite reversion on aging first occurred at cell boundaries and only on over-aging (8 h at 540 °C and 4 h at 600 °C) intracellular austenite could appear.

Reversion of austenite during aging in wrought alloys can be used to tune ductility and fracture toughness. Viswanathan and co-workers [8], by investigating a wrought 18-Ni 350 maraging steel, stated that reversed austenite causes a decrease in yield strength and ultimate tensile strength but it is beneficial to tensile ductility and impact toughness in the initial stages of over-aging. The same authors also investigated the morphology of reversed austenite formed at different stages of over-aging. It is to remark that in the wrought alloy, austenite appeared both as submicrometric-size precipitates at boundaries of martensite blocks and as much coarser intragranular pockets, around five micrometres in size.

In the SLMed samples of the present investigation, retained austenite was already found in as-built samples and further precipitated, mainly at boundaries of cells, in a very dispersed form on aging. It can be reasonably supposed that their tiny size and fine dispersion, as opposed to the micrometric pocket-like phases found in wrought alloys, is such to avoid a substantial toughening action as crack arrester phase.

Finally, it is to remark that the austenite reversion was stimulated in the present investigation by prolonged aging treatments (i.e., over-aging). However, the progression of aging generates a number of combined effects that have to be carefully analysed before drawing any conclusion about the present results. Aging mainly promotes: (i) the reversion of martensite into softer austenite; (ii) the formation of strengthening precipitates; (iii) the coarsening of precipitates and embrittlement of alloy on over-aging.

The combined effects of age hardening and softening induced by formation of reversed austenite in the investigated SLMed alloy can be better analysed by replotted the full dataset of tensile properties, as shown in Figure 13. The inverse relation between yield strength and tensile ductility is readily observed in Figure 13a where clustering of the data points into two distinct regions is also noticed. A first group of data referred to aged samples is visible on the top left corner of the plot, while the three data points pertaining to as built samples are displayed on the right side of the plot, showing moderate strength levels, but higher tensile ductility.

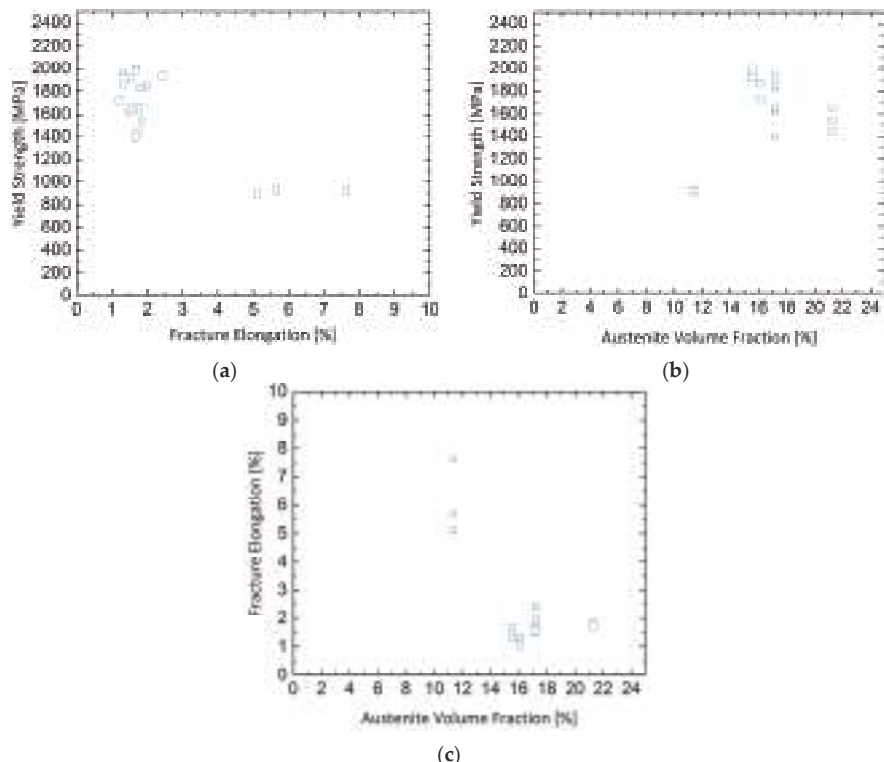


Figure 13. Relation between 0.2% yield strength, tensile elongation at fracture, and austenite volume fraction for the SLM processed 18-Ni 300 steel.

Both fracture elongation and yield strength can then be independently plotted as a function of austenite volume fraction, as depicted in Figure 13b,c, respectively. These figures highlight an unexpected trend considering that austenite can act, in principle, as a soft and more ductile constituent in steel microstructures. These results remark an important difference brought by the peculiar microstructural features generated by SLM processing with respect to the microstructure found in wrought products. Indeed, the highest yield strength and lower tensile elongation found for peak-aged samples (that also feature higher fractions of austenite) over the as-built condition are believed to be mainly due to the overwhelming effect of strengthening precipitates, whereas the concurrent reversion of the γ -Fe phase seems to play a minor role.

5. Conclusions

A study was undertaken to investigate the effects of selective laser melting on 18-Ni 300 maraging steel microstructure and mechanical behaviour. The main conclusions can be summarized as follows:

A submicrometric cellular microstructure was detected in the as-built samples. Evidence of epitaxial growth across different laser tracks was revealed. After high-temperature solution annealing, the traces of solidification were lost and the cellular structure was replaced by fairly coarse martensite blocks. Small fraction of austenite were preferentially located at block boundaries.

A comparison about the aging behaviour of the as-built and the solution-treated alloy revealed that the precipitation sequence during aging and hardness evolution are substantially equivalent.

X-ray diffraction and microstructural observation showed that aging also promotes a partial reversion of martensite into austenite. A shift to higher aging temperatures and over-aging further increased the amount of γ -Fe phase.

Different aging temperatures were selected to evaluate tensile performance of the peak-aged and over-aged samples as a function of the amount of reversed austenite. The results showed that aging promotes a dramatic increase in strength over the as built condition, but also a drop in tensile ductility. Among aged and over-aged samples, no systematic changes were found in tensile properties as a function of measured austenite.

It is suggested that, as opposed to the trend expected in corresponding wrought maraging alloys, the submicrometric structure inherited by the rapid solidification condition brought by selective laser melting are such that changes in tensile strength and ductility are mainly governed by the effects given by the strengthening precipitates, whereas the concurrent reversion of the γ -Fe phase seems to play a minor role.

Acknowledgments: The financial support of Regione Lombardia (Bando Creatività Linea 2, AddMe.Lab project) is acknowledged.

Author Contributions: R.C. and J.N.L. performed the experiments. A.T. contributed to XRD analysis and discussion of results. R.C. and M.V. wrote the paper. M.V. supervised the project.

Conflicts of Interest: The authors declare no conflicts of interest.

References

- Pardal, J.M.; Tavares, S.S.M.; Terra, V.F.; da Silva, M.R.; dos Santos, D.R. Modeling of precipitation hardening during the aging and overaging of 18Ni-Co-Mo-Ti maraging 300 steel. *J. Alloy. Compd.* **2015**, *393*, 109–113. [CrossRef]
- Sha, W.; Cerezo, A.; Smith, G.D.W. Phase Chemistry and Precipitation Reactions in Maraging Steels: Part I. Introduction and Study of Co-Containing C-300 Steel. *Metall. Trans. A* **1993**, *24A*, 1221–1232. [CrossRef]
- Pardal, J.M.; Tavares, S.S.M.; Fonseca, M.P.C.; Abreu, H.F.G.; Silva, J.J.M. Study of the austenite quantification by X-ray diffraction in the 18Ni-Co-Mo-Ti maraging 300 steel. *J. Mater. Sci.* **2006**, *41*, 2301–2307. [CrossRef]
- Guo, Z.; Sha, W.; Li, D. Quantification of phase transformation kinetics of 18 wt. % Ni C250 maraging steel. *Mater. Sci. Eng. A* **2004**, *373*, 10–20. [CrossRef]
- Tewari, R.; Mazumder, S.; Batra, I.S.; Dey, G.K.; Banerjee, S. Precipitation in 18 wt. % maraging steel of grade 350. *Acta Mater.* **2000**, *48*, 1187–1200. [CrossRef]
- Jägle, E.A.; Choi, P.P.; van Humbeeck, J.; Raabe, D. Precipitation and austenite reversion behavior of a maraging steel produced by selective laser melting. *J. Mater. Res.* **2014**, *29*, 2072–2079. [CrossRef]
- Li, X.; Yin, Z. Reverted austenite during aging in 18Ni (350) maraging steel. *Mater. Lett.* **1995**, *24*, 239–242. [CrossRef]
- Viswanathan, U.K.; Dey, G.K.; Sethumadhavan, V. Effects of austenite reversion during overageing on the mechanical properties of 18 Ni (350) maraging steel. *Mater. Sci. Eng. A* **2005**, *398*, 367–372. [CrossRef]
- Tavares, S.S.M.; Abreu, H.F.G.; Neto, J.M.; da Silva, M.R.; Popa, I. A thermomagnetic study of the martensite-austenite phase transition in the maraging 350 steel. *J. Alloy. Compd.* **2003**, *358*, 152–156. [CrossRef]
- Kempen, K.; Yasa, E.; Thijss, L.; Kruth, J.-P.; van Humbeeck, J. Microstructure and mechanical properties of Selective Laser Melted 18Ni-300 steel. *Phys. Proc.* **2011**, *12*, 255–263. [CrossRef]
- Casalino, G.; Campanelli, S.L.; Contuzzi, N.; Ludovico, A.D. Experimental investigation and statistical optimization of the selective laser melting process of a maraging steel. *Opt. Laser Technol.* **2015**, *65*, 151–158. [CrossRef]
- Croccolo, D.; de Agostinis, M.; Fini, S.; Olmi, G.; Vranic, A.; Ciric-Kostic, S. Influence of the build orientation on the fatigue strength of EOS maraging steel produced by additive metal machine. *Fat. Fract. Eng. Mater. Struct.* **2016**. [CrossRef]
- Murr, L.E.; Martinez, E.; Amato, K.N.; Gaytan, S.M.; Hernandez, J.; Ramirez, D.A.; Shindo, P.W.; Medina, F.; Wicker, R.B. Fabrication of metal and alloy components by additive manufacturing: Examples of 3D materials science. *J. Mater. Res. Technol.* **2012**, *1*, 42–54. [CrossRef]

14. Frazier, W.E. Metal additive manufacturing: A review. *J. Mater. Eng. Perform.* **2014**, *23*, 1917–1928. [CrossRef]
15. Gu, D.D.; Meiners, W.; Wissenbach, K.; Poprawe, R. Laser additive manufacturing of metallic components: Materials, processes and mechanisms. *Int. Mater. Rev.* **2012**, *57*, 133–164. [CrossRef]
16. Casati, R.; Lemke, J.; Vedani, M. Microstructure and Fracture Behavior of 316L Austenitic Stainless Steel Produced by Selective Laser Melting. *J. Mater. Sci. Technol.* **2016**. [CrossRef]
17. Bauereiß, A.; Scharowsky, T.; Körner, C. Defect generation and propagation mechanism during additive manufacturing by selective laser melting. *J. Mater. Process. Technol.* **2014**, *214*, 2522–2528. [CrossRef]
18. Shamaantha, C.R.; Narayanan, R.; Iyer, K.J.L.; Radhakrishnan, V.M.; Seshadri, S.K.; Sundararajan, S.; Sundaresan, S. Microstructural changes during welding and subsequent heat treatment of 18Ni (250-grade) maraging steel. *Mater. Sci. Eng.* **2000**, *A287*, 43–51. [CrossRef]
19. Menapace, C.; Lonardelli, I.; Molinari, A. Phase transformation in a nanostructured M300 maraging steel obtained by SPS of mechanically alloyed powders. *J. Therm. Anal. Calorim.* **2010**, *101*, 815–821. [CrossRef]



© 2016 by the authors. Licensee MDPI, Basel, Switzerland. This article is an open access article distributed under the terms and conditions of the Creative Commons Attribution (CC BY) license (<http://creativecommons.org/licenses/by/4.0/>).

Article

A Lightweight Structure Redesign Method Based on Selective Laser Melting

Li Tang, Chunbing Wu *, Zhixiong Zhang, Jianzhong Shang and Chao Yan

College of Mechatronics and Automation, National University of Defense Technology, Changsha 410073, China; tangli@nudt.edu.cn (L.T.); zxxnudt2010@sina.com (Z.Z.); jz_shang_nudt@163.com (J.S.); mech_yan@foxmail.com (C.Y.)

* Correspondence: wuchunbing14@nudt.edu.cn; Tel.: +86-155-7086-4869

Academic Editor: Manoj Gupta

Received: 10 September 2016; Accepted: 1 November 2016; Published: 16 November 2016

Abstract: The purpose of this paper is to present a new design method of lightweight parts fabricated by selective laser melting (SLM) based on the “Skin-Frame” and to explore the influence of fabrication defects on SLM parts with different sizes. Some standard lattice parts were designed according to the Chinese GB/T 1452-2005 standard and manufactured by SLM. Then these samples were tested in an MTS Insight 30 compression testing machine to study the trends of the yield process with different structure sizes. A set of standard cylinder samples were also designed according to the Chinese GB/T 228-2010 standard. These samples, which were made of iron-nickel alloy (IN718), were also processed by SLM, and then tested in the universal material testing machine INSTRON 1346 to obtain their tensile strength. Furthermore, a lightweight redesigned method was researched. Then some common parts such as a stopper and connecting plate were redesigned using this method. These redesigned parts were fabricated and some application tests have already been performed. The compression testing results show that when the minimum structure size is larger than 1.5 mm, the mechanical characteristics will hardly be affected by process defects. The cylinder parts were fractured by the universal material testing machine at about 1069.6 MPa. These redesigned parts worked well in application tests, with both the weight and fabrication time of these parts reduced more than 20%.

Keywords: 3D printing; selective laser melting (SLM); part redesign; SLM structure performance; frame structure reconstruction

1. Introduction

There is an increasing demand for lightweight parts in the aerospace, automotive, medical industries and other fields with good mechanical characteristics and shorter manufacturing times. However, there are often redundant materials in conventional parts because of the conventional manufacturing processes' inherent restrictions, which make it difficult to get a lightweight component.

Selective laser melting (SLM) is an additive manufacturing (AM) process which can directly make complex three-dimensional metal parts according to Computer Aided Design (CAD) data by selectively melting successive layers of metal powders [1]. It is an alternative to conventional manufacturing processes [2,3]. The tool-less fabrication and geometric freedom offered by SLM show great potential to make advanced lightweight structures and products which are highly desired by engineering sectors. It permits new design methods for lightweight structures that were not possible before because of the limitations of conventional manufacturing processes.

Currently, there are some approaches for lightweight parts design with the use of SLM. Among all of the methods, the design of cellular structures and structure topological optimization are very common.

The cellular structure design method replaces the interior structures of the parts with cellular structures which have relatively less mass than solid material. Cellular structures can be classified into two categories: stochastic porous structures and periodic cellular lattice structures according to the distribution of the internal micro-structure. Stochastic porous structures are filled with open or closed voids that distribute randomly, whereas periodic cellular lattice structures consist of repeating unit cells leading to a uniform structure. Because of the uneven distribution of materials, periodic lattice structures show finer mechanical characteristics than stochastic porous structures when they have the same volume fraction [4,5]. A few previous works have been done to study the manufacturing of lightweight cellular structures with the use of SLM. Campanelli et al. [6] investigated a lattice structure comprised of four vertical strut columns and four pairs of struts. This structure was made by SLM using titanium alloy Ti6Al4V. A campaign was planned to compare the behavior of the lattice structure with variable cells, truss sizes and vertical bars as reinforcements. They used Taguchi's method to minimize the number of experiments. Compression tests were performed to study the mechanical behavior of the lattice structures. They demonstrated that when the cell size is smaller, and the size of the strut edge and the relative density are the highest, this structure shows the highest strength. Wang et al. [7] investigated the design rules and the key points to fabricate porous structures. Thin walls, cylinders with different geometrical dimensions and overhanging structures with different inclined angles were designed and fabricated to obtain the SLM fabricating resolution and the critical inclined angle for designing the porous structures. The experiments for fabricating porous structures with different sizes were also conducted. The results showed that the porous structure can be well fabricated by SLM.

Hernandez et al. [8] researched the micro-structure and dimensional accuracy of the as-manufactured lattices with the same morphology with the exception of the strut diameter, which was varied systematically. They found that the variation in the compressive yield stress with the strut diameter is in good accordance with simple models based on compressive deformation rather than shearing or buckling. Besides, struts normal to the build direction showed more significant defects. To examine the effect of cellular lattice structures on the strength of parts, Mahshid et al. [9] analyzed the collapse strength of lattice structures by finite element (FE) and mathematical models. Compression tests of the solid, hollow, non-rotated-closed-cellular and rotated-closed-cellular samples were performed. The results showed that the cellular structures heavily influence the compression strength and showed only an increase of 11.4% at the highest point with respect to hollow specimens.

Sing et al. [10] investigated the dimensional accuracy and compressive behavior of cellular lattice structures with different unit cell types, namely the square pyramid, truncated cube and octahedron unit cells. Analysis of variance (ANOVA) was also carried out to determine the significance of various process and design parameters on the dimensional accuracy and compressive strength of the lattice structures. They found that the processing parameters, such as laser power and laser scan speed, have no significant effect on the elastic constant but have a significant effect on the powder adhesion on the struts, affecting the dimensional accuracy. However, geometrical design parameters such as the unit cell type and strut diameter have significant effects on the elastic constant but not on the dimensional accuracy of the lattice structures.

These previous works showed that the manufacturability of cellular lattice structures was often affected by the lattice unit size. Besides, the mechanical characteristics of lattice micro-structures are always affected by manufacturing defects, especially when the unit size is very small.

Another common method of lightweighting is the use of structure topological optimization. This design method generates an optimized material distribution for particular purposes by minimizing a suitable objective within the limited space. Some previous works have investigated this method to take advantage of the SLM process. Brandt et al. [11] studied the design, manufacture and examination of high-value aerospace components and investigated the geometric optimization of the aerospace bracket from Ti-6Al-4V alloy. Xiao et al. [12] examined the design and fabrication of bio-material scaffolds using topological optimization with the SLM process. An optimization procedure was

proposed to seek a micro-structure of maximum stiffness with the constraint of volume fraction optimization. The inverse homogenization theory was also applied to estimating the effective mechanical properties of scaffold materials which are arrayed by periodical base cells.

However, the structure topological optimization will always change the shape of the components. The shape of parts should not change, especially when the parts are assembled with other traditional components or should meet the requirements of aerodynamics.

This paper investigates a new design method for lightweight parts manufactured by selective laser melting (SLM) based on the “Skin-Frame” and explores the influence of machining defects on SLM parts which have different sizes by the experimental method. The procedures of the novel, lightweight redesign method were researched. A stopper and connecting plate were redesigned with this method. These redesigned parts were fabricated by SLM and showed good mechanical characteristics. The results show that the lightweight parts designed by this method can satisfy the use requirements.

2. Experimental Section

2.1. Materials

The lattice structures and tensile test samples were made from an iron-nickel alloy (IN718) powder with an average particle size of $30 \pm 10 \mu\text{m}$. The chemical composition of the powder consists of Ni (53.5%), Cr (19%), Fe (18.3%), Nb (5%), Mo (3% max), Ti (1% max), Al (0.43% max). The SEM micro-graph of the IN718 powder is shown in Figure 1. It has good mechanical characteristics and is widely used in aerospace industry. All samples for this study were manufactured by EOSINT M280 system which utilized a 200 W ytterbium fiber laser. This machine has an effective building volume of $250 \text{ mm} \times 250 \text{ mm} \times 325 \text{ mm}$. Tensile candidates were fabricated in a vertical build orientation, with the cylinder axis parallel to the beam direction.

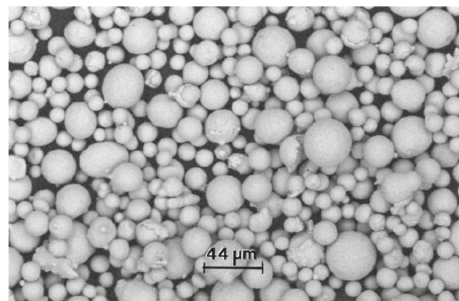


Figure 1. SEM micro-graph of the IN718 powder.

The 100 μm diameter laser beam was scanned at 1200 mm/s in argon gas environments surrounding the building parts. The oxygen level in the process chamber was maintained below 0.1%. The building platform was preheated to 80 $^{\circ}\text{C}$ and maintained at that temperature. The hatch spacing was 0.05 mm and the layer thickness was 50 μm with a spot diameter of 0.1 mm.

2.2. Process of Tensile Test

Tensile samples were designed according to the Chinese GB/T 228-2010 standard. Figure 2 shows the sizes of samples for the tensile experiment. The diameter of parts is 10 mm while the rest of the parameters depend on the test machine. The samples were designed by CAD software then exported as a single STL file format to the SLM machine for manufacturing.

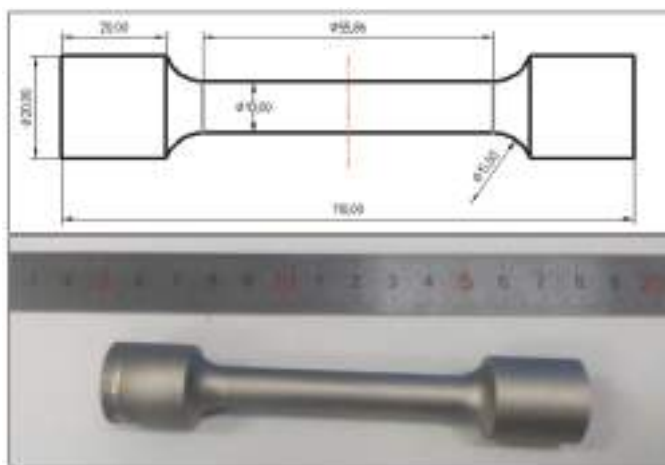


Figure 2. Dimensions of the tensile test sample.

The experiments were performed in the universal material testing machine INSTRON 1346 (Instron, Norwood, MA, USA) at room temperature with a loading speed of $0.008 \text{ mm}\cdot\text{s}^{-1}$. The strain rate is approximately $1 \times 10^{-3} \text{ s}^{-1}$. The maximum load of this machine is 2000 KN with a loading accuracy of $\pm 5\%$. The samples were clamped on the machine and the load was gradually increased until the samples were fractured to get their tensile curve. The tensile strength and other properties can be calculated by Equation (1) and the tensile curve:

$$\sigma = \frac{P}{S} \quad (1)$$

where σ is the section stress, P and S are the maximum load and section area, respectively.

$$\varepsilon = \frac{L - L_0}{L_0} \quad (2)$$

The elongation percentage ε can be calculated by initial length L_0 and fracture length L .

2.3. Compression Test of Lattice Structure

Compression test candidates were designed according to the Chinese GB/T 1452-2005 standard. The compression samples have the sandwich construction with 16 cylinder units in the middle. The height of a cylinder unit is 15 mm and the thickness of the panels is 1 mm with a parallelism tolerance of 0.1 mm.

Because of the thermal stress brought by the temperature difference during the SLM process, the warping deformation of thin-walled parts such as the panel will always occur as shown in Figure 3a. The deformation will have an impact on the dimensional accuracy and structural properties of the parts. So the samples were produced by the SLM process with additional skin on the vertical direction to avoid large deformation and get a higher parallelism tolerance as shown in Figure 3b. The additional skin was cut by wire-electrode cutting as shown in Figure 3c.



Figure 3. Large curling of direct manufacturing candidate (a), small curling of sample fabricated with additional skin after wire-electrode cutting (b) and sample fabricated with additional skin (c).

The diameters of the cylinders are 0.5 mm, 1.0 mm, 1.5 mm, 2.0 mm, 2.5 mm, respectively as shown in Figure 4. The compression tests were performed in the MTS Insight 30 compression testing machine (MTS, Minneapolis, MN, USA) at room temperature with a loading speed of 0.05 mm s^{-1} . The control strategy is Posn. The samples were tested in a constant loading speed in this strategy. The maximum load of this machine is 30 KN with a loading accuracy of $\pm 5\%$. This experiment was recorded by a camera to help to study the trends of yield process of different structure sizes.



Figure 4. Compression test samples with different parameters.

3. Lightweight Parts Redesign Method

This method disassembled parts by its shape and force condition and reconstructed the inner structure of each divided one by corresponding the framework structure which was optimized by the finite element method, and then mixed them together with the main framework. Optimized foundation frameworks can be reserved to build the framework library, which can greatly shorten the design time using this method. The basic flow of this approach is shown in Figure 5.

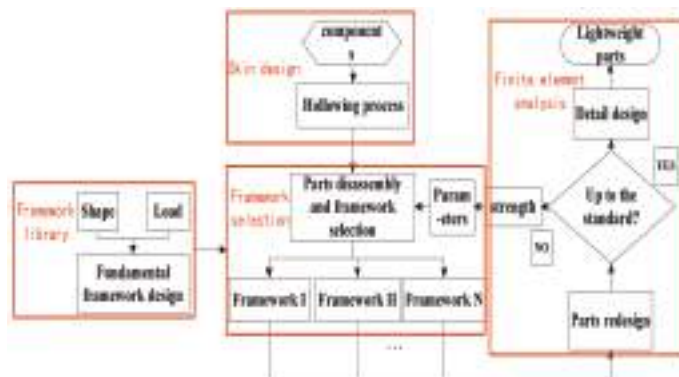


Figure 5. Flow chart of lightweight redesign method.

The main steps include three aspects as follows:

1. Design of the skin

A suitable skin thickness of the components is necessary to maintain the shape of parts. This paper studied the strain and stress of parts with different skin thicknesses and loads.

2. Parts disassembly and framework design

The components were disassembled by their shape and force conditions. Different optimized frameworks were selected from the framework library or were newly designed to fill the disassembled parts. These newly designed frameworks can be reserved at the framework library by their shape and load. Use of the framework library can greatly shorten the design period compared with topology optimization of the whole part. The design of new parts can be as easy as selecting fundamental frameworks to fill the parts.

3. Finite element analysis and details of parts

We assembled the divided parts together by their topology structure and study the characteristics of components using the finite element method. Improve the details such as the metal outlet position of the metal powder according to the SLM process.

3.1. Design of Skin

The quality of thin-wall parts manufactured by the SLM process will be affected by their thickness. The thicker the thin-wall parts are, the better the quality will be. However, thick walls will bring about a higher weight of the components, which makes it difficult to get lightweight parts. The optimum thickness of the skin was studied by the finite element analysis of an empty cube with different loads and wall thicknesses as shown in Figure 6.

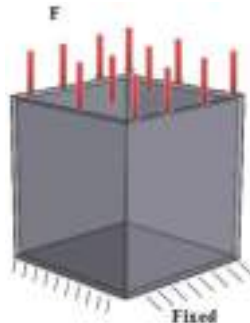


Figure 6. Model of thin-wall parts for finite element analysis.

The side length of the cube is 100 mm. The bottom side was fixed and uniform loads of 500 N and 1000 N were applied, respectively, to the top side to test the mechanical performance of different thin walls under various loads. The results of the finite element analysis are reported in Table 1 and Figures 7 and 8.

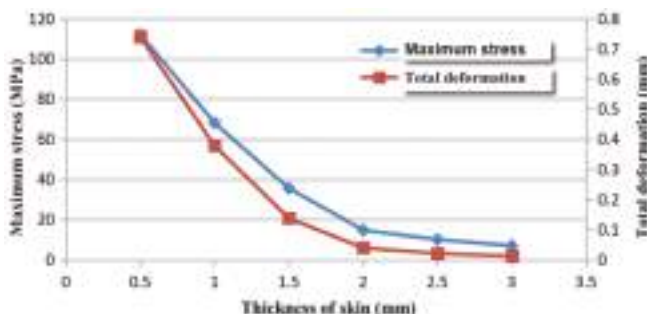
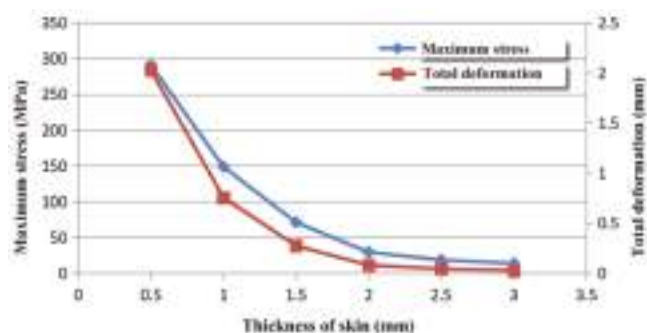
Table 1. Analysis result of thin-wall parts with different thicknesses and loads.

Thickness (mm)	Load (N)	Maximum Stress (MPa)	Maximum Strain (mm)	Weight (g)
0.5	500	112.4	0.73937	238
	1000	290.75	2.028	
1	500	68.054	0.37832	470
	1000	148.36	0.75461	
1.5	500	35.469	0.13709	699
	1000	70.939	0.27418	

Table 1. Cont.

Thickness (mm)	Load (N)	Maximum Stress (MPa)	Maximum Strain (mm)	Weight (g)
2	500	14.705	0.039352	922
	1000	29.411	0.078705	
2.5	500	10.02	0.020339	1141
	1000	18.385	0.043148	

It is shown in Figures 7 and 8 that the maximum stress and strain decrease with the increase of the thickness of the skin. The decrease trend becomes gentle when the thickness of the skin is greater than 2 mm. These results allow us to conclude that the most suitable thickness of the skin is 2 mm to obtain a lightweight component produced by the SLM process.

**Figure 7.** Stress and strain of skin under load of 500 N.**Figure 8.** Stress and strain of skin under load of 1000 N.

3.2. Parts Disassembly and Framework Design

The parts can be divided by their force conditions such as the bending moment, torque, tensile, compression, shearing force or a possible combination of them. The shapes of the components also need to be considered. The elementary shapes of the structure include: cuboid, cylinder, ring, sphere, L shape and so on.

Finally, the auxiliary functions of each part should be taken into account. The common assistant functions include: bolt mounting hole, key-way, locations and so on. The parts were disassembled as shown in Figure 9. Each divided one should be redesigned for a lighter structure after the disassembly. The topological optimization of frameworks design was performed using Optistruct software (Altair, Troy, NY, USA). Some typical structures were redesigned as follows.

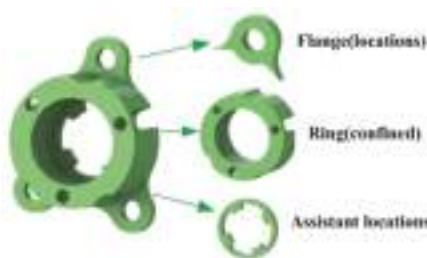


Figure 9. An example of parts disassembly.

3.2.1. Flange Frame with Torque

The flange often bears the torsional moment from its bolt holes. According to the following conditions, the optimal design of the framework of the structure was carried out.

- (1) Objective function: minimum structure mass
- (2) Condition: flange bears torsion load
- (3) Boundary conditions: the bolt holes are fixed and the inner surface of the flange is applied to the torque
- (4) Design space: brown region in graph
- (5) Minimum thickness: 0.006 m
- (6) Design constraints: meeting the strength requirements with minimum mass

According to the topology optimization conditions above, the original part model was defined as shown in Figure 10a. The framework obtained by topology optimization can be seen in Figure 10b. This new structure was taken into ANSYS Workbench to analyze its strength. The stress distribution on the structure became uniform after optimization, as shown in Figure 10c.

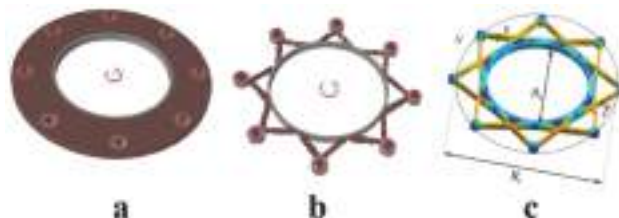


Figure 10. The original flange model (a), flange framework obtained by topology optimization (b), stress distribution of flange frame (c).

The comparison of the stress distribution density before and after optimization is shown in Figure 11. As can be seen from Figure 11, the two structures have the same maximum stress and the average stress of the optimized structure became larger. Thus, the utilization ratio of the structure was improved.

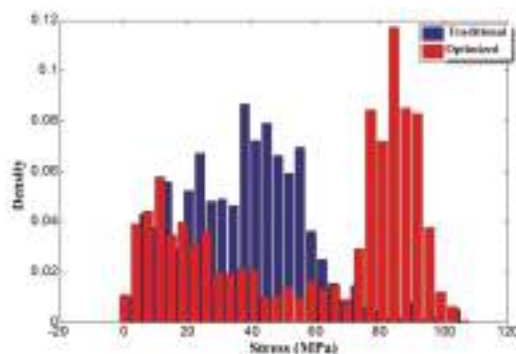


Figure 11. Stress distribution density of traditional and optimized flange.

The main parameters of the flange frame are:

- N: number of mounting holes;
- D_1 : location diameter of mounting holes;
- D_2 : diameter of inner ring;
- ε : thickness of flange;
- ζ : ratio of outer and inner ring;
- γ : thickness of dowel bar;
- μ : equivalent stress;
- M: applied torque;
- σ_s : yield strength of material

The equivalent stress μ can be calculated by following formulas:

$$\mu = \frac{\sigma_s}{MD_2\varepsilon} \quad (3)$$

$$\zeta = \frac{D_1}{D_2} \quad (4)$$

The thickness of the dowel bar γ is variable to get parts with different performances. The structures with different parameters were analyzed by ANSYS Workbench. The analysis results of structures with constant $\zeta = 1.6$ and $N = 12$, respectively, are shown in Figure 12.

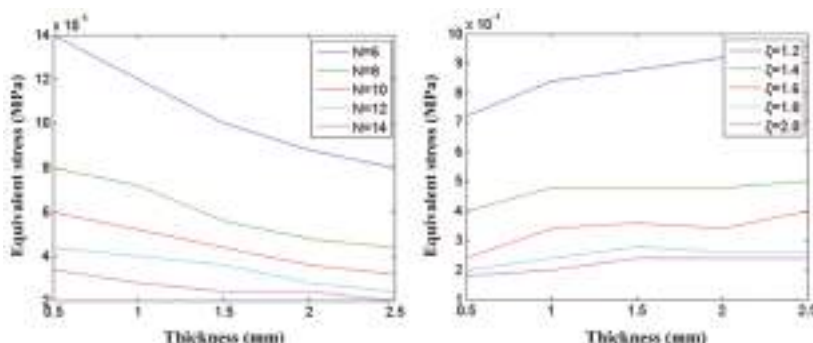


Figure 12. Influence of design parameters on the structural stress of the flange.

3.2.2. Rectangular Frame with Bending Moment

The cuboid applied bending moment was analyzed in this section. According to the following conditions, the optimal design of the framework was carried out.

- (1) Objective function: minimum structure mass
- (2) Condition: cuboid bearing bending load
- (3) Boundary conditions: the left surface is fixed and the right surface is applied to the surface force
- (4) Design space: brown region in graph
- (5) Minimum thickness: 0.006 m
- (6) Design constraints: meeting the strength requirements with minimum mass

According to the topology optimization conditions above, the original part model was defined as shown in Figure 13a. The topology optimization method was used to get the framework shown in Figure 13b. The final structure after optimization can be seen in Figure 13c. The thickness of frame η was taken as a design parameter to get parts with different performances.

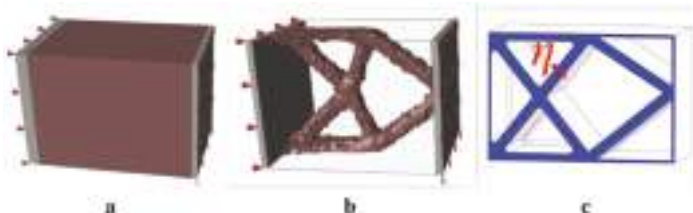


Figure 13. The original cuboid model (a), rectangular frame obtained by topology optimization (b), the final rectangular frame after optimization (c).

3.2.3. Ring Frame with Torque

The bidirectional torsional moment was applied to the ring. The optimal conditions were set as follows.

- (1) Objective function: minimum structure mass
- (2) Condition: inner race bearing torsion load
- (3) Boundary conditions: the outer ring is fixed and the inner race is applied to torque
- (4) Design space: brown region in graph
- (5) Minimum thickness: 0.006 m
- (6) Design constraints: meeting the strength requirements with minimum mass

The traditional part model is shown in Figure 14a. The preliminary framework can be obtained by the topology optimization method as shown in Figure 14b. The final part structure after optimization can be seen in Figure 14c.

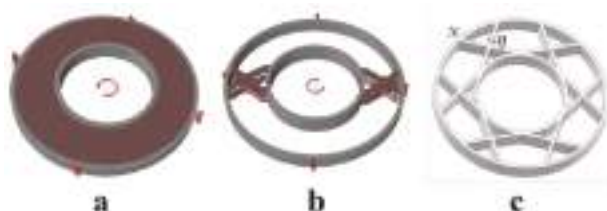


Figure 14. The original ring model (a), ring frame obtained by topology optimization (b), the final ring frame after optimization (c).

The comparison between the stress distribution density of the traditional (Figure 14a) and optimized parts (Figure 14c) is shown in Figure 15. As can be seen from Figure 15, the average stress of the optimized structure became larger. Thus, the efficiency of the structure was improved.

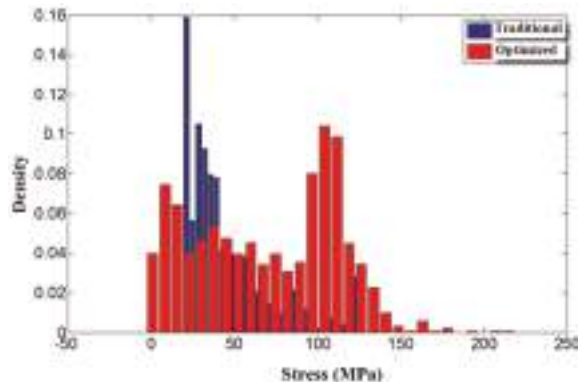


Figure 15. Stress distribution density of traditional and optimized rings.

To get components with different performances, the number of stiffeners N and the thickness of the frame η were taken as design parameters. Figure 16 shows the finite element analysis results which illustrate the influence of the number of stiffeners N and the thickness of frame η on the structure stress. The performance of the structure improved with these two parameters.

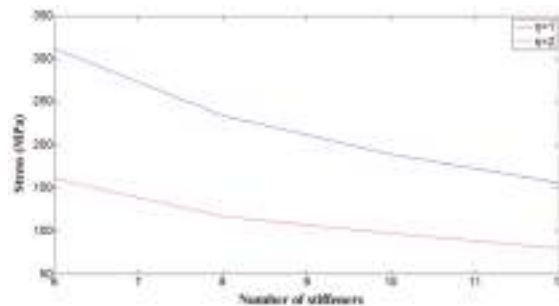


Figure 16. Influence of design parameters on the structural stress of ring.

3.2.4. L-Shape Frame with Bending Moment

The L-shape structure often bears the bending moment. The optimization conditions are defined as follows.

- (1) Objective function: minimum structure mass
- (2) Condition 1: one end is fixed and the other end is applied to the vertical load;
- (3) Condition 2: one end is fixed and the other end is applied to the horizontal load
- (4) Boundary condition: the right boundary is fixed and the left surface is applied to the surface force
- (5) Design space: brown region in graph
- (6) Minimum thickness: 0.006 m
- (7) Design constraints: meeting the strength requirements with minimum mass

According to the topology optimization conditions above, the original part model was defined as shown in Figure 17a. The topology optimization method was used to get the framework shown in Figure 17b. The final structure after optimization can be seen in Figure 17c. The thickness of frame η was taken as a design parameter.

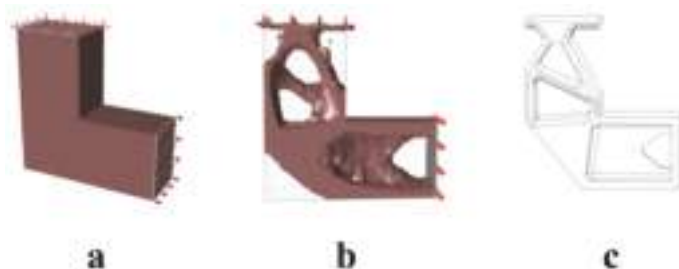


Figure 17. The original L-shape model (a), L-shape frame obtained by topology optimization (b), the final L-shape frame after optimization (c).

3.3. Detail Design

There are some detailed structures such as the fillet, chamfer, keyway, gear teeth, splines, mounting hole and so on which are important when the parts cooperate with other components. To ensure the functions of these structures, they should not be redesigned.

After the reconstruction of the structures, stress concentration may occur because of the sharp change of the cross-section area caused by the intersecting frame. In order to improve the parts' performance, the fillets of the frames need to be considered, which can help to reduce the local stress concentration.

There are still some powders in the closed holes of the redesigned parts manufactured by the SLM process which will increase the weight and cost of the components. Thus, powder outlets should be considered to discharge powders smoothly. The fillets and powder outlets are shown in Figure 18.

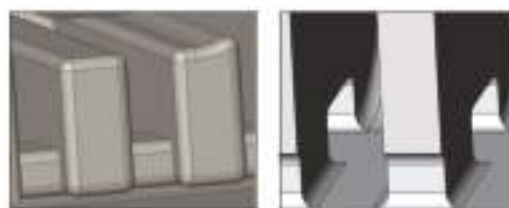


Figure 18. The fillets and powder outlets of SLM parts.

3.4. Application

3.4.1. Case 1: Stopper

The stopper was used in an automatic device to avoid the forward movement of this device. The actual installation and use conditions of this part are shown in Figure 19.

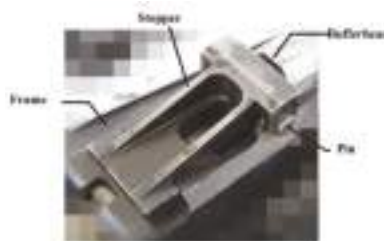


Figure 19. The use conditions of stopper.

According to the design method researched before, the redesign processes of the stopper are shown as follows.

1. Model building and design of the skin

The model can be made by 3D scanning and reverse engineering technology. The optimized thickness of the skin is 2 mm according to the previous work.

2. Stopper structure severing and framework design

The stopper can be divided into four parts by their force conditions and shapes: the L-shape structure with bending moment, the rectangular structure one with bending moment, the rectangular structure two with bending moments, and the thin-wall structure. The framework of each divided part was redesigned by the method studied in Section 3. Then the redesigned stopper was connected by their topological relationship. The reconstruction result is shown in Table 2.

Table 2. Disassembly of stopper.

Number	Design Objects	Shape	Load	Design Parameters	Result
0			Skin	Thickness of skin β	
1		L shape	Bending moment	Thickness of frame λ	
2		Rectangular	Pressure	Thickness of frame η Number of frame N_1	
3		Rectangular	Pressure	Thickness of frame α Number of frame N_2	
4		Thin-wall structure		∞	

3. Finite element analysis and detail design of the stopper

The original and reconstructed stopper models were introduced into ANSYSY Workbench for finite element analysis to show the change of stress distribution. Other detailed designs such as fillets and powder outlets were completed in this stage. The two stoppers have the same maximum stress. In addition, the average stress of the optimized stopper became larger.

A load of 1000 KN was applied to the back surface of the stopper while the boundary conditions were added by its actual conditions. The stress distributions of the stopper with different inner

structures are shown in Figure 20. The stress of the original structure concentrates at a low level, which leads to a waste of material. For the original stopper, the mass is 795.2 g and the maximum stress is 211.52 MPa. The stress distribution level of the redesigned stopper increased to a higher level, which can be seen in Figure 21. The weight of the redesigned stopper decreased to 580.0 g with a weight reduction of about 27%. The maximum stress of the redesigned stopper is only 209.77 MPa.

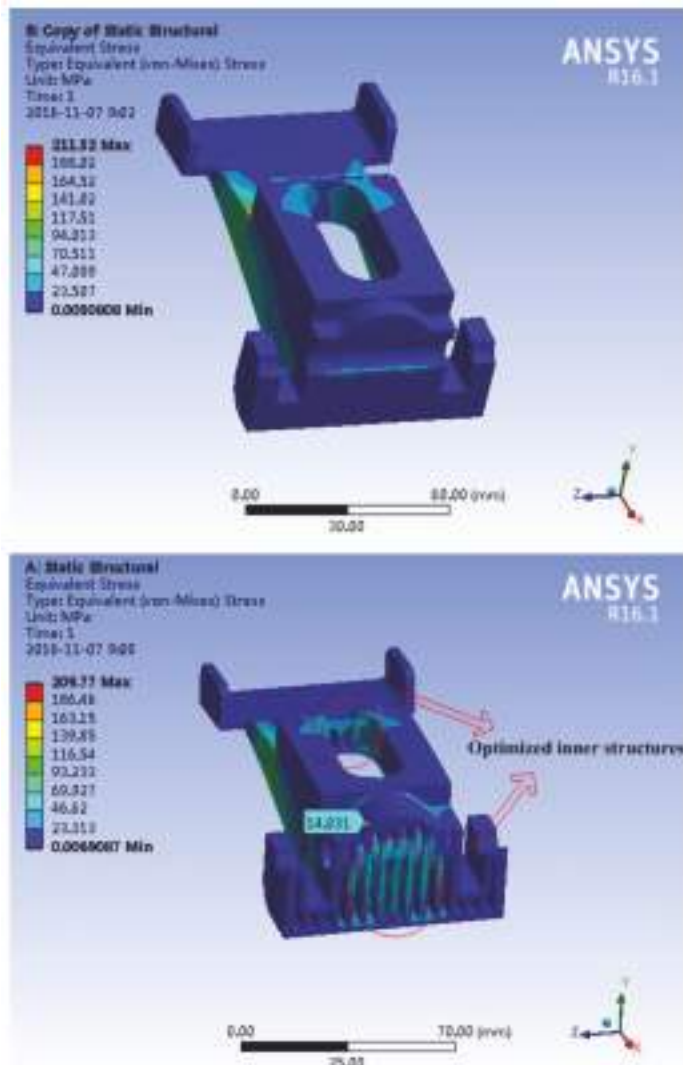


Figure 20. Stress distribution of original (up) and redesigned (down) stopper.

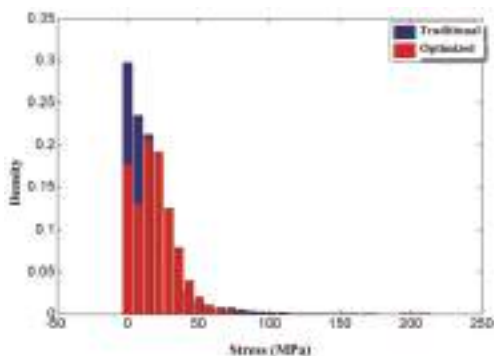


Figure 21. Stress distribution density of traditional and optimized stopper.

3.4.2. Case 2: Connecting Plate

The connecting plate with inner splines is always used to transfer torque between the main step-down gear and side reducer of a heavy tracked vehicle. It connects with the main reducer by bolts and transfers torque by the splines. The actual use conditions of the connecting plate are shown in Figure 22.



Figure 22. The use conditions of the connecting plate.

Similarly, the redesign processes of the connecting plate are as follows.

1. Model building and design of the skin

The model can be made by 3D scanning measuring and reverse engineering technology. The optimized thickness of the skin is 2 mm according to the previous work.

2. Connecting plate structure severing and framework design

The connecting plate can be divided into three parts by their force conditions and shapes: the flange structure with torque, the ring structure with torque and the spline structure. The framework of each divided plate was redesigned by the method studied in Section 3. Then the redesigned connecting plate was connected by their topological relationship. The reconstruction result is shown in Table 3.

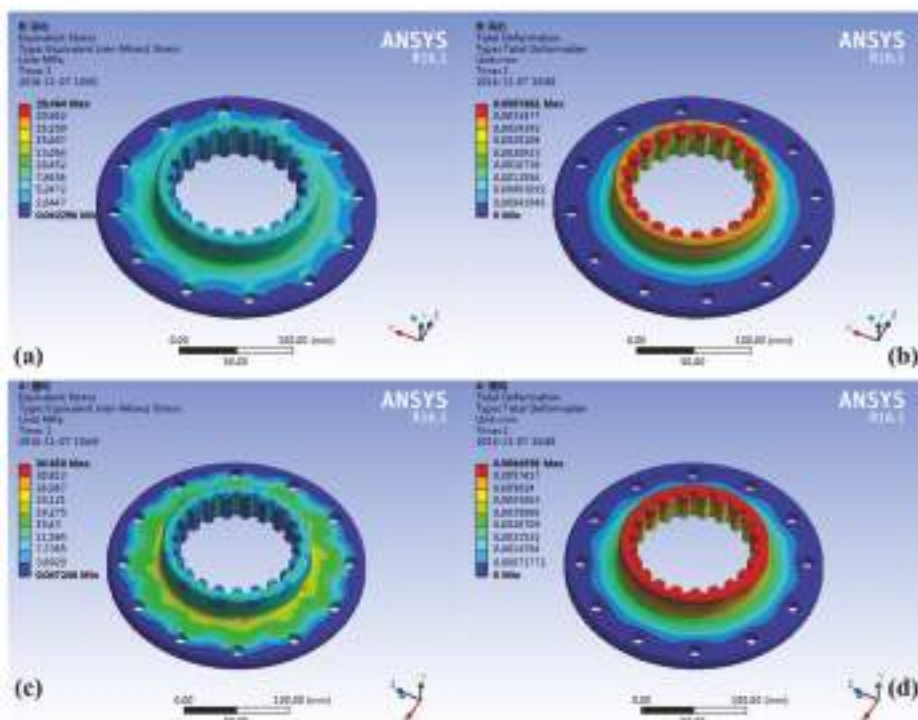
3. Finite element analysis and detail design of the connecting plate

The original and reconstructed connecting plate models were introduced into ANSYSY Workbench (Pittsburgh, CA, USA) for finite element analysis to show the change of the stress distribution. Other detailed designs such as fillets and powder outlets were completed in this stage.

Table 3. Disassembly of connecting plate.

Number	Design Objects	Shape	Load	Design Parameters	Result
1		Flange	Torque	Thickness of frame θ	
2		Ring	Torque	Thickness of frame ν Number of frame N_3	
3		Spline	Stress	∞	

The boundary conditions were added by its actual conditions. The stress distributions of the original (Figure 23a) and optimized connecting plates (Figure 23c) were compared. The maximum stress of the solid connecting plate is 23.464 MPa in Figure 23a. The maximum stress of the redesigned one is 34.66 MPa, as seen in Figure 23c. At the same time, the maximum deformation of the original connecting plate appeared to be 0.0087 mm in Figure 23b compared with the redesigned one of 0.0064 mm, shown in Figure 23d. The mass of the original connecting plate is 3733.6 g. The weight decreased to 2150.9 g with a weight reduction of about 42.4%. The strength can meet the requirements and the distribution of stress became more uniform.

**Figure 23.** Stress distribution of original connecting plate (a), deformation of original connecting plate (b), stress distribution of redesigned connecting plate (c), deformation of redesigned connecting plate (d).

There are some independent cavities created by the inner frames. Every cavity was given a powder outlet of 1 mm diameter at the appearance of parts to discharge redundant powders. The final design model is shown in Figure 24. The red zone shows the powder outlets of the connecting plate.



Figure 24. Final design model of the connecting plate.

The weight of an armored vehicle is 22,500 kg. The redesigned connecting plate was assembled in this vehicle to test its performance in various conditions. The test includes a straight drive test, a pivot turn test, and a brake test at 15 km/h and 30 km/h, respectively. Besides, this vehicle run over 30 km on a gravel road. The assembly procedures are shown in Figure 25.



Figure 25. The assembly of reduction gear (A), tightening of bolts on connected plate (B), position adjustment of connected plate (C), finish of connected plate assembly (D).

4. Results and Discussion

The results of the tensile experiments are shown in Table 4. The cylinder samples were fractured at about 1069.6 MPa, weaker than 1340 MPa, which is the normal value of the tensile strength of IN718 parts manufactured by casting. This may be because of the micro-segregation of IN718 during processing.

Table 4. Results of tensile tests.

Material	Process	Yield Strength/MPa	Tensile Strength/MPa	Elongation
IN718	cast	1100	1340	12%
	SLM X-Y	780	1069.6	30.9%
	Z	634	980	-

The results of the compression tests are shown in Figure 26. The samples of 0.5 mm and 1.0 mm diameter were compressed perpendicularly while the sample of 1.5 mm occurred with lateral

compression. The samples of 2.0 mm and 2.5 mm were not fractured because of the limitation of the test machine.

The compression curves were recorded in Figure 27. At the beginning of the experiment the deformation of samples was elastic. Some support cylinders of the 0.5 mm sample yielded when the load increased to 180 MPa because of the local defects caused by the SLM process. At the same time, the modulus of elasticity of the parts decreased and the elastic deformation continued to occur. All the support cylinders yielded when the load increased to 338 MPa. The defects created by the SLM process may weaken the performance of parts, especially when the size of the structure is rather small.

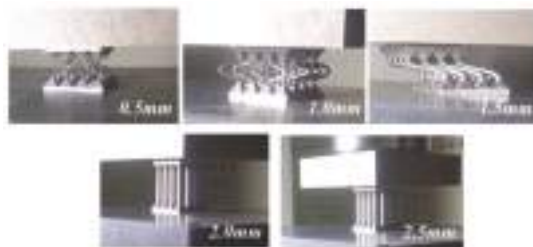


Figure 26. Results of compression tests.

Elastic deformation also occurred in the compression test of the 1.0 mm and 1.5 mm samples. When the displacement exceeded 0.75 mm, these parts yielded. Because of the limitation of the equipment, only a portion of the compression curves of the 2.0 mm and 2.5 mm samples were recorded.

The equivalent elastic modulus and yield stress can be calculated by the compression curves. The calculation results are shown in Table 5. It can be seen from Table 5 that the performance degradation of the parts becomes significant when the size of the structure is small. The mechanical properties of the small-size lattice structure might be poor due to the high aspect ratio of the rods. Higher aspect ratios increase the tendency of the structure to buckle, leading to poor mechanical properties.

Table 5. Calculation results of compression tests.

Number	Equivalent Diameter/mm	Yield Stress/MPa	Equivalent Stiffness/GPa
0.5 mm	2	180 (First) 338 (second)	49.03
1.0 mm	4	620.2	63.85
1.5 mm	6	694	57.33
2.0 mm	8		35.60
2.5 mm	10		30.45

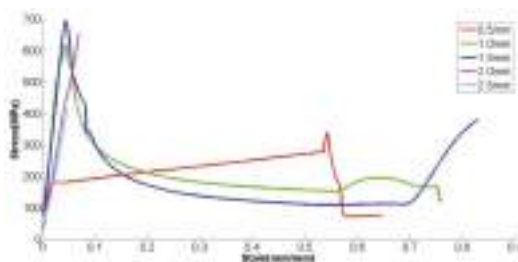


Figure 27. Compression curves of different sized samples.

The yield stress increases with the increase of the structure size. When the sizes were between 1.0 and 1.5 mm, the structure gradually returned to normal yield strength levels of the material. Thus, when the minimum structure size is more than 1.5 mm, the mechanical characteristics will almost not be affected by the defects brought by the SLM process.

The redesigned stopper and connecting plate were manufactured by the SLM process and the results are shown in Figure 28. The mass of the original stopper is 795.2 g and that of the redesigned one is 580.0 g with a weight reduction of about 27%. At the same time, the mass of the solid connecting plate is 3733.6 g. The weight decreased to 2150.9 g with a weight reduction of about 42.4% after the redesign of the inner structures.



Figure 28. Final redesigned stopper (**up**) and connecting plate (**down**) with original parts.

Besides, after the application test shown in Figure 25, the connecting plate was taken out to check for damage. There are only slight wear marks on the tooth surface, and other parts of the structure were still in good condition. According to these tests we can conclude that the proposed lightweight structure redesign method can decrease the weight and cost of parts. Besides, the redesigned components have good mechanical characteristics and can meet the requirements of use.

5. Conclusions

In this paper, the tensile tests of parts manufactured by the SLM process were performed to study the characteristics of SLM components. The samples were fractured at about 1069.6 MPa in tensile tests, weaker than 1340 MPa, which is the normal value of the tensile strength of IN718 parts manufactured by casting. This maybe because of the micro-segregation of IN718 during SLM processing. A group of standard parts which have lattice structures with different sizes were manufactured by SLM. The mechanical tests of these candidates were also performed to study the trends of the yield process of different structure sizes. The compression testing results show that when the minimum structure size is larger than 1.5 mm, the mechanical characteristics will hardly be affected by process defects.

This paper investigated a new design method of lightweight parts manufactured by selective laser melting (SLM) based on the “Skin-Frame”. This method disassembled parts by their shapes and force conditions and reconstructed the inner structures of each divided one by the corresponding framework structures which were optimized by the finite element method. Then, we mixed them together by their topological relationship. Optimized foundation frameworks can be reserved to build a framework library, which can greatly shorten the design time using this method. The design of new parts can be as easy as selecting fundamental frameworks to fill the parts, though, of course, it requires substantial time to build this library. The stopper and connecting plate were redesigned by this method, with weight decreases of about 27% and 42.4%, respectively. Besides, the connecting

plate was tested in an armored vehicle in various conditions. The results show that the redesigned components can meet the requirements of use and decrease the cost and weight of parts.

The findings in this paper provide a foundation for lightweight part design. This research illustrates that parts manufactured by the SLM process with a small size are more vulnerable to process defects. This redesign method has been applied in some automobile parts such as the stopper and connecting plate. The cost and manufacture time of SLM parts can be cut down with this method. This method is a complement to current lightweight design methods. It can also be widely used in the fields of the automotive industry, aviation industry, spacecraft and so on.

This design method only focused on some common parts such as the stopper and connecting plate. Thus, the universality of the method was limited by the component types analyzed before. The mechanical properties of the lattice structure in the compression tests might be poor due to the high aspect ratio of the rods. Further study should improve the universality of this method. Smaller-aspect-ratio samples will be fabricated and tested to eliminate this confusion in future research.

Acknowledgments: The authors would like to thank Qingbiao Zhang for the preparation of 3D printed specimens by the SLM process.

Author Contributions: Li Tang and Chunbing Wu conceived and designed the experiments; Chunbing Wu performed the experiments; Li Tang, Chunbing Wu and Zhixiong Zhang analyzed the data; Jianzhong Shang and Chao Yan wrote the paper.

Conflicts of Interest: The authors declare no conflict of interest.

Nomenclature

D_1	location diameter of mounting hole
D_2	diameter of inner ring
L	fracture length
L_0	initial length
N	number of mounting hole
P	maximum load
S	section area
γ	thickness of dowel bar
σ	section stress
ε	elongation percentage
η	thickness of frame

References

1. Kruth, J.P.; Froyen, L.; Vaerenbergh, J.V.; Mercelis, P.; Rombouts, M.; Lauwers, B. Selective laser melting of iron-based powder. *J. Mater. Process. Technol.* **2004**, *149*, 616–622. [CrossRef]
2. Parthasarathy, J.; Starly, B.; Raman, S.; Christensen, A. Mechanical evaluation of porous titanium (Ti6Al4V) structures with electron beam melting (EBM). *J. Mech. Behav. Biomed. Mater.* **2010**, *3*, 249–259. [CrossRef] [PubMed]
3. Harrysson, O.L.A.; Cansizoglu, O.; Marcellin-Little, D.J.; Cormier, D.R.; West, H.A. Direct metal fabrication of titanium implants with tailored materials and mechanical properties using electron beam melting technology. *Mater. Sci. Eng. C* **2008**, *28*, 366–373. [CrossRef]
4. Evans, A.G.; Hutchinson, J.W.; Fleck, N.A.; Ashby, M.F.; Wadley, H.N.G. The topological design of multifunctional cellular metals. *Prog. Mater. Sci.* **2001**, *46*, 309–327. [CrossRef]
5. Cansizoglu, O.; Harrysson, O.; Cormier, D.; West, H.; Mahale, T. Properties of Ti–6Al–4V non-stochastic lattice structures fabricated via electron beam melting. *Mater. Sci. Eng. A* **2008**, *492*, 468–474. [CrossRef]
6. Campanelli, S.L.; Contuzzi, N.; Ludovico, A.D.; Caiazzo, F.; Cardaropoli, F.; Sergi, V. Manufacturing and Characterization of Ti6Al4V Lattice Components Manufactured by Selective Laser Melting. *Materials* **2014**, *7*, 4803–4822. [CrossRef]

7. Wang, D.; Yang, Y.; Liu, R.; Xiao, D.; Sun, J. Study on the designing rules and processability of porous based on selective laser melting. *J. Mater. Process. Technol.* **2013**, *213*, 1734–1742. [CrossRef]
8. Hernandez-Nava, E.; Smith, C.J.; Derguti, F.; Tammas-Williams, S.; Leonard, F.; Withers, P.J.; Todd, I.; Goodall, R. The effect of defects on the mechanical response of Ti-6Al-4V cubic lattice structures fabricated by electron beam melting. *Acta Mater.* **2016**, *108*, 279–292. [CrossRef]
9. Mahshid, R.; Hansen, H.N.; Hojbjerre, K.L. Strength analysis and modeling of cellular lattice structures manufactured using selective laser melting for tooling applications. *Mater. Des.* **2016**, *104*, 276–283. [CrossRef]
10. Sing, S.L.; Yeong, W.Y.; Wiria, F.E.; Tay, B.Y. Characterization of Titanium Lattice Structures Fabricated by Selective Laser Melting Using an Adapted Compressive Test Method. *Exp. Mech.* **2016**, *56*, 735–748. [CrossRef]
11. Brandt, M.; Sun, S.J.; Leary, M.; Feih, S.; Elambasseriil, J.; Liu, Q.C. High-Value SLM Aerospace Components: From Design to Manufacture. *Adv. Mater. Res.* **2013**, *633*, 135–147. [CrossRef]
12. Xiao, D.; Yang, Y.; Su, X.; Wang, D.; Luo, Z. Topology Optimization of Microstructure and Selective Laser Melting fabrication for Metallic Biomaterial Scaffolds. *Trans. Nonferr. Met. Soc. China* **2012**, *22*, 2554–2561. [CrossRef]



© 2016 by the authors. Licensee MDPI, Basel, Switzerland. This article is an open access article distributed under the terms and conditions of the Creative Commons Attribution (CC BY) license (<http://creativecommons.org/licenses/by/4.0/>).

Article

Effect of the Thermodynamic Behavior of Selective Laser Melting on the Formation of In situ Oxide Dispersion-Strengthened Aluminum-Based Composites

Lianfeng Wang ^{1,4,5}, Jiubin Jue ^{2,3}, Mujian Xia ^{2,3}, Lijie Guo ^{1,5}, Biao Yan ⁴ and Dongdong Gu ^{2,3,*}

¹ Shanghai Aerospace Equipments Manufacturer, Shanghai 200245, China; wlf149@163.com (L.W.); guolijie149@163.com (L.G.)

² College of Materials Science and Technology, Nanjing University of Aeronautics and Astronautics, Yudao Street 29, Nanjing 210016, China; jiubinjue@hotmail.com (J.J.); xmjnuaa@nuaa.edu.cn (M.X.)

³ Institute of Additive Manufacturing (3D Printing), Nanjing University of Aeronautics and Astronautics, Yudao Street 29, Nanjing 210016, China

⁴ Material Science and Engineering Department, Tongji University, Shanghai 200092, China; 84016@tongji.edu.cn

⁵ Shanghai Research Center of Complex Metal Parts by Additive Manufacturing, Shanghai 200245, China

* Correspondence: dongdonggu@nuaa.edu.cn; Tel.: +86-25-5211-2626

Academic Editor: Manoj Gupta

Received: 18 July 2016; Accepted: 9 November 2016; Published: 19 November 2016

Abstract: This paper presents a comprehensive investigation of the phase and microstructure, the thermodynamic behavior within the molten pool, and the growth mechanism of in situ oxide dispersion-strengthened (ODS) aluminum-based composites processed by a selective laser melting (SLM) additive manufacturing/3D printing process. The phase and microstructure were characterized by X-ray diffraction (XRD) and a scanning electronic microscope (SEM) equipped with EDX, respectively. The thermodynamic behavior within the molten pool was investigated for a comprehensive understanding on the growth mechanism of the SLM-processed composite using a finite volume method (FVM). The results revealed that the in situ $\text{Al}_2\text{Si}_4\text{O}_{10}$ ODS Al-based composites were successfully fabricated by SLM. Combined with the XRD spectrum and EDX analysis, the new silica-rich $\text{Al}_2\text{Si}_4\text{O}_{10}$ reinforcing phase was identified, which was dispersed around the grain boundaries of the aluminum matrix under a reasonable laser power of 200 W. Combined with the activity of Marangoni convection and repulsion forces, the characteristic microstructure of SLM-processed $\text{Al}_2\text{Si}_4\text{O}_{10}$ ODS Al-based composites tended to transfer from the irregular network structure to the nearly sphere-like network structure in regular form by increasing the laser power. The formation mechanism of the microstructure of SLM-processed $\text{Al}_2\text{Si}_4\text{O}_{10}$ ODS Al-based composites is thoroughly discussed herein.

Keywords: selective laser melting; aluminum matrix composites; microstructure; thermodynamic behavior; formation mechanism

1. Introduction

Aluminum matrix composites (AMCs) have been widely used in many applications, especially in the aerospace, defense, and automobile industries, due to its unique combination of light weight, high specific strength, and excellent wear performance [1]. Nevertheless, the limited wear resistance and other mechanical properties become a serious barrier for the application where abrasive and erosion phenomena exist. Thus, a considerable number of previous efforts have been attempted

to prepare ceramic particle reinforced aluminum matrix composites, coatings, or both to improve the corresponding properties of aluminum [2]. Normally, in order to enhance the performance of aluminum, the ceramic particles are employed as reinforcements to be directly added to the molten aluminum. For instance, the additive of Al_2O_3 and B_4C ceramic particles were added to the aluminum composites to strengthen the mechanical properties [3]. However, owing to the considerably poor wettability between ceramics particle and aluminum, a poor interfacial bonding between the reinforcements and the matrix is generated, which considerably influences the mechanical performances of the AMCs. In the literature, the *in situ* synthesis of the reinforcements of the particle-reinforced metal matrix composites is a new technique, which is achieved by adding element and compound powder or performs into the molten aluminum. In the case of *in situ* synthesis, the desired reinforced particles can be synthesized directly using the chemical reaction between the reactants in the melt [4]. *In situ* reaction processes involving particle-reinforced composite systems eliminate interfacial compounds in favor of nucleation and growth from the parent matrix phase to form more thermodynamically stable reinforced compounds. Meanwhile, the composites possess contaminant-free reinforcement/matrix interfaces, and the *in situ* Al_2O_3 particles are fine and can enhance the strength and ductility of the composite. Compared with the previous techniques, advantages are as follows: (i) the distribution of the *in situ* reinforcements are more homogeneous in the whole microstructures and more thermodynamically stable; (ii) the *in situ* reinforcements have a metallurgical bonding with the matrix, which results in a strong interfacial bonding between the reinforcements and the matrix. Recently, some metal oxides (e.g., Fe_2O_3 , MnO_2 , and CuO) were added to molten aluminum to produce Al_2O_3 particle reinforcement with a high performance, low cost, and good wettability, which can take the external load and the good interfacial cohesion between Al_2O_3 and the matrix [4]. In an *in situ* Al/CuO composite system, oxygen atoms diffuse along the powder surfaces and the lattice and grain boundaries during synthesis, and an oxide film on the surface of a metal powder has a significant effect on the bonding properties of the powder. In this case, the oxide film can accelerate the bonding between particles when the film thickness is less than critical. The *in situ* SLM reaction of Al/ Fe_2O_3 powder mixtures released extra heat and collaborated with laser energy, which can modify the visual surface and microstructural appearance or alter material characteristics, and the hardness of composite was increased [5]. Further taking the Al_2O_3 as the raw material, the high-performance $\text{Al}_2\text{Si}_4\text{O}_{10}$ reinforced aluminum was *in situ* synthesized by powder metallurgy technique and the resultant mechanical properties of AMCs was considerably enhanced [6]. Although the presence of reinforcements *in situ* synthesized in the aluminum composites can strengthen the performance of the corresponding aluminum matrix efficiently, the conventional AMCs reinforced by *in situ* synthesized reinforcements using micro-scale particles commonly have a remarkably coarse microstructure with attendant poor mechanical performance resulting from a slow cooling rate in traditional manufacturing processes [7].

Additive manufacturing (AM)/3D printing (3DP) refers to the process of fabricating three-dimensional near-net-shaped components directly from powder particles in a layer-by-layer manner. It enables a number of technical and economic advantages, e.g., improving the cost-competitiveness for low volume production, reducing the environmental impact of manufacture, and increasing design complexity [8]. Selective laser melting (SLM), a newly developed AM/3DP process, is based on the principle of material incremental manufacturing and considered a promising AM technology for metallic parts, due to its flexibility in feedstock and shapes. SLM provides possibilities to fabricate the geometrically complex components by user-defined computer-aided design (CAD) files without tools or molds that would be difficult to develop by conventional manufacturing methods. It enables the quick fabrication of the geometry-complex components directly from powders. Under the irradiation of the high-energy laser beam, SLM fabricates parts in a layer-wise fashion by selectively fusing and consolidating the thin layers of the loose powder [9]. Generally, the geometrically complex components are fabricated by SLM with a high dimensional precision and good surface integrity without other subsequent process requirements, which the conventional techniques (e.g., casting and machining)

cannot keep pace with easily [10]. Moreover, during SLM, the temperature of the powder-bed where the applied high energy laser beam is irradiated reaches a maximum temperature of 10^5 K, and is followed by a rapid cooling at a rate up to 10^{6-7} K/s as the laser beam moves away, which involves a rapidly melted and solidified powder metallurgical mechanism and affects the forging of non-equilibrium phases with fine grained microstructures with superior metallurgical properties [11,12]. In this case, due to the extremely large cooling rate, a considerably fine microstructure is obtained, and the resultant performances are efficiently enhanced. The application of SLM in the fabrication of AMCs is expected to create newly mechanical and technological opportunities, because of the potential for developing novel *in situ* composites with unique mechanical properties.

Previous research has mainly been focused on the fabrication of high-performance AMCs by SLM using ceramic particles, such as TiC [13], AlN [14], and B4C [15]. Although the above-mentioned AMCs fabricated by SLM enhance the mechanical properties, a poor bonding strength between the reinforcements and the aluminum was also generated. To date, there are very few studies on *in situ* oxide dispersion-strengthened (ODS) AMCs fabricated by SLM, which are believed to possess unmatchable advantages compared with the conventional components. AlSi10Mg is normally used in the automotive industry for its high specific strength, in applications where fatigue performance is also critical. Therefore, according to the excellent properties of $\text{Al}_2\text{Si}_4\text{O}_{10}$, this paper focuses on the *in situ* synthesized $\text{Al}_2\text{Si}_4\text{O}_{10}$ ODS Al-based composites and the attendant growth mechanism. The $\text{Al}_2\text{O}_3/\text{AlSi10Mg}$ composite powders were prepared by the processing of high-energy ball milling; subsequently, the $\text{Al}_2\text{Si}_4\text{O}_{10}/\text{Al}$ composites were produced by SLM to obtaining desirable parts with novel microstructures. The attendant chemical composition, the microstructure characterization, and the formation mechanism of the composites were studied in detail.

2. Materials and Methods

2.1. Preparation of Samples

The gas atomized pre-alloy powders of AlSi10Mg powder (a purity of 99.7%) were used as the starting material with a near spherical shape and a mean particle size of 30 μm . The Al_2O_3 powders (a purity of 99.5%) with a polygonal morphology and a mean particle size of 9 μm were used as reinforcements. The $\text{Al}_2\text{O}_3/\text{AlSi10Mg}$ composite powders were mechanically milled with a weight ratio of 80:20 in a Fritsch Pulverisette 4 planetary mill (Idar-Oberstein, Germany), using a ball-to-powder weight ratio of 10:1, a rotation speed of 200 rpm, and a milling time of 8 h. As depicted in Figure 1a, the small-size reinforcements of Al_2O_3 were homogeneously dispersed around the AlSi10Mg composite powders after milling. The SLM experimental system was developed by Nanjing University of Aeronautics and Astronautics and consisted of an YLR-500-SM Ytterbium fiber laser (Burbach, Germany) with a power of ~ 500 W and a spot size of 70 μm , an automatic powder layering apparatus (Nanjing, China), an inert argon gas protection system, and a computer system for process control. The schematic of SLM processing is shown in Figure 1b. The detailed processing of the concerned SLM procedures is described in [16]. The samples were fabricated with dimensions of $8 \times 5 \times 5$ mm³. Moreover, the corresponding processing parameters of SLM were set as follows: the power of the laser beam was settled at 100 W, 150 W, and 200 W, with a scan speed of 400 mm/s, a spot size of 70 μm , a hatch spacing of 50 μm , and a powder-bed thickness of 50 μm .

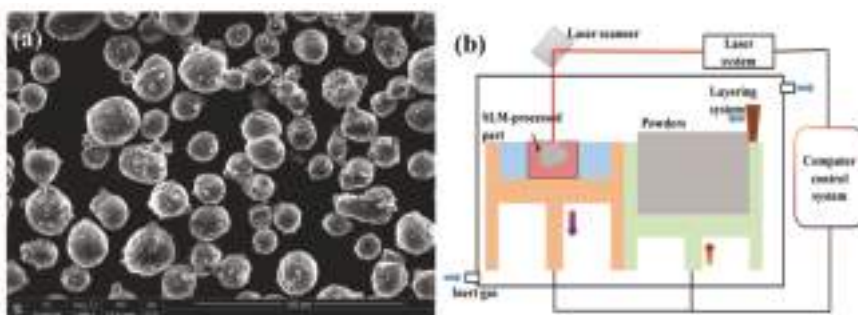


Figure 1. Morphologies of the homogeneously mixed $\text{Al}_2\text{O}_3/\text{AlSi10Mg}$ composite powders processed by ball milling (a); the schematic of SLM processing (b).

2.2. Characterization of Composition

The SLM-processed specimens for metallographic examinations were cut, ground, and polished according to standard procedure, and then etched with a solution consisting of HF (1.0 mL), HCl (1.5 mL), HNO_3 (2.5 mL), and distilled water (95 mL) for about 10 s. An Olympus PMG3 optical microscope (OM, Tokyo, Japan) was used to observe surface morphology of the SLM-processed specimens. X-ray diffraction (XRD, Karlsruhe, German) was employed to identify the phase. Microstructures were obtained with a field emission scanning electronic microscope (FE-SEM, Tokyo, Japan), which was equipped with EDX for the determination of chemical compositions.

2.3. Numerical Simulation

To further investigate the thermodynamic behavior within the molten pool during the selective laser melting $\text{Al}_2\text{O}_3/\text{AlSi10Mg}$ composite, a physical model was established using a finite volume method (FVM) and the corresponding physical properties of materials was properly settled according to [17]. The heat and mass transfer, the surface tension induced by the temperature gradient, and the movement of laser beam power with a Gaussian energy distribution was taken into account in the numerical model. Moreover, the in situ reaction of Al_2O_3 and AlSi10Mg was considered, and the resultant phase transition from Al_2O_3 and AlSi10Mg to the in situ $\text{Al}_2\text{Si}_4\text{O}_{10}$ reinforcements was taken into consideration, including the heat transition during SLM. Meanwhile, some assumptions were also addressed in our physical model:

- (1) The evaporation of molten liquid material was ignored when the maximum temperature of the molten material did not exceed the boiling temperature.
- (2) The reflectivity was regarded as a constant by varying the laser absorption of the aluminum alloy powder.
- (3) The conductivity and melt viscosity were considered to be time-dependent.

The effect of the applied laser power on the temperature distribution and velocity field was investigated. The temperature counter and velocity field of the Y-Z cross-section ($X = 150 \mu\text{m}$) were obtained to investigate the influence of the laser power on the thermodynamic behavior within the molten pool during SLM.

3. Results and Discussion

3.1. Phases and Composition Identification

Figure 2 depicts the typical XRD spectrum of SLM-processed composites. It was evident that the peaks characterized with relatively strong diffraction intensities were identified as the aluminum matrix, i.e., the AlSi10Mg phase. Meanwhile, the primary phase of Si was also generated during SLM, which was mainly consistent with the previous reports. The diffraction peaks with relatively weak intensity corresponding to the new silica-rich phase (aluminum silicate, i.e., $\text{Al}_2\text{Si}_4\text{O}_{10}$) was identified, revealing the general formation of the in situ synthesized $\text{Al}_2\text{Si}_4\text{O}_{10}$ reinforced AMCs.

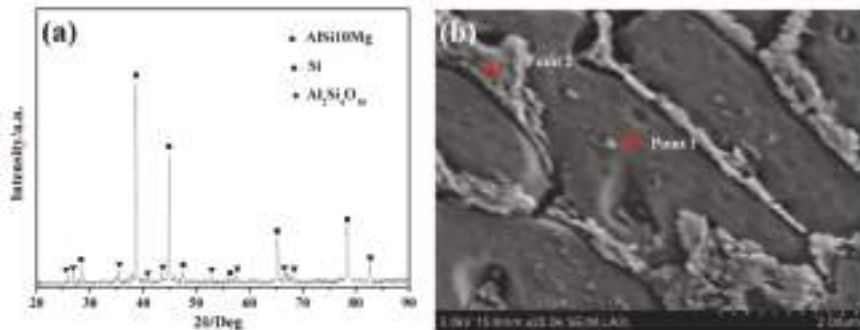


Figure 2. XRD spectrum (a) and the field emission scanning electronic microscope (FE-SEM) images showing the characteristic microstructure (b) of the SLM-processed composites at 150W and 400 mm/s.

The microstructure of SLM-processed composites is shown in Figure 2b. It was clearly observed that the quite fine cellular microstructure was obtained with an ellipse shape. EDX spectra of the two different phases above were obtained to determine their respective chemical composition quantitatively, and the relevant results are illustrated in Table 1. It was revealed that the phase (Point 1, Figure 2b) was rich in Al elements with a small amount of Si and O elements dissolved in the aluminum matrix, which was considered the aluminum matrix. The higher concentration of oxygen could have been ascribed to the diffusion of the Al_2O_3 reinforcement. On the other hand, the molten liquid aluminum tended to oxidize during SLM due to the residual oxygen within the operating chamber [11], whereas the phase (Point 2, Figure 2b) was mainly composed of Al, Si, and O elements with an atomic ratio of approximate 2:4:10, which revealed that the new phase of in situ synthesized $\text{Al}_2\text{Si}_4\text{O}_{10}$ reinforcements were generated. Moreover, as seen from the EDX results, the high cooling rate induced by SLM can effectively extend the solid solubility of Si in the aluminum matrix, leading to a supersaturated solid solution of 6.07%. Further analysis of the EDX result of the aluminum matrix indicated SLM could largely extend the solid solubility of Si in α -Al, leading to a supersaturated solid solution of 6.07%. Thus, it is reasonable to conclude that the in situ $\text{Al}_2\text{Si}_4\text{O}_{10}$ phase was generated, and the attendant in situ $\text{Al}_2\text{Si}_4\text{O}_{10}/\text{AlSi10Mg}$ composites were successfully prepared by SLM combined with the XRD and EDX results.

Table 1. EDX element analysis of Point 1 and Point 2 in Figure 2b showing the chemical compositions in the SLM-processed $\text{Al}_2\text{Si}_4\text{O}_{10}/\text{AlSi10Mg}$ composites.

Position	Elements (at. %)			
	Al	Si	O	Mg
Point 1	89.1	5.75	4.74	0.41
Point 2	12.56	24.98	62.46	-

3.2. Microstructure Characterization

The typical microstructures on the cross-section of SLM-processed composites at variable laser powers are shown in Figure 3. As a relatively low laser power of 100 W was used, the characteristic microstructure presented in a network structure and appeared to be irregular. Moreover, a considerable number of irregular $\text{Al}_2\text{Si}_4\text{O}_{10}$ reinforcements were evidently observed with a nearly nano-scale diameter. They were highly inclined to connect with each other coherently and aggregated into clusters in a fairly large region of the SLM-processed composites (marked by white dash lines in Figure 3a). SLM is widely known to be characterized by an extremely large cooling rate as high as $10^6\text{--}8 \text{ K/sin}$, a low laser energy density, and a small lifespan of the molten pool. In this situation, reinforcements would spread insufficiently and tended to aggregate in most of the regions of the composites [12]. As the laser power was increased to 150 W, the microstructure was observed with an ellipse shape, and the $\text{Al}_2\text{Si}_4\text{O}_{10}$ reinforcements were distributed along the boundary of the Al matrix. However, a slight number of $\text{Al}_2\text{Si}_4\text{O}_{10}$ reinforcements were aggregated in a certain region of the composites (marked by white dash lines in Figure 3b). As the laser power was elevated to 200 W, the in situ $\text{Al}_2\text{Si}_4\text{O}_{10}$ reinforcements were exhibited along the boundary of Al matrix in a nearly sphere-like forming. Meanwhile, the network microstructure of SLM-processed composite performed regularly (Figure 3c). This phenomenon was attributed to Marangoni convection [2,17]. As a large laser power was used, a considerable intensity of Marangoni convection was obtained, which evidently favored the sufficient spreading of reinforcements. Thus, the reinforcements could be distributed uniformly under a reasonable laser power. The AlSi10Mg molten liquid was formed due to the actions of laser beam source irradiated the powder-bed system, and unimpeded motion of molten aluminum into the interconnected network of channels and crevices occurs between Al_2O_3 particles via capillary action. Under this situation, the $\text{Al}_2\text{Si}_4\text{O}_{10}$ reinforcements existing around the AlSi10Mg matrix obviously disappear.

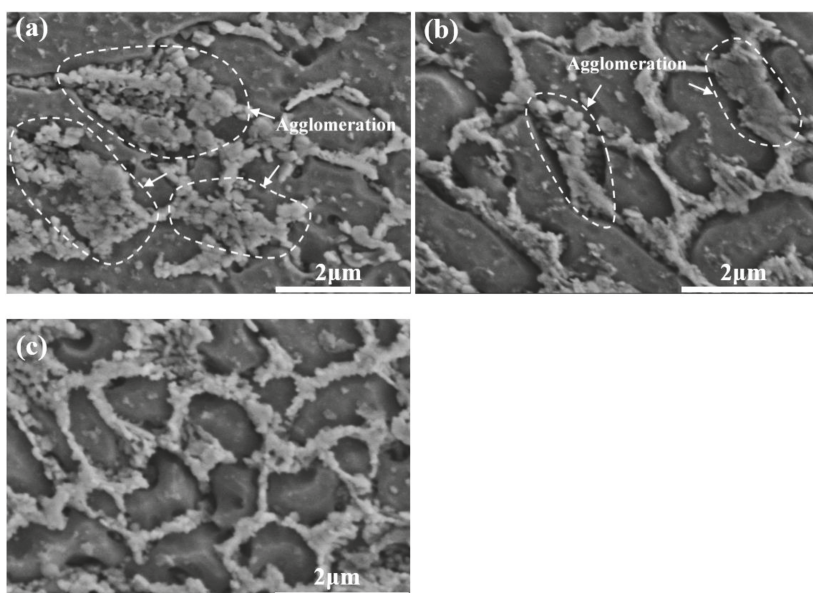


Figure 3. FE-SEM images of the microstructures of SLM-processed composites at 100 W, 400 mm/s (a); 150 W, 400 mm/s (b); 200 W, 400 mm/s (c).

3.3. Thermodynamic Behavior of Molten Pool

The calculated temperature counter and velocity fields within the molten pool in the cross-sectional view at variable laser power are shown in Figure 4. According to the temperature contour plots, it was clear that the peak temperature presented at the center underneath the laser beam with Gaussian distribution and decreased radially outward. The peak temperature was elevated ranging from 1350 K to 1760 K by increasing the laser power. Meanwhile, the temperature gradients were observed to be varied with variable laser power, resulting in the formation of Marangoni convection within the molten material shown on the right side of each picture in Figure 4. It is evident that the velocity of the molten material is enhanced by increasing the laser power. This is attributed to the decrease in the dynamic viscosity (μ) of the molten material and the surface tension (γ) [17–20]. The peak temperature of the simulation on SLM-processed composites was far below the melting point of reinforcements, leading to the reinforcements remaining solid in the molten pool. Thus, it was reasonable to consider that the reinforcements within the molten pool tended to migrate under Marangoni convection. Accordingly, the intensity of the velocity of the molten material significantly affects the dispersion states of the reinforcements. A low laser power also weakened the Marangoni convection and the attendant thermal capillary forces, thereby slowing down the molten liquid flow and migration of reinforcements. Consequently, the nano-scaled solid reinforcements tended to aggregate within the molten pool under the action of each particle, resulting in a severe agglomeration of the reinforcing particulates. By increasing the applied laser power to 150 W, the recirculation was intensified, and the distribution state of reinforcement can thus be enhanced. As a large laser power of 200 W was applied, a high peak temperature was obtained and resultant Marangoni convection was generated with a low viscosity and a high motioning velocity, favoring the sufficient dispersion of the reinforcements within the molten pool. On the other hand, repulsive forces prefer to strengthen between $\text{Al}_2\text{Si}_4\text{O}_{10}$ reinforcements when the amount of Al melt is sufficient in the molten pool [21]. In the combined effect of Marangoni convection and repulsion forces, the dispersive network-structure of the $\text{Al}_2\text{Si}_4\text{O}_{10}$ -reinforced Al matrix is accordingly obtained at the appropriate SLM conditions. Thus, a reasonable laser power is beneficial for obtaining a homogeneous distribution of reinforcement in the aluminum matrix.

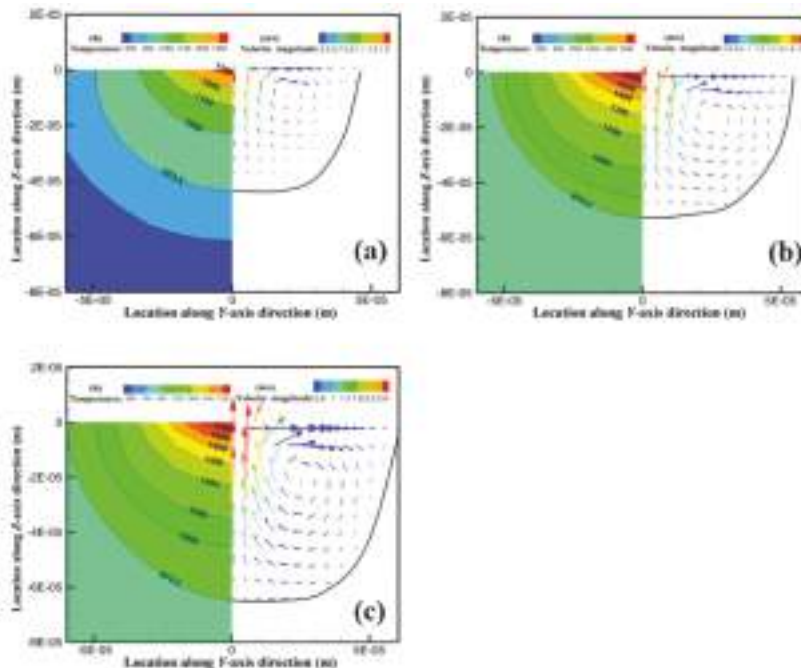


Figure 4. Simulated temperature counter and velocity fields within the melt pool in the cross-sectional view at different processing parameters: (a) 100 W, 400 mm/s; (b) 150 W, 400 mm/s; (c) 200W, 400 mm/s.

3.4. Formation Mechanism of SLM-Processed Composites

Zawrah et al. [6] designed and prepared Al_2O_3 -SiC-mullite reinforced Al-based composites by reaction sintering; meanwhile, new silica phase $\text{Al}_2\text{Si}_4\text{O}_{10}$ was found by decreasing the amount of mullite. Zawrah considered that the formation of the $\text{Al}_2\text{Si}_4\text{O}_{10}$ phase might be attributed to the reaction between Al_2O_3 and SiO_2 . Similarly, for the SLM-processed Al-based composites in this study, Al_2O_3 also acted as a raw material. To explicitly illustrate the formation mechanism of in situ $\text{Al}_2\text{Si}_4\text{O}_{10}$ during SLM processing, the corresponding schematic diagram is shown in Figure 5a. As the laser beam fleetly moves over the powder bed, powder particles melt rapidly, and the temperature within the formed tiny molten pool shows a heterogeneous distribution due to the usage of a Gaussian heat source. Consequently, a surface tension gradient emerged due to the existence of a temperature gradient, resulting in the formation of Marangoni convection. Based on an investigation by Gu et al. [22], Al_2O_3 particles are continuously pushed and gather under the combined effects of Marangoni convection and torque around the particle, forming a ring-like structure observed in Figure 3. According to the Gibbs–Kelvin formula, fine embossment existing on the surface of an Al_2O_3 particle can give rise to a remarkable increase in saturated vapor pressure, thus contributing to the partial melting behavior of the Al_2O_3 particle. As a result, part of the dissociative [Al] and [O] atoms were released into the molten pool and interacted with dissociative [Si] atoms in the melt. The reaction could be described as



During the in situ reaction, the Al_2O_3 particle acted as the oxygen resource, providing sufficient [O] atoms for the formation of the new phase $\text{Al}_2\text{Si}_4\text{O}_{10}$. Hence, the aluminum silicate phase precipitated attachment to the remaining Al_2O_3 particles.

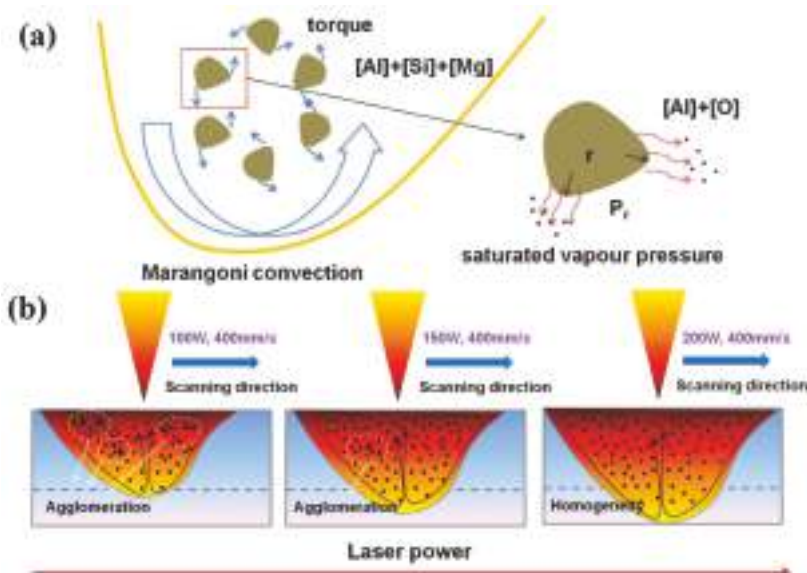


Figure 5. Schematic of the formation mechanism of the in situ $\text{Al}_2\text{Si}_4\text{O}_{10}$ phase (a) and particle distribution (b) during SLM processing.

Based on the above experiment results, it has been concluded that laser energy input can significantly influence the distribution of ex-situ Al_2O_3 and in situ $\text{Al}_2\text{Si}_4\text{O}_{10}$ particles within the molten pool. The underlying factor contributing to the dispersion state of reinforcement is the input energy and resultant operative temperature [23–25]. For a clearer understanding of the distribution evolution of reinforcement particles, the corresponding schematics are shown in Figure 5b. At a relatively low laser power, the temperature within the molten pool is limited, consequently increasing the viscosity of the melt and weakening Marangoni convection. Moreover, the nucleation sites of the $\text{Al}_2\text{Si}_4\text{O}_{10}$ phase are confined to the top region of the molten pool. Under the weak Marangoni convection, Al_2O_3 – $\text{Al}_2\text{Si}_4\text{O}_{10}$ multi-particles drive toughly toward the boundary of the molten pool and finally agglomerate in the solidified front. As the applied laser power increases, the Marangoni convection is remarkably enhanced due to the elevated temperature within the molten pool, thus accelerating the migration of reinforcement particles toward the bottom part of the molten pool. Taking into account the limited temperature rise, agglomeration still occurs when reinforcement particles are migrated to the middle region of the molten pool. As laser power further increases, the nucleation sites of the $\text{Al}_2\text{Si}_4\text{O}_{10}$ phase significantly increase; meanwhile, the Marangoni convection is strong enough to guarantee the homogenous distribution of reinforcement particles.

4. Conclusions

- (1) The in situ $\text{Al}_2\text{Si}_4\text{O}_{10}$ /Al composites were fabricated via SLM. The new silica-rich phase (aluminum silicate, i.e., $\text{Al}_2\text{Si}_4\text{O}_{10}$) was identified via XRD spectrum and EDX analysis. The composites also presented a network microstructure, i.e., the $\text{Al}_2\text{Si}_4\text{O}_{10}$ reinforcements aggregated around the aluminum matrix.

- (2) The characteristic microstructure of the in situ $\text{Al}_2\text{Si}_4\text{O}_{10}$ /Al composites via SLM tended to transfer from the irregular network structure to a nearly sphere-like network structure in regular forming by increasing the laser power.
- (3) As a high laser power was employed, a high peak temperature was acquired correspondingly, and the resultant Marangoni convection was generated with a high velocity, favoring the sufficient dispersion of the reinforcements within the molten pool.
- (4) The formation mechanism of in situ $\text{Al}_2\text{Si}_4\text{O}_{10}$ and the distribution evolution of the reinforcement particles during the SLM processing of $\text{Al}_2\text{O}_3/\text{AlSi10Mg}$ mixed powder were present. Formation of the in situ $\text{Al}_2\text{Si}_4\text{O}_{10}$ phase could be attributed to the reaction among dissociative [Al], [O], and [Si] atoms, and the distribution of reinforcement particles was speculated to be influenced significantly by Marangoni convection and the viscosity of the molten material.

Acknowledgments: The authors gratefully acknowledge the financial support from the Shanghai Aerospace Science and Technology Innovation Fund (No. SAST2015053).

Author Contributions: D.D. Gu, J.B. Jue, and M.J. Xia formulated this research with cooperation from L.F. Wang and L.J. Guo. J.B. Jue and M.J. Xia performed the experimental and simulation work, with the help of D.D. Gu, interpreted the results, and prepared and revised the manuscript. All co-authors contributed to manuscript proof and submissions.

Conflicts of Interest: The authors declare no conflict of interest.

References

1. Tjong, S.C. Novel Nanoparticle-Reinforced Metal Matrix Composites with Enhanced Mechanical Properties. *Adv. Eng. Mater.* **2007**, *9*, 639–652. [[CrossRef](#)]
2. Gu, D.D.; Yuan, P.P. Thermal evolution behavior and fluid dynamics during laser additive manufacturing of Al-based nanocomposites: Underlying role of reinforcement weight fraction. *J. Appl. Phys.* **2015**, *118*, 233109. [[CrossRef](#)]
3. Vijaya Ramnath, B.; Elanchezhian, C.; Jaivignesh, M.; Rajesh, S.; Parswanjanan, C.; Siddique Ahmed Ghias, A. Evaluation of mechanical properties of aluminium alloy-alumina-boron carbide metal matrix composites. *Mater. Des.* **2014**, *58*, 332–338. [[CrossRef](#)]
4. Yang, B.; Sun, M.; Gan, G.S.; Xu, C.G.; Huang, Z.J.; Zhang, H.B.; Fang, Z.Z. In situ Al_2O_3 particle-reinforced Al and Cu matrix composites synthesized by displacement reactions. *J. Alloy. Compd.* **2010**, *494*, 261–265. [[CrossRef](#)]
5. Dadbakhsh, S.; Hao, L.; Jerrard, P.G.E.; Zhang, D.Z. Experimental investigation on selective laser melting behaviour and processing windows of in situ reacted Al/ Fe_2O_3 powder mixture. *Powder Technol.* **2012**, *231*, 112–121. [[CrossRef](#)]
6. Zawrah, M.F.; Aly, M.H. In situ formation of Al_2O_3 -SiC-mullite from Al-matrix composites. *Ceram. Int.* **2006**, *32*, 21–28. [[CrossRef](#)]
7. Olakanmi, E.O.; Cochrane, R.F.; Dalgarno, K.W. A review on selective laser sintering/melting (SLS/SLM) of aluminium alloy powders: Processing, microstructure, and properties. *Prog. Mater. Sci.* **2015**, *74*, 401–477. [[CrossRef](#)]
8. Leary, M.; Mazur, M.; Elambasseri, J. Selective laser melting (SLM) of AlSi12Mg lattice structures. *Mater. Des.* **2016**, *98*, 344–357. [[CrossRef](#)]
9. Prashanth, K.G.; Scudino, S.; Chaubey, A.K.; Löber, L.; Wang, P.; Attar, H.; Schimansky, F.P.; Pyczak, F.; Eckert, J. Processing of Al-12Si-TNM composites by selective laser melting and evaluation of compressive and wear properties. *J. Mater. Res.* **2016**, *31*, 55–65. [[CrossRef](#)]
10. Attar, H.; Löber, L.; Funk, A.; Calin, M.; Zhang, L.C.; Prashanth, K.G.; Scudino, S.; Zhang, Y.S.; Eckert, J. Mechanical behavior of porous commercially pure Ti and Ti-TiB composite materials manufactured by selective laser melting. *Mater. Sci. Eng. A* **2015**, *625*, 350–356. [[CrossRef](#)]
11. Gu, D.D.; Meiners, W.; Wissenbach, K.; Poprawe, R. Laser additive manufacturing of metallic components: Materials, processes and mechanisms. *Int. Mater. Rev.* **2012**, *57*, 133–164. [[CrossRef](#)]
12. Das, M.; Balla, V.K.; Basu, D.; Bose, S.; Bandyopadhyay, A. Laser processing of SiC-particle-reinforced coating on titanium. *Scr. Mater.* **2010**, *63*, 438–441. [[CrossRef](#)]

13. Gu, D.D. *Laser Additive Manufacturing of High-Performance Materials*; Springer: Berlin/Heidelberg, Germany, 2015; pp. 175–197.
14. Dai, D.H.; Gu, D.D. Influence of thermodynamics within molten pool on migration and distribution state of reinforcement during selective laser melting of AlN/AlSi10Mg composites. *Int. J. Mach. Tool. Manu.* **2016**, *100*, 14–24. [CrossRef]
15. Chang, F.; Gu, D.D.; Dai, D.H.; Yuan, P.P. Selective laser melting of in situ $\text{Al}_4\text{SiC}_4 + \text{SiC}$ hybrid reinforced Al matrix composites: Influence of starting SiC particle size. *Surf. Coat. Tech.* **2015**, *272*, 15–24. [CrossRef]
16. Gu, D.D.; Shen, Y.F. WC-Co particulate reinforcing Cu matrix composites produced by direct laser sintering. *Mater. Lett.* **2006**, *60*, 3664–3668. [CrossRef]
17. Yuan, P.P.; Gu, D.D.; Dai, D.H. Particulate migration behavior and its mechanism during selective laser melting of TiC reinforced Al matrix nanocomposites. *Mater. Design.* **2015**, *82*, 46–55. [CrossRef]
18. Read, N.; Wang, W.; Essa, K.; Moataz, M.A. Selective laser melting of AlSi10Mg alloy: Process optimization and mechanical properties development. *Mater. Design.* **2015**, *65*, 417–424. [CrossRef]
19. Zhang, B.C.; Bi, G.J.; Nai, S.; Sun, C.N.; Wei, J. Microhardness and microstructure evolution of TiB_2 reinforced Inconel 625/ TiB_2 composite produced by selective laser melting. *Opt. Laser Technol.* **2016**, *80*, 186–195. [CrossRef]
20. Wang, D.; Song, C.H.; Yang, Y.Q.; Bai, Y.C. Investigation of crystal growth mechanism during selective laser melting and mechanical property characterization of 316L stainless steel parts. *Mater. Design.* **2016**, *100*, 291–299. [CrossRef]
21. Gu, D.D.; Shen, Y.F.; Wu, X.J. Formation of a novel W-rim/Cu-core structure during direct laser sintering of W-Cu composite system. *Mater. Lett.* **2008**, *62*, 1765–1768. [CrossRef]
22. Gu, D.D.; Wang, H.Q.; Dai, D.H. Rapid fabrication of Al-based bulk-form nanocomposites with novel reinforcement and enhanced performance by selective laser melting. *Scr. Mater.* **2015**, *96*, 25–28. [CrossRef]
23. Kurt, H.I.; Oduncuoglu, M. Formulation of the Effect of Different Alloying Elements on the Tensile Strength of the in situ Al-Mg₂Si Composites. *Metals* **2015**, *5*, 371–382. [CrossRef]
24. Casati, R.; Vedani, M. Metal Matrix Composites Reinforced by Nano-Particles. *Metals* **2014**, *4*, 65–83. [CrossRef]
25. Subramanian, J.; Seetharaman, S.; Gupta, M. Processing and Properties of Aluminum and Magnesium Based Composites Containing Amorphous Reinforcement: A Review. *Metals* **2015**, *5*, 743–762. [CrossRef]



© 2016 by the authors. Licensee MDPI, Basel, Switzerland. This article is an open access article distributed under the terms and conditions of the Creative Commons Attribution (CC BY) license (<http://creativecommons.org/licenses/by/4.0/>).

Article

Investigation on Porosity and Microhardness of 316L Stainless Steel Fabricated by Selective Laser Melting

Shahir Mohd Yusuf ¹, Yifei Chen ¹, Richard Boardman ², Shoufeng Yang ¹ and Nong Gao ^{1,*}

¹ Materials Research Group, Faculty of Engineering and the Environment, University of Southampton, Southampton SO17 1BJ, UK; symy1g12@soton.ac.uk (S.M.Y.); chenyifeiuk@sina.com (Y.C.); S.Yang@soton.ac.uk (S.Y.)

² μ -VIS X-Ray Imaging Centre, Faculty of Engineering and The Environment, University of Southampton, Southampton SO17 1 BJ, UK; rpb@soton.ac.uk

* Correspondence: n.gao@soton.ac.uk; Tel.: +44-23-8059-3396

Academic Editor: Manoj Gupta

Received: 5 January 2017; Accepted: 15 February 2017; Published: 20 February 2017

Abstract: This study investigates the porosity and microhardness of 316L stainless steel samples fabricated by selective laser melting (SLM). The porosity content was measured using the Archimedes method and the advanced X-ray computed tomography (XCT) scan. High densification level ($\geq 99\%$) with a low average porosity content (~0.82%) were obtained from the Archimedes method. The highest porosity content in the XCT-scanned sample was ~0.61. However, the pores in the SLM samples for both cases (optical microscopy and XCT) were not uniformly distributed. The higher average microhardness values in the SLM samples compared to the wrought manufactured counterpart are attributed to the fine microstructures from the localised melting and rapid solidification rate of the SLM process.

Keywords: porosity; microhardness; Selective Laser Melting (SLM); advanced X-ray computed tomography (XCT)

1. Introduction

Additive manufacturing (AM) is an advanced manufacturing process which involves layer-wise material addition to fabricate three-dimensional (3D) objects based on pre-defined Computer Aided Design (CAD) data. This technology possesses the advantage of design flexibility, which enables the fabrication of parts with complex geometries and intricate features compared to traditional processes such as casting and forging. In addition, the additive nature of this process allows components to be manufactured with much less raw material wastage which could reduce material costs and the environmental footprint [1,2]. The AM of metal components has evolved from rapid prototyping (RP) to fabrication of functional metallic components for end use such as in the automotive, biomedical and aerospace industries [3,4].

Various AM processes for metals have been well described and reviewed [5,6]. Selective laser melting (SLM) is one of the major AM technologies that has been used to process a number of metals and alloys, e.g., Ti6Al4V [7], β -type Ti–24Nb–4Zr–8Sn [8,9], Ni superalloy [10] and 316L stainless steel (316L SS) [11], for a wide range of applications, including bone implants [12], turbine blades [13] and automotive pistons [3]. In SLM technology, the laser beam is used to completely melt metal powder layers spread on a powder bed to form near-net-shaped components. In this process, 3D models are first sliced into 2D cross-sections with a set thickness value. The laser beam then scans the cross-section of the designed part layer by layer before selectively fusing them on top of each other, which enables the final 3D part to be formed directly.

316L SS, in particular, is highly attractive for biomedical and marine applications due to its excellent corrosion resistance and relatively superior ductility compared to other materials [14–16]. Current research on AM of 316L SS is not only limited to single-material processing, but also extends to composites. For example, Al Mangour et al. [17] studied the SLM of TiC-reinforced 316L SS matrix nanocomposites and found that the addition of fine TiC particles remarkably improved the microhardness and wear performance of the fabricated parts. This is because of the increase in the densification level and the homogeneous microstructure distribution as a result of enhanced reinforcement/matrix wettability. In addition, studies on the SLM of TiB₂/316L SS nanocomposites were also carried out with varying results. For example, superior compression yield strength and ductility were obtained when processing this nanocomposite without a hot isostatic pressing (HIP) post-processing due to the formation of homogeneously dispersed TiB₂ particles forming nanoscaled structures [18]. However, HIP treatment was found to reduce the hardness and wear resistance due to the high-temperature annealing effect [19]. Nevertheless, the flexibility of AM processes to fabricate such composites provides a promising future, especially for parts requiring complex geometries.

Although SLM is able to manufacture almost fully dense parts (~98%–99%), the presence of residual porosity in SLM-fabricated parts hinders high-strength and fatigue resistance applications [20]. Similar to conventionally manufactured parts, the mechanical properties of components built by SLM are influenced by the resulting microstructure and porosity profiles (size and morphology) [1,21]. Hence, it is important to understand the microstructure and porosity formation and how their behaviour influences the mechanical properties of the completed parts. Thus, this study aims to investigate the microstructure, porosity distribution and microhardness of 316L SS parts fabricated by SLM, in particular by using the advanced X-ray computed tomography (XCT) technique.

2. Materials and Methods

Gas-atomised 316L SS powders (Concept Laser GmbH, Lichtenfels, Germany) with diameters ranging from 15 to 40 µm were used in this study. The as-supplied material composition of this alloy is shown in Table 1. The low P, C and S contents in 316L SS reduce the susceptibility of this material to sensitisation (grain boundary carbide precipitation), in which sensitisation could reduce the mechanical properties of the fabricated parts.

Table 1. Chemical composition (wt. %) of 316L SS powders used in this study.

Component	Fe	Cr	Ni	Mo	Mn	Si	P	C	S
wt. %	Bal.	16.5–18.5	10.0–13.0	2.0–2.5	<2.0	<1.0	<0.045	<0.030	<0.030

All AM 316L SS samples were fabricated by using Concept Laser M2 Laser Cusing SLM machine (Concept Laser GmbH, Lichtenfels, Germany) in an inert gas environment. The processing parameters used in this study were as follow: (i) laser power: 200 W; (ii) scan speed: 1600 mm/s; and layer thickness: 50 µm. The samples were built using the “island” scan strategy to reduce the residual stress in the completed parts (Figure 1) [22,23].

In this study, three samples were fabricated by SLM and one sample was made by using the conventional wrought manufacturing (WM) technique. The SLM samples were built along the z-axis (vertically). For optical microscopy, cube-shaped AM samples (originally 8 mm × 8 mm × 8 mm) were cut into 4 mm × 4 mm square cross-sections along the x-y, y-z and x-z planes using a wire electrical discharge machine. They are then mounted on conductive bakelite, ground using 120, 800, and 1200 grits abrasive papers and polished using 6 µm and 1 µm diamond paste to obtain mirror-like surface finish. In order to reveal the microstructures, the polished samples were etched using Kalling’s No. 2 reagent (50 mL HCl, 50 mL ethanol, 2 g copper chloride for 100 mL of etchant) for approximately 30 s. Olympus BX41M-LED optical microscope (Tokyo, Japan) was used to observe the microstructure on the metallographic specimens.

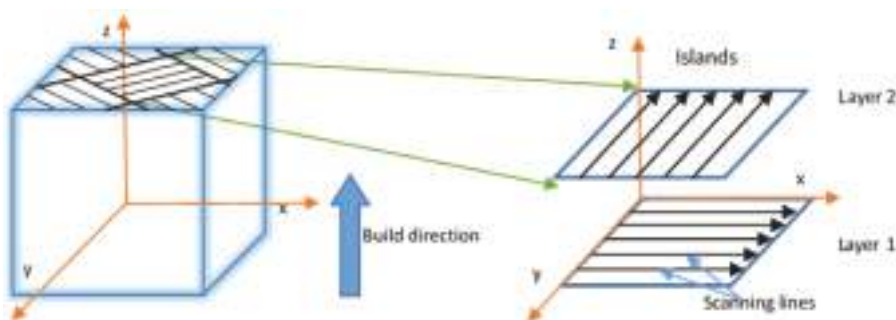


Figure 1. “Island” scanning strategy, shaped like checkerboards employed in the SLM process of 316L SS samples.

Vickers microhardness (HV) measurements were taken along the cross-sections using FM-300 Microhardness Tester (Future-Tech Corp, Kanagawa, Japan). The distance between each indentation was 1 mm and the applied load was 100 gf with dwell time of 10 s. The measurements at each position were repeated three times and the average HV values were calculated. In addition, HV values were also obtained from the cube-shaped 316L SS sample manufactured by WM using similar testing conditions.

The average porosity in the SLM-built samples was calculated using the well-known Archimedes method. On the other hand, the pore size distribution was determined using optical microscopy (GenICam software, Basler AG, Ahrensburg, Germany) from 15 micrographs for each sample. In addition, one AM sample (approximately $10\text{ mm} \times 10\text{ mm} \times 15\text{ mm}$) was subjected to advanced X-ray computed tomography (XCT) scan to obtain information on porosity as this sample had a relatively complex geometry compared to the other samples. This sample was first scanned under low resolution using Nikon Benchtop CT160Xi (Nikon Metrology, Herts, UK) to obtain the general porosity distribution. Then, a small region with the highest porosity content was chosen to undergo detailed scanning using 160 kV Zeiss XRadia 510 Versa (Carl Zeiss Microscopy GmbH, Jena, Germany) with high resolution of $3.2\text{ }\mu\text{m}$ for 20 h. After reconstruction and handling of raw images from the XCT scan results, VG Studio Max software (Volume Graphics GmbH, Heidelberg, Germany) was used as a 3D visualisation tool to obtain detailed porosity distribution in the small region of interest. The porosity in XCT-scanned samples was defined using the Otsu method described in Ref. [24].

3. Results and Discussion

3.1. Microstructure

Figure 2a shows the cross-sectional views on the $x-y$ (scan direction) plane, while Figure 2b,c shows the cross-sectional views on the $x-z$ and $y-z$ planes (build direction), respectively. These melted scan tracks are representative of the solidified melt pool for each layer on the powder bed. The curved “fish-scale”-like geometries observed in the $x-z$ and $y-z$ (build direction) planes are due to the semi-circular shape of the melt pool and the partial re-melting of successively deposited layers which have been solidified [23]. These overlapping geometries also demonstrate successful fusion of powder particles and bonding within each layer, similar to the work carried out by Cherry et al. [1] and Yasa and Kruth [20].

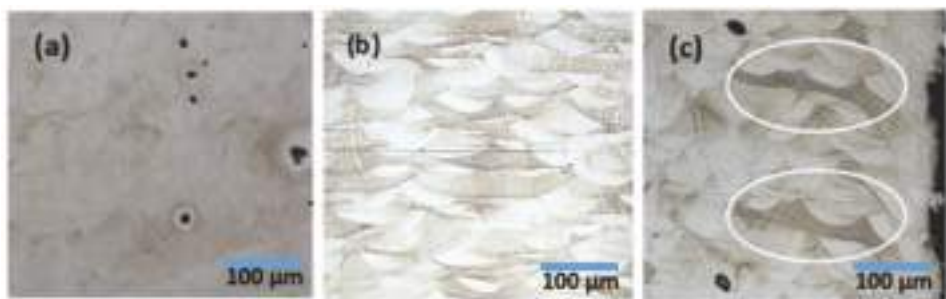


Figure 2. Cross-sectional views of SLM samples on (a) $x-y$ plane; (b) $x-z$ plane; and (c) $y-z$ plane.

A fine cellular-dendritic microstructure could be observed in the SLM-fabricated samples as shown in Figure 3. This is a common characteristic for metal materials fabricated by AM processes as a result of the rapid solidification rates in the locally melted areas (selectively laser-scanned regions) which were experienced because of short laser-material interaction time during the build process [25–27].

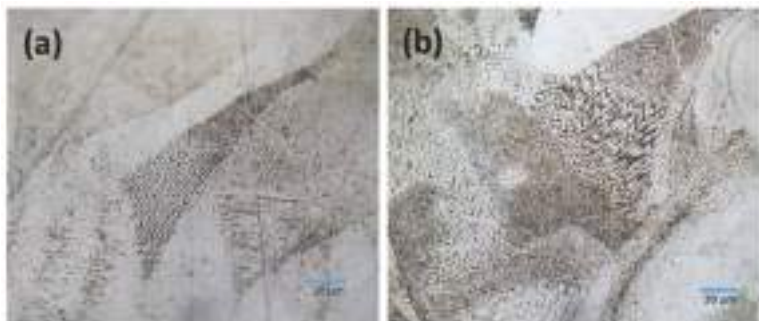


Figure 3. (a) and (b) show fine cellular-dendritic microstructures in SLM-fabricated 316L SS specimens.

It is well understood that the microstructures obtained in AM-processed metal parts, which depend on the applied processing parameters, strongly influence the mechanical properties of the parts, e.g., the densification levels, yield and tensile strengths and microhardness. Furthermore, the fine microstructures obtained via AM processes lead to improvements in tensile strength and microhardness compared to conventional manufacturing techniques [28,29].

3.2. Porosity

Figure 4 shows the average pore size distribution in the AM 316L SS samples obtained by optical microscopy. The pore sizes ranged from $\sim 5 \mu\text{m}$ to $\sim 45 \mu\text{m}$, where the smaller pores ($\leq 5 \mu\text{m}$) accounted for the majority (~60%) and the larger pores ($> 30 \mu\text{m}$) accounted for less than 3%. The average porosity of the SLM specimens was calculated to be $0.82\% \pm 0.36\%$, which means that a high densification level ($\geq 99\%$) was achieved.

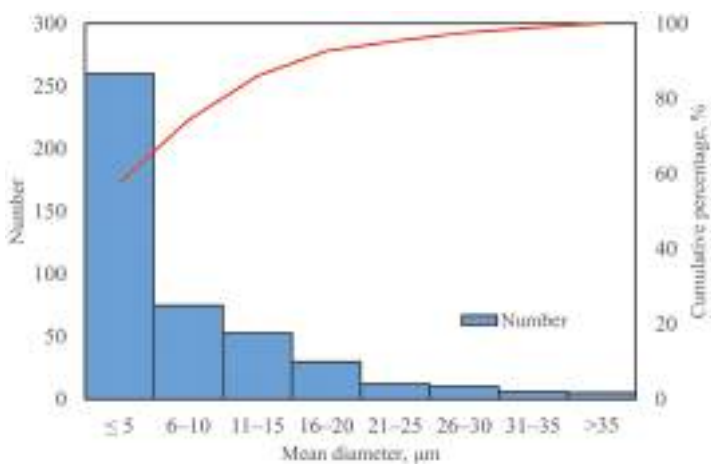


Figure 4. Pore size distribution in SLM samples, obtained from optical microscopy. Red curve represents the cumulative pore distribution.

However, the pores were not evenly distributed throughout the cut specimens and some of them were concentrated more in certain areas compared to others. It was observed that for the samples cut along the $x-y$ plane (along the scan direction), the pores were mainly concentrated at the boundary of the “island” which was employed as the scan strategy during SLM in this study (Figure 5). In other words, the pores were located at the overlapping area between two “islands”, similar to the work carried out by Gustmann et al. [30]. Interestingly, aligned pores appeared regularly along the build direction for the samples cut along the $x-z$ and $y-z$ planes (Figure 6). This could be the result of inclusions such as oxides present upon solidification of the molten pool [31–33]. Nevertheless, the porosity content at these regions with a high porosity concentration amounted up to $\sim 1.68\%$, which is still a small figure as a whole but is relatively higher than the average porosity content calculated.

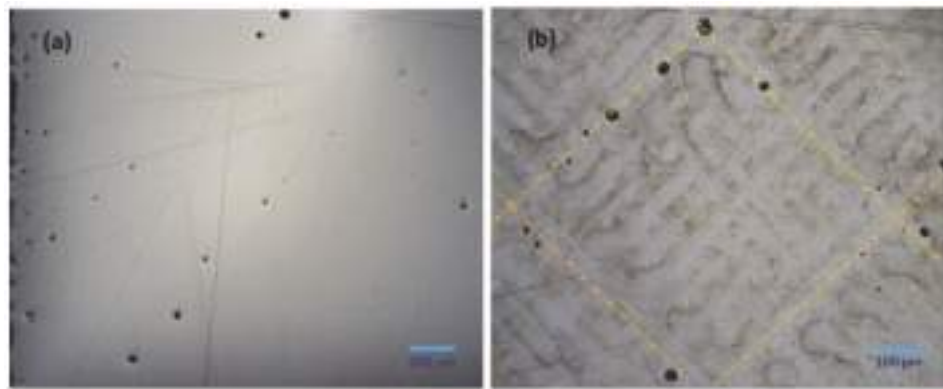


Figure 5. Micrographs showing porosity distribution for the (a) un-etched and (b) etched specimen cut along the $x-y$ plane.

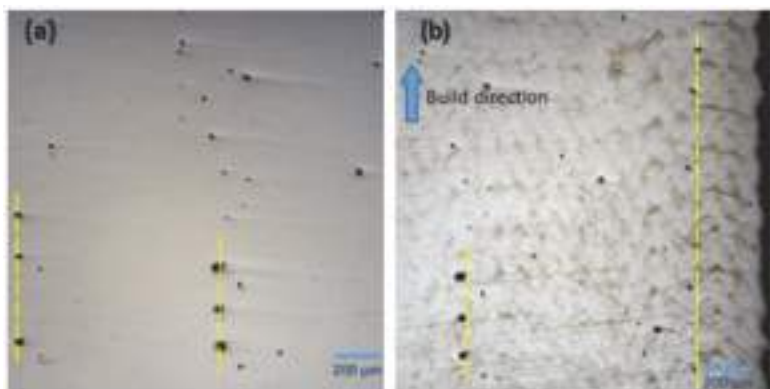


Figure 6. Aligned pores at successive solidified layers for: (a) un-etched and (b) etched specimens cut along the $x-z$ plane. Similar results were observed for specimens in the $y-z$ plane.

On the other hand, after the initial scanning of one SLM sample which had a relatively complex geometry (Figure 7a) by using advanced X-ray computed tomography (XCT) under a low resolution, a small region near the inner circle profile of the sample was found to have the highest porosity content compared to other regions throughout the sample (Figure 7b). Through detailed scanning of this region under high resolution, the porosity content was found to be 0.61%, with pore sizes ranging from $5\text{ }\mu\text{m}$ to $\sim 74\text{ }\mu\text{m}$, as shown in Figure 8. The porosity content in the scanned region was also not evenly distributed, with the majority of the pores concentrated close to the surface (inner wall) of the scanned region (Figure 9). However, a comparative study on porosity could not be carried out because only one sample was subjected to the XCT scan. Hence, the results obtained were not representative for all 316L SS samples fabricated by SLM.

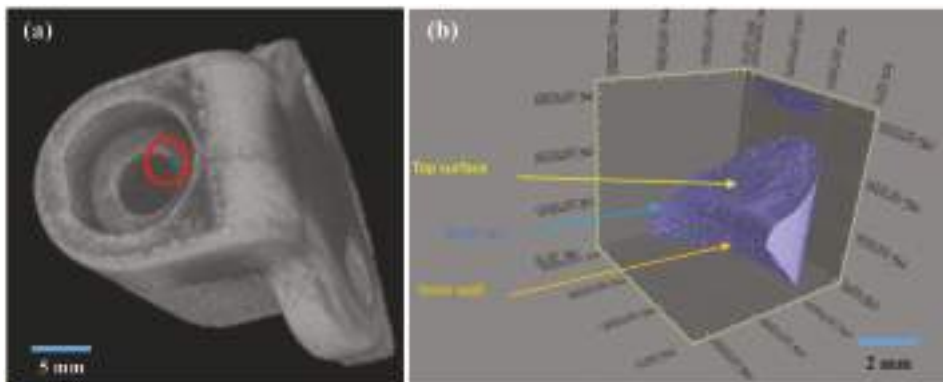


Figure 7. (a) Three-dimensional view of the AM-fabricated sample with a relatively complex geometry; (b) 3D view of the small region near the inner circle profile (red circle in 7a) further observed under high resolution.

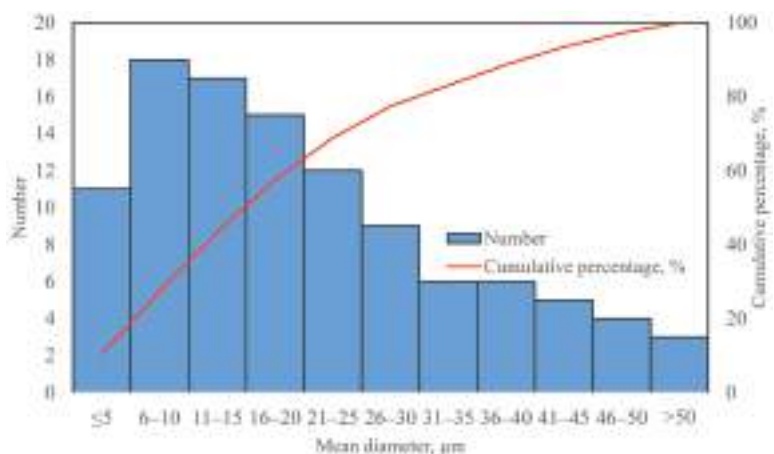


Figure 8. Pore size distribution for SLM sample shown in Figure 7b, obtained via XCT scan. Red curve represents the cumulative pore distribution.

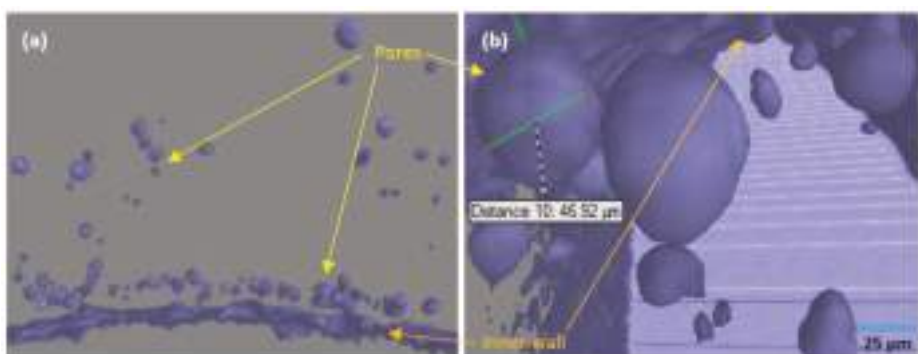


Figure 9. (a) Majority of the pores in the CT-scanned sample were observed close to the surface (inner wall) of the region in study; (b) Example of pore shape and size near the inner wall region.

Nevertheless, the XCT scan could be a better method to study the porosity distribution in AM-fabricated samples. This is because it is a non-destructive technique which enables detailed 3D visualisation of internal pores in the samples (Figure 9) without physically and chemically disrupting the sample, as compared to the conventional metallographic preparation for optical microscopy observation. However, only a small percentage of small pore sizes ($<5 \mu\text{m}$ mean diameter) could be captured with the $3.2 \mu\text{m}$ resolution of the XCT scan used in this study compared to those obtained using optical microscopy. In addition, a much higher cost and longer time are required to obtain a higher resolution to detect smaller pore sizes, which is the current limitation of this technology.

Porosity is a common defect observed in the AM of metal parts, and it can be controlled by adjusting various processing parameters, e.g., the scan speed, laser power and layer thickness. In general, there are two types of porosities including gas-induced porosity and process-induced porosity [34]. Spherical-shaped gas pores could arise during the gas atomisation of the 316L SS feedstock material prior to SLM processing and continue to be present in the final parts. On the other hand, pores resulting from process-induced porosity are typically non-spherical. They are formed when either: (a) the energy applied is insufficient to completely melt the powder feedstock, causing lack of fusion between each adjacent scan and between successive layers [35]; or (b) excessive

energy is applied, resulting in spatter ejection [36]. In this study, spherical pores dominated the non-spherical ones, where rectangular-shaped pores were visible only near the edges of the cut specimens. This indicates that most of the porosity defects in the SLM samples were due to gas pores during the gas atomisation of the 316L SS powders, similar to the work carried out by Tammas-Williams et al. [37]. The gas pores could be produced due to the presence of moisture or contaminants on the surface of the powder particles [38]. These pores could also be formed by the reactions between O₂ and C which are present in small amounts during SLM processing, causing CO or CO₂ gas entrapment in the SLM-built parts [39]. The non-uniform pore distribution in this process could be caused by one of the following factors: (i) the variation of surface roughness [40]; and (ii) the layer-wise build manner of the AM [41]. The variation in surface roughness results in an inhomogeneous powder distribution that leads to an inconsistent melt flow and an unstable molten pool in the successive layers [42]. These, in turn, contribute to the discontinuities in the scan track formation, and hence the irregular pore distribution obtained in this study. Nevertheless, these defects (pores and voids) are detrimental to the quality of AM-fabricated metal parts, especially as they reduce mechanical properties such as yield and tensile strength.

3.3. Microhardness

The results of the Vickers microhardness (HV) tests were evaluated by: (i) comparing HV values of SLM samples for different cut planes (*x-y*, *x-z* and *y-z*) as shown in Figure 10; and (ii) comparing HV values of SLM and WM samples (Figure 11).

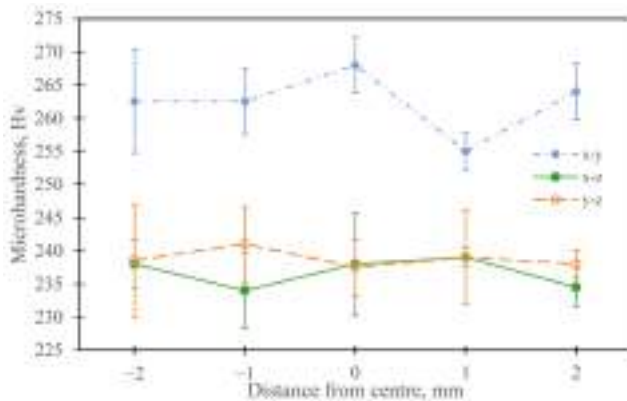


Figure 10. Average microhardness (HV) values for SLM specimens in the *x-y*, *x-z* and *y-z* planes.

From Figure 10, it can be observed that the average microhardness values for the SLM specimens in *x-y*, *x-z* and *y-z* planes are 262 HV, 237 HV, and 239 HV, respectively. The microhardness of the SLM samples at the *x-y* plane (scan direction) was the highest compared to the other two planes which had similar but considerably lower HV values. The discrepancy of the microhardness in each plane indicates anisotropy in SLM, which is typical of AM processes for metal components [28,43–45]. This is because of the layer-wise build approach with the “island” scan strategy in AM processes, which means localised melting of powder particles that often results in non-homogeneous morphologies and anisotropic grain structures [46,47]. However, the similar average HV values in the *x-z* and *y-z* planes indicated a more uniform microhardness distribution in the build direction compared to the scan direction for the SLM-processed samples. Figure 11 shows the average microhardness values of the SLM samples (228 HV), which were higher than those of the WM sample (192 HV). This is consistent with various literature, in which the microhardness of AM 316L SS parts is typically higher than that of conventionally manufactured 316L SS parts [28,48]. Higher microhardness in AM 316L SS samples

is attributed to the fine-grain microstructures obtained in the completed parts resulting in a higher dislocation density of austenite cells [49]. This makes slip motion along the grain boundaries difficult, thus increasing its strength and resistance to deformation. Although there is some porosity content in the SLM samples in this study, the defect is not expected to have a significant impact on the mechanical properties of the final part since the SLM processing was able to yield high densification levels (>99%) and the average porosity was also very low (~0.33%). Nevertheless, the porosity-microhardness relationship is an important aspect to consider when SLM is used to manufacture functional parts such as bone implants and industrial tools.

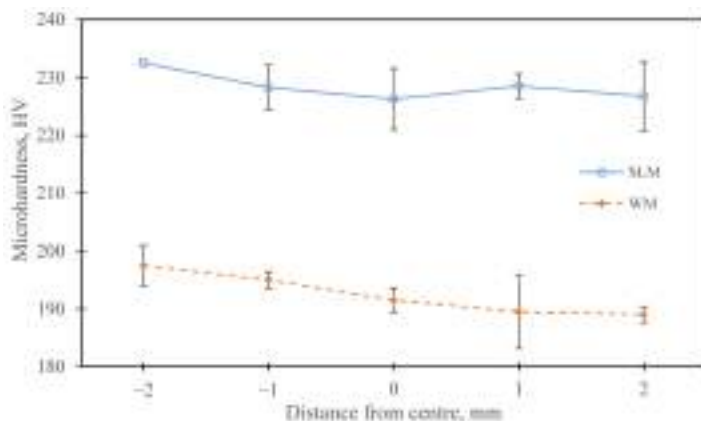


Figure 11. Average microhardness (HV) values for SLM and WM specimens.

4. Conclusions

The SLM-built 316L SS samples were able to achieve high densification levels (>99%) with a low average porosity content (~0.82%). Even though the porosity content in the SLM-built parts was very low, the pores were not evenly distributed throughout the samples. The highest porosity content in the concentrated regions was found to be ~1.68% which was higher than the overall average. Such low porosity content does not show an obvious impact on the mechanical properties of the AM 316L SS samples produced in this study. The higher average microhardness values of the SLM-fabricated 316L SS parts compared to their wrought manufactured counterpart were primarily attributed to the localised melting of the powder layers, and the rapid heating/cooling cycle involved during SLM contributed to the fine-grain microstructures in the completed parts.

Author Contributions: Shahir Mohd Yusuf analysed the data and wrote the manuscript; Yifei Chen carried out the experiments and analysed the data; Richard Boardman prepared and carried out the XCT scan; Shoufeng Yang and Nong Gao are experts in additive manufacturing (AM) and metallurgy, respectively, and they also managed and supervised the project.

Conflicts of Interest: The authors declare no conflict of interest.

References

- Cherry, J.A.; Davies, H.M.; Mehmood, S.; Lavery, N.P.; Brown, S.G.R.; Sienz, J. Investigation into the effect of process parameters on microstructural and physical properties of 316L stainless steel parts by selective laser melting. *Int. J. Adv. Manuf. Technol.* **2014**, *76*, 869–879. [[CrossRef](#)]
- Yusuf, S.M.; Gao, N. Influence of energy density on metallurgy and properties in metal additive manufacturing. *Mater. Sci. Technol.* **2017**. [[CrossRef](#)]
- Guo, N.; Leu, M.C. Additive manufacturing: Technology, applications and research needs. *Front. Mech. Eng.* **2013**, *8*, 215–243. [[CrossRef](#)]

4. Zhang, L.C.; Attar, H. Selective Laser Melting of Titanium Alloys and Titanium Matrix Composites for Biomedical Applications: A Review. *Adv. Eng. Mater.* **2016**, *4*, 463–475. [CrossRef]
5. Frazier, W.E. Metal Additive Manufacturing: A Review. *J. Mater. Eng. Perform.* **2014**, *23*, 1917–1928. [CrossRef]
6. Gu, D.D.; Meiners, W.; Wissenbach, K.; Poprawe, R. Laser additive manufacturing of metallic components: Materials, processes and mechanisms. *Int. Mater. Rev.* **2012**, *57*, 133–164. [CrossRef]
7. Rafi, H.K.; Karthik, N.V.; Gong, H.; Starr, T.L.; Stucker, B.E. Microstructures and mechanical properties of Ti6Al4V parts fabricated by selective laser melting and electron beam melting. *J. Mater. Eng. Perform.* **2013**, *22*, 3872–3883. [CrossRef]
8. Liu, Y.J.; Li, S.J.; Wang, H.L.; Hou, W.T.; Hao, Y.L.; Yang, R.; Sercombe, T.B.; Zhang, L.C. Microstructure, defects and mechanical behavior of beta-type titanium porous structures manufactured by electron beam melting and selective laser melting. *Acta Mater.* **2016**, *113*, 56–67. [CrossRef]
9. Liu, Y.J.; Wang, H.L.; Li, S.J.; Wang, S.G.; Wang, W.J.; Hou, W.T.; Hao, Y.L.; Yang, R.; Zhang, L.C. Compressive and fatigue behavior of beta-type titanium porous structures fabricated by electron beam melting. *Acta Mater.* **2017**, *126*, 58–66. [CrossRef]
10. Liu, F.; Lin, X.; Yang, G.; Song, M.; Chen, J.; Huang, W. Microstructure and residual stress of laser rapid formed Inconel 718 nickel-base superalloy. *Opt. Laser Technol.* **2011**, *43*, 208–213. [CrossRef]
11. Riemer, A.; Leuders, S.; Thöne, M.; Richard, H.A.; Tröster, T.; Niendorf, T. On the fatigue crack growth behavior in 316L stainless steel manufactured by selective laser melting. *Eng. Fract. Mech.* **2013**, *120*, 15–25. [CrossRef]
12. Hao, L.; Dadbakhsh, S.; Seaman, O.; Felstead, M. Selective laser melting of a stainless steel and hydroxyapatite composite for load-bearing implant development. *J. Mater. Process. Technol.* **2009**, *209*, 5793–5801. [CrossRef]
13. Mathisen, M.B. In-Situ Tensile Testing Combined with EBSD Analysis of Ti-6Al-4V Samples from Components Fabricated by Additive Layer Manufacture. Master's Thesis, Norwegian University of Science and Technology, Trondheim, Norway, June 2012.
14. Yan, C.; Hao, L.; Hussein, A.; Young, P.; Raymont, D. Advanced lightweight 316L stainless steel cellular lattice structures fabricated via selective laser melting. *Mater. Des.* **2014**, *55*, 533–541. [CrossRef]
15. Verlee, B.; Dormal, T.; Lecomte-Beckers, J. Density and porosity control of sintered 316L stainless steel parts produced by additive manufacturing. *Powder Metall.* **2012**, *55*, 260–267. [CrossRef]
16. Dewidar, M.; Khalil, A.; Lim, J.K. Processing and mechanical properties of porous 316L stainless steel for biomedical applications. *Trans. Nonferr. Met. Soc. China* **2007**, *17*, 468–473. [CrossRef]
17. AlMangour, B.; Grzesiak, D.; Yang, J.M. Selective laser melting of TiC reinforced 316L stainless steel matrix nanocomposites: Influence of starting TiC particle size and volume content. *Mater. Des.* **2016**, *104*, 141–151. [CrossRef]
18. AlMangour, B.; Grzesiak, D.; Yang, J.M. Rapid fabrication of bulk-form TiB₂/316L stainless steel nanocomposites with novel reinforcement architecture and improved performance by selective laser melting. *J. Alloy. Compd.* **2016**, *680*, 480–493. [CrossRef]
19. AlMangour, B.; Grzesiak, D.; Yang, J.M. Selective laser melting of TiB₂/316L stainless steel composites: The roles of powder preparation and hot isostatic pressing post-treatment. *Powder Technol.* **2017**, *309*, 37–48. [CrossRef]
20. Yasa, E.; Kruth, J.P. Microstructural investigation of Selective Laser Melting 316L stainless steel parts exposed to laser re-melting. *Proced. Eng.* **2011**, *19*, 389–395. [CrossRef]
21. Jinhui, L.; Ruidi, L.; Wenxian, Z.; Liding, F.; Huashan, Y. Study on formation of surface and microstructure of stainless steel part produced by selective laser melting. *Mater. Sci. Technol.* **2010**, *26*, 1259–1264. [CrossRef]
22. Carter, L.N.; Martin, C.; Withers, P.J.; Attallah, M.M. The influence of the laser scan strategy on grain structure and cracking behaviour in SLM powder-bed fabricated nickel superalloy. *J. Alloy. Compd.* **2014**, *615*, 338–347. [CrossRef]
23. Thijss, L.; Kempen, K.; Kruth, J.P.; van Humbeeck, J. Fine-structured aluminium products with controllable texture by selective laser melting of pre-alloyed AlSi10Mg powder. *Acta Mater.* **2013**, *61*, 1809–1819. [CrossRef]
24. Otsu, N. A threshold selection method from gray-level histograms. *IEEE Trans. Syst. Man. Cybern.* **1979**, *9*, 62–66. [CrossRef]

25. Lu, Y.; Wu, S.; Gan, Y.; Huang, T.; Yang, C.; Junjie, L.; Lin, J. Study on the microstructure, mechanical property and residual stress of SLM Inconel-718 alloy manufactured by differing island scanning strategy. *Opt. Laser Technol.* **2015**, *75*, 197–206. [CrossRef]
26. Zhou, X.; Li, K.; Zhang, D.; Liu, X.; Ma, J.; Liu, W.; Shen, Z. Textures formed in a CoCrMo alloy by selective laser melting. *J. Alloy. Compd.* **2015**, *631*, 153–164. [CrossRef]
27. Hedberg, Y.S.; Qian, B.; Shen, Z.; Virtanen, S.; Odnevall Wallinder, I. In vitro biocompatibility of CoCrMo dental alloys fabricated by selective laser melting. *Dent. Mater.* **2014**, *30*, 525–534. [CrossRef] [PubMed]
28. Zietala, M.; Durejko, T.; Polanski, M.; Kunce, I.; Plocinski, T.; Zielenski, W.; Lazinska, M.; Stepnowski, W.; Czujko, T.; Kurzydlowski, K.J.; et al. The microstructure, mechanical properties and corrosion resistance of 316L stainless steel fabricated using laser engineered net shaping. *Mater. Sci. Eng. A* **2016**, *677*, 1–10. [CrossRef]
29. Zhong, Y.; Liu, L.; Wikman, S.; Cui, D.; Shen, Z. Intragranular cellular segregation network structure strengthening 316L stainless steel prepared by selective laser melting. *J. Nucl. Mater.* **2016**, *470*, 170–178. [CrossRef]
30. Gustmann, T.; Neves, A.; Kühn, U.; Gargarella, P.; Kiminami, C.S.; Bolfarini, C.; Eckert, J.; Pauly, S. Influence of processing parameters on the fabrication of a Cu-Al-Ni-Mn shape-memory alloy by selective laser melting. *Addit. Manuf.* **2016**, *11*, 23–31. [CrossRef]
31. Marya, M.; Singh, V.; Marya, S.; Hascoet, J.Y. Microstructural Development and Technical Challenges in Laser Additive Manufacturing: Case Study with a 316L Industrial Part. *Metall. Mater. Trans. B Process Metall. Mater. Process. Sci.* **2015**, *46*, 1654–1665. [CrossRef]
32. Liu, Z.H.; Zhang, D.Q.; Sing, S.L.; Chua, C.K.; Loh, L.E. Interfacial characterization of SLM parts in multi-material processing: Metallurgical diffusion between 316L stainless steel and C18400 copper alloy. *Mater. Charact.* **2014**, *94*, 116–125. [CrossRef]
33. Dadbakhsh, S.; Hao, S. Effect of Al alloys on selective laser melting behaviour and microstructure of in situ formed particle reinforced composites. *J. Alloy. Compd.* **2012**, *541*, 328–334. [CrossRef]
34. Sames, W.J.; List, F.A.; Pannala, S.; Dehoff, R.R.; Babu, S.S. The metallurgy and processing science of metal additive manufacturing. *Int. Mater. Rev.* **2016**, *6608*, 1–46. [CrossRef]
35. King, W.E.; Barth, H.D.; Castillo, V.M.; Gallegos, G.F.; Gibbs, J.W.; Hahn, D.E.; Kamath, C.; Rubenchik, A.M. Observation of keyhole-mode laser melting in laser powder-bed fusion additive manufacturing. *J. Mater. Process. Technol.* **2014**, *214*, 2915–2925. [CrossRef]
36. Körner, C.; Bauereiß, A.; Attar, E. Fundamental consolidation mechanisms during selective beam melting of powders. *Model. Simul. Mater. Sci. Eng.* **2013**, *21*, 1–18. [CrossRef]
37. Tammas-Williams, S.; Zhao, H.; Léonard, F.; Derguti, F.; Todd, I.; Prangnell, P.B. XCT analysis of the influence of melt strategies on defect population in Ti-6Al-4V components manufactured by Selective Electron Beam Melting. *Mater. Charact.* **2015**, *102*, 47–61. [CrossRef]
38. Frazier, W.E. Direct digital manufacturing of metallic components: Vision and roadmap. In Proceedings of the 21st Annual International Solid Freeform Fabrication Symposium, Austin, TX, USA, 9–11 August 2010; pp. 717–732.
39. Campanelli, S.L.; Contuzzi, N.; Angelastro, A.; Ludovico, A.D. Capabilities and Performances of the Selective Laser Melting Process. In *New Trends in Technologies: Devices, Computer, Communication and Industrial Systems*; Er, M.J., Ed.; InTech Europe: Rijeka, Croatia, 2010; pp. 233–252.
40. Qiu, C.; Panwisawas, C.; Ward, M.; Basoalto, H.C.; Brooks, J.W.; Attallah, M.M. On the role of melt flow into the surface structure and porosity development during selective laser melting. *Acta Mater.* **2015**, *96*, 72–79. [CrossRef]
41. Maskery, I.; Aboulkhair, N.T.; Corfield, M.R.; Tuck, C.; Clare, A.T.; Leach, R.K.; Wildman, R.D.; Ashcroft, I.A.; Hague, R.J.M. Quantification and characterisation of porosity in selectively laser melted Al-Si10-Mg using X-ray computed tomography. *Mater. Charact.* **2016**, *111*, 193–204. [CrossRef]
42. Kang, N.; Coddet, P.; Liu, Q.; Liao, H.; Coddet, C. In-situ TiB/near α Ti matrix composites manufactured by selective laser melting. *Addit. Manuf.* **2016**, *11*, 1–6. [CrossRef]
43. Niendorf, T.; Leuders, S.; Riemer, A.; Richard, H.A.; Tröster, T.; Schwarze, D. Highly anisotropic steel processed by selective laser melting. *Metall. Mater. Trans. B Process Metall. Mater. Process. Sci.* **2013**, *44*, 794–796. [CrossRef]

44. Qiu, C.; Adkins, N.J.E.; Attallah, M.M. Microstructure and tensile properties of selectively laser-melted and of HIPed laser-melted Ti-6Al-4V. *Mater. Sci. Eng. A* **2013**, *578*, 230–239. [CrossRef]
45. Dai, N.; Zhang, L.C.; Zhang, J.; Zhang, X.; Ni, Q.; Chen, Y.; Wu, M.; Yang, C. Distinction in corrosion resistance of selective laser melted Ti-6Al-4V alloy on different planes. *Corros. Sci.* **2016**, *111*, 703–710. [CrossRef]
46. Wu, A.S.; Brown, D.W.; Kumar, M.; Gallegos, G.F.; King, W.E. An Experimental Investigation into Additive Manufacturing-Induced Residual Stresses in 316L Stainless Steel. *Metall. Mater. Trans. A Phys. Metall. Mater. Sci.* **2014**, *45*, 6260–6270. [CrossRef]
47. Thijss, L.; Montero Sistiaga, M.L.; Wauthle, R.; Xie, Q.; Kruth, J.P.; van Humbeeck, J. Strong morphological and crystallographic texture and resulting yield strength anisotropy in selective laser melted tantalum. *Acta Mater.* **2013**, *61*, 4657–4668. [CrossRef]
48. Tolosa, I.; Garcíandía, F.; Zubiri, F.; Zapirain, F.; Esnaola, A. Study of mechanical properties of AISI 316 stainless steel processed by “selective laser melting”, following different manufacturing strategies. *Int. J. Adv. Manuf. Technol.* **2010**, *51*, 639–647. [CrossRef]
49. Saeidi, K.; Gao, X.; Zhong, Y.; Shen, Z.J. Hardened austenite steel with columnar sub-grain structure formed by laser melting. *Mater. Sci. Eng. A* **2015**, *625*, 221–229. [CrossRef]



© 2017 by the authors. Licensee MDPI, Basel, Switzerland. This article is an open access article distributed under the terms and conditions of the Creative Commons Attribution (CC BY) license (<http://creativecommons.org/licenses/by/4.0/>).

Article

Case Studies on Local Reinforcement of Sheet Metal Components by Laser Additive Manufacturing

Markus Bambach ^{1,*}, Alexander Sviridov ¹, Andreas Weisheit ² and Johannes Henrich Schleifenbaum ^{2,3}

¹ Mechanical Design and Manufacturing, Brandenburg University of Technology Cottbus-Senftenberg, Konrad-Wachsmann-Allee 17, 03046 Cottbus, Germany; sviridov@b-tu.de

² Fraunhofer Institute for Laser Technology ILT/Chair for Laser Technology LLT, RWTH Aachen, Steinbachstraße 15, 52074 Aachen, Germany; andreas.weisheit@ilt.fraunhofer.de (A.W.); johannes.henrich.schleifenbaum@ilt.fraunhofer.de (J.H.S.)

³ Digital Additive Production, RWTH Aachen, Steinbachstraße 15, 52074 Aachen, Germany

* Correspondence: bambach@b-tu.de; Tel.: +49-355-69-3108

Academic Editor: Manoj Gupta

Received: 31 December 2016; Accepted: 20 March 2017; Published: 25 March 2017

Abstract: This paper details two case studies that make use of laser metal deposition for local reinforcement of sheet metal components. Two benchmark scenarios are investigated, both using aluminum alloys: (i) using laser cladding to increase the stiffness of a pre-formed component, and (ii) applying a local cladding on sheet metal for increasing the thickness prior to a hole-flanging operation. The results show that both routes are viable. Applying claddings onto sheet metal before a metal forming operation must ensure suitable formability, which may be limited by the layer material and undesired changes in the microstructure of the sheet. The limited formability has to be taken into account in the design of the forming operation. Cladding onto already formed components has to cope with inevitable distortion of the component. Nevertheless, introducing additive manufacturing into the field of sheet metal forming opens the possibility to produce new products such as tailored laser-cladded blanks, combinations of sheet and bulk components and to develop new methods such as stiffness management in lightweight design.

Keywords: tailored blanks; additive manufacturing; laser deposition welding

1. Introduction

In many applications, local reinforcement of sheet metal components may be necessary or desired, e.g.:

- to support highly loaded areas that bear fasteners or joints;
- to create functional elements;
- to compensate for sheet thinning occurring during metal forming operations;
- to manufacture parts for vehicle derivatives from series parts;
- for acoustic reasons or
- for corrosion and wear protection.

Figure 1 shows a typical application where a local reinforcement would be useful to improve the performance of the component without resorting to a sheet metal of increased thickness. The rivet nut in Figure 1a could be replaced by a formed flange (created by a hole-flanging operation) into which a thread is cut. This solution would save weight and reduce the risk of corrosion attack. Replacing the rivet nut by a formed flange is only feasible if the flange provides sufficient sheet thickness. Flanging operations, however, typically lead to sheet thinning, as shown in Figure 1b.

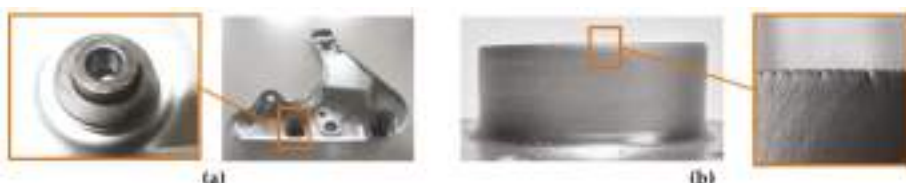


Figure 1. (a) A rivet nut inserting loads into a sheet metal component; (b) Hole-flanging operation with extreme thinning of the flange.

Tailored blanks and patchwork blanks [1] are semi-finished products with a variable thickness. They allow for material cost savings of up to 10% [2] and can have thickness differences of up to 50% within a steel strip/blank [3]. Three main types of tailored blanks can be distinguished [1], Figure 2:

- Tailor Welded Blanks (TWB), where sheet metal blanks with a different thickness are joined by a welding process;
- Tailor Rolled Blanks (TRB), where thickness variations in the sheet metal are accomplished by changing the roll gap height during rolling; and
- Patchwork Blanks (PB), where a local increase in the sheet thickness is made possible by welding, gluing or soldering sheet metal patches onto sheet metal blanks.

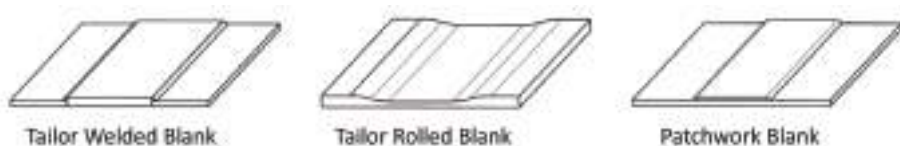


Figure 2. Three main variants of tailored blanks.

As shown in Figure 2, both the geometry of the thickened zones and the course of the sheet thickness are geometrically limited with commercially available tailored blanks. Even patchwork blanks, the most flexible variant of tailored blanks, have several limitations from a technological and economic point of view, including:

- a constant, not load-optimized thickness of the patch;
- the production of scrap during blanking of the patches;
- a high susceptibility to corrosion in the gap between sheet metal and patch;
- a problematic further processing (including low formability and springback);
- with patches attached by gluing a high susceptibility to ageing.

A possible solution for the application shown in Figure 1 is to manufacture local reinforcements using emerging additive manufacturing processes such as Laser Metal Deposition (LMD). In this paper, the term 'laser cladding' will be used, which stands for the same technology but is more precise with respect to the fact that layers are deposited. The principle of laser cladding is shown in Figure 3. The laser beam melts a thin layer of the substrate as well as the introduced powder particles, leading to a layer with nearly 100% density and metallurgical bonding to the substrate. The powder is fed by a disc feeder in a carrier gas stream of argon. The carrier gas also shields the melt pool from the surrounding atmosphere [4]. The method is primarily used for local wear protection [5] and for the repair of high-quality components, e.g., jet-engine parts [6]. Compared to other cladding methods like PTA (Plasma Transferred Arc) laser cladding has the advantage of high precision and minimum heat

input. However, the deposition of the material to the component can lead to intolerable distortion of the sheet so that it is possibly more advantageous to use it to reinforce the semi-finished product.

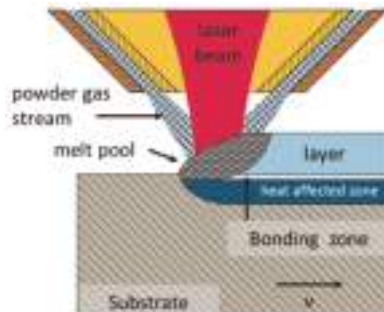


Figure 3. Principle of powder-based laser cladding.

Basic knowledge about the possibilities of using additive manufacturing for local modification of semi-finished products and components as well as comparative studies of the properties and economy compared to available solutions are lacking at the moment. This work details two case studies investigating the possibilities offered by laser cladding for increasing the sheet thickness of semi-finished and formed components.

2. Materials and Methods

2.1. Materials

The nominal compositions of the materials used are listed in Table 1. As sheet material, the aluminum alloy EN AW 6082 was chosen. As powder material, two similar Al-Si-alloys were chosen that exhibit good performance in laser additive manufacturing [7]. For both alloys, experience and parameters for laser cladding are available at the Fraunhofer ILT (AlSi10Mg) and BTU Cottbus-Senftenberg (AlSi12); therefore, no parameter studies for cladding had to be conducted. However, it should be noted that for the demonstrator II (see Section 2.4) a limited formability of the cladded layer will result due to the high Si content. The demonstrator is formed by a hole-flanging operation with fairly limited plastic deformation. Future investigations will include wrought aluminum alloys to allow for larger plastic deformation.

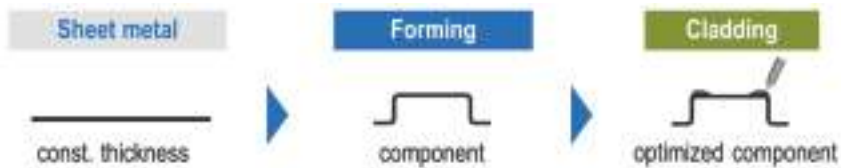
Table 1. Nominal composition (wt. %) of the sheet material and the powder for laser cladding.

Materials	Si	Fe	Mn	Mg	Al
Sheet EN AW 6082	0.7–1.3	max. 0.5	0.4–1.0	0.6–1.2	Balance
Powder AlSi10 Mg	9–11	max. 0.55	max. 0.45	max. 0.45	Balance
Powder AlSi12	11–13	not specified	not specified	not specified	Balance

2.2. Overview of Application Scenarios

The case studies investigated in the remainder of this work represent two application scenarios of local reinforcements and two different process chains:

1. **In the first case, cladding is applied to the formed component:** the increase in sheet thickness improves the stiffness of the component. In this case, a sizing operation (numerical optimization) needs to be performed to determine the optimal thickness profile.



2. In the second case, laser cladding is applied to the semi-finished product before forming: as forming operation, hole flanging is considered. Since flanging may reduce the sheet thickness, thickening by cladding may allow the desired minimum sheet thickness to remain, e.g., for cutting a thread into the flange, as shown in Figure 1.



In the following, both routes are described individually.

2.3. Demonstrator I: Stiffness Management of Pre-Formed Part

2.3.1. Demonstrator Geometry and Optimization Task

An idealized suspension dome made of the aluminum wrought alloy EN AW 6082 is used as a demonstrator (Figure 4) to analyze the possibility of stiffness management by local, additively manufactured reinforcements. The basic part shown in Figure 4a is a cylindrical cup with a wall thickness of 1 mm and a central hole in the top face. In a real suspension dome, the suspension would be fastened to the central hole, which would transmit the suspension forces into the car body structure.

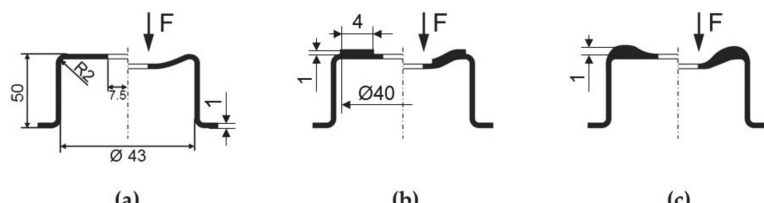


Figure 4. Demonstrator geometry as basis variant (a) and possible alternatives with increased stiffness: patchwork blank (b) and tailored laser cladding (c).

Based on the given component geometry, we look for possibilities to increase the part stiffness under the central load using a minimum of added material. Such an increase in stiffness could be required in a variant with a heavier engine or, alternatively, simply to save weight. Thus, we look for a thickness distribution that minimizes the deflection of the hole edge and design it using patchwork blanks, Figure 4b, and using a laser-cladded reinforcement, Figure 4c. The total added material volume is equal in both cases. The case study should show the advantages of the stiffness-optimized variant compared to the basic variant and the patchwork blank.

To define the geometry of the laser cladding, a sizing optimization of the basic variant was carried out using Abaqus/TOSCA to determine an optimal non-linear thickness distribution resulting in a

substantial increase in stiffness. The rim around the central hole was loaded with a vertical force of 600 N, which is low enough to cause only elastic deflection. In the sizing optimization, the top face of the part was selected as design region. The area around the central hole was excluded to account for the fact that a flat region is needed to apply the external load. This would also be the case in a real suspension dome.

The solver minimizes the displacement of the loaded rim under the constraint that the added material volume must not exceed the volume of the patch with a cross section of 1×4 mm in Figure 4b. Also, a maximum thickness increase of 1 mm is specified. The result of sizing optimization is compared to the stiffness of both other cases. The comparison of all cases was performed using finite element analysis. In addition, laser cladding experiments were carried out to produce the tailored cladding shown in Figure 4c. The stiffness of the basic variant and of the part with local reinforcement was tested in experiments under static loads.

2.3.2. Laser Cladding Experiments

In order to approach the solution with reinforcement, experimental trials using laser cladding were performed. A ring-shaped thickening of AlSi10Mg with a width of 4 mm, a thickness of 1 mm and an outer diameter of 40 mm was applied to a pre-shaped sample (alloy EN AW 6082) with a wall thickness of 1 mm, according to Figure 4a. The laser source was a fiber coupled diode laser ($\lambda = 1025$ and 1040 nm) with an output power of 2 kW. The beam diameter was 0.6 mm, the intensity distribution top hat. The beam followed a spiral path with a pitch of 0.3 mm per revolution. Cladding was performed with a feed of 4000 mm/min, a laser power of 860 W and a powder feed rate of 1.2 g/min. Three layers had to be cladded to achieve the desired thickness. A laser clad specimen was cut and a cross section was prepared using standard metallographic techniques.

2.3.3. Testing of Component Stiffness

In order to estimate the potential of the local reinforcement, thickened by tailored laser cladding (Figure 4c) and non-thickened (Figure 4a) components were tested under static loads in a Zwick Z250 testing machine (Zwick GmbH & Co. KG, Ulm, Germany). Surface machining operations were applied before testing to improve the surface quality and to correct the geometry for precise comparison of the results. Furthermore this allows a parallel alignment of the top face where the load is applied to the bottom pedestal. During the experiments the force-displacement characteristics were recorded.

2.4. Demonstrator II: Flanging of Locally Clad Sheet

2.4.1. Demonstrator Geometry

This demonstrator is concerned with the manufacturing of a local cladding on sheet metal blanks, which are subsequently processed by hole flanging. Hole flanges are important functional elements in many sheet metal parts. They provide stiffness, allow for positioning and fixation, etc. Increasing the wall thickness of the flange may be necessary for subsequent operations such as cutting a thread into the flange, as detailed in the introduction of the paper. The case study comprises the manufacturing of cladded blanks in two different variants, cladding on the outside of the flange, Figure 5a, and on the inside of the flange, Figure 5b.



Figure 5. Investigated types of the cladding for local reinforcement: cladding on the outside of flange (a) and cladding on the inside of the flange (b).

2.4.2. Production of Tailored Laser-Cladded Blanks

As sheet metal, the aluminum alloy EN AW 6082 was chosen, as in the first demonstrator. Circular blanks of 2 mm thickness and 76 mm diameter were cut. As powder for laser cladding, the cast alloy AlSi12 was used. A Trumpf TruLaser Cell 7040 (TRUMPF GmbH & Co. KG, Ditzingen, Germany) operated with a CO₂ laser with a maximum power of 5000 W was used for cladding. The sheet metal blank was cooled during the welding process using a water-cooled aluminum plate, which was positioned below the sample. At the same time, the specimen was held in place by a fixture system to reduce the heat-induced warping. Claddings with a diameter of 20 mm and a thickness of 0.75 mm were programmed. The final height of the cladding relative to the base sheet was 0.7 mm on average. A laser power of 3400 W, a feed rate of 400 mm/min, a powder mass flow rate of 1.6 g/min and a mixture of helium and argon as shielding gas were used as process parameters. Three cladding strategies were investigated (Figure 6).

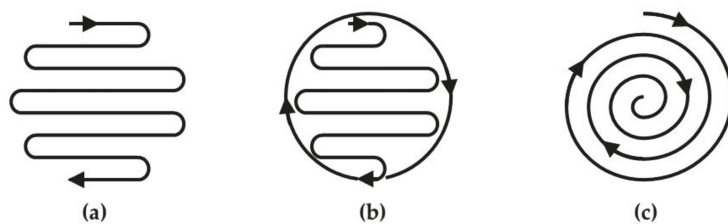


Figure 6. Investigated cladding strategies for creating a disc-shaped reinforcement. (a) straight path of the laser beam with parallel offset; (b) straight path of the laser beam with parallel offset + circular outline; (c) spiral path of laser beam.

2.4.3. Light Optical Microscopy (LOM)

Laser-clad specimens were cut and cross sections were prepared. The samples were ground flat with successively finer grades of SiC paper and then diamond polished until all deep scratches from grinding were removed (9 µm/for 10 min, 3 µm/for about 30 min, 1 µm/for 5 min). In the final stage, the samples were etched with Keller reagent (3 mL HCl + 5 mL HNO₃ + 1 mL HF + 190 mL water) for revealing the ‘weld microstructure’. The microscopic examination of the etched samples was conducted using an optical microscope from Leica Mikrosysteme Vertrieb GmbH, Wetzlar, Germany.

2.4.4. Hole-Flanging Experiments

Hole-flanging operations in sheet metal parts are typically performed using a punch that deforms a pierced sheet metal into a matrix, see Figure 7a. The sheet metal is clamped using a blank holder. In the case considered here, the area deformed by the flanging operation is thickened using laser cladding. The specimen geometry is shown in Figure 7b.

Table 2 gives an overview of the experimental tests that were performed. In addition to samples with a cladding of 0.7 mm on specimens with 2.0 mm thickness, monolithic sheet metal of 2.0 mm and 2.5 mm thickness was tested. The thickness of the inclad specimens corresponds to the clearance between punch and matrice for $t = 2.5$ mm and is smaller in the case of $t = 2$ mm. For the cladded specimens, a slightly larger thickness was chosen to exert pressure during forming, hence decreasing the chance to damage the relatively brittle clad material.

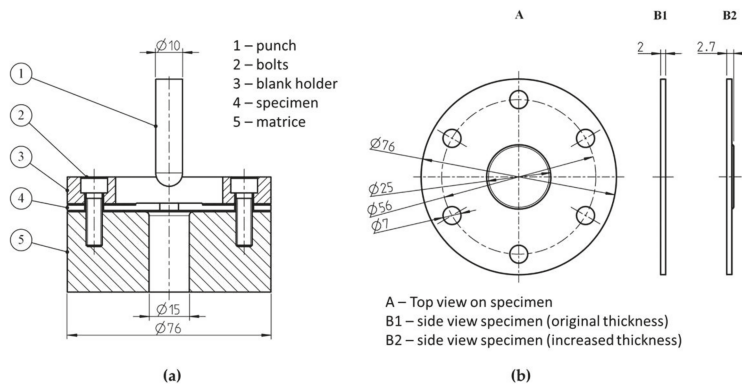


Figure 7. (a) Test set-up for hole-flanging; (b) specimen geometry with and without cladding.

Table 2. Overview of hole-flanging experiments.

Thickness [mm]	Cladding Position	Hole Diameter [mm]	Hole Expansion [%]
2.0/2.5	None	8.0	25.0
2.7	inside/outside	8.0	25.0
2.0/2.5	None	7.5	33.3
2.7	inside/outside	7.5	33.3
2.0/2.5	None	7.0	42.9
2.7	inside/outside	7.0	42.9

3. Results

3.1. Results for Demonstrator I—Stiffness Management

3.1.1. Results of the Sizing Optimization

The solution of the sizing optimization is shown in Figure 8 in terms of thickness increase vs. thickness of base material. An optimal increase in stiffness under the given mass constraint is obtained by a non-linear increase in sheet thickness in a ring-shaped area close to the central hole. Sizing optimization yields a smooth transition between thickened area and the flat top face of the component towards the outer radius of the part, and a jump in sheet thickness towards the central hole.

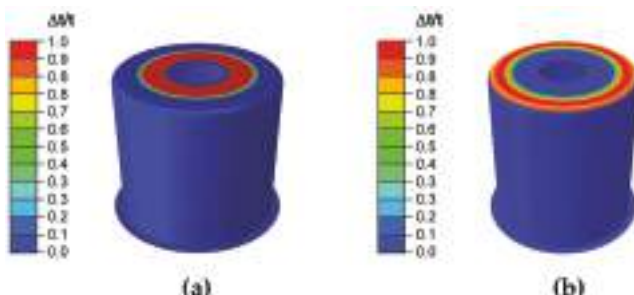


Figure 8. Result of sizing optimization. (a) Optimum thickness distribution; (b) Optimum under the constraint that an inner radius of 15 mm is not used for cladding.

Obviously, a maximum increase in stiffness is achieved by supporting the edge of central hole with additional material. However, laser cladding close to the unsupported inner hole leads to a significantly higher risk of distortion than in the case of cladding at the outer edge of the dome. To evaluate the influence of the position of the cladded layer on the distortion simulations of the plastic strain caused by the laser cladding process were performed. To this end, single circular paths of the laser cladding process were simulated and the occurrence of plastic deformation was monitored. According to the experimental settings, the beam diameter was set to 0.6 mm, the feed rate was 4000 mm/min and the laser power was 860 W. The moving laser spot is simulated as moving heat source using the user subroutine *DFLUX in the ABAQUS finite element solver. The top hat distribution used in the experiment is specified through this routine. Laser spot size, power and feed rate match the experimental values. It is assumed that 60% of the laser energy are absorbed by the material in accordance with earlier investigations. The simulation considered only the heat input by the laser source and no powder flow and build-up volume. It is therefore only a rough estimation of the stresses and strains occurring. The results given in Figure 9 show that circular laser paths close to the inner hole lead to small plastic deformation, i.e., permanent distortion of the component. For a distance of more than 15 mm from the center, no plastic deformation is observed.

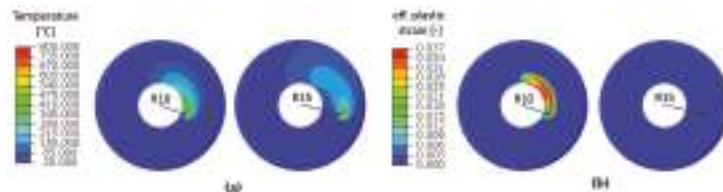


Figure 9. Simulation of heat input during laser cladding (a) and plastic deformation due to thermal stresses (b).

Based on these findings, a second design was calculated which penalizes the distance to the center hole, i.e., the closer the thickness increase is situated to the central hole, the higher the penalty, Figure 8b. This led to a second, pareto-optimal variant which is compared to the initially found design and to the reference cases of a homogeneous thickness and a patchwork blank in the following.

3.1.2. Microstructure of the Cladding

Figure 10 shows a cross section of the cladded layers, which exhibits the typical fine dendritic microstructure of primary solidified Al crystals (light) and interdendritic solidified Si (dark). Firm bonding to the substrate is observed.

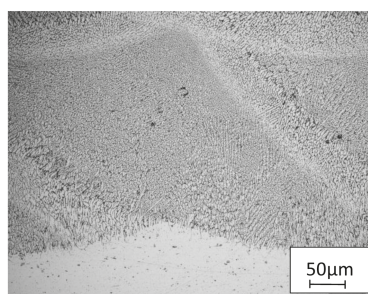


Figure 10. Microstructure of as-clad AlSi10Mg; Al solid solution (light) and Si (dark).

3.1.3. Stiffness Properties of the Reinforced Parts

Figure 11 shows the results obtained by testing the basic variant and the optimized design which contains a thickened area in the radius region. In this case, with six percent added mass, a stiffness increase of 95% was obtained. This is more than the stiffness increase obtained with a patchwork blank of constant thickness. Figure 12b shows a comparison to a patchwork blank that uses a patch of the same mass as the produced cladding. The chosen design still outperforms the patchwork blank but falls behind the possibilities offered by sizing optimization, Figure 12c. This solution increases the stiffness by 163% with only 4.7% added mass, but will probably lead to distortion of the component.

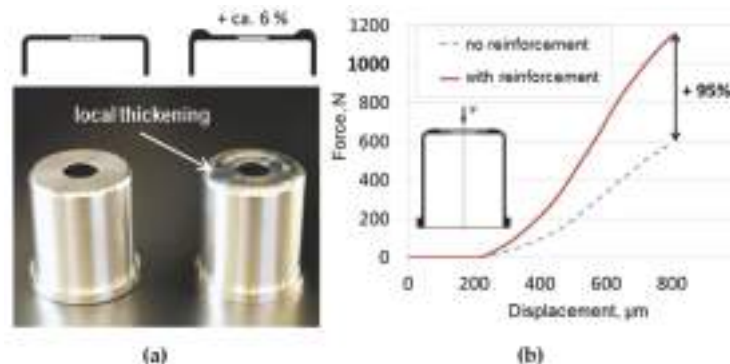


Figure 11. (a) Original part and part with local reinforcement; (b) Results of static testing.

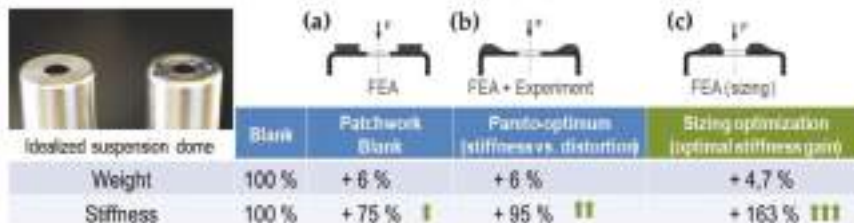


Figure 12. Increase in stiffness and weight for three different reinforcements. (a) Patchwork blank; (b) Tailored laser cladding, pareto-optimum; (c) Tailored laser cladding, sizing optimization.

3.2. Results for Demonstrator II—Hole-Flanging of Tailored Laser-Cladded Blanks

3.2.1. Laser Cladding Strategies

Figure 13 shows the results of the three different cladding strategies, revealing that strategy with the spiral path of the laser beam (Figure 13c) yields the cladding with the most appropriate surface. Strategies with straight path with parallel offset of the laser beam (Figure 13a,b) did not allow to produce claddings without defects in the start and end positions.

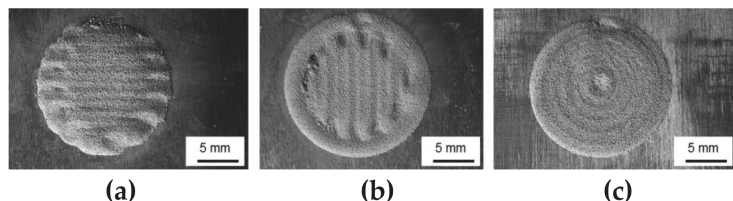


Figure 13. Comparison of different path strategies for laser cladding. (a) straight path with parallel offset of the laser beam; (b) straight path with parallel offset of the laser beam + circular outline; (c) spiral path of the laser beam.

3.2.2. LOM of the Cladding

The cladding shown in Figure 13c was analyzed metallographically. The interface between base material and clad layer is shown in Figure 14. The micrographs indicate a good connection between the base material and the deposited layers. Three different zones can be distinguished: the deposition layer, a thin heat affected zone and the base material. The former solid–liquid interface deeply penetrates into the substrate which results in about 50% dissolution between base and clad material. It can be seen that the solidification of the melt starts at the boundary of the base material in a columnar way. The high cooling rate associated with a rapid solidification promotes a fine dendritic microstructure in the deposited layer. The transition between cladding and base material is smooth. Hence, no stiffness jump and no stress localization are to be expected, which may be advantageous compared to patchwork blanks. The samples showed some porosity of the clad layer. A pore is magnified in Figure 14c.

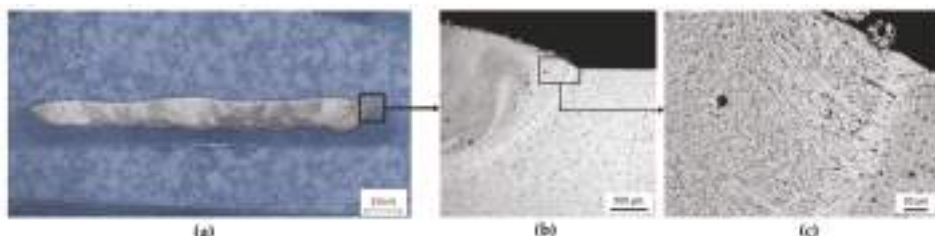


Figure 14. (a) overview of clad layer (b) micrograph of the interface cladding—base material; (c) a pore in the cladding.

3.2.3. Hole-Flanging Experiments

The results of the flanging experiments show that the flanging operation with monolithic sheet metal was feasible with all hole expansion ratios (cf. Table 2). For the specimens with a cladding on the inside of the flange (facing the punch), cracks were observed in the radius of the flange, which is stretched during forming. Cladding on the outside of the flange led to failure primarily in the edge of the cut hole. Examples of these failures are shown in Figure 15. Figure 16b shows a micrograph through a crack that was generated in the cladding during forming. The curvature of the crack propagation indicates that the crack has formed along the grain boundaries where the brittle Si phase is concentrated. Figure 17 shows the results of successful flanging experiments with and without cladding, with machined holes of seven-millimeter radius.



Figure 15. Testing of original part and part with local reinforcement.

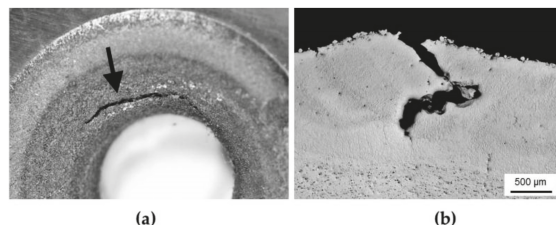


Figure 16. Micrograph of a crack that occurred in the cladding during plastic deformation. (a) overview of clad layer in the hole area; (b) Micrograph through a crack.

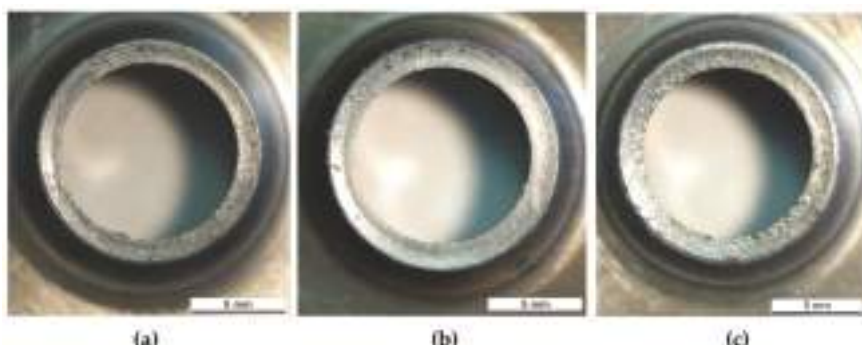


Figure 17. Results of successful hole-flanging experiments, (a) $t = 2$ mm, no cladding; (b) $t = 2.5$ mm, no cladding. (c) $t = 2.7$ mm, 0.7 mm cladding.

4. Discussion

The results obtained in the two case studies will be discussed regarding general viability and applicability of laser cladding to sheet metal components, as well as regarding production time and material efficiency:

General viability and scope of application. Two application scenarios were studied which use laser cladding for local reinforcement of sheet metal components, i.e., local cladding of a component for increased stiffness and local cladding to increase the sheet thickness in the wall of a flange produced by hole flanging.

Laser cladding of an already manufactured component opens up the possibility to use additive manufacturing for stiffness management, a new field of application. The challenge here is not the cladding process of a suitable material but the reduction of distortion and a minimum change in

the microstructure (and thus the properties) of the base material. Since laser cladding would be the last process step in the manufacturing route of the component, straightening and often also a heat treatment is no option. Future work has to focus on sizing optimization (minimized clad areas and clad thickness), on strategies to quickly extract the heat by cooling and to explore adequate cladding strategies which minimize distortion.

Cladding a sheet prior to forming also causes distortion, which must be handled in the same way as for cladding on an already formed component (see above). However, straightening might also be an option. A major issue is the formability of the laser-cladded material. In this respect, the best choice will be to use the same material as the substrate, and to perform a heat treatment prior to forming. In this study, AlSi12 was used for reasons of availability of powder and process parameters. It is known that these alloys have limited formability. However, the flanging experiments and the metallographic analysis show that, to some extent, hole flanging of laser-cladded aluminum blanks seems possible. Although the ultimate strain of AlSi12 is in the range of five to six percent, a hole expansion ratio of 1.4 was achieved in the case where the cladding is inside the flange. The total sheet thickness of the unclad material (2.0 mm and 2.5 mm) was chosen in such a way that the sheet is drawn into the die with (2.0 mm) and without (2.5 mm) clearance. Forming is feasible in both cases for all hole expansion ratios. In case of the clad material, the likeliness of failure in the brittle clad layer is reduced by forming under direct contact pressure of the punch, which exerts a stress state of favorable triaxiality. This way, the largest of the three hole expansion ratios was viable while the smaller expansion ratios showed failure. Presumably, the presence of larger pores caused failure in the latter cases. Formability of laser clad material will be subject to large variance in the as-built condition since the size and spatial distribution of pores cannot be controlled. Forming of specimens with laser claddings on the outside of the flange led to failure in all cases, presumably due to the fact that the superimposed pressure was missing in these cases. However, it seems viable to plastically deform clad material to some extent under large superimposed pressure.

Nevertheless, future work should focus on cladding the same or at least similar alloys. To improve formability, laser heat treatment directly after cladding may be an option. If suitable alloys are tested and their suitability for forming is proven, a new type of tailored lightweight material, tailored laser-cladded blanks, would be available, with the potential to outperform existing tailored blanks in applications where freely designed reinforcements are needed.

Production considerations. Additive manufacturing is still a time-consuming process and therefore it is unlikely that tailored laser-cladded blanks or components will be an option for mass production. However, introducing the dieless additive manufacturing processes such as laser cladding into conventional production chains of sheet metal components offers the potential for producing locally reinforced parts, which can be produced without the manufacturing of a new tools or the use of fasteners or connectors. The process times in the two case studies was in the order of 10–20 s, which is compatible even with cycle times in the automotive industry.

Material efficiency. Additive manufacturing processes based on metal powder are typically considered more energy intensive than conventional manufacturing processes due to the production of powder, of which only a limited fraction of the size distribution is used, and due to the fact that the powder is melted in the additive manufacturing process. In lightweight components, high material efficiency may be achieved by application of additive manufacturing processes (mainly laser cladding), since the production of patches used in patchwork blanks by blanking/piercing operations creates a large amount of waste. Also, additive manufacturing opens up the chance of distributing the material precisely according to the applied loads. With locally variable material thicknesses, minimal weight designs may be achieved so that in total, less material is used in a given sheet metal component than with conventional solutions. Reinforcements can also be applied to plate or bulk components, which could be explored in future studies.

5. Conclusions

In the present study, it was explored whether additive manufacturing, i.e., laser cladding, could be used to manufacture flexibly applicable local patches to locally increase the stiffness or thickness of a sheet metal blank or sheet metal component. The following conclusions can be drawn from the presented results:

- Laser cladding can be used to locally reinforce sheet metal blanks with respect to lightweight design considerations. The resulting tailored laser-cladded blanks are a new type of lightweight material which can be designed such that they outperform currently available tailored blanks in lightweight design performance.
- Limited formability was observed to be the main obstacle of applying tailored laser-cladded blanks as semi-finished products. While the case study in the paper focuses on Al-Si of low formability, formability of laser-clad material could be improved using weldable wrought alloys and heat treatment prior to forming.
- Laser cladding may also be used for stiffness management of already formed components. However, the results of a pure sizing optimization may not be manufactured without distortion, which seems to be the main limiting factor for laser cladding on formed components.
- A constrained sizing optimization led to a design with minimum danger of distortion but reduced stiffness increase compared to the optimum found by sizing optimization.
- Application of additive manufacturing in sheet metal forming offers potentials for developing new products such as tailored laser-cladded blanks and for developing new lightweight design methods such as stiffness management of components, by integrating sizing optimization, distortion control and laser cladding.

Future work should also explore other applications of additively manufactured features on sheet metal components, i.e., functional features such as electrical contacts, pedestals or transitions to bulk components.

Acknowledgments: The depicted results were achieved to a great extent in the project “Materialeffiziente Herstellung belastungsgangepasster Blechbauteile mit durch Laseradditiv aufgebrachten flexiblen Verstärkungszonen” (Ref.-No. AiF 19292BG), which is financed and supervised by the European Research Association for Sheet Metal Working (EFB). In the scope of the programme to promote Industrial Collective Research they were funded by the German Federation of Industrial Research Associations (AiF) with means of the Federal Ministry of Economic Affairs and Energy (BMWi) on the basis of a decision by the German Bundestag. This funding is gratefully acknowledged.

Author Contributions: Bambach, M. devised the applications and experiments, performed the numerical simulations and wrote and edited the manuscript; Sviridov, A. performed the forming experiments and analyzed the experimental data; Weisheit, A. and Schleifenbaum, J.H. performed the laser cladding experiments of demonstrator I, the metallographic analysis and interpreted the results.

Conflicts of Interest: The authors declare no conflict of interest.

References

1. Merklein, M.; Johannes, M.; Lechner, M.; Kuppert, A. A review on tailored blanks—Production, applications and evaluation. *J. Mater. Process. Technol.* **2014**, *214*, 151–164. [CrossRef]
2. Buchmayr, B.; Figala, G.; Wunsch, K. Lokale fertigungstechnische Verstärkungskonzepte zur Erhöhung der Materialeffizienz. *BHM Berg Hüttenmännische Monatshefte* **2010**, *155*, 307–312. (In German). [CrossRef]
3. Hirt, G.; Dávalos-Julca, D.H. Tailored profiles made of tailor rolled strips by roll forming—part 1 of 2. *Steel Res. Int.* **2012**, *83*, 100–105. [CrossRef]
4. Weisheit, A.; Backes, G.; Gasser, A.; Wissenbach, K.; Poprawe, R. Powder injection: The key to reconditioning and generating components using laser cladding. *Geoforum* **2001**, *60*, 53–61.
5. Kaierle, S.; Barroi, A.; Noelke, C.; Hermsdorf, J.; Overmeyer, L.; Haferkamp, H. Review on Laser Deposition Welding: From Micro to Macro. *Phys. Procedia* **2012**, *39*, 336–345. [CrossRef]

6. Gasser, A. Fertigen und Instandsetzen mit generative Laserverfahren. *Maschinemarkt* **2014**, *38*, 44–47.
7. Weisheit, A.; Gasser, A.; Backes, G.; Jambor, T.; Pirch, N.; Wissenbach, K. Direct Laser Cladding, Current Status and Future Scope of Application. In *Laser-Assisted Fabrication of Materials*; Majumdar, J.D., Mann, I., Eds.; Springer Series in Material Science: Heidelberg, Germany, 2013.



© 2017 by the authors. Licensee MDPI, Basel, Switzerland. This article is an open access article distributed under the terms and conditions of the Creative Commons Attribution (CC BY) license (<http://creativecommons.org/licenses/by/4.0/>).

Article

Morphology Analysis of a Multilayer Single Pass via Novel Metal Thin-Wall Coating Forming

Xin Wang ^{*}, Jun Du, Zhengying Wei, Xuewei Fang, Guangxi Zhao, Hao Bai, Wei Liu, Chuanqi Ren and Yunfei Yao

State key Laboratory of Manufacturing System Engineering, Xi'an Jiaotong University, Xi'an 710049, China; jundu2010@mail.xjtu.edu.cn (J.D.); zywei@mail.xjtu.edu.cn (Z.W.); fangxuewei0920@gmail.com (X.F.); zgx6464946@gmail.com (G.Z.); zzujixiebaihao@163.com (H.B.); tyutliuwei@163.com (W.L.); legend7718@163.com (C.R.); yyf931012@stu.xjtu.edu.cn (Y.Y.)

* Correspondence: linkwangxin@aol.com; Tel.: +86-15667083308

Academic Editor: Manoj Gupta

Received: 30 June 2016; Accepted: 24 November 2016; Published: 9 December 2016

Abstract: Through using a novel micro-coating metal additive manufacturing (MCMAM) process in this study, the forming characteristics of the multilayer single-pass specimens were investigated. The forming defects including the porosity and the bonding quality between layers were analyzed. Moreover, we also attempted to study the effect of process parameters such as flow rate, deposition velocity, and layer thickness on the forming morphology. Based on the results, the optimization of process parameters was conducted for the fabrication of thin-wall MCMAM. Finally, estimation criteria for the integrity of the interfacial bond were established.

Keywords: additive manufacturing; forming defects; bonding quality; forming morphology

1. Introduction

Additive manufacturing (AM) has attracted much attention from the public due to its unique advantages, such as unrivaled design freedom and short lead times [1]. It can produce high-performance metal components rapidly using alloy powder or wires as raw material and applying a high-power laser or electron beam as a heat source [2–5]. However, the high capital costs and slow throughput printing have severely restricted its application.

To overcome the shortages of traditional AM, micro-coating metal additive manufacturing (MCMAM) has been proposed as a commercial manufacturing technology. Compared with traditional metal AM technologies, MCMAM has shown several advantages. At first, it provides a higher material utilization than selective laser melting (SLM) with a high deposition rate. Second, it produces less dust pollution than powder-based equipment when the powder material was recycled. Third, it has a lower equipment cost than SLM and electron beam machining (EBM) [6].

Xiong et al. investigated the forming characteristics of a multilayer single pass with the application of GMAW-based additive manufacturing [7]. Jorge et al. developed a fused deposition modeling (FDM) system for metals that can deposit electronic structures directly [8]. Yao et al. adopted a metal droplet deposition manufacturing process to reduce product development time as well as the cost of manufacturing [9]. However, deposition accuracy was difficult to control. In addition, the novel metal additive manufacturing process proposed in this paper was analyzed using a numerical simulation method. Nevertheless, the influences of process parameters on the forming morphology have never been mentioned [10].

Therefore, this paper is aimed at investigating the effects of the major process parameters on the forming morphology and the bonding quality between layers during the micro-coating additive

manufacturing. Moreover, a statistical investigation on the surface finish of fabricated specimens was also performed.

2. Experimental Procedure

In order to increase the productivity and reduce cost, a novel metal micro-coating technology—micro-coating metal additive manufacturing (MCMAM)—was proposed. A special micro-coating nozzle was designed. Molten metal is transported from the channel of the fused-coating nozzle to the region between the horizontal moving substrate and the thermal capillary flow. When the melt contacts the substrate or pre-solidified layers, cooling and solidification begin at the interface of the melt and substrate. The solidified structure will keep moving at the same speed and in the same direction as the substrate. The rapidly moving and advancing solidification front under cooling conditions will produce strong shear stress in the melt near the solidification front. Moreover, the interfacial shear stress may be able to shed the newly formed dendrites. The new forming process can significantly enhance metal forming efficiency. As a result, it is especially suitable for the fabrication of large structures in aerospace, the automobile industry, and national defense.

2.1. Experimental System

A schematic illustration of the principle of the MCMAM process and experimental platform is presented in Figure 1a. The equipment of MCMAM includes a pressure control system, an argon gas protection system, and a machine control system on the basis of a movable platform. In this experiment, the MCMAM was used to form specimens by controlling the motion of the 3D platform in accordance with data information. The 3D platform system has a PMAC (programmable multi-axis controller). Under the combined action of gas pressure, hydrostatic pressure, and surface tension, the molten metal flows through the channel in the fused-coating head, as shown in Figure 1b,c.

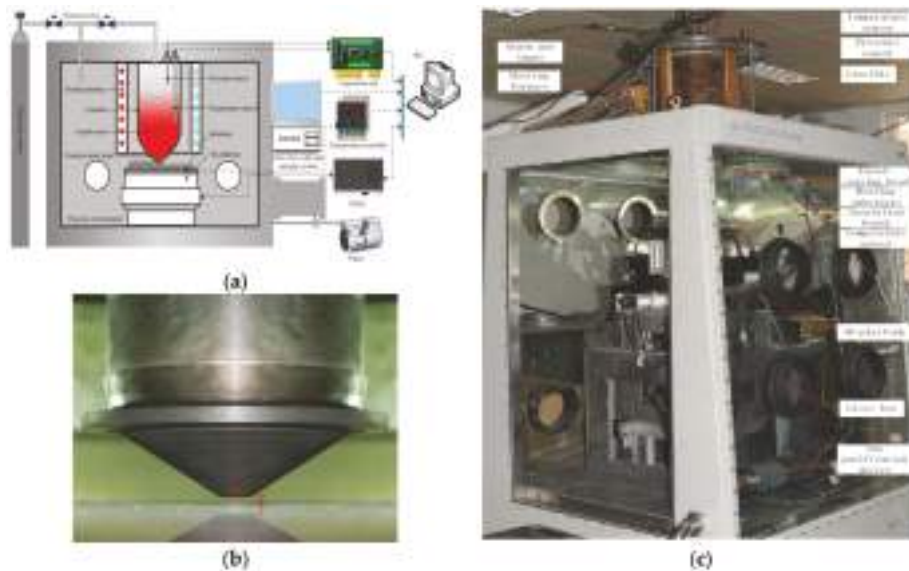


Figure 1. (a) Molten metal micro-coating equipment schematic diagram. (b) Nozzle practicality picture. (c) Molten metal micro-coating equipment practicality picture.

2.2. Arrangement of the Experiments

To evaluate the feasibility and the control parameters of the designed experiment, a Sn63Pb37 alloy was involved in this work. According to actual situation, the crucible temperature was heated to 270 °C, the initial distance between the micro-coating nozzle and the substrate was set to 1.6 mm, the substrate temperature was set to 90 °C, and the argon mass flowmeter pressure was set to 100 KPa. Single-layer single pass (SLSP) experimental conditions are shown in Table 1.

Table 1. Experimental condition of micro-coating metal additive manufacturing (MCMAM).

Property and Parameter	Value
Coating head temperature	270 °C
Heating substrate	90 °C
Argon mass flowmeter	20–70 mm ³ /s
Deposition velocity	9–24 mm/s
Initial distance	1.6 mm
Layer thickness	0.9–2.1 mm
Coating nozzle	0.3 mm
Pressure	100 KPa
Glove box	Ar (99.999%) (20 ppm)
Size of copper-clad substrate	300 mm × 200 mm × 10 mm
SLSP deposited length	130 mm
multilayer single pass deposited length	100 mm

3. Results and Discussion

As a basic unit, the forming process of a single-track specimen should be primarily investigated. There are many process parameters in the MCMAM forming process, including the deposition velocity, the flow rate, the distance from the nozzle to the workpiece, the heating temperature, the nozzle size, and the heat dissipation conditions, having great impacts on the final forming quality of specimens. The present paper focuses on the deposition velocity, the flow rate, and the layer thickness; thus, other factors are kept constant.

3.1. Preliminary Experiments to Determine the Process Window of SLSP

In this section, the effect of flow rate and deposition velocity on the forming morphology is explored. The flow rate varied from 20 to 70 mm³/s, and the deposition velocity varied from 9 to 24 mm/s. According to the parameters presented in Table 1, a set of preliminary experiments had been conducted. Moreover, the SLSP combination was evaluated according to the surface morphology and the relationship between the process parameters and the forming morphology of SLSP were analyzed, the results of which can be found in Figure 2.

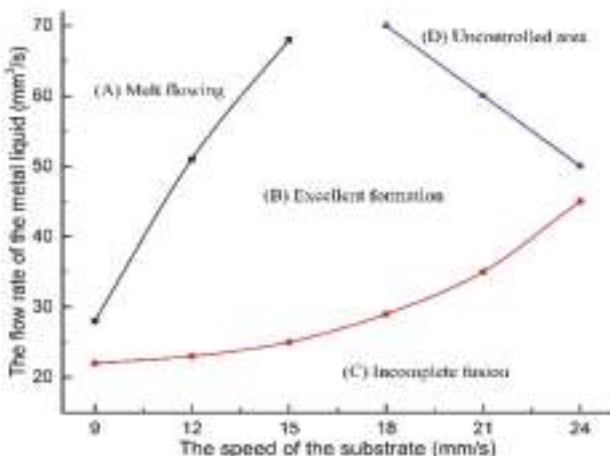


Figure 2. Process parameter set of various forming morphology in a single-layer single pass (SLSP).

The process parameters were divided into four categories. With a relatively low deposition velocity and high flow rate, Category A can easily cause an accumulation of the melt because the feeding speed of the melt is too high for the given deposition velocity, leading to a significant increment of the micro-coating width and an accumulation of molten metal at the starting and stopping of the SLSP. These problems remain unfavorable to the successful operation of the multilayer single-pass (MLSP) process. As a result, the forming efficiency was low, as shown in Figure 3a. For Category C, with a high deposition velocity and a low flow rate, the molten metal dragged due to surface tension, which caused necking. The position of necking leads to a decrease in mechanical properties in SLSP. The subsequent experiments in Region C were consequently discarded, as presented in Figure 3c. For Category D, with a high flow rate and deposition velocity, micro vibration occurred in the 3D-platform. Hence, the forming defects were aggravated, resulting in burr and distortions, as shown in Figure 3d. For Category B, the flow rate matched well with the deposition velocity, and the surface quality was satisfactory, as shown in Figure 3b.



Figure 3. Various forming morphology with different combinations of process parameters. (a) Melt flowing. (b) Excellent formation. (c) Incomplete fusion. (d) Uncontrolled area.

3.2. Influence of the Distance between the Nozzle and the Top Surface of the Previous Layer

In this section, only the layer thickness is discussed in order to maintain other parameter consistency. One goal of this experiment was to achieve multilayer deposition. After one layer was deposited, the platform was moved downward for a distance in the z-direction, and another layer was deposited over the previous one. The forming process of the MLSP is more complicated than the SLSP due to the complex morphologies of the pre-deposited layer. In this section, the forming process is based on the optimized process windows of the SLSP. Each thin-walled specimen has twelve layers that are 100 mm in length. If the forming defect occurs in the current layer, the forming process must be terminated.

The process parameters of Category B in Figure 2 were used. In the experiment, the deposition velocity was 18 mm/s, the flow rate was 50 mm³/s, and the layer thickness was set to 0.9 mm, 1.2 mm, 1.5 mm, 1.8 mm, and 2.1 mm, respectively, the platform was moved downward for a distance in the z-direction. Figure 4 mainly shows the experimental results. As shown in Figure 4a, the nozzle contacted completely with the workpiece when the thickness was 0.9 mm, resulting in wider layers, which was beneficial for the formation of a new layer, as good bonding quality can be achieved between layers. As shown in Figure 4b, when the thickness was 1.2 mm, the thin-wall was not too wide with heat capillary flow pressure and heat capillary flow, resulting in the most complex forming state. As shown in Figure 4c, the molten metal generated a drag angle when the thickness was 1.5 mm, which will be discussed in detail in the next section. As shown in Figure 4d, when the thickness was 1.8 mm, the random jet from the molten metal affected the forming morphology, which led to the failure of the subsequent deposition process. As shown in Figure 4e, the nozzle separated completely from the workpiece when the thickness was 2.1 mm. In addition, the high-speed melt had a strong impact on the free surface of the melt.

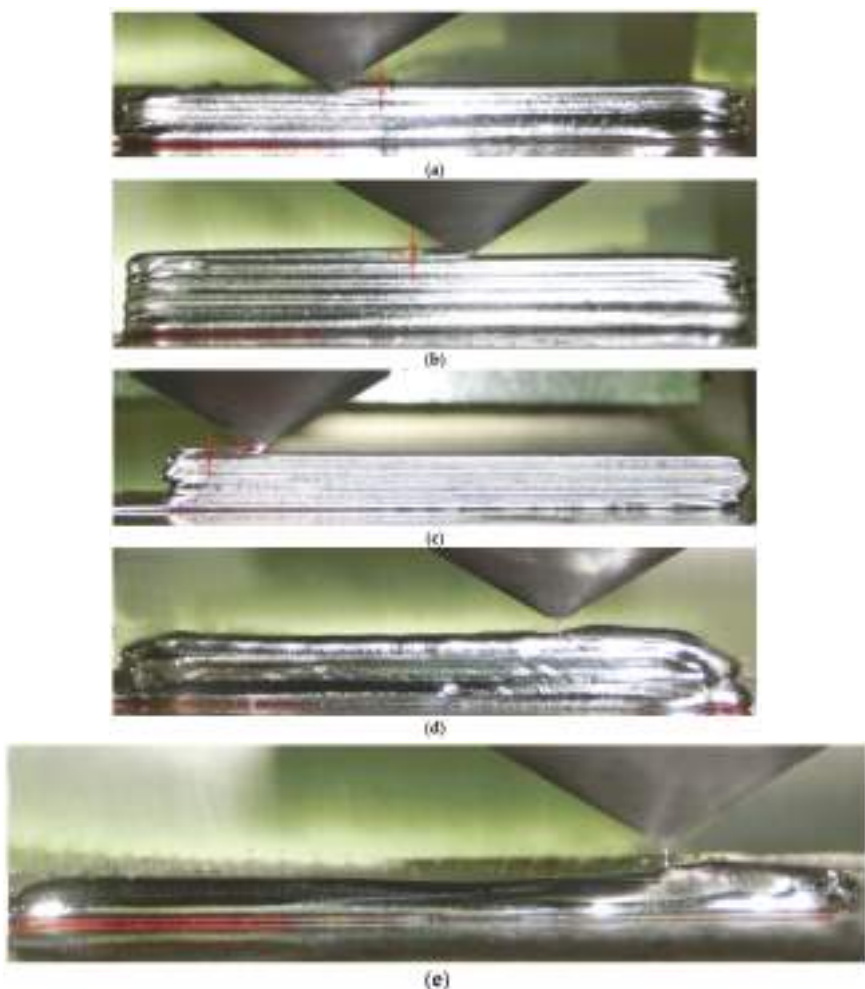


Figure 4. The deposited specimens in different layer thickness. (a) $\delta = 0.9$ mm. (b) $\delta = 1.2$ mm. (c) $\delta = 1.5$ mm. (d) $\delta = 1.8$ mm. (e) $\delta = 2.1$ mm.

To conclude, layer thickness is one of the major factors influencing the forming morphology. Different layer thicknesses will produce a compression or a jet. When the layer thickness is larger than 1.5 mm, the molten metal jet will negatively affect the free surface of the melt, usually causing damage to the previous layers or massive overflowing. When the layer thickness is smaller than 1.2 mm, the width of thin-wall specimens increases due to the nozzle extrusion pressure and, as a result, usually reduces the forming efficiency. The flat forming morphology can be achieved when the layer thickness is between 1.2 mm and 1.5 mm.

The forming morphology of the workpieces in Figure 4b,c are better than the others. Consequently, the process parameters of these two workpieces were applied to form a thin wall, as shown in Figure 5. In Figure 5a, the previous several layers were deposited with a good overlapping rate. However, the cumulative error made the bonding quality decrease, and the porosity increased during the subsequent depositions when the thickness was 1.5 mm. In Figure 5b, the layer thickness matches well with the height of the actual specimens. The ideal workpiece was obtained without any defects, and the morphology of each layer was uniform when the thickness was 1.2 mm.

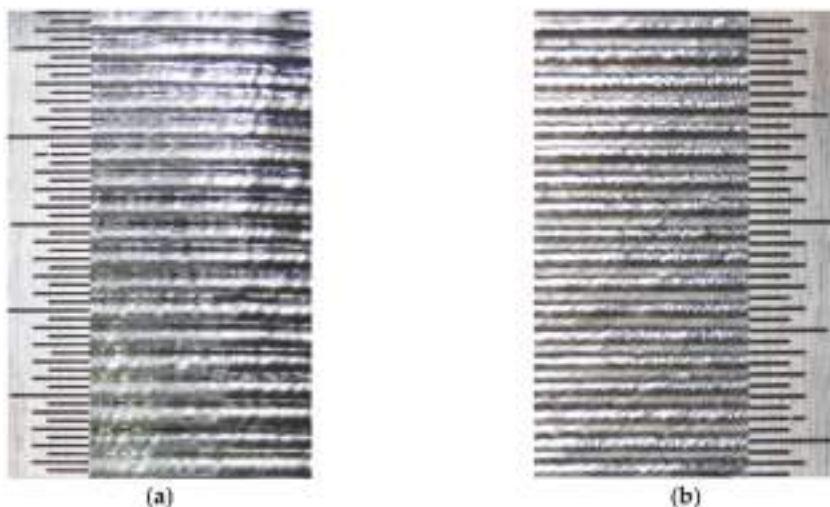


Figure 5. The deposited specimens in different layer thickness. (a) $\delta = 1.5$ mm. (b) $\delta = 1.2$ mm.

3.3. Waviness and Cross-Section Morphology Analysis of Thin-Walled Specimens

The layer thickness and surface quality remain the most important issues to be taken into consideration for the thin-walled experiments. The waviness was applied to evaluate the surface quality, including three major indexes (W_a , W_q and W_z). The indexes, W_a , W_q , and W_z , denote the arithmetical mean deviation of the assessed profile, the root mean square deviation of the assessed profile, and the maximum height of the assessed profile, respectively. In addition, it was found that the waviness of the formed specimens is greatly affected by the layer thickness. As illustrated in Figure 6a, the thin-walled specimen was formed based on the following process parameters: a deposition velocity of 18 mm/s, a flow rate of 50 mm³/s, and a layer thickness of 1.2 mm. The cross section of the specimen is shown in Figure 6b, and the corresponding measured data was shown in Figure 6c. The waviness indexes were analyzed, and the results are as follows: $W_a = 0.9448$, $W_q = 0.963$, and $W_z = 0.303$.

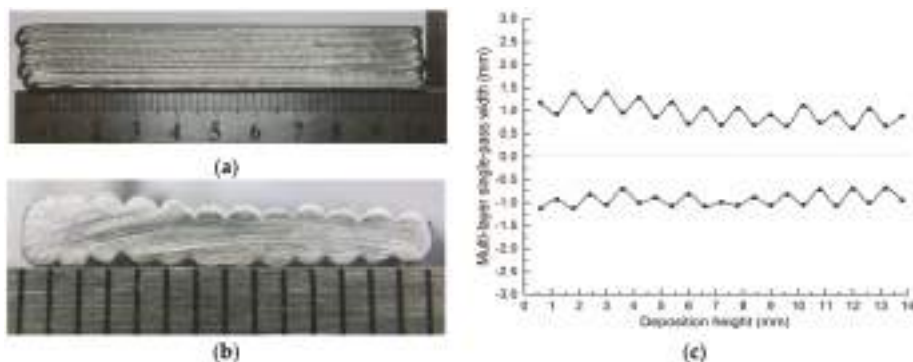


Figure 6. Thin wall with a 1.2 mm layer thickness for each layer: (a) Main view. (b) Cross-section view. (c) Cross-section data statistics.

4. Conclusions

To conclude, a new metal 3D printing process—micro-coating metal additive manufacturing (MCMAM)—was investigated in this paper. The forming morphologies of the deposited thin-walled specimens were analyzed, and the main findings are summarized as follows:

- The MCMAM technology is considered an economical and effective forming process. The forming efficiency of the MCMAM up to $50 \text{ mm}^3/\text{s}$ (viz. 1490 g/h) is doubled, compared to the metal droplet deposition.
- The layer thickness is one of the major factors, influencing the forming morphology. The forming morphology of the thin-wall specimen is relatively the best when the layer thickness is set to 1.2 mm, and the metallurgical bonding of the adjacent layers can be obtained.
- The waviness was used to analyze the forming morphology of the thin-walled specimen. The values of the surface waviness indexes are $Wa = 0.9448$, $Wq = 0.963$, and $Wz = 0.303$ when the layer thickness is 1.2 mm.

Acknowledgments: Project supported by the State Key Development Program Research of China (2016YFB1100400), the national project (20140530) “3D Printing Electrical Fittings Droplet Forming and Shaping the Experimental Prototype Development Platform”, the China Postdoctoral Science Foundation (2014m560764) “Study on Metal Micro Jet Droplet Electromagnetic Confinement Deposition Forming Mechanism” and the Fundamental Research Funds for the Central Universities (xjj2016124).

Author Contributions: Jun Du and Zhengying Wei conceived and designed the experiments; Xin Wang, Xuewei Fang, and Guangxi Zhao performed the experiments; Hao Bai and Wei Liu analyzed the data; Chuanqi Ren and Yunfei Yao contributed reagents/materials/analysis tools; Xin Wang wrote the paper.

Conflicts of Interest: The authors declare no conflict of interest.

References

1. Beaman, J.J.; Deckard, C.R. Selective Laser Sintering with Assisted Powder Handling. U.S. Patent 4938816, 1990.
2. Arcella, F.G.; Froes, F.H. Producing titanium aerospace components from powder using laser forming. *JOM* **2000**, *52*, 2–30. [CrossRef]
3. Clare, A.T.; Chalker, P.R.; Davies, S.; Sutcliffe, C.J.; Tsopanos, S. Selective laser melting of high aspect ratio 3D nickel–titanium structures two way trained for MEMS applications. *Int. J. Mech. Mater. Des.* **2008**, *4*, 181–187. [CrossRef]
4. Aiyiti, W. Investigation of the overlapping parameters of MPAW-based rapid prototyping. *Rapid Prototyp. J.* **2006**, *12*, 165–172. [CrossRef]

5. Xiong, J.; Zhang, G.; Zhang, W. Forming appearance analysis in multi-layer single-pass GMAW-based additive manufacturing. *Int. J. Adv. Manuf. Technol.* **2015**, *80*, 1767–1776. [CrossRef]
6. Heralic, A.; Christiansson, A.K.; Ottosson, M.; Lennartson, B. Increased stability in laser metal wire deposition through feedback from optical measurements. *Opt. Lasers Eng.* **2010**, *48*, 478–485. [CrossRef]
7. Xiong, J.; Zhang, G. Adaptive control of deposited height in GMAW-based layer additive manufacturing. *J. Mater. Process. Technol.* **2014**, *214*, 962–968. [CrossRef]
8. Mireles, J.; Espalin, D.; Roberson, D.A.; Zinniel, B.; Medina, F.; Wicker, R. Fused Deposition Modeling of Metals. In Proceedings of the Solid Freeform Fabrication Symposium, Austin, TX, USA, 6–8 August 2012; pp. 836–845.
9. Yao, Y.; Gao, S.; Cui, C. Rapid prototyping based on uniform droplet spraying. *J. Mater. Process. Technol.* **2004**, *146*, 389–395.
10. Du, J.; Wei, Z.; Wang, X.; Fang, X.; Zhao, G. A novel high-efficiency methodology for metal additive manufacturing. *Appl. Phys. A* **2016**, *122*, 945. [CrossRef]



© 2016 by the authors. Licensee MDPI, Basel, Switzerland. This article is an open access article distributed under the terms and conditions of the Creative Commons Attribution (CC BY) license (<http://creativecommons.org/licenses/by/4.0/>).

MDPI AG
St. Alban-Anlage 66
4052 Basel, Switzerland
Tel. +41 61 683 77 34
Fax +41 61 302 89 18
<http://www.mdpi.com>

Metals Editorial Office
E-mail: metals@mdpi.com
<http://www.mdpi.com/journal/metals>



MDPI AG
St. Alban-Anlage 66
4052 Basel
Switzerland

Tel: +41 61 683 77 34

Fax: +41 61 302 89 18

www.mdpi.com



ISBN 978-3-03842-592-2